

Special Scientific Issue of Institute of Isotopes,  
Hungarian Academy of Sciences

# EFNUDAT – Slow and Resonance Neutrons

Proceedings of the Scientific Workshop on Nuclear Data Measurements,  
Theory and Applications  
Normafa Hotel, Budapest, Hungary  
23–25 September 2009

Edited by Tamás Belgya

**EFNUDAT**   
European Facilities for Nuclear Data Measurements



**IIAS**



# **EFNUDAT – Slow and Resonance Neutrons**

## **Proceedings**

**of the 2<sup>nd</sup> EFNUDAT workshop on Neutron Measurements,  
Theory and Applications**

23–25 September 2009  
Normafa Hotel, Budapest, Hungary

**Edited by Tamás Belgya**

**Proceedings of the 2<sup>nd</sup> EFNUDAT workshop  
EFNUDAT – Slow and Resonance Neutrons**

**Legal Notice**

Neither the Institute of Isotopes nor any person acting on behalf of the Institute of Isotopes is responsible for the use which might be made of this publication.

**© Institute of Isotopes, HAS, 2010**

Reproduction is authorised provided the source is acknowledged

**Editor**

*Tamás Belgya*

Department of Nuclear Research  
Institute of Isotope, Hungarian Academy of Sciences  
E-mail: [belgya@iki.kfki.hu](mailto:belgya@iki.kfki.hu)  
Tel.: +36-1-392-2539  
Fax: +36-1-392-2584

**Published by**

Institute of Isotope, Hungarian Academy of Sciences  
Konkoly-Thege u. 29–33  
1121 Budapest  
Hungary  
Home page: [http://www.iki.kfki.hu/index\\_en.shtml](http://www.iki.kfki.hu/index_en.shtml)

**Responsible publisher**

*László Wojnarovits, director*

**ISBN 978-963-7351-19-8**

*Printed in Hungary*

## Foreword

The first scientific workshop of EFNUDAT (European Facility for Nuclear Data Measurements) project was held at the JRC IRMM in Geel, Belgium, chaired by *Franz-Josef Hamsch*, Neutron Physics Unit, JRC IRMM. Its proceedings are available at <http://www.efnudat.eu/workshops.html>.

The second scientific workshop on Nuclear Data Measurements, Theory and Applications entitled “EFNUDAT – Slow and Resonance Neutrons” was held in the Normafa Hotel, Budapest, Hungary, 23–25 September 2009. The workshop was organized by the Department of Nuclear Research of the Institute of Isotopes. The organizers were advised by an International Advisory Board. Its members were *Gerard Barreau* (CEN, Bordeaux-Gradignan, France), *Eckart Grosse* (FZ, Rossendorf, Germany), *Frank Gunsing* (CEA, Saclay, France), *Franz-Josef Hamsch* (JRC IRMM, Geel, Belgium), *Alberto Mengoni* (IAEA, Vienna, Austria), *Masumi Oshima* (JAEA, Tokai-Mura, Japan), *Peter Schillebeeckx* (JRC IRMM, Geel, Belgium).

The workshop focused on nuclear data measurements using slow and resonance neutrons, their applications to the development of nuclear reactors and to waste management, and to the development of theoretical models of excitation and deexcitation. Presentations of facilities, experimental setups, and new data acquisition systems were also welcomed.

The 32 oral presentations at the workshop covered the latest achievements in the field of nuclear data measurements in Europe, in the United States and Japan. Six invited speakers introduced the main topics of the workshop. About one third of the presentations were delivered by young scientists, and more than 45 persons participated the workshop.

The workshop was organized within the EFNUDAT project with its full financial support for the speakers. The EFNUDAT is an Integrated Infrastructure Initiative project within the 6<sup>th</sup> Framework Program of the European Community. The main objective of EFNUDAT is to promote the coherent use and integration of infrastructure related services via networking as well as transnational access to the participating facilities for nuclear data measurements and joint research activities. More details on EFNUDAT can be found at <http://www.efnudat.eu/>.

Finally, I would like to give thanks to the International Advisory Board for their valuable advice, which helped me to set up a really good program, and also to all of the speakers whose contributions made up the program.

I would like to express my special thank to the members of our local organization committee *Katalin Gméling*, *Zoltán Kis*, *Zsolt Révay*, *László Szentmiklósi*, *Veronika Szilágyi* and to our workshop secretary *Zita Tóth*, who helped to make this workshop a successful one.

Budapest, July 2010



Tamás Bélgya



# Contents

<b>Foreword</b>	iii
<b>High-resolution neutron cross-section measurements at the Oak Ridge Electron Linear Accelerator</b>	1
<i>K. H. Guber</i>	
<b>A new TOF facility at J-PARC MLF</b>	9
<i>M. Igashira, Y. Kiyanagi, M. Oshima</i>	
<b>Neutron cross section measurements in the resonance region at GELINA</b>	15
<i>P. Sieglér, P. Schillebeeckx, S. Kopecký</i>	
<b>Measurements of neutron total cross-sections of Niobium &amp; Palladium from 0.1 to 100 eV</b>	21
<i>A. K. M. Moinul Haque Meaze, M. Shakilur Rahman, G. N. Kim, Y. D. Oh</i>	
<b>The neutron resonance parameters of <math>^{197}\text{Au}</math> from transmission, capture and self-indication measurements at GELINA</b>	27
<i>C. Massimi, A. Borella, S. Kopecký, M. Moxon, P. Schillebeeckx</i>	
<b>Status and perspectives of the n_TOF facility at CERN</b>	33
<i>M. Calviani, S. Andriamonje, J. Andrzejewski, L. Audouin, V. Bécáres, F. Becvár, F. Belloni, B. Berthier, E. Berthoumieux, M. Brugger, F. Calviño, D. Cano-Ott, C. Carrapiço, P. Cennini, F. Cerutti, E. Chiaveri, M. Chin, N. Colonna, G. Cortés, M. Cortés-Giraldo, I. Dillmann, C. Domingo-Pardo, I. Duran, M. Fernández-Ordóñez, A. Ferrari, S. Ganesan, G. Giubrone, M. B. Gómez-Hornillos, I. F. Gonçalves, E. González-Romero, F. Gramegna, C. Guerrero, F. Gunsing, S. Harrisopulos, M. Heil, K. Ioannides, E. Jericha, Y. Kadi, F. Käppeler, D. Karadimos, M. Krücka, E. Leebos, C. Lederer, H. Leeb, R. Losito, M. Lozano, J. Marganiec, S. Marrone, T. Martínez, C. Massimi, P. F. Mastinu, M. Meaze, E. Mendoza, A. Mengoni, P. M. Milazzo, M. Mosconi, R. Nolte, M. C. Ovejero, C. Paradela, A. Pavlik, J. Perkowski, R. Plag, J. Praena, J. M. Quesada, T. Rauscher, R. Reifarth, C. Rubbia, R. Sarmiento, G. Tagliente, J. L. Tain, D. Tarrío, L. Tassan-Got, G. Vannini, V. Variale, P. Vaz, A. Ventura, V. Vlachoudis, R. Vlastou, Z. Vykydal, A. Wallner, C. Weiß</i>	
<b>Characterization of the new neutron beam at n_TOF-Ph2</b>	39
<i>C. Guerrero, S. Andriamonje, J. Andrzejewski, L. Audouin, V. Bécáres, F. Bečvář, F. Belloni, B. Berthier, E. Berthoumieux, M. Brugger, M. Calviani, F. Calviño, D. Cano-Ott, C. Carrapiço, P. Cennini, F. Cerutti, E. Chiaveri, M. Chin, N. Colonna, G. Cortés, M. Cortés-Giraldo, I. Dillmann, C. Domingo-Pardo, I. Duran, M. Fernández-Ordóñez, A. Ferrari, S. Ganesan, I. Giomataris, G. Giubrone, M. B. Gómez-Hornillos, I. F. Gonçalves, E. González-Romero, F. Gramegna, F. Gunsing, S. Harrisopulos, M. Heil, K. Ioannides, E. Jericha, Y. Kadi, F. Käppeler, D. Karadimos, M. Krücka, E. Leebos, C. Lederer, H. Leeb, R. Losito, M. Lozano, J. Marganiec, S. Marrone, T. Martínez, C. Massimi, P. F. Mastinu, M. Meaze, E. Mendoza, A. Mengoni, P. M. Milazzo, M. Mosconi, R. Nolte, M. C. Ovejero, T. Papaevangelou, C. Paradela, A. Pavlik, J. Perkowski, R. Plag, J. Praena, J. M. Quesada, R. Reifarth, C. Rubbia, R. Sarmiento, G. Tagliente, J. L. Tain, D. Tarrío, L. Tassan-Got, G. Vannini, V. Variale, P. Vaz, A. Ventura, V. Vlachoudis, R. Vlastou, Z. Vykydal, A. Wallner, C. Weiß (The n_TOF Collaboration)</i>	
<b>Preliminary formulation of a nuclear data roadmap for designing the European Spallation Source (ESS)</b>	45
<i>M. P. W. Chin, F. Plewinski, C. Kharoua, E. Noah, M. Lindroos</i>	

<b>Using neutron resonances for non-destructive material analysis: the ANCIENT CHARM project</b>	<b>51</b>
<i>E. Perelli Cippo, G. Gorini, P. Schillebeeckx, M. C. Moxon and the Ancient Charm collaboration</i>	
<b>Neutron resonance-capture analysis and artifacts studied at the GELINA facility</b>	<b>59</b>
<i>H. Postma, P. Schillebeeckx and the Ancient Charm collaboration</i>	
<b>Nuclear data measurements with slow neutrons at Institut Laue Langevin</b>	<b>65</b>
<i>U. Köster</i>	
<b>Slow neutron facilities at the National Physical Laboratory, UK</b>	<b>75</b>
<i>N. P. Hawkes, P. Kolkowski, D. J. Thomas</i>	
<b>Cross section measurements for thermal neutron-induced reactions on actinides at the ILL reactor</b>	<b>81</b>
<i>A. Letourneau, E. Dupont, P. Mutti, S. Panebianco</i>	
<b>Measurements of Thermal-Neutron Capture Cross-Sections for Radioactive Nuclides</b>	<b>87</b>
<i>S. Nakamura</i>	
<b>Photon strength in heavy nuclei in correlation to the number of valence nucleons</b>	<b>93</b>
<i>E. Grosse, A. R. Junghans and the transmutation research team of FZD</i>	
<b>Preparation and characterization of thin film nuclear targets by vacuum evaporation</b>	<b>101</b>
<i>D. Sapundjiev, G. Sibbens, A. Moens, K. Luyckx, M. Peeters, R. Eykens, Y. Aregbe</i>	
<b>Model defects for nuclear data evaluation</b>	<b>109</b>
<i>St. Gundacker, H. Leeb</i>	
<b>Determination of thermal radiative capture cross section</b>	<b>115</b>
<i>T. Belgya</i>	
<b>Determination of the total neutron capture cross section for <math>^{58}\text{Ni}(n,\gamma)^{59}\text{Ni}</math> reaction</b>	<b>121</b>
<i>Z. Kis, T. Belgya, L. Szentmiklósi, F. Gunsing</i>	
<b>Preparatory experiments for cold-neutron induced fission studies at IKI</b>	<b>127</b>
<i>A. Oberstedt, S. Oberstedt, R. Billnert, J. Karlsson, X. Ledoux, J.-G. Marmouget, F.-J. Hamsch</i>	
<b>VERDI – a double (v, E) fission fragment spectrometer</b>	<b>133</b>
<i>S. Oberstedt, R. Borcea, Th. Gamboni, W. Geerts, F.-J. Hamsch, R. Jaime Tornin, A. Oberstedt, M. Vidali</i>	
<b>The effect of pulse pile-up from proton recoils</b>	<b>139</b>
<i>E. Birgersson, F.-J. Hamsch, A. Oberstedt, S. Oberstedt</i>	
<b>MCNPX simulation for optimization of efficiency of a <math>4\pi</math> neutron detector for beta delayed neutron emission measurements</b>	<b>145</b>
<i>V. Gorlychev, M. B. Gómez Hornillos, G. Cortés, R. Caballero-Folch, A. Poch, C. Pretel, J. L. Taín, D. Cano-Ott, F. Calviño, T. Martínez</i>	
<b>Characterization of neutron detectors for nuclear technology applications</b>	<b>149</b>
<i>T. Martinez, J. Agramunt, A. Algora, A. Aprahamian, D. Cano-Ott, L. M. Fraile, A. R. Garcia, A. Gottardo, C. Guerrero, M. D. Jordan, H. Mach, E. Mendoza, M. Mosconi, R. Nolte, M. C. Ovejero, E. Reillo, J. L. Tain, J. J. Valiente, D. Villamarin</i>	
<b>Cross-section Measurements of (n,xn) Threshold Reactions</b>	<b>155</b>
<i>O. Svoboda, A. Krása, M. Majerle, J. Vrzalová, V. Wagner</i>	
<b>Author Index</b>	<b>163</b>

# High-resolution neutron cross-section measurements at the Oak Ridge Electron Linear Accelerator

*Klaus H. Guber<sup>1)</sup>*

1) Oak Ridge National Laboratory, P.O. Box 2008, Oak Ridge, TN 37831-6356, USA  
[guberkh@ornl.gov](mailto:guberkh@ornl.gov)

**Abstract:** Over the last three decades, the Oak Ridge Electron Linear Accelerator (ORELA) has produced many neutron-induced cross-section data. ORELA is the only high-power white neutron source with excellent time resolution still operating in the United States and is ideally suited for experiments to measure neutron fission, total, ( $n,\alpha$ ), and capture cross sections in the energy range from 1 eV to as high as several MeV. Recent measurements have included neutron capture measurements on  $^{39,41}\text{K}$ ,  $^{35,37}\text{Cl}$ , F, Mn,  $^{58,60}\text{Ni}$ ,  $^{53}\text{Cr}$ , natural Cr,  $^{48}\text{Ti}$ , natural Ti, and  $^{95}\text{Mo}$  and total cross-section measurements on natural Cl, natural K,  $^{95}\text{Mo}$ , Mn,  $^{53}\text{Cr}$ , natural Cr,  $^{48}\text{Ti}$ , natural Ti, and  $^{64}\text{Zn}(n,\alpha)$ . Many of these measurements were carried out to support the U.S. Nuclear Criticality Safety Program. Concerns have been raised about many of the older nuclear data evaluations important for criticality safety. For example, the time-of-flight resolution and accuracy of some of the existing data are too poor for new evaluations and thus applications. Several of these data are also important input parameters for the ongoing nuclear astrophysics program, which investigates the s-process nucleosynthesis in asymptotic giant branch stars. Here the Maxwellian-averaged neutron capture cross sections at  $kT = 8$  and 30 keV are of importance. This paper provides an overview of the high-resolution cross-section measurement facility ORELA and describes the current measurement activities.

## Introduction

Concerns about data deficiencies in some existing cross-section evaluations from libraries such as ENDF/B, JEFF, or JENDL for nuclear criticality calculations have been a prime motivator for new cross-section measurements at the Oak Ridge Electron Linear Accelerator (ORELA). There are many troubles associated with existing nuclear data, such as problems related to improper pulse-height weighting functions, neutron sensitivity backgrounds, poorly characterized samples, poor time-of-flight (TOF) resolution, and too restricted energy range. For example, corrigenda were published after discovering errors in the computer data reduction code. (Correction factors ranged from 0.7480 to 1.1131 for 46 nuclides from  $^{24}\text{Mg}$  to  $^{232}\text{Th}$  [1] and from 0.9507 to 1.208 for 47 nuclides from  $^{23}\text{Na}$  to  $^{206}\text{Pb}$  [2].) Deficiencies in nuclear data may occur in the resolved- and unresolved-resonance regions. Consequently, evaluated data may not be adequate for nuclear criticality calculations in which effects such as self-shielding, multiple scattering, or Doppler broadening are important. Furthermore, many evaluations for nuclides having small neutron capture cross sections are erroneously large because the neutron sensitivity of the old measurements was underestimated. Although their neutron capture cross sections are small, these nuclides can be important absorbers in many criticality calculations, and accurate cross-section data are essential. Over the last four decades, many neutron-induced cross-section measurements have been performed at ORELA. It is ideally suited to measure fission, neutron total, and capture cross sections in the resolved energy range from 1 eV to  $\sim 700$  keV, depending on the nuclide. This energy range is most important for nuclear criticality safety applications, in which the neutron spectrum shifts from thermal to higher energies.

## Nuclear data

High-quality nuclear data are vital for the design and analysis of any nuclear system, such as reactor cores, fuel elements, and storage of mixtures of nuclear waste with other materials, as well as burned fuel elements. Pertinent nuclear data are also necessary for waste transmutation, accelerator-driven systems, and GEN-IV reactor design. All state-of-the-art analysis codes for nuclear systems rely on the use of evaluated cross-section data from nuclear data libraries. Some of the problems related to nuclear data found in the data libraries are portrayed here in more detail.

The validity of the calculated pulse-height weighting function used in the neutron capture experiments was questioned after a 20% discrepancy was found in the neutron width of 1.15-keV resonance in Fe measured with  $C_6D_6$  compared to transmission measurements. Using an experimentally determined weighting function, Corvi et al. [3] demonstrated that this discrepancy could be resolved. On the other hand, using the Monte Carlo code EGS4 [4], Perey et al. [5] showed that a careful calculation of the weighting function could also resolve this problem.

The neutron sensitivity of the experimental setup was often underestimated in previous neutron capture experiments. This background is caused by neutrons scattered from the sample and captured in the detector or surroundings within the time corresponding to the width of the resonance. As a consequence, many evaluations for nuclides having small neutron capture cross sections are erroneously large, as shown in Fig.1 in the case of neutron capture on natural Ti. Although the neutron capture cross sections are small, they can be important absorbers in criticality calculations, and accurate cross-section data are essential.

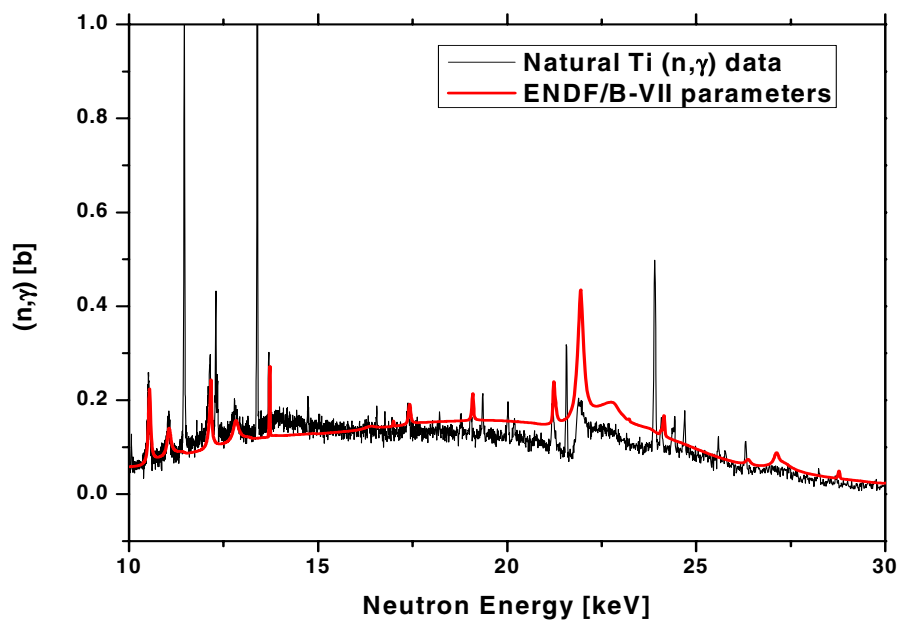


**Figure 1.** Comparison of new ORELA experimental data for natural Ti with the ENDF/B-VII evaluation (red line) reveals problems with old nuclear data.

Usually, enriched samples are used in the experiments, but the sometimes poorly characterized chemical composition of the samples result in large systematic errors in some measurements. The inventory form of the enriched isotope materials are, in many cases, oxides. They are known to be hygroscopic and can pick up water fairly easy. This could result in a change of the chemical composition of the oxide, if not treated correctly. Without precautions, the rising water content in the sample could lead (via moderation effects) to false large results.

Many of the older cross-section measurements were performed with too-large data binning because of the limiting computer storage systems. As a result, the obtained data sets sometimes have too few data points over the resonance for the analysis programs, such as SAMMY [6], to accurately calculate the corrections of experimental effects such as Doppler broadening, self-shielding, and multiple scattering. Finally, many of the older experiments were run with an energy cutoff of around 3 keV because there was no interest in the resonance data below that cutoff. However, this missing energy range is sometimes of importance for nuclear criticality calculations.

## Experimental setup at ORELA

ORELA is the only high-power white neutron source with excellent time resolution in the keV neutron energy range still operating in the United States (Fig. 2). ORELA consists of a 180-MeV electron linear accelerator, neutron-producing water-cooled Ta-target, underground and evacuated flight tubes, sophisticated detectors, and data acquisition systems. It is a highly flexible accelerator with a varying repetition rate between 1 and 1000 Hz and a neutron burst width between 2 and 30 ns. This leads to an average neutron flux of  $10^{14}$  neutrons per second. Simultaneous measurements are possible at 18 detector stations on 10 separate flight paths at distances between 9 and 200 m from the neutron source. The TOF technique is used for measuring neutron-induced cross-section data in the energy range of a few eV up to 50 MeV, such as transmission measurements (total cross sections), capture cross sections, fission cross sections, elastic cross sections, and neutron production cross sections.

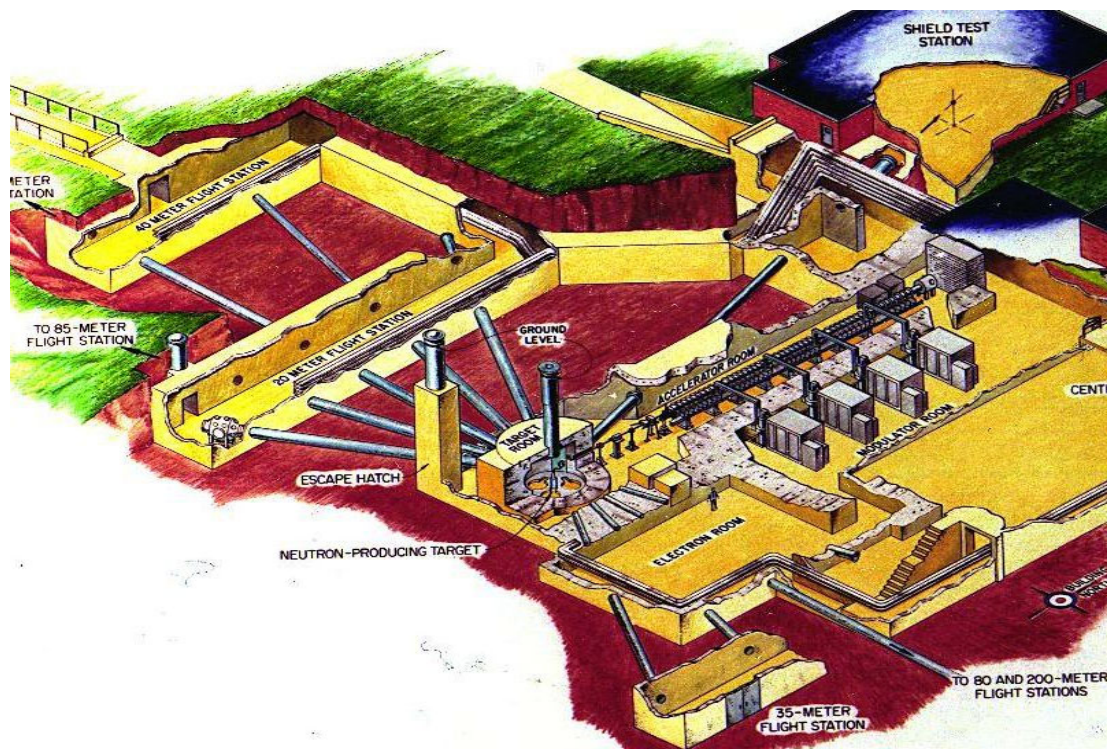


**Figure 2.** Layout of ORELA

### Capture measurements

The neutron capture experiments were performed at the 40-m flight station of ORELA using flight path 7. The employed experimental technique was the pulse-height-weighting method using a pair of deuterated benzene ( $C_6D_6$ ) detectors. Compared to the old ORELA setup [7], the capture system has been improved in several ways. First, the amount of structural material surrounding the sample and detectors to reduce the background due to sample-scattered neutrons (neutron sensitivity) was minimized. This was achieved by removing the massive Al-sample changer and replacing the beam pipe with a thin carbon fiber tube. In addition, the massive detector housings were removed and replaced with reduced-mass detector mounts. Second, the more neutron-sensitive  $C_6F_6$   $\gamma$ -ray detectors were replaced with  $C_6D_6$ , which has much lower neutron sensitivity. More details about these improvements can be found in the papers by Koehler et al. [8, 9], in which the impact of the neutron sensitivity was impressively demonstrated in a high-resolution TOF measurement for  $^{88}Sr$ . For the two prominent resonances at 289 and 325 keV with neutron widths  $g\Gamma_n = 24,932$  and  $22,082$  eV, respectively, a reduction of capture widths by an average factor of five was reported. And finally, the more sophisticated computer code EGS4 was used to calculate the appropriate detector weighting function for each experiment. All structural materials within 30 cm of the detectors, including the sample, were incorporated into these calculations. The code was used to calculate the response functions of the detector for various monoenergetic  $\gamma$ -rays. The resulting pulse-height spectra were then broadened using a resolution function. The final

weighting function was calculated from these broadened spectra using a least-squares fitting code.

With this setup (Fig. 3), several neutron capture cross-section experiments were performed over the last few years, mainly on isotopes that have small  $(n,\gamma)$  cross sections and are of interest to the nuclear criticality and safety community. Samples measured included extremely high-purity Al (0.01520 atom/b and 0.04573 atom/b), high-purity natural Si sample (0.07831 atom/b), natural LiCl sample (0.09812 atom/b), Teflon (for fluorine) sample (0.05086 atom/b), and a natural  $K_2CO_3$  sample (0.0088791 atom/b), as well as an enriched  $^{41}KCl$  sample. More recent measurements included Mn (0.018986 atom/b), natural Cr (0.018813735 atom/b),  $^{53}Cr$  (0.0133 atom/b),  $^{58}Ni$  (0.036354314 atom/b),  $^{60}Ni$  (0.036598 atom/b), natural Ti (0.035184887 atom/b) and  $^{48}Ti$  (0.009138552 atom/b).

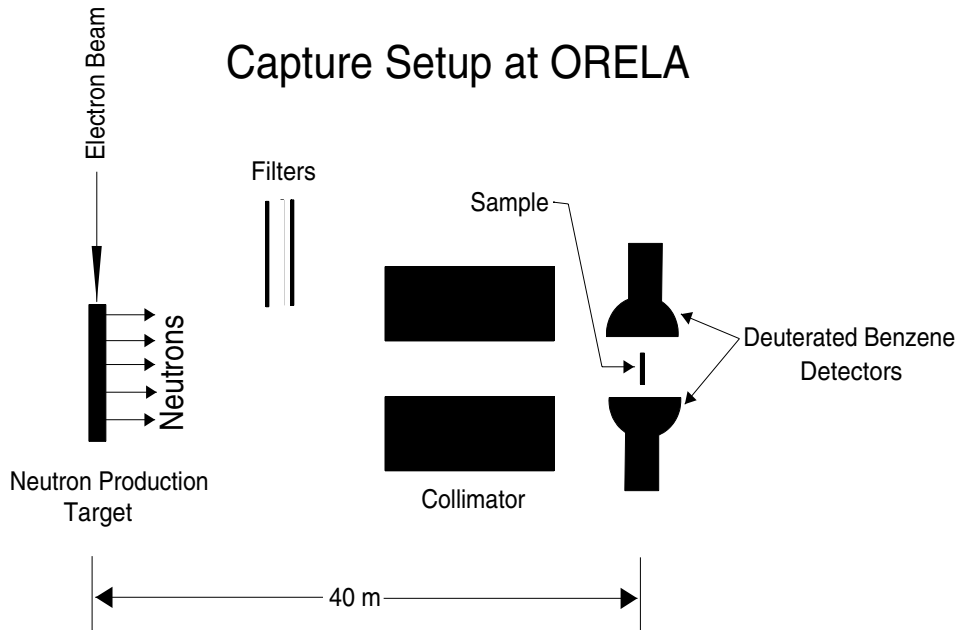


**Figure 3.** Schematic sketch of the neutron capture setup at ORELA.

To reduce the  $\gamma$ -ray background from the neutron production target, a 1.27-cm-thick Pb filter was used, and a  $0.48\text{-g/cm}^2$   $^{10}B$  filter served to eliminate pulse overlap by absorbing low-energy neutrons. Otherwise, these neutrons would be interpreted from the data-acquisition system as higher-energy neutrons from the next neutron pulse. Normalization of the capture efficiency was carried out in a separate measurement using the “saturated resonance” technique by means of the 4.9-eV resonance from a gold sample [10]. A 0.5-mm-thick  $^6Li$ -glass scintillator at a distance of 39.695 m from the neutron target was used to monitor the neutron flux.

### Transmission measurements

High-resolution transmission experiments for determining the total cross sections are not only indispensable for an evaluation, but also a necessity for the analysis of neutron capture cross sections to apply all the corrections for the experimental effects. Because capture experiments cannot be performed with an infinitely thin sample (in fact, sometimes the samples are quite thick), the corrections for self-shielding and multiple scattering can be sizeable. Therefore, corresponding total cross-section measurements were made when needed. In addition, some resonances with small radiation widths are not visible in the neutron capture data and vice versa. For the Al transmission measurements, the two samples (0.0189 and 0.1513 atom/b) were mounted in the sample changer positioned about 10 m from the neutron target in the beam of ORELA. For the Cl transmission measurement, a natural  $CCl_4$  (thickness for Cl 0.2075 atom/b) sample was used with a corresponding C compensator in the open beam. For the K transmission, two metallic samples (0.013367 and 0.10517 atom/b) were mounted in a sealed brass holder. To complement the more recent

capture measurements, transmission experiments were conducted in which no good-quality data were available. This was the case for Mn (0.118227521 atom/b), natural Cr (0.05310 and 0.0262696 atom/b),  $^{53}\text{Cr}$ -oxide (0.017984 atom/b), natural Ti (0.05297 atom/b), and  $^{48}\text{Ti}$ -oxide (0.028186 atom/b).

A presample collimation limited the beam size to about 2.54 cm on the samples and allowed only neutrons from the water moderator part of the neutron source to be used. The neutron detector was an 11.1-cm-diameter, 1.25-cm-thick  $^6\text{Li}$ -glass scintillator positioned in the beam at 79.815 m from the neutron source. The scintillator was viewed on edge by two 12.7-cm-diameter photomultipliers that were placed outside the neutron beam to decrease backgrounds. To reduce systematic uncertainties, the samples and their compensators or corresponding empty containers were periodically cycled through the neutron beam, and the neutron flux was recorded for each sample and cycle. Additional measurements with a thick polyethylene sample were used to determine the gamma-ray background from the neutron source.

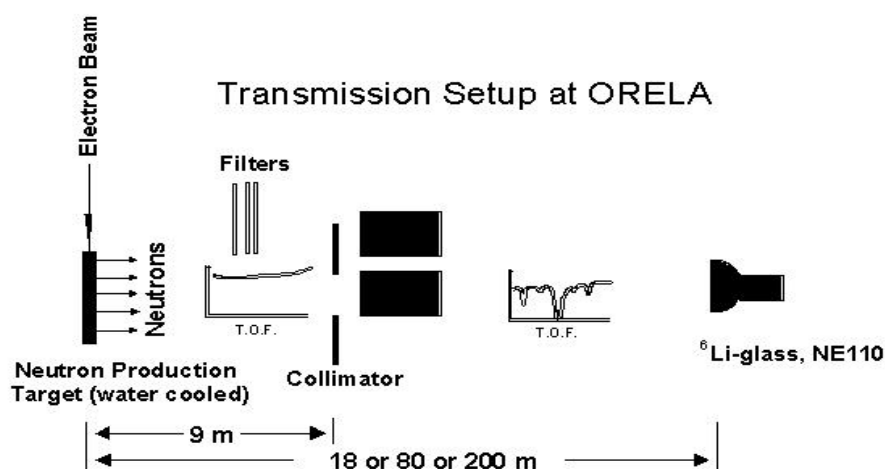


**Figure 4.** Schematic sketch of the neutron transmission experimental setup using flight path 1 at ORELA

## Results from ORELA

The results of our capture and transmission experiments from past years sometimes show differences compared to the evaluated nuclear data file for all isotopes measured. This can be seen in Figs. 1 and 5, in which the neutron capture cross sections of natural Ti and  $^{48}\text{Ti}$  are shown compared to the cross sections calculated using the most recent resonance parameter set from the ENDF/B-VII library. SAMMY was used to calculate the neutron capture cross section, including all experimental effects. In most cases, resonances up to 600 keV were resolved with sufficient statistics. Together with the high-resolution transmission data (for example, compare to Fig. 6), good data sets are now available for new evaluations.

In general, all of our new and recent neutron capture cross sections are smaller than previous results. Our new capture data show that in many previous cases, capture widths were severely overestimated, and resonances were missed as a result of large backgrounds. Results from our new total cross-section measurements will help in the analysis of our new capture cross-section measurements.

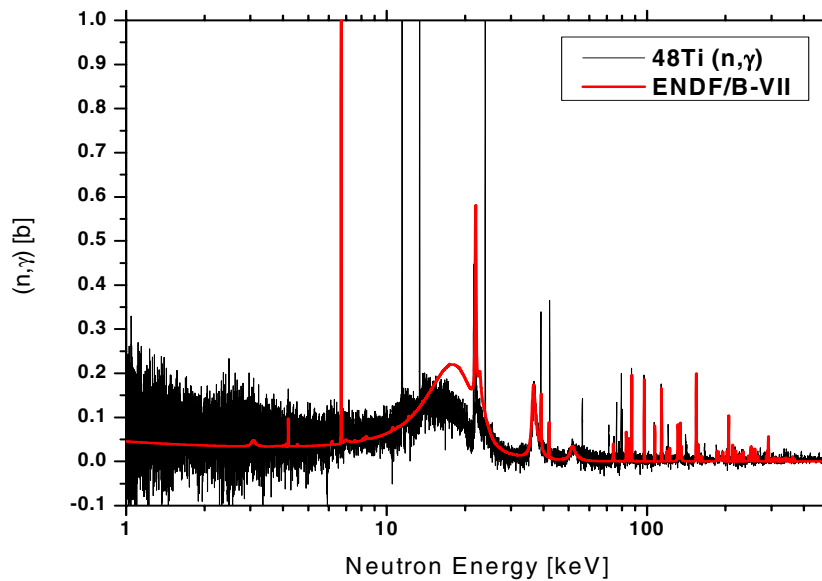


**Figure 5.** Neutron capture on  $^{48}\text{Ti}$ -oxide compared to ENDF/B-VII evaluation parameters

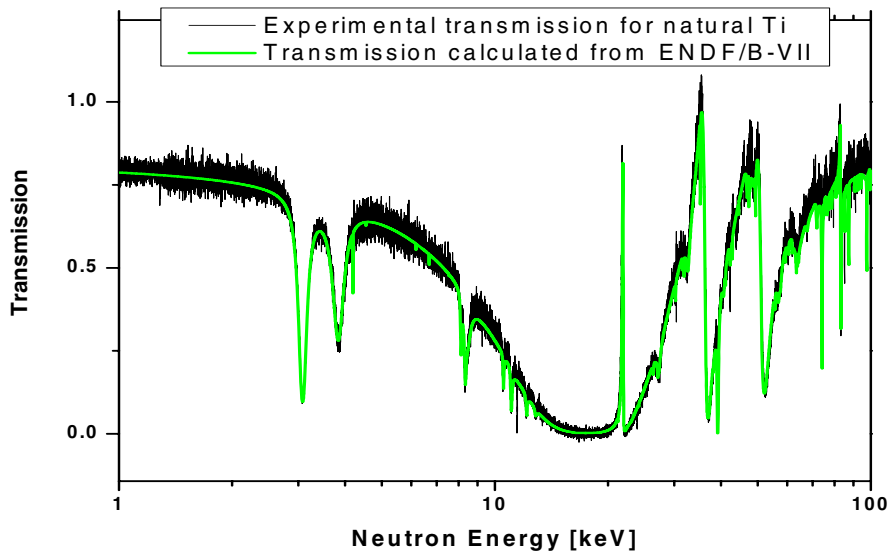


**Figure 6.** Transmission data for natural Ti compared to parameters from the ENDF/B-VII evaluation

The observed discrepancies between our data and evaluations from nuclear data libraries mainly have two causes. First, the use of improper weighting functions resulted in mismatched detector response functions. In the new experiments, the more sophisticated computer code MCNP was used for the correct determination of the weighting function. Second, underestimated neutron sensitivity of the experimental apparatus led to previous capture cross sections that were too large. In addition, the better characterized samples, superior TOF resolution, and well-understood experimental apparatus and backgrounds helped to produce more reliable cross-section data in the present case.

The neutron total and capture cross-section data will be analyzed using the computer code SAMMY. This analyzing program applies all the necessary corrections for experimental effects, such as Doppler and resolution broadening, self-shielding, and multiple-scattering effects to the data. The resonance parameters obtained are the basis for an evaluation of the

cross sections calculated by the Nuclear Data Group of the Nuclear Science and Technology Division of Oak Ridge National Laboratory. When they are available and suitable, evaluations will include other existing experimental data sets. The final result will then be checked for consistencies using criticality benchmark calculations. As an example, the final result of the evaluation for the neutron capture cross section for the nickel isotope 58 [11] is shown in Fig. 7. In these data sets, resonances can be resolved up to 700 keV with sufficient statistics.

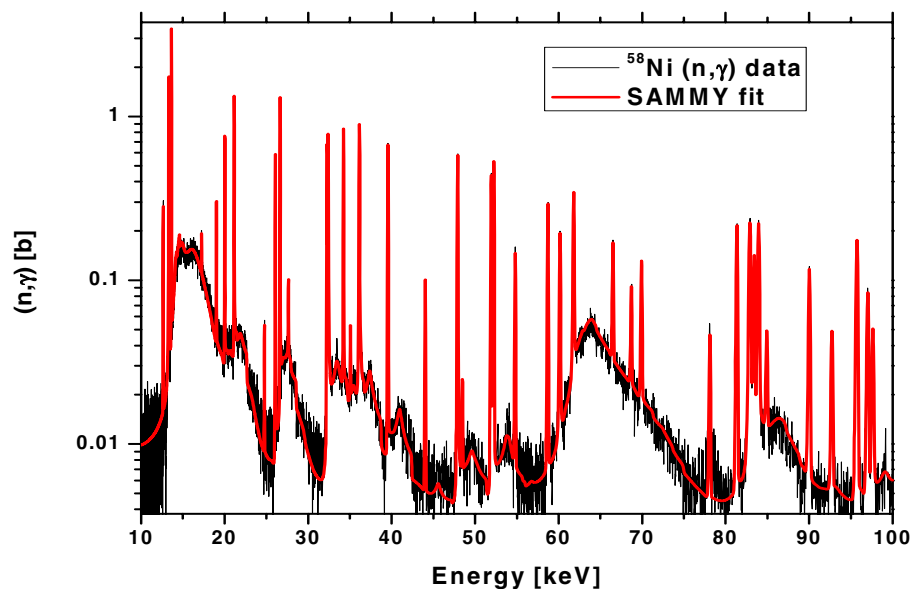


**Figure 7.** Results of the new  $^{58}\text{Ni}$  evaluation compared to  $(n,\gamma)$  data from ORELA

## Conclusion

To support the Nuclear Criticality Safety Program, new neutron total and capture measurements at ORELA were performed over broad energy ranges. The obtained results were then analyzed using the multilevel R-matrix code SAMMY. In all analyzed and evaluated cases, the researchers were able to extend the resolved resonance region to much higher energies than the existing evaluations. These new evaluations should lead to much more reliable nuclear criticality calculations.

One particular finding is to be emphasized. Over the past 10 years, the results of the new neutron capture cross section measurements at ORELA for samples with large scattering cross sections have shown the tendency to be smaller than the data found in the nuclear data libraries. Therefore, many of the older measurements for samples with small capture cross sections are questionable or at least much more uncertain, especially if the applied corrections for neutron sensitivity were sizeable.

## Acknowledgements

ORNL is managed by UT-Battelle, LLC, for the U.S. Department of Energy under Contract No. DE-AC05-00OR22725. The work that is presented in this paper was sponsored by the U.S. Department of Energy Nuclear Criticality Safety Program.

## References

- [1] R. L. Macklin and R. R. Winters, *Nucl. Sci. Eng.* **78**, 110–111 (1981).
- [2] B. J. Allen, J. W. Boldeman, and R. L. Macklin, *Nucl. Sci. Eng.* **82**, 230–231 (1982).
- [3] F. Corvi, A. Prevignano, and H. Liskien, *Nucl. Instrum. Methods* **A265**, 475–484 (1988).
- [4] W. R. Nelson, H. Hirayama, and D. W. O. Rogers, *The EGS4 Code System*, Stanford Linear Accelerator Center Report SLAC-265 (Stanford, CA) (1985).
- [5] F. G. Perey, J. O. Johnson, T. A. Gabriel, R. L. Macklin, R. R. Winters, J. H. Todd, and N. W. Hill, in *Nuclear Data for Science and Technology*, edited by S. Igarasi, Mito, Japan, May 30–June 3, 1988, JAERI Conference Proceedings, pp. 379–382.
- [6] N. M. Larson, 2006. ORNL/TM-9179/R8, Oak Ridge National Laboratory, 2008.

- [7] Macklin, R. L., and Allen, B. J., Nucl. Instrum. Methods **91**, 565 (1971).
- [8] P. E. Koehler, R. R. Spencer, R. R. Winters, K. H. Guber, J. A. Harvey, N. W. Hill, and M. S. Smith, Phys. Rev. C **54**, 1463–1477 (1996)
- [9] P. E. Koehler, R. R. Winters, K. H. Guber, T. Rauscher, J. A. Harvey, S. Raman, R. R. Spencer, J. C. Blackmon, D. C. Larson, D. W. Bardanyan, and T. A. Lewis, Phys. Rev. C **62**, 055803-1 (2000).
- [10] R. L. Macklin, J. Halperin, and R. R. Winters, Nucl. Instrum. Methods **164**, 213 (1979).
- [11] H. Derrien, L.C. Leal, K.H. Guber, D. Wiarda, and G. Arbanas, WONDER 2009.

## A new TOF facility at J-PARC MLF

Masayuki Igashira<sup>1)</sup>, Yoshiaki Kiyanagi<sup>2)</sup>, Masumi Oshima<sup>3)</sup>

- 1) Research Laboratory for Nuclear Reactors, Tokyo Institute of Technology, 2-12-1-N1-26 O-okayama, Meguro-ku, Tokyo, Japan, 152-8550,
- 2) Graduate School of Engineering, Hokkaido University, Kita-13, Nishi-8, Kita-ku, Sapporo, Japan, 060-8628
- 3) Nuclear Science and Engineering Directorate, Japan Atomic Energy Agency, 2-4 Shirakata-shirane, Tokai-mura, Naka-gun, Ibaraki-ken, Japan, 319-1195

[iga@nr.titech.ac.jp](mailto:iga@nr.titech.ac.jp)

**Abstract:** Japan Proton Accelerator Research Complex (J-PARC) includes Materials and Life Science Facility (MLF) for neutron and muon beam experiments. The spallation neutron source at J-PARC MLF will be one of the highest intensity neutron sources in the world. We have constructed a new Time-Of-Flight (TOF) facility, named “Neutron-Nucleus Reaction Instrument (NNRI)”, at the beam line No.4 (BL04) of J-PARC MLF to measure accurate neutron capture cross sections for long lived fission products (LLFP) and minor actinides (MA). The samples we are now considering are Cm isotopes as MA, and Tc-99, I-129 and so on as LLFP. For the measurement, a Ge detector system covering a large solid angle has been improved and installed in NNRI. A NaI(Tl) detector system has been also installed. In May 2008, the first neutron beam was delivered at J-PARC MLF, and we started the test of NNRI. In June 2009, we performed preliminary measurements for Cm-244, I-129, etc. In the present paper, we describe the details of NNRI and the preliminary measurements.

### Introduction

Accurate neutron cross section data for long lived fission products (LLFP) and minor actinides (MA) are indispensable for the estimation of their production and transmutation rates in advanced reactor systems such as fast reactors and accelerator-driven systems. Japan Proton Accelerator Research Complex (J-PARC) includes Materials and Life Science Facility (MLF) for neutron and muon beam experiments. The spallation neutron source at J-PARC MLF will be one of the highest intensity neutron sources in the world. It is very useful to perform neutron cross section measurements at the high intensity neutron source, because it enables us to obtain the data with a small amount of sample.

In this situation, we are now executing a project on the nuclear data. The major part of this project is the measurement of neutron capture cross sections of MA and LLFP, using the J-PARC MLF neutron source. Therefore, we have constructed a new Time-Of-Flight (TOF) facility, named “Neutron-Nucleus Reaction Instrument (NNRI)”, at the beam line No.4 (BL04) of J-PARC MLF.

The samples we are now considering are Cm isotopes as MA, and Tc-99, I-129 and so on as LLFP. For the measurement, a Ge detector system covering a large solid angle has been improved and installed in NNRI. A NaI(Tl) detector system has been also installed. In May 2008, the first neutron beam was delivered at J-PARC MLF, and we started the test of NNRI. In June 2009, we performed preliminary measurements for Cm-244, I-129, etc. In the present paper, we describe the details of NNRI and the preliminary measurements.

### Neutron-nucleus reaction instrument

The neutron-nucleus reaction instrument (NNRI) was designed for the neutron capture cross section measurement, and has been made and installed at J-PARC MLF BL04. NNRI consists of radiation shields, collimators, choppers, filters, and so on as well as radiation detector systems.

The radiation shields were designed so as to satisfy the dose limit determined by J-PARC, 1  $\mu\text{Sv/h}$ , at the outer boundaries of NNRI and widen experimental areas as large as possible, based on the neutron and gamma-ray transport calculation with a Monte-Carlo code, PHITS [1]. The radiation shields, composed of iron, concrete and borax resin, were made on the basis of the design, and installed at BL04, as shown in Figure 1. A Ge detector system is

located about 22 m from the coupled neutron moderator (liquid hydrogen) of J-PARC MLF, and a NaI(Tl) detector system is located about 27 m from the moderator.

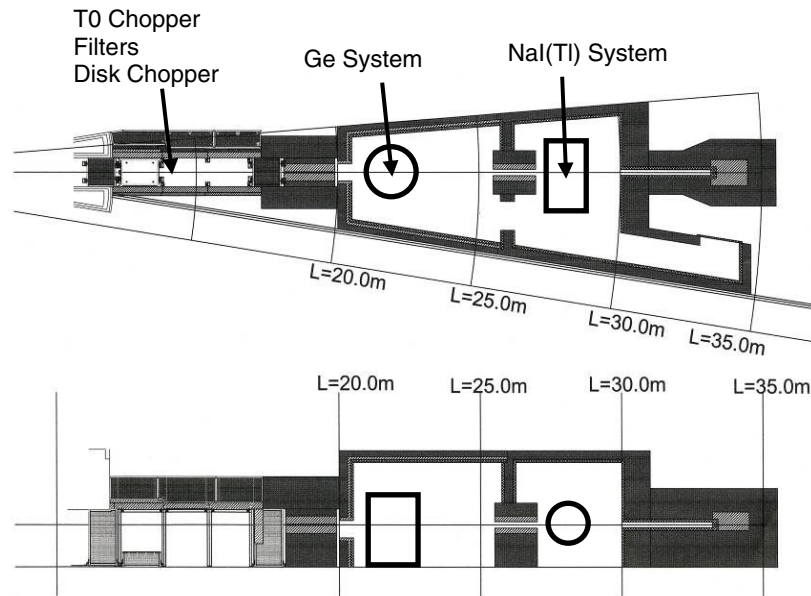


**Figure 1.** Drawing of the installed radiation shields, and the positions of the gamma-ray detection systems and other equipments

The neutron beam collimation system has been designed so as to obtain an intense and clean neutron flux at the sample position of about 22 m or 27 m, based on the PHITS calculation. The standard diameter of the neutron beam at the sample position is 20 mm. The diameter of 6 mm or the square of 40 mm can be selected optionally.

A T0 chopper has been designed, made and installed at about 13 m from the moderator. The T0 chopper cuts the neutron burst with energies higher than about 10 eV, and is used for the cross section measurement in the low-energy region below several eV. A double disk chopper has been also designed, made and installed at about 15 m. This chopper acts as a band filter, and transmits eV neutrons.

A filter system has been developed and installed between the T0 and double disk choppers. It has eight filters, *i.e.* 13-mm thick Pb, 25-mm thick Pb, Mn, Co, In, Ag, Cd, Al filters, which are remote-controlled independently. The two Pb filters are prepared as the shield against the gamma-ray flush from the moderator. The Mn, Co, In, Ag, and Al filters are the notch filters for the neutron beam. The Cd filter prevents the overlap of low-energy neutrons with high-energy neutrons of the next neutron pulse.

A Ge detector system covering a large solid angle has been developed. In a past project on nuclear data [2], a Ge detector system composed of two cluster and four clover Ge detectors and Bi<sub>4</sub>Ge<sub>3</sub>O<sub>12</sub> (BGO) anti-coincidence shield detectors was developed. This Ge detector system has been improved to make its detection efficiency higher and to install it in the narrow space at the 22-m position from the neutron moderator in Figure 1. The improved Ge detector system is composed of the two cluster Ge detectors, eight coaxial Ge detectors, BGO anti coincidence shield detectors and a detector shield, as shown in Figure 2.

A NaI(Tl) detector system shown in Figure 3 has been also installed at the 27-m position in Figure 1. The NaI(Tl) detector system was developed at the Tokyo Institute of Technology, and is composed of a set of two NaI(Tl) spectrometers. Each spectrometer is composed of a NaI(Tl) detector (the diameter of 330 mm and the length of 203 mm, or the diameter of 203 mm and the length of 203 mm), an anti-coincidence annular plastic detector, and a detector shield.

Two types of neutron monitor detectors applicable to the high intensity neutron beam have been also developed. One is the current mode scintillation detectors, and the other is an indirect neutron monitor composed of a small C<sub>6</sub>D<sub>6</sub> gamma-ray detector and a standard capture sample such as <sup>197</sup>Au.

Data acquisition systems for the Ge detector system, the NaI(Tl) detector system, and the neutron monitor systems have been also developed. In particular, that for the Ge detector

system is quite new one which utilizes high-speed (8000 MIPS) digital signal processors (DSP).

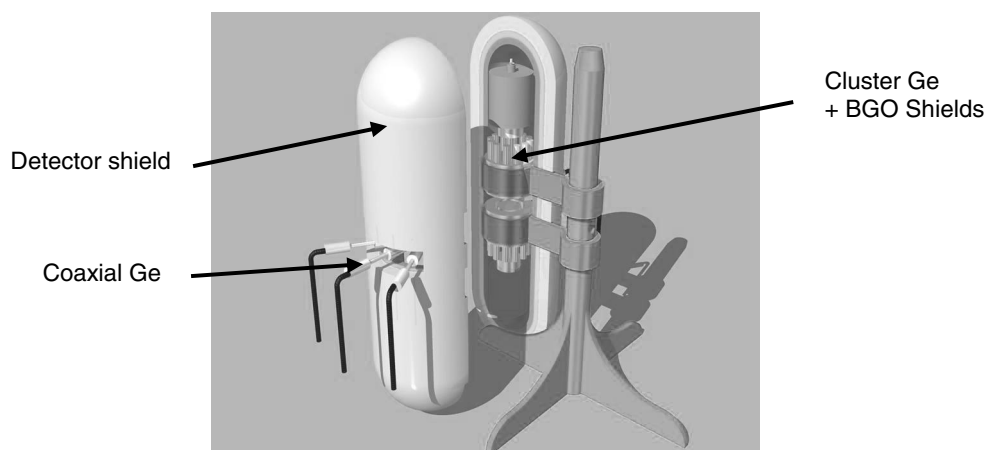


**Figure 2.** Schematic view of the Ge detector system of NNRI

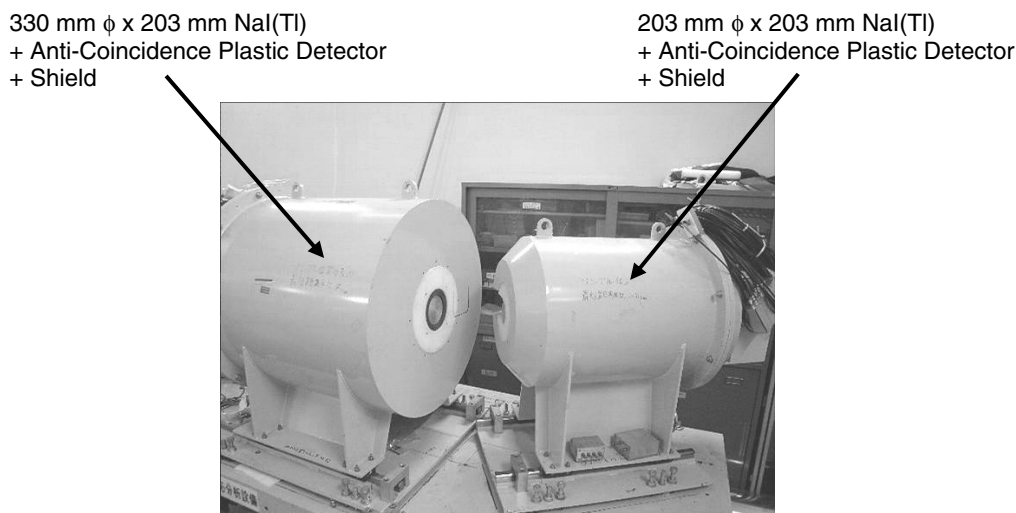


**Figure 3.** Photograph of the NaI(Tl) detector system of NNRI

### Sample preparation

There are two points in the preparation of MA and LLFP samples to make the capture cross section measurement successful. One is the preparation of an appropriate amount of sample to make the measurement by detecting prompt capture gamma rays with a TOF method. Too much sample causes a severe background due to its own radioactivity; on the other hand too small sample does not emit enough capture gamma-rays. The other is sample characterization, *i.e.* chemical and isotopic analysis of sample impurity. Therefore, we have prepared a small amount of unsealed sample taken from the same rod as each sealed capture sample to analyze the impurity.

Considering the first point described above, we have already prepared Cm-244, Cm-246, Tc-99, Zr-93 and I-129 samples. A Pd-107 sample will be also prepared in November 2009. As an example, the isotopic composition of the Cm-244 and Cm-246 samples is shown in Table 1. The isotopic purity of the Cm-244 is rather high, 91.64%, but that of the Cm-246 sample is low, only 58%. The net weight of the Cm-244 or Cm-246 sample is about 1 mg, and the total radioactivity is about 1 GBq.

**Table 1.** Isotopic composition [%] of the Cm-244 and Cm-246 samples

	Cm-242	Cm-243	Cm-244	Cm-245	Cm-246	Cm-247	Cm-248
Cm-244 sample	0.03	0.02	91.64	2.19	5.86	0.15	0.11
Cm-246 sample	0	0	29.04	1.04	58.02	2.85	9.05

### Preliminary measurement

After the basic test of NNRI using neutron beams, preliminary measurements were performed for Cm-244, Tc-99, and so on in June 2009 using both the Ge and NaI(Tl) detector systems. Neutron beams were produced by 3-GV, 20-KW proton beams (repetition rate: 25 Hz; beam structure: double bunch, bunch width: 80 ns, bunch interval: 600 ns).

Prompt capture gamma rays from each sample were detected by means of a neutron TOF method. As an example, a TOF spectrum for the Tc-99 sample obtained from the measurement with the Ge detector system is shown in Figure 4, where background components are roughly subtracted but the dead time correction is not performed. Concerning the 5.58-eV resonance, the shape is strongly distorted due to the dead time effect. Moreover, as seen from the expanded spectrum, each resonance is split into two peaks due to the double-bunch beam effect.

- Tc-99: 78mg, 6.3 mm  $\phi$  x 0.3 mmt metal target
- Measurement time: 15.7 hours.
- Contribution from target case (aluminum) is subtracted.
- No gamma-ray energy selection.
- Dead time correction is not yet applied.

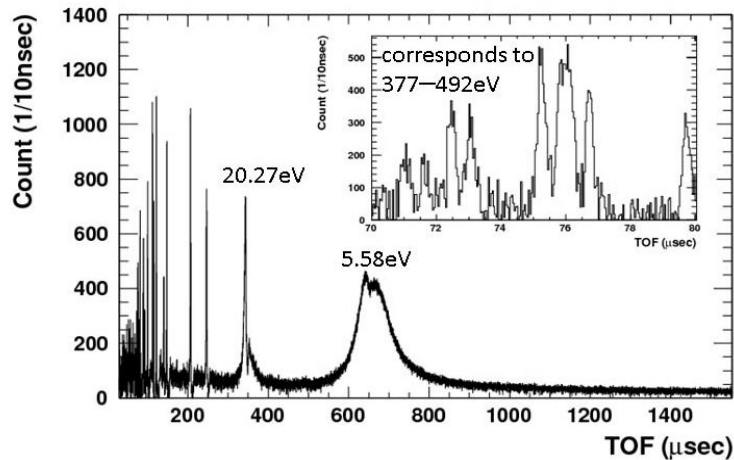


**Figure 4.** Preliminary TOF spectrum for the Tc-99 sample obtained from the measurement with the Ge detector system

From the preliminary measurement, the Ge detector system is expected to be applicable to the measurement up to about 10 keV at the moment. However, the high energy resolution of the Ge detector system is very useful to distinguish the signal and background gamma rays from the objective and impurity nuclides, respectively. Some methods distinguishing the signal and background gamma rays, *e.g.* a method using strong ground-state transitions in the residual nuclide [3], have been developed from separate experiments using the Ge detector system and the electron linear accelerator neutron source at the Kyoto University.

The neutron capture experiment using an NaI(Tl) detector system and a pulse-height weighting technique [4] has been already established [5], although the correction for the sample impurities should be made with existing neutron capture cross section data for the impurities. The NaI(Tl) detector system is expected to be applicable to the measurement up to about 100 keV at the moment. Therefore, agreement of both results by the Ge and NaI(Tl) detector systems in the overlap region, *i.e.* below about 10 keV, will confirm the reliability of both results.

## Conclusion

We have commissioned NNRI at J-PARC MLF BL04 to measure the neutron capture cross sections for MA and LLFP such as Cm-244, Cm-246, Tc-99, I-129. From the preliminary measurements, the Ge and the NaI(Tl) detector systems are expected to be applicable to the measurements up to about 10 keV and about 100 keV, respectively, at the moment. After the improvement of the shields around the Ge and NaI(Tl) detector systems, NNRI will be again utilized for the measurements from October 2009.

## Acknowledgements

The present study is the result of "Study on nuclear data by using a high intensity pulsed neutron source for advanced nuclear system" entrusted to Hokkaido University by the Ministry of Education, Culture, Sports, Science and Technology of Japan (MEXT).

## References

- [1] H. Iwase, K. Niita and T. Nakamura, *J. Nucl. Sci. Technol.*, 39 (2002) 1142.
- [2] M. Igashira, et al., *Proc. Int. Conf. on Nuclear Data for Science and Technology*, 26 Sep. - 1 Oct., 2004, AIP Conference Proceedings 769, Part 1 (2005) 601.
- [3] M. Oshima, et al., *Proc. Int. Conf. on Nuclear Data for Science and Technology*, 22-27 April., 2007, *EDP Sciences* (2008) 603.
- [4] R. L. Macklin and J. H. Gibbons, *Phys. Rev.*, 159 (1967) 1007.
- [5] S. Mizuno, M. Igashira and K. Masuda, *J. Nucl. Sci. Technol.*, 36 (1999) 493.



## Neutron cross section measurements in the resonance region at GELINA

*Peter Siegler<sup>1)</sup>, Peter Schillebeeckx<sup>1)</sup>, Stefan Kopecky<sup>1)</sup>*

1) EC-JRC, Institute for Reference Materials and Measurements, Retieseweg 111, B-2440 Geel, Belgium

[peter.siegler@ec.europa.eu](mailto:peter.siegler@ec.europa.eu)

**Abstract:** Neutron cross section measurements in the resonance region have been performed systematically at the linear accelerator of the IRMM in Geel. Those measurements consist of series of neutron capture and transmission experiments under different accelerator conditions as well as using various experimental set-ups. The obtained full set of complementary neutron cross section data allow for a more precise determination of the underlying nuclear data over a wide energy range. Data can be provided for evaluation from the thermal neutron energy up to the unresolved resonance energy region. The presentation will focus on the experimental facilities, detector techniques in use as well as on the results concerning Cd as an example for a measurement campaign.

### Introduction

The GELINA facility at the Institute for Reference Materials and Measurements in Geel is a white neutron source for high resolution neutron cross section measurements. During the last years our work is mainly devoted to provide cross section data for reactor safety and transmutation. In this presentation we will give an overview about the specific experimental facilities, the complex process of measurement and data reduction as well as experimental results with regard to a series of <sup>nat</sup>Cd measurements between 2007 and 2009.

### GELINA time-of-flight measurements

All described experiments were performed at GELINA, the white neutron source at the Institute for Reference Materials and measurements. It uses a linear electron accelerator which accelerates electrons up to 150 MeV and has a peak current of 12 A. The repetition rate can be varied between 40 and 800 Hz. The electron pulses have a duration of approximately 1ns, owing to the post-acceleration compression magnet. The electrons impinge on a mercury cooled rotary target, which consists of depleted uranium. There, the electrons create Bremsstrahlung, and through ( $\gamma,n$ ) and ( $\gamma,f$ ) reactions neutrons are produced. Two beryllium canned water containers, with dimension of 4 x 10 x 10 cm, are positioned above and below the neutron production target, for moderating the neutrons. Using different collimation conditions the experiments can either use fast or thermal spectrum.

Up to 12 experiments can be performed simultaneously at the flight paths which disperse radial from the target, flight path lengths between 10 m and 400 m can be chosen.

The neutron flux is monitored by BF<sub>3</sub> counters that are located in the ceiling and walls of the neutron target room.

### Transmission Setup

For the total cross section measurements two different transmission setups are in use. In both setups the beam diameter is reduced to approximately 4.5 cm at the sample and the detectors position, by a combination of Li-carbonate plus resin and copper collimators. Neutron-overlap filters (Cd or <sup>10</sup>B) are inserted at the sample position, as well as lead filters to reduce the intensity of the gamma-flash. Furthermore black-resonance filters for estimating the background can be inserted at the sample position.

One setup uses a flight path length of 26.45 m, with the sample position at approx. 10 m. The detector system is a ½" thick lithium-glass scintillator, with a diameter of 4 inch that is viewed by two photomultiplier tubes (EMI9823QKB). To separate a valid neutron event from the photomultiplier noise, a coincidence between the timing and amplitude of the signals from both tubes is required.

For the second setup the detector system is placed at a distance of 49.34 m from the neutron target, with the respective sample position at 25 m. The detector is a lithium-glass scintillator

of ¼" thickness and 4" diameter mounted inside an aluminium sphere. Such a design should make the light collection independent of the interaction spot, providing an amplitude signal which is proportional to the produced light in the glass. A pulse-height window selects the alpha-peak of the  ${}^6\text{Li}(n,\alpha)$  reaction to distinguish a neutron event from background events.

Both setups use in-house build fast-timing-digitizers, which have a time-resolution of 0.5 ns for measuring the time-of-flight. The time-of-flight data are recorded in histogram mode. The amplitude information of the detector and the monitor counts are recorded for off-line checking of the stability of the electronic setup and the accelerator. To reduce the impact of instabilities on the transmission measurement, typically every 20 minutes the sample-in and open-beam measurements are cycled.

### Capture Setup

Capture measurements are performed on three experimental stations, differing only in flight path length with available distances at 10 m, 30 m and 60 m.

Similar to the transmission measurements the beam diameter at the sample station had to be reduced to approximately 7.45 cm using Li-carbonate plus resin, copper and lead collimators. Air conditioning is installed at the measurement stations to keep the sample at a constant temperature and to minimize a drift of the electronics. Photons produced by the neutron capture in the sample materials are detected by four cylindrical  $\text{C}_6\text{D}_6$  detectors (NE230). To reduce the effects caused by anisotropy of the primary dipole radiation the detectors were mounted at an angle of 125 degrees in respect to the neutron beam. To minimize the detection of scattered neutrons in the detector system, the scintillators were mounted directly on quartz-windowed photo-multipliers. The pulse height weighing technique is used to create a detector response proportional to the energy of the registered gamma. A description of the method and of the calculation of the weighting function can be found in [1].

The flux-shape is determined with a Frisch-gridded  ${}^{10}\text{B}$  ionisation chamber which is operated with a continuous flow of an argon (90%) and methane (10%) mixture. The boron sample itself consists of approximately  $1.25 \cdot 10^{-5}$  atoms/barn of  ${}^{10}\text{B}$  evaporated on a 30  $\mu\text{m}$  Al backing.

The amplitude and the time-of-flight of each event are recorded in list-mode for off-line data reduction. This allows for a very careful monitoring of the stability of the detection system. The linearity of the scintillator system is checked periodically, every weekend while the accelerator is shut down, by measuring the 661.7 keV line of the  ${}^{133}\text{Cs}$  decay and the 6.13 MeV line from a  ${}^{238}\text{Pu}+{}^{13}\text{C}$  source. Furthermore, the 2.2 MeV gamma-line from the neutron capture, a permanently present background in our measurements, is used to verify the stability.

### Data reduction

The different elements of the data reduction process which are systematically applied to all measurements at GELINA are described in the following chapter.

#### Dead time correction

Already the first step of any data-reduction can introduce correlation into the experimental data – the dead time correction, as this correction depends on the count rate in a given period before an event occurs. Furthermore is this correction highly non-linear, therefore a careful analysis – and possible reduction of the dead-time – and the dead-time distribution should help to reduced the systematic uncertainties.

We have studied in detail the different approaches to the dead-time correction, and how accurately they can correct the experimental data. These tests were done with simulated spectra as well as with spectra that were taken with dead-times ranging from 300ns to 4 $\mu\text{s}$ . It was concluded that correction up to a factor of two can be performed to an accuracy better than one percent [2].

#### Background correction

The background is estimated with the black resonance technique. i.e. filters are inserted into the beam that remove all the neutron at one given energy, typical filter materials are W, Cs, Mo, Au, etc. When using this technique it should be always kept in mind, that the insertion of any filter will alter the beam condition and consequently the background. Therefore the black resonance filter has either to stay in the beam while the experiment is performed or the effect of the filter on the background has to be estimated. For doing so, an analysis of the various background components is important.

At GELINA, background measurements – using black resonance techniques, polyethylene filters etc – and Monte-Carlo calculations for the target-source configuration were performed to identify the different sources for the background. The biggest contribution – especially at higher neutron energies is caused by hydrogen capture, i.e. neutrons are thermalized in the moderator and then captured by a hydrogen atom. This process produces photons with energy of 2.2 MeV that travel through the beam-line, the sample, and continue towards the detector where they are detected. In case of a transmission experiment, the energy deposited in the lithium-glass detectors is comparable to the energy released in a neutron event. Therefore this background component can hardly be suppressed by pulse-height discrimination. The time-distribution of these photons can be derived by analytical considerations, accounting for the storage time in the moderator or by Monte-Carlo simulations.

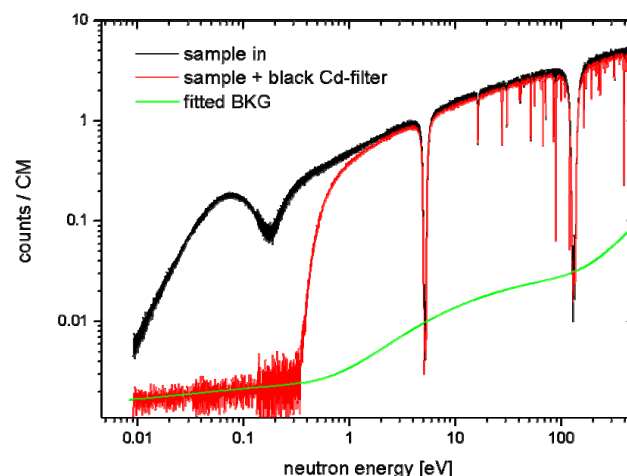


**Figure 1.** Transmission spectra showing measurements and background estimation.

The second component at longer times can either be caused by neutron scattered from the detectors or from neighbouring flight-path. It is important to highlight the fact that all experiments at GELINA are performed under constant background conditions with respect to neighbouring flight-path.

The background spectra can then be described as function of the neutron time-of-flight by combinations of exponential or power functions. All the parameters can be derived from fits to experimental data. In Figure 1 the background component as a function of the neutron energy for the transmission setup is depicted for a  $^{nat}\text{Cd}$  sample. For the transmission measurements the background is below 10 % and well understood. Therefore one can estimate that the overall uncertainties induced by background correction should not exceed 1% on the observed yields resp. transmission factors.

### Normalisation

The normalisation of capture yields can be either done using well know resonance with  $\Gamma_n \ll \Gamma_\gamma$  (e.g. the 1.15 keV resonance in Fe). If one requires that  $n\sigma \ll 1$ , ( $n$  the sample thickness in atoms/barn and  $\sigma$  the peak cross section) the capture area is mostly determined by  $\Gamma_n$ , and an independent transmission measurement can provide the normalisation. In all the presented cases this procedure was used to check on the normalisation that has been determined by the second method, using a saturated resonance.

For a saturate resonance, it is required that  $n\sigma \gg 1$ , then capture yield is given by the ratio  $\Gamma_\gamma / (\Gamma_n + \Gamma_\gamma)$ . If one chooses a resonance with  $\Gamma_\gamma \gg \Gamma_n$ , the capture yield is almost unity, and it can be shown that in this case the capture yield is almost independent on the resonance parameters and the sample thickness (see [1]). This approach was used either with the 4.9 eV resonance of Au or the 5.2 eV resonance in Ag.

### AGS

The data processing is usually carried out using the AGS-package [3]. This package calculates the dead time correction, carries out the background fitting and subtraction,

normalization and determines the transmission of the sample as a function of time-of-flight. The package also includes the propagation of uncertainties and creates a covariance matrix, starting from the uncorrelated uncertainties due to counting statistics.

## Experimental results

On the example of the recent measurement campaign related to  $^{nat}\text{Cd}$  we will give experimental results and the influence of changed resonance parameters.

### Cadmium

It has been suggested that the capture and scattering cross sections of natural cadmium are not well described by the resonance parameters that are given in the evaluated data files. In particular, doubts on the parameters of the first resonance of  $^{113}\text{Cd}$  at 0.178 eV have been raised. This resonance is of high importance in the interpretation in many integral experiments, such as neutron activation analysis, in which cadmium foils are used to shield from thermal neutrons. A more recent study [4] tested the ENDF/B-VII evaluation on the same integral experiment. That study concluded that the resonance parameters of the resonance of  $^{113}\text{Cd}$  at 0.178 eV and the thermal cross section of  $^{113}\text{Cd}$  needed to be adjusted. The evaluated resonance parameters for the 0.178 eV resonance of  $^{113}\text{Cd}$  come from only a handful of experiments (see Table 1). The two latest and most accurate ones, differ in the given neutron widths by approximately 5% or more than six standard deviations. The agreement between the other two parameters of this resonance is satisfactory. So far the larger of the two values had been included in most of the evaluations. Mosteller et al. [4] showed that using the smaller of these values improved the agreement between experimental and calculated results of an integral experiment. To clarify the situation and to provide data for a new evaluation, a set of transmission experiments was performed at GELINA. The goal was to determine the neutron and capture width of the 0.178 eV resonance and reduce the uncertainties. The capture and the neutron width are needed to better than 1%, and the energy of the resonance is required to better than 0.1 meV. In these transmission measurements two uniformly thin metallic samples and a solution sample were used. The use of thin powder samples is not advised due to the inherent inhomogeneities in the thickness. Not accounting for these inhomogeneities in the sample thickness will lead to an underestimation of the neutron width and an overestimation of the capture width of a resonance [5].

Considering the importance of the 0.178 eV resonance it was deemed necessary to perform experiments solely devoted to study this resonance. In total four samples, their properties are given in Table 1, were prepared for those studies. It was considered essential that different sample types, i.e. metal foils and solution samples were used. With such an approach the influence of sample properties (the homogeneity of thin foils cannot be always guaranteed and for solution samples similarly problems with homogeneity and material content in the measured volume) on the extracted resonance parameters should be minimized.

**Table 1.** Cadmium samples used in transmission measurements to determine the 0.178 eV resonance

thickness (atoms/barn)	sample type	Flight-path length
$1.4 \cdot 10^{-4}$	solution	25 m
$1.38 \cdot 10^{-4}$	foil	50 m
$2.24 \cdot 10^{-4}$	foil	50 m
$2.8 \cdot 10^{-4}$	solution	25 m

To further control the estimated uncertainties, all four samples were fitted individually and simultaneously with the resonance shape analysis code REFIT [6]. With respect to the lowest lying resonance of  $^{113}\text{Cd}$  we have determined the following resonance parameters:  $E_{\text{res}} = 178.7 \pm 0.1$  meV,  $\Gamma_{\gamma} = 113.5 \pm 0.2$  meV and  $\Gamma_n = 0.640 \pm 0.004$  meV. These parameters have been used subsequently in estimation on the effects on an integral experiment as described in [4]. This experiment is described in detail in the international handbook of evaluated criticality safety benchmark experiments as HEU-SOLTHERM- 049 [7]. For our calculations, the parameters of the first resonance of  $^{113}\text{Cd}$ , resonance energy, neutron width and capture width were changed from the ENDF/B-VII to the values derived from our experiment.

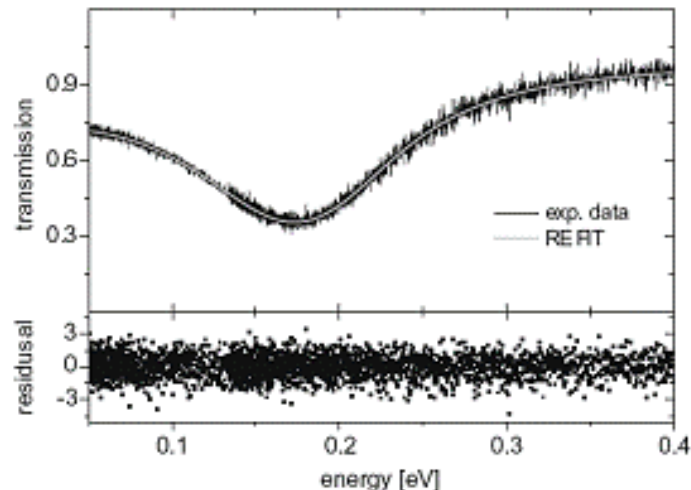


**Figure 2.** Fit to a 30  $\mu\text{m}$  metallic Cd sample

The changes are significant but not quite big enough to bring calculations and experiments in agreement. This might be an indication that higher energy cadmium resonances or the thermal cross sections for other cadmium isotopes play an important role.

In total eight more samples (see Table 2) were used for determining transmission factors and capture yields over an energy range from thermal to 100 keV. For this set of experiments it is expected that the resolution of our data will allow the extraction of resonance parameters up to an energy around 1 keV.

**Table 2.** Cadmium samples used in transmission and capture measurements

thickness (atoms/barn)	type	Flight-path length
$1.38 \cdot 10^{-4}$	capture	10 m
$3.40 \cdot 10^{-4}$	capture	10 m
$5.4 \cdot 10^{-4}$	transmission	50 m
$1.10 \cdot 10^{-3}$	capture	30 m
$2.36 \cdot 10^{-3}$	capture	30 m
$4.67 \cdot 10^{-3}$	capture	30 m
$9.34 \cdot 10^{-3}$	capture	10 m
	transmission	25 m, 50 m
$2.34 \cdot 10^{-2}$	transmission	50 m
$1.20 \cdot 10^{-1}$	transmission	25m, 50m

## Conclusion

We have described, using the measurements on  $^{\text{nat}}\text{Cd}$  as an example, the experimental capabilities and the treatment of experimental results obtained at the GELINA time-of-flight facility. During the last years it has become obvious that not only the documentation of final results but also the control and documentation of experimental conditions is crucial for their further use and dissemination. Under this view all measurements at GELINA have been harmonized in their set-up, the signal treatment and acquisition systems and the handling of their raw data. In this way the reproducibility and quality of data can be drastically improved. This allows moreover for the verification of the data as well as for a comparison with results obtained under different experimental conditions and is one of the main prerequisites for a successful evaluation of any nuclear data.

## References

- [1] Borella A. et al., Nucl. Instr. and Methods A577(2007) 626-640
- [2] Mihailescu L.C., 2008, to be submitted
- [3] Bastian C. et al, 2006, PHYSOR-2006 - American Nuclear Society's Topical Meeting on Reactor Physics
- [4] Mosteller R.D. et al, 2008, PHYSOR-2008, contribution 088

- [5] Kopecky S. et al, Proceedings of the Intern. Conf. on Nuclear Data for Science and Technology, 2008, p. 623
- [6] Moxon M. et al, REFIT-2007, UKNSF(2006) p.216
- [7] NEA Nuclear Science Committee, International Handbook of Evaluated Critical Safety Benchmark Experiments, NEA/NSC/DOC(95)03, September 2008

## Measurements of neutron total cross-sections of Niobium & Palladium from 0.1 to 100 eV

*A.K.M. Moinul Haque Meaze<sup>1)</sup>, M. Shakilur Rahman<sup>2)</sup>, G. N. Kim<sup>2)</sup>  
and Y. D. Oh<sup>3)</sup>*

1) Istituto Nazionale di Fisica Nucleare (INFN), Sezione di Bari, V. Orabona N. 4,  
70126, Bari, Italy

2) Department of Physics, Kyungpook National University, 702-701 Daegu, Korea

3) Pohang Accelerator Laboratory, Pohang University of Science and Technology,  
790-784 Pohang, Korea

[Moinul.Meaze@ba.infn.it](mailto:Moinul.Meaze@ba.infn.it)

**Abstract:** The neutron total cross-sections and resonance parameters of Niobium (Nb) and Palladium (Pd) were measured in the neutron energy regions from 0.1 to 100 eV by using the time-of-flight (TOF) method at the Pohang Neutron Facility (PNF), Republic of Korea. The PNF consists of an electron linear accelerator, a water-cooled Tantalum (Ta) target with a water moderator, and a 12.06 m long time-of-flight path. A  ${}^6\text{Li-ZnS(Ag)}$  scintillator with a diameter of 12.5 cm and a thickness of 1.6 cm was used as a neutron detector. High purity natural Nb and Pd metallic sheets with thickness of 15 mm (0.0833 atoms/barn) and 1 mm (0.0068 atoms/barn) respectively, were used for the neutron transmission measurements. The notch filters composed of Cobalt (Co), Indium (In), and Cadmium (Cd) were used to estimate the background level and also to calibrate energy. In order to reduce the gamma-ray background from Bremsstrahlung and from neutron capture, we employed a neutron-gamma separation system based on their different pulse shapes. The resonance parameters of  ${}^{\text{nat}}\text{Nb}$  and  ${}^{\text{nat}}\text{Pd}$  were obtained from the transmission ratio by using the SAMMY code, which utilizes both Doppler and resolution broadening effects and Bayes' generalized least squares technique. The present measurements were compared with the existing experimental and the evaluated reactions data files.

### Introduction

Neutron cross-sections & resonance parameters are basic quantities of nuclear data that plays important roles in nuclear science and technologies. The neutron induced reaction data can be used for obtaining information of the internal structure of atomic nuclei and their constituents. The possibility of achieving a chain reaction, to design and develop nuclear reactors, neutron cross-sections are important. The accurate knowledge of the cross-sections is crucial for designing nuclear reactors. Study of neutron cross-sections substantially provides the quantitative nuclear data requisite to many engineering applications. On the other-hand the cross-section databases have to be constantly modified to enhance the predictive power of computational methods for the nuclear reactor analysis, design, maintenance, etc.

We have measured neutron total cross-sections and resonance parameters of Niobium and Palladium in the incident neutron energy range of 0.10-100 eV at the Pohang Neutron Facility, Pohang, Republic of Korea.

Nb is a rare, soft, grey, ductile transition metal that can be found in the pyrochlore minerals. It is mostly used in alloys, superconducting materials, welding, nuclear industries, electronics, optics, jewelry, etc. Pd is also a rare but lustrous silvery-white metal that can be found by mining, recycling from scrapped catalytic converters. It is used in jewelry, dentistry, watch making, blood sugar testing strips, aircraft spark plugs, surgical instruments, etc. Due to many applications of these materials the exact cross-sections should be known.

### Experimental Details

The PNF consists of a 100 MeV electron linac, water-cooled Ta target and a 12.06 m long evacuated flight tube. The electron linac consists of a thermionic RF-gun, an alpha magnet, four quadruple magnets, two SLAC-type accelerating sections, a quadruple triplet and a beam-analyzing magnet. The linac was operated with energy 65 MeV, repetition rate 10-15

Hz, pulse width 1-1.5  $\mu$ s, peak beam current 30-50mA. As a photo-neutron target, it is necessary to use heavy mass materials in order to produce intense neutrons by way of bremsstrahlung under high-power electron beams. We used Ta as the target material, which has high density (16.6 g-cm<sup>-3</sup>), high melting point (3017°C) and high resistant against the corrosion by cooling water. The TOF tubes were made by stainless steel with two different radii of 7.5 and 10 cm. The neutron beam line was equipped with a four-position sample changer that can allow the simultaneous transmissions measurement for 4 samples. For the transmission experiment neutron beam also should be passed without any sample. So at the same time maximum 3 samples can be measured. The neutron source, data acquisition systems of PNF are given in next sections in brief but the details may be seen in refs. [1, 2].

### Pulsed Neutron Source

Pulsed neutrons were produced from a water-cooled Ta target in a water tank as a neutron moderator. The target is composed of 10 Ta plates with a radius of 2.45 cm and an effective thickness of 7.4 cm. There is a 0.15 cm water gap between Ta plates for cooling the target effectively. The housing of the target is made by titanium (Ti). The calculated neutrons yield per kW of beam power for electron energy above 60 MeV at the Ta target was  $1.9 \times 10^{12}$  n/s [3]. The neutron energy distributions with and without water moderator of the PNF were shown in ref. [3]. The electron beam produced by the linear accelerator hits the Ta target, located in the center of a cylindrical water moderator contained in an aluminium cylinder with a thickness of 0.5 cm, a radius of 15 cm and a height of 30 cm and the target is aligned vertically with the center of the TOF tube. Water moderator slowed down the generated neutrons and water was 3 cm above the target surface. The neutron collimation system was composed from H<sub>3</sub>BO<sub>3</sub>, Pb, and Fe collimators. During the transmission measurement of Nb and Pd samples the linac was operated with the beam energy of 65 MeV, repetition rate of 10 Hz, and pulse width of 1  $\mu$ s.

### Data Acquisition System

To measure neutron TOF spectra there are three different data acquisition systems, which are NIM, CAMAC, and VME based systems. Generally, the NIM based system is used to separate neutron-gamma events and also we may accumulate the neutron TOF spectra. The CAMAC system can be used to operate sample changer and also to take TOF spectra. Additionally, the VME system may be used if there are any problems with the NIM or CAMAC systems. We can select the different channel widths for each crate so that we can cover different expected incident neutron energy ranges. The detailed explanations of the Data Acquisitions are given in Refs. [1, 2].

### Samples and Data Taking

In the measurement period the exposition times for the Nb and Pd samples were 15 minutes (9000 pulses of PNF linac); for empty position, it was also 15 minutes. Thus, the acquisition time for the samples was the same as for the total open beam measurements. The interleaving sequence of free position of the sample changer was chosen to minimize the influence of slow and (/or) small variation of the neutron beam intensity. If the beam intensity variations or its drift was fast and (/or) large, then these partial measurements were excluded from the total statistics. The total data taking times for Nb and Pd samples and for open beam measurement were 65 hrs.

A set of notch filters of Co, In and Cd plates with thickness of 0.5 mm, 0.2 mm and 0.5 mm respective, was used to determine the background and also to calibrate the incident neutron energy.

### Data Processing

To subtract the background we used the notch filters of Co, In, and Cd. After normalizing the events for notch filters, we fitted the notch filter's neutron time of flight spectra by considering black resonance's with an exponential fitting function

$$y = A_1 \exp(-x/t_1) + y_0, \quad (1)$$

where  $A_1$ ,  $t_1$ , and  $y_0$  are constants and  $x$  is the channel number of the time digitizer. After that we subtracted background from the normalized Nb, Pd, and open beam TOF spectra. The TOF spectra of the Nb and Pd samples along with the result of background fit (base lines) are shown in **Figure 1(a)** and **1(b)**.

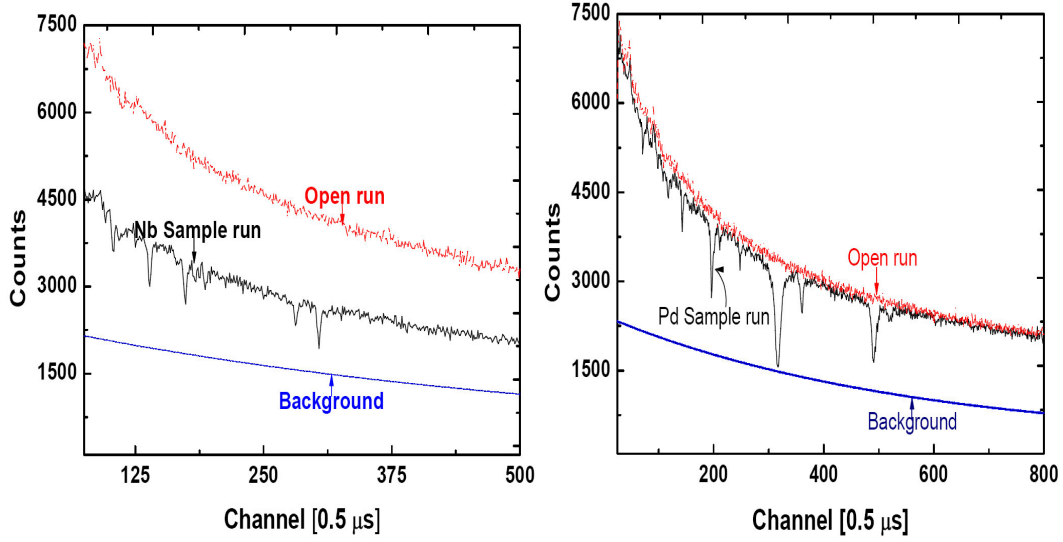


**Figure 1:** (a) TOF spectra of Nb, Open run and Background, (b) TOF spectra of Pd, Open run and Background

### Total cross-sections measurements

From the Nb and Pd sample (and open run) TOF spectra we have subtracted the normalized background to obtain the net TOF spectra. The transmission rate of neutrons at the  $i$ -th group energy  $E_i$  is defined as the fraction of incident neutrons passing through the sample compared to that in the open beam. Thus, the neutron total cross-section is related to the neutron transmission rate  $T(E_i)$  as follows:

$$\sigma(E_i) = -\frac{1}{\sum_j N_j} \ln T(E_i) \quad (2)$$

$$T(E_i) = \frac{[I(E_i) - IB(E_i)]/M_i}{[O(E_i) - OB(E_i)]/M_o} \quad (3)$$

where  $N_j$  is the atomic density per  $\text{cm}^2$  of the  $j$ -th isotope in the sample.  $I(E_i)$  is the sample-in while  $O(E_i)$  is the sample-out counts,  $IB(E_i)$  and  $OB(E_i)$  are the same for the background counts, and  $M_i$  and  $M_o$  are monitor counts for the sample-in and the open beam, respectively. We assumed monitor counts to be equal during the measurements. We estimated the background level by using the resonances of the Co, In, and Cd notch-filters as it was presented above. The neutron energy  $E$  in eV corresponding to each channel  $l$  in the TOF spectrum is derived from the following relation:

$$E = \left\{ \frac{72.3 \times L}{I \times W - \tau_0} \right\}^2, \quad (4)$$

where  $L$  is the neutron flight path in meters,  $W$  is the channel width in microseconds, and  $\tau_0$  is the time difference between the start time from the RF trigger and the real time zero when the neutron burst was produced. The flight path length  $L$  and  $\tau_0$  are determined by fitting channel numbers corresponding to the well-known resonance energies of the samples by using Eq. (4). In this experiment, we used  $W = 0.5 \mu\text{s}$  and found  $L = (12.06 \pm 0.02) \text{ m}$  and  $\tau_0 = (7.15 \pm 0.01) \mu\text{s}$  from the fitting. Then the energy resolution can be written by the expression as

$$\frac{\Delta E}{E} = 2 \frac{\Delta t}{t}, \quad (5)$$

where the uncertainty ( $\Delta t$ ) of the neutron TOF ( $t$ ) is composed of uncertainties due to the flight path (2 cm), the moderator thickness (3 cm), the pulse width of the electron beam (1  $\mu\text{s}$ ), the channel width of the time encoder (0.5  $\mu\text{s}$ ), and the time jitter (negligibly small) from the neutron detector. The relative energy resolutions for various neutron energies of 0.01, 0.1, 1, 10, and 100 eV are 0.59%, 0.60%, 0.65%, 1.01%, and 2.63%, respectively. The total cross-

sections deduced from these measurements are compared to previous reported data [4-13]. They are graphically presented in **Figure 2(a)** and **2(b)**.

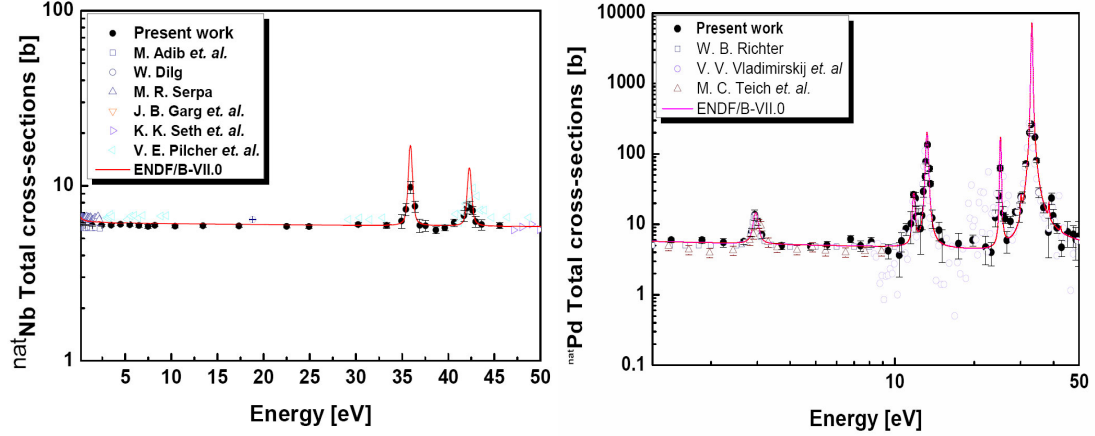


**Figure2: (a) Total cross-sections of Nb, (b) Total cross-sections of Pd**

### Determination of Resonance parameters

To determine the resonance parameters for each resonance peak, we have fitted all the transmission as well as total cross-section data of Nb and Pd with the code SAMMY [14]. By using this code the neutron total cross-sections were evaluated from the multilevel R-matrix theory [15] in the Reich-Moore approximation [16] as follows:

$$\sigma_T = \frac{2\pi}{k^2} g \left\{ 1 - \cos 2\phi \left( 1 - \frac{\Gamma_1 \Gamma}{2d} \right) - \sin 2\phi \frac{\Gamma_1 (E_\lambda - E)}{d} \right\} \quad (6)$$

Here  $k$  is the wave number associated with the incident channel,  $\phi$  the potential scattering phase shift,  $g$  the spin statistical factor,  $E$  the neutron energy, and  $E_\lambda$  is the resonance energy. Parameters  $\Gamma$  and  $\Gamma_1$  are the total width and the partial width of the decay channel 1, respectively. The quantity  $d$  is defined as:

$$d = \left\{ (E_\lambda - E)^2 + \left( \frac{\Gamma}{2} \right)^2 \right\} \quad (7)$$

In the SAMMY code the Bayes' theorem (generalized least squares) is used to fit the experimental data to get the resonance parameters. For the Doppler broadening and resolution analysis, the MULTI method [17] is applied: the free gas model is applied to the Doppler broadening and the convolution of Gaussian and exponential function to the resolution. The transmissions and SAMMY fitting curves are shown in **Figure 3(a)** and **3(b)**.

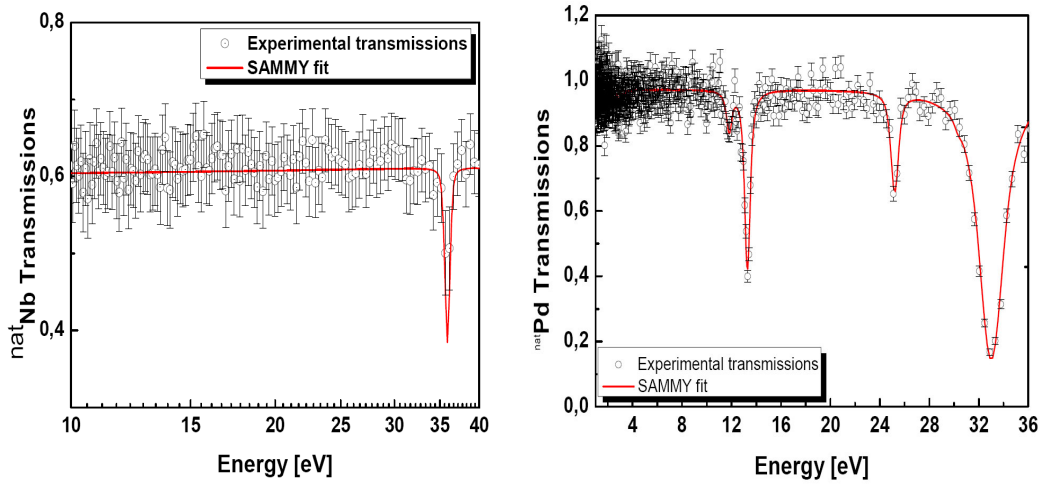


**Figure3: (a) Nb Transmissions and SAMMY Fit, (b) Pd Transmissions and SAMMY Fit.**

The evaluated resonance parameters with others reported values [18-22] are given in **table 1(a)** and **1(b)**. In the table J is the spin,  $E_\lambda$  is the resonance energy,  $\Gamma_\gamma$  is the gamma width, and  $\Gamma_n$  is the neutron width.

**Table 1(a): Resonance parameters of  $^{93}\text{Nb}$**

J/I	$E_\lambda$ [eV]	$\Gamma_\gamma$ [meV]	$\Gamma_n$ [meV]	
5/1	Present	$35.9220 \pm 0.0202$	$215.57 \pm 17.98$	$0.078 \pm 0.041$
	Saplakoglu <i>et. al.</i>	35.90	$205 \pm 51$	$0.079 \pm 0.006$
	Jackson	35.9	$215 \pm 40$	$0.056 \pm 0.005$
	Mughabghab	$35.9 \pm 0.1$	$209 \pm 80$	$0.056 \pm 0.005$
	ENDF/B-VII.0	35.90	209	0.101
4/1	Present	$42.2878 \pm 0.0642$	$228.47 \pm 22.32$	$0.079 \pm 0.007$
	Saplakoglu <i>et. al.</i>	42.2	$256 \pm 84$	$0.065 \pm 0.006$
	Jackson	42.2	$260 \pm 20$	$0.055 \pm 0.006$
	Mughabghab	$42.3 \pm 0.1$	$222 \pm 40$	$0.053 \pm 0.003$
	ENDF/B-VII.0	42.30	222	0.096
3/1	Present	$93.8784 \pm 0.0391$	$179.87 \pm 20.80$	$0.444 \pm 0.006$
	Saplakoglu <i>et. al.</i>	94.3	$220 \pm 46$	$0.275 \pm 0.015$
	Jackson	94.3	$215 \pm 50$	$0.267 \pm 0.015$
	Mughabghab	$94.3 \pm 0.1$	$180 \pm 30$	$0.273 \pm 0.024$
	ENDF/B-VII.0	94.3	180	0.497

**Table 1(b): Resonance parameters of  $^{105}\text{Pd}$**

J/I	$E_\lambda$ [eV]	$\Gamma_\gamma$ [meV]	$\Gamma_n$ [meV]	
3/0	Present	$11.8221 \pm 0.0250$	$226.29 \pm 10.33$	$0.331 \pm 0.015$
	Smith <i>et. al.</i>	$11.780 \pm 0.007$	$150 \pm 2$	$0.1800 \pm 0.0017$
	Satveloz <i>et. al.</i>	$11.790 \pm 0.02$	$151.1 \pm 2.1$	$0.21 \pm 0.01$
	ENDF/B-VII.0	11.79	151.40	0.180
2/0	Present	$13.2960 \pm 0.0148$	$350.95 \pm 18.48$	$2.846 \pm 0.216$
	Smith <i>et. al.</i>	$13.222 \pm 0.007$	$163 \pm 7$	$3.192 \pm 0.120$
	Satveloz <i>et. al.</i>	$13.230 \pm 0.01$	$174.5 \pm 3.4$	$2.29 \pm 0.03$
	ENDF/B-VII.0	13.23	174.50	2.748
3/0	Present	$25.2138 \pm 0.0036$	$458.56 \pm 10.97$	$2.517 \pm 0.005$
	Smith <i>et. al.</i>	$25.09 \pm 0.01$	$151 \pm 6$	$3.068 \pm 0.086$
	Satveloz <i>et. al.</i>	$25.15 \pm 0.01$	$135.1 \pm 2.5$	$3.92 \pm 0.05$
	ENDF/B-VII.0	25.15	135.10	3.360
2/0	Present	$30.3310 \pm 0.0026$	$163.59 \pm 8.07$	$0.162 \pm 0.022$
	Smith <i>et. al.</i>	$30.05 \pm 0.02$	$152 \pm 4$	$0.3086 \pm 0.0048$
	Satveloz <i>et. al.</i>	$30.12 \pm 0.02$	$151.7 \pm 4.1$	$0.36 \pm 0.02$
	ENDF/B-VII.0	30.12	151.70	0.432
3/0	Present	$39.3806 \pm 0.1745$	$168.65 \pm 15.04$	$0.865 \pm 0.006$
	Smith <i>et. al.</i>	$38.43 \pm 0.02$	$158 \pm 8$	$0.3240 \pm 0.0154$
	Satveloz <i>et. al.</i>	$38.44 \pm 0.02$	$154.1 \pm 6.7$	$0.35 \pm 0.01$
	ENDF/B-VII.0	38.44	154.10	0.30
3/0	Present	$42.0443 \pm 0.0083$	$150.99 \pm 19.37$	$0.072 \pm 0.079$
	Smith <i>et. al.</i>	$42.56 \pm 0.02$	$159 \pm 14$	$0.0566 \pm 0.0017$
	ENDF/B-VII.0	42.58	150	0.06
3/0	Present	$55.0659 \pm 0.0146$	$447.79 \pm 26.90$	$5.993 \pm 0.288$
	Smith <i>et. al.</i>	$55.23 \pm 0.02$	$158 \pm 11$	$6.686 \pm 0.1714$
	ENDF/B-VII.0	55.21	150	5.740
3/0	Present	$66.7421 \pm 0.0027$	$155.47 \pm 8.445$	$1.6500 \pm 0.0001$
	Smith <i>et. al.</i>	$68.27 \pm 0.02$	$159 \pm 17$	$1.577 \pm 0.051$
	Satveloz <i>et. al.</i>	$68.32 \pm 0.04$	$137 \pm 15$	$1.88 \pm 0.02$
	ENDF/B-VII.0	68.32	137	1.611

## Conclusions

The neutron total cross-sections of Nb and Pd from 0.1 to 100 eV were determined from sample-in and sample-out transmissions measurements at the Pohang Neutron Facility (PNF), South Korea. Resonance parameters were determined by a consistent analysis in which corrections for Doppler broadening, resolution broadening, and other experimental effects were incorporated to the Bayesian SAMMY code.

PNF transmissions data sets were analyzed sequentially so that each fit was connected to the previous set by the SAMMY parameters covariance matrix, thereby obtained energies and widths. The experimental transmissions data and SAMMY extracted data are good with  $\chi^2/N$  values 1.05 and 1.51, respectively for Nb and Pd samples.

To obtain improved resonance parameters it may be necessary to measure capture cross-sections as well. The PNF, Korea is on the way setting up a  $4\pi$  BGO gamma detector and the capture cross-section experiments will be carried out very soon.

## References

- [1] T. F. Wang, A. K. M. M. H. Meaze *et. al.*, Nucl Inst and Meth in Phy Res, B, 266, 561, 2008.
- [2] A. K. M. M. H. Meaze, Hossain Ahmed *et. al.*, J. Kor. Phy. Soc. 48, 827, 2006.
- [3] K. Devan, A.K.M. Moinul Haque Meaze *et. al.*, J. Kor. Phy. Soc. 49, 89, 2006.
- [4] M. Adib, A. Abdel-Kawy *et. al.*, Egyptian report to the I.N.D.C., No.2, 4, 1981
- [5] W. Dilg, Zeitschrift fuer Naturforschung, Section A, Vol.29, 1750, 1974
- [6] M. R. Serpa, Idaho Nuclear Corp. USA, Reports No.1407, 143, 1970
- [7] J. B. Garg, J. Rainwater *et. al.*, Phy Rev, 137, B547, 1965
- [8] K. K. Seth, D. J. Hughes *et. al.*, Phy Rev, 110, 692, 1958
- [9] V. E. Pilcher, R. L. Zimmerman, EXFOR Accession No. 3619, <http://www-nds.iaea.org/exfor/exfor.htm>
- [10] Biel Richter, J Atomkernenergie, 9, 307, 1965
- [11] V. V. Vladimirkij, I. A. Radkevich *et. al.*, 1st UN Conf. Peaceful Uses Atomic Energy, Geneva 1955 Vol.4, 22, 1955
- [12] M. C. Teich, P. J. Schweitzer *et. al.*, Nuclear Sci & Eng., 30, 145, 1967
- [13] Evaluated Nuclear Data File ENDF/B-VII.0, Brookhaven National Laboratory, USA, <http://www.nndc.bnl.gov/>
- [14] N. M. Larson, "RSICC Peripheral Shielding Routine Collection SAMMY-M2a: A Code System for Multilevel R-Matrix Fits to Neutron Data Using Bayes' Equations (PSR-158, SAMMY-M2a)", Oak Ridge National Laboratory, 1999
- [15] A. M. Lane and R. G. Thomas, "R-matrix theory on nuclear reaction", Rev. Mod. Phys. 30, 257, 1958.
- [16] C.W. Reich and M.S. Moore, "Multilevel Formula for the Fission Process", Phys. Rev. 111, 929, 1958.
- [17] F. A. George, "MULTI, A FORTRAN Code for Least-Square Shape Fitting of Neutron Cross-Section Data Using the Reich-Moore Multilevel Formalism," LA-5473-MS, Los Alamos Scientific Laboratory, 1974.
- [18] A. Saplakoglu, L. M. Boolinger *et. al.*, Phy Rev 109, 1258, 1958
- [19] H. E. Jackson, Phy Rev, 11, 378, 1963.
- [20] S. F. Mughabghab, Atlas of Neutron Resonances: Resonance Parameters and Thermal cross sections, Z = 1-100, Elsevier, 5<sup>th</sup> Edition, 2006
- [21] D. A. Smith, J. D. Bowman *et. al.*, Phy Rev C, 65, 024607(2002)
- [22] P. Satveloz, E. Cornelis *et. al.*, Report from CEC-countries and CEC to NEANDC No. 209L., Belgium, 53, 1979.

# The neutron resonance parameters of $^{197}\text{Au}$ from transmission, capture and self-indication measurements at GELINA

*C. Massimi<sup>1)</sup>, A. Borella<sup>2)</sup>, S. Kopecky<sup>2)</sup>, M. Moxon<sup>3)</sup>, P. Schillebeeckx<sup>2)</sup>*

1) University and INFN sez. Bologna, Via Irnerio 46, Bologna, Italy, I-40126

2) EC-JRC-IRMM, Retieseweg 111 B-2440 Geel

3) Hyde Copse 3 Marcham, UK

[massimi@bo.infn.it](mailto:massimi@bo.infn.it)

**Abstract:** Transmission, capture and self-indication measurements on  $^{197}\text{Au}$  have been performed at the neutron time-of-flight facility GELINA at EU-JRC-IRMM in Belgium. In this paper we describe the status of the measurements. Part of this work was performed within the framework of EFNUDAT project, with the aim of improving resonance parameters for the  $^{197}\text{Au}(n, \gamma)$  cross section.

## Introduction

Neutron induced reaction cross-sections are of great importance for reactor physics. They also play a role in several other fields, including astrophysics and fundamental physics. The radiative capture cross-section of Au is often used to normalise capture data. Therefore this reaction constitutes a reference for the measurement of  $(n, \gamma)$  reactions. The  $\text{Au}(n, \gamma)$  cross-section is also used for the absolute determination of neutron flux by activation measurements.

The neutron capture reaction  $^{197}\text{Au}(n, \gamma)$  is considered as a standard [1] for thermal neutrons and in the energy range between 0.2 MeV to 2.5 MeV. The aim of this work is to improve the cross section data and to extend the energy region of the  $\text{Au}(n, \gamma)$  standard in the resolved and unresolved resonance region.

In the resolved resonance region, which includes the thermal region, the reaction cross-sections can be described in terms of resonance parameters, which reflect the properties of the excited states like energy, decay widths, spin and parity. This is done by means of the R-matrix theory. A complete resonance analysis of the transmission, capture, and self-indication data was performed using the least squares, multi-level R-matrix code REFIT [2] to obtain a single set of resonance parameters from all three types of measurements.

## The GELINA facility

The Geel LINear Accelerator (GELINA) of the Institute for Reference Materials and Measurements (IRMM) at Geel has been designed and built especially for high-resolution neutron cross-section measurements [3, 4]. GELINA is a multi-user time-of-flight facility, providing a pulsed white neutron source, with a neutron energy range between 1 meV and 20 MeV. Intense pulsed electron beams, at repetition rates up to 800 Hz and with peak currents up to 12 A in a 10 ns time interval, are accelerated to an energy of up to 150 MeV in the linear electron accelerator. The electron bunches are compressed using a specially designed post-acceleration compression magnet to a duration of less than 1 ns (and, accordingly, peak currents of up to 120 A) [5, 6]. These high-energy electrons generate Bremsstrahlung in a uranium target, where neutrons are mainly produced by  $(\gamma, n)$  and  $(\gamma, f)$  reactions. To enhance the neutron intensity in the low energy domain, two water-filled Be containers are used as moderators. Using suitable collimators, either the direct (fast) neutron spectrum with very good time resolution may be used, or the moderated (slow) neutron spectrum at reduced energy resolution.

The determination of nuclear resonance parameters from a Resonance Shape Analysis (RSA) of TOF-data requires an accurate description of the response function of the spectrometer. A detailed investigation of the GELINA response functions, using Monte Carlo calculations, has been performed by Coceva and Magnani [7]. To validate the resolution function of GELINA a  $^{56}\text{Fe}(n, \gamma)$  capture measurements at a 60 m Flight Path (FP) station was performed [8].

## The experiment

Several gold samples of different thickness ranging from 5  $\mu\text{m}$  up to 1 mm were used to find a good compromise between energy resolution and statistics even for weak resonances. The samples used with their characteristics are listed in Table 1. Capture measurements have been carried out at a 12.5, 30, and 60 m (nominal) flight path, while transmission measurements have been performed at the 30 and 50 m (nominal) flight path, both types of measurements with repetition rates of 50 and 800 Hz. The self-indication measurement was carried out at a 30 m flight path and at 50 Hz operation mode.

The TOF of a neutron was determined by the time between the start signal, given at each electron burst, and the stop signal from the detectors. This time was measured with a Fast Time Coder with a 0.5 ns resolution, designed at the IRMM [9].

**Table 1.** General description of Gold disc(top) and squared(botom) samples measured at GELINA. Uncertainty on areal density is of the order of 0.1%, or less.

Sample Name	Thickness		Diameter (mm)	Weight (g)
	Nomimal (mm)	Calculated (atoms/barn)		
T2	1.10	$6.007 \times 10^{-3}$	$80.00 \pm 0.05$	$98.75 \pm 0.05$
C2	0.53	$3.097 \times 10^{-3}$	$80.00 \pm 0.05$	$50.92 \pm 0.002$
TPNP08/16	0.52	$3.026 \times 10^{-3}$	$80.04 \pm 0.05$	$50.9234 \pm 0.0005$
C1	0.12	$6.642 \times 10^{-4}$	$80.00 \pm 0.05$	$10.9200 \pm 0.0005$
TPNP08/17	0.11	$5.945 \times 10^{-4}$	$80.06 \pm 0.06$	$9.7685 \pm 0.0002$
T1	0.11	$5.940 \times 10^{-4}$	$80.00 \pm 0.05$	$9.766 \pm 0.002$
S1	0.05	$2.906 \times 10^{-4}$	$80.00 \pm 0.05$	$4.777 \pm 0.001$
TP0736/1	0.01	$5.765 \times 10^{-5}$	$80.02 \pm 0.02$	$0.9483 \pm 0.0001$
TP0736/2	0.01	$5.861 \times 10^{-5}$	$80.02 \pm 0.02$	$0.9640 \pm 0.0001$
TP0736/3	0.005	$2.772 \times 10^{-5}$	$80.02 \pm 0.04$	$0.4559 \pm 0.0001$

Sample Name	Thickness		Sizes (mm)	Weight (g)
	Nomimal (mm)	Calculated (atoms/barn)		
TPNP08/14	1.00	$5.825 \times 10^{-3}$	50.45x50.39	$48.4330 \pm 0.0005$
TPNP08/15	1.00	$5.841 \times 10^{-3}$	50.42x50.45	$48.5957 \pm 0.0005$
TPNP08/20	1.00	$5.905 \times 10^{-3}$	50.42x50.45	$48.5957 \pm 0.0005$
FILTER	0.11	$5.886 \times 10^{-4}$	217x220	$91.9 \pm 0.1$

## Transmission setups

Table 2 summarizes the details of the transmission experiments. Transmission measurements have been performed at two different stations with the neutron detectors placed a 26.45 m and 49.34 m distance from the neutron producing target. For these stations the angle between the flight path and the normal to the moderator is  $9^\circ$ . The samples were placed almost halfway between the detector and the neutron producing target in an automatic sample changer which is operated by the data acquisition system. Two  $\text{BF}_3$  proportional counters were used to monitor the output and stability of the accelerator and to normalise the sample-in and sample-out measurements to the same total neutron fluence.

At 26.45 m the setup uses a detector system of a  $\frac{1}{2}$ " thick lithium-glass scintillator, with a diameter of 4 inch that is viewed by two photomultiplier tubes (EMI9823QKB). To separate a valid neutron event from the photomultiplier noise, a coincidence between the signals of both tubes is required.

At 49.34 m the detector system is a lithium-glass scintillator of  $\frac{1}{4}$ " thickness and 4" diameter mounted inside an aluminium sphere.

In both cases a pulse-height window selects the alpha-peak of the  ${}^6\text{Li}(n,\alpha)$  reaction to distinguish a neutron event from background events. A detailed description of the experimental setup for transmission measurements at GELINA can be found in [10] and [11].

## Capture setups

Capture measurements have been performed at three measurement stations with nominal flight path distance 12.5 m, 30 m and 60 m. Details about the experimental conditions are

summarized in Table 3. The moderated neutron beam was collimated to about 75 mm in diameter at the sample position for each measurement station. The detection set-up, i.e.  $\gamma$ -ray detectors, neutron flux detector, electronics and data acquisition system, at the three measurement stations were very similar.

**Table 2.** Transmission measuring sequence at the 26.45 m and at the 49.45 m flight paths.

Flight Path	Frequency	Sample	Filters	
			Overlap	Background
49.34 m	50 Hz	10.0 $\mu\text{m}$	Cd	Na, Co
49.34 m	50 Hz	20.0 $\mu\text{m}$	Cd	Na, Co
49.34 m	50 Hz	50.0 $\mu\text{m}$	Cd	Na, Co
49.34 m	800 Hz	3.0 mm	$^{10}\text{B}$	Na, Co
26.45 m	50 Hz	3.0 mm		Pb, Na, Co, Rh
26.45 m	400 Hz	3.0 mm	$^{10}\text{B}$	Pb, Na, Co, Rh
26.45 m	800 Hz	3.0 mm	$^{10}\text{B}$	Pb, Na, Co, Rh

The detection systems consisted of a set of  $\text{C}_6\text{D}_6$  detectors with each detector positioned at an angle of  $125^\circ$  with respect to the direction of the neutron beam. To minimize the detection of scattered neutrons in the detector system, the scintillators were mounted directly on quartz-windowed photo-multipliers. The pulse height weighing technique was used to create a detector response proportional to the energy of the registered gamma. A description of the method and of the calculation of the weighting function can be found in [8]. For each detector the anode signal of the PMT is used to determine the time arrival of the neutron creating the capture event and the signal of the 9th dynode to provide information about the energy deposited by the detected  $\gamma$ -ray. The discrimination level of the capture detection system at 12m, 30m, and 60m corresponded to 200 keV, 150 keV and 150 keV deposited energy, respectively. The shape of the neutron spectrum at each station was continuously measured with a Frisch gridded ionization chambers placed about 80 cm before the capture sample: at the 12.5 m and 30 m station a double chamber was used with a cathode loaded with two back-to-back layers of about  $40 \mu\text{g}/\text{cm}^2$   $^{10}\text{B}$  each (the  $^{10}\text{B}$  layers were evaporated on a 30- $\mu\text{m}$ -thick aluminium backing). The chamber at the 60 m station consisted of three back-to-back layers of  $40 \mu\text{g}/\text{cm}^2$   $^{10}\text{B}$  evaporated on an aluminium backing. The chambers were operated with a continuous flow of a mixture of argon (90%) and methane (10%) at atmospheric pressure. The TOF and the pulse height of the detected events were recorded in list mode using a data acquisition system developed at the IRMM [12]. The list mode recording allowed a continuous stability check of the detection systems and an off-line application of the weighting function. The stability of both the detection systems and the accelerator operating conditions (i.e. frequency, current and neutron output) were verified in cycles of 1 hour. The linearity and resolution of the  $\text{C}_6\text{D}_6$  detectors was monitored weekly by measurements of the 2.6 MeV  $\gamma$ -ray from the  $^{232}\text{Th}$  decay chain.

#### Self-indication setup

Self-indication measurements have been carried out at the 30 m flight path using the same set up as the one used for capture measurements. A Au filter was placed at the beginning of the neutron beam pipe, far from the measurement station. It was a squared metal disc 21.7x22.0 cm, with a thickness of  $n_t = 5.886 \times 10^{-4}$  atoms/barn (nominal thickness 0.11 mm). The thickness of the Au sample was similar:  $n_c = 5.945 \times 10^{-4}$  atoms/barn (nominal thickness 0.11 mm). This combination of sample and filter thicknesses has been optimized for the 4.9 eV resonance. To determine the self-indication ratio, a capture measurement in the same conditions, i.e. only with the gold filter removed from the neutron beam line, is needed. Obviously the anti overlap filters as well as the fixed background filters are the same during both measurements. A Cd, Na and Au filter configuration was used.

#### Data reduction

To derive the transmission and the capture yield from the raw TOF spectra the data reduction package AGS (Analysis of Generic TOF Spectra) developed at the IRMM [13] was used.

**Table 3.** Capture measuring sequence at the 12.8, 28 and 60 m FP, a compromise to cover the energy range of interest with good energy resolution and statistic was found with these combinations

	Sample	Filters Overlap	Background
FP 12 m, 50 Hz 4 C <sub>6</sub> D <sub>6</sub> pyramid	T2 - 1.0 mm		Co, Bi, Na
	C2 - 0.5 mm		W, Co, Bi, Na
	C2 - 0.5 mm		Ag, W, Co, Bi, Na
	C2 - 0.5 mm		Co, Bi, Na
	C2 - 0.5 mm	Cd	Co, Bi, Na
	C1 - 0.1 mm		Co, Bi, Na
	S1 - 0.05 mm		Co, Bi, Na
	N2 - 0.01 mm		Co, Bi, Na
	N3 - 0.005 mm		Co, Bi, Na
FP 12 m, 50 Hz 2 C <sub>6</sub> D <sub>6</sub> cilinder	C2 - 0.5 mm		Co, Bi, Na
	C2 - 0.5 mm	Cd	Co, Bi, Na
FP 30 m, 50 Hz 2 C <sub>6</sub> D <sub>6</sub> cilinder	T2 - 1.0 mm	Cd	Na, Pb
	C2 - 0.5 mm	Cd	Na, Pb
	C2 - 0.5 mm	Cd	W, Co, Na, Pb
	C1 - 0.1 mm	Cd	Na, Pb
	N17 - 0.1 mm	Cd	Na, Pb
	S1 - 0.05 mm	Cd	Na, Pb
	N2 - 0.01 mm	Cd	Na, Pb
	N3 - 0.005 mm	Cd	Na, Pb
FP 30 m, 800 Hz 2 C <sub>6</sub> D <sub>6</sub> cilinder	T2 - 1.0 mm	<sup>10</sup> B	Pb, Al
	C2 - 0.5 mm	<sup>10</sup> B	Pb, Al
	T1 - 0.1 mm	<sup>10</sup> B	Pb, Al
	T1 - 0.1 mm	<sup>10</sup> B	Pb, Al, S
	T1 - 0.1 mm	<sup>10</sup> B	Pb, Al, Na
FP 60 m, 800 Hz 4 C <sub>6</sub> D <sub>6</sub> cilinder	C1 - 0.1 mm	<sup>10</sup> B	Co, Na
	C1 - 0.1 mm	<sup>10</sup> B	Co, Na

This package includes the most important spectra manipulations, such as: dead time correction, background fitting and subtraction, and normalization. The package includes a full propagation of uncertainties, starting from the uncorrelated uncertainties due to counting statistics. The final transmission and capture yield, deduced from the raw TOF spectra, includes a complete covariance matrix accounting for both uncorrelated and correlated uncertainty components.

The dead time of the detection chain was monitored continuously by a registration of the time-interval distribution between successive events. To reduce systematic bias effect due to the dead time only the parts of the time-of-flight spectra with a dead time correction less than 20% were considered for the data analysis.

The background as a function of TOF was derived by the black resonance technique [14]. To monitor the background level all measurements have been performed with at least one fixed black resonance filter in the beam. The background over the time range of interest was determined by an analytical expression. The free parameters in the expression were adjusted to the dips observed in the TOF spectrum resulting from measurements with black resonance filters. The black resonance filters used for the different measurement campaigns are listed in Table 2 and Table 3. The background level was at maximum of the order of 1%, with the only exception of the transmission sample-in measurement at 4.9 eV, where it was 10%.

The normalization of capture yields and self-indication data was done by means of the saturated resonance technique [15] applied to the 4.9 eV Au resonance.

### Resonance shape analysis of the experimental data

The REFIT code, based on the Reich-Moore approximation of the multi-level R-matrix formalism, was used to calculate resonance parameters performing a simultaneous fit of several data sets. In the RSA the adjusted resonance parameters were the energy and the

neutron and radiation width. The energy was determined from the transmission at 49.34 m, where the time-energy calibration was adjusted to the  $^{238}\text{U}$  resonance at  $6.673\pm 0.001$  eV. The statistical spin factor and, when possible, the parity of the resonance have been determined by an evaluation of the  $\chi^2$  resulting from the fit. This method consists in repeating the fit to the same resonance for different allowed statistical spin factors and different parities and evaluating the resulting  $\chi^2$ . This method was particularly enhanced by the results of the self-indication measurement, indeed the larger variation on  $\chi^2$  values have been observed in this data set. When it was not possible to assign the statistical spin factor  $g$  or parity, we used the one listed in ENDF/B-VII library.

## Results and conclusions

The work here presented was intended to provide an important contribution to an ongoing effort to improve the cross section data for  $^{197}\text{Au}$  in the resolved and unresolved resonance region. Transmission, capture and self-indication measurements have been performed on a large variety of Au samples and experimental conditions. The combination of complementary measurements allows to derive resonance parameters in a deterministic way and to reduce the impact of systematic effects caused by the experimental conditions.

A particularly important result of this work is the determination of the total angular momentum and partial widths of the 4.9 eV resonance, which is often employed for normalization purposes. Thanks to a self-indication measurement, and to the use of very thin samples in transmission and capture measurements, it was possible to determine the total angular momentum of this resonance, confirming the value present in evaluated data files.

An important validation of the results was provided by the measurement of the  $\text{Au}(n, \gamma)$  cross section at thermal energy, which is quoted with a 0.1% uncertainty. When using the normalization obtained from the saturated resonance at 4.9 eV resonance, the thermal cross-section was reproduced within 1%, thus confirming the reliability of the measurement data reduction and analysis procedure. Moreover the shape in the thermal region can be used to adjust the negative resonance(s).

## Acknowledgements

This work was supported by the EFNUDAT project. CM is particularly indebted to Gianni Vannini for insightful discussions and suggestions.

## References

- [1] <http://www-nds.iaea.org/standards/>
- [2] M.C. Moxon, J.B. Brisland, GEEL, REFIT, "A least square fitting program for resonance analysis of neutron transmission and capture data computer code", AEA-INTEC-0630, AEA Technology, October 1991
- [3] A. Benussan, J.M. Salomé, NIM, 155 (1981) 11
- [4] M. Flaska, A. Borella, D. Lathouwers, L. C. Mihailescu, W. Mondelaers, A. J. M. Plompen, H. van Dam, and T. H. J. J. van der Hagen NIM A, 531, 392-406 (2004)
- [5] D. Tronc, J.M. Salomé, and K.H. Böckhoff, NIM, 228 (1985) 217
- [6] J.M. Salomé, Physicalia Mag., 8 (1986) 261-272
- [7] C. Coceva and M. Magnani, IRMM internal report GE/R/ND/06/96 – 1996
- [8] A. Borella, A. Brusegan, P. Schillebeeckx, K. Volev, G. Aerts, F. Gunsing, International Workshop on P&T and ADS Development, SCK•CEN, Mol, Belgium, October 6-8, 2003
- [9] S. de Jonge, "Fast Time Digitizer Type 8514 A", Internal Report GE/DE/R/24/87, IRMM, Geel
- [10] A. Borella, F. Gunsing, M.C. Moxon, P. Schillebeeckx and P. Siegler, Phys. Rev. C 76 (2007) 014605 1-10
- [11] S. Kopecky and A. Brusegan, Nucl. Phys. A 773 (2006) 173
- [12] J. Gonzalez, C. Bastian, S. de Jonge and K. Hofmans, "Modular Multi Parameter Multiplexer MPPM. Hardware description and user guide", Internal Report GE/R/INF/06/97, IRMM, Geel
- [13] C. Bastian, AGS, "a set of UNIX commands for neutron data reduction", Proc. Int.Conf. On Neutron Research and Industry, Crete, Greece, 1996, Ed. G. Vourvopoulos, SPIE - The International Society for Optical Engineering, Vol. 2867, 611, 1997
- [14] D.B. Syme, NIM 198 (1982) 357-364
- [15] R.L. Macklin et al., NIM 164 (1979) 213



## Status and perspectives of the n\_TOF facility at CERN

*M. Calviani<sup>1)</sup>, S. Andriamonje<sup>1)</sup>, J. Andrzejewski<sup>3)</sup>, L. Audouin<sup>4)</sup>, V. Bécaries<sup>2)</sup>, F. Becvár<sup>5)</sup>, F. Bellon<sup>6)</sup>, B. Berthier<sup>4)</sup>, E. Berthoumieux<sup>7)</sup>, M. Brugger<sup>1)</sup>, F. Calviño<sup>8)</sup>, D. Cano-Ott<sup>2)</sup>, C. Carrapiço<sup>9)</sup>, P. Cennini<sup>1)</sup>, F. Cerutti<sup>1)</sup>, E. Chiaveri<sup>1)</sup>, M. Chin<sup>1)</sup>, N. Colonna<sup>10)</sup>, G. Cortés<sup>9)</sup>, M. Cortés-Giraldo<sup>11)</sup>, I. Dillmann<sup>12)</sup>, C. Domingo-Pardo<sup>13)</sup>, I. Duran<sup>14)</sup>, M. Fernández-Ordóñez<sup>2)</sup>, A. Ferrari<sup>1)</sup>, S. Ganesan<sup>15)</sup>, G. Giubrone<sup>16)</sup>, M.B. Gómez-Hornillos<sup>8)</sup>, I.F. Gonçalves<sup>9)</sup>, E. González-Romero<sup>2)</sup>, F. Gramegna<sup>17)</sup>, C. Guerrero<sup>2)</sup>, F. Gunsing<sup>7)</sup>, S. Harrisopulos<sup>18)</sup>, M. Heil<sup>13)</sup>, K. Ioannides<sup>19)</sup>, E. Jericha<sup>20)</sup>, Y. Kadi<sup>1)</sup>, F. Käppeler<sup>21)</sup>, D. Karadimos<sup>19)</sup>, M. Krlická<sup>5)</sup>, E. Leebos<sup>1)</sup>, C. Lederer<sup>22)</sup>, H. Leeb<sup>20)</sup>, R. Losito<sup>1)</sup>, M. Lozano<sup>11)</sup>, J. Marganiec<sup>3)</sup>, S. Marrone<sup>10)</sup>, T. Martinez<sup>2)</sup>, C. Massim<sup>23)</sup>, P.F. Mastinu<sup>17)</sup>, M. Meaze<sup>10)</sup>, E. Mendoza<sup>2)</sup>, A. Mengoni<sup>24)</sup>, P.M. Milazzo<sup>6)</sup>, M. Mosconi<sup>25)</sup>, R. Nolte<sup>25)</sup>, M.C. Ovejero<sup>2)</sup>, C. Paradela<sup>14)</sup>, A. Pavlik<sup>22)</sup>, J. Perkowski<sup>3)</sup>, R. Plag<sup>13)</sup>, J. Praena<sup>11)</sup>, J.M. Quesada<sup>11)</sup>, T. Rauscher<sup>29)</sup>, R. Reifarth<sup>13)</sup>, C. Rubbia<sup>1,26)</sup>, R. Sarmiento<sup>9)</sup>, G. Tagliente<sup>10)</sup>, J.L. Tain<sup>16)</sup>, D. Tarrío<sup>14)</sup>, L. Tassan-Got<sup>4)</sup>, G. Vannini<sup>23)</sup>, V. Variale<sup>10)</sup>, P. Vaz<sup>9)</sup>, A. Ventura<sup>24)</sup>, V. Vlachoudis<sup>1)</sup>, R. Vlastou<sup>27)</sup>, Z. Vykydal<sup>28)</sup>, A. Wallner<sup>22)</sup>, C. Weiß<sup>20)</sup>*

- 1) CERN, Geneva, Switzerland
- 2) Centro de Investigaciones Energeticas Medioambientales y Technologicas (CIEMAT), Madrid, Spain
- 3) Uniwersytet Łódzki, Lodz, Poland
- 4) Centre National de la Recherche Scientifique/IN2P3 - IPN, Orsay, France
- 5) Charles University, Prague, Czech Republic
- 6) Istituto Nazionale di Fisica Nucleare, Trieste, Italy
- 7) Commissariat à l'Énergie Atomique (CEA) Saclay - Irfu, Gif-sur-Yvette, France
- 8) Universitat Politècnica de Catalunya, Barcelona, Spain
- 9) Instituto Tecnológico e Nuclear (ITN), Lisbon, Portugal
- 10) Istituto Nazionale di Fisica Nucleare, Bari, Italy
- 11) Universidad de Sevilla, Spain
- 12) Physik Department E12 and Excellence Cluster Universe, Technische Universität München, Munich, Germany
- 13) GSI Helmholtzzentrum für Schwerionenforschung GmbH, Darmstadt, Germany
- 14) Universidade de Santiago de Compostela, Spain
- 15) Bhabha Atomic Research Centre (BARC), Mumbai, India
- 16) Instituto de Fisica Corpuscular, CSIC-Universidad de Valencia, Spain
- 17) Istituto Nazionale di Fisica Nucleare, Laboratori Nazionali di Legnaro, Italy
- 18) National Centre of Scientific Research (NCSR), Demokritos, Greece
- 19) University of Ioannina, Greece
- 20) Atominstytut, Technische Universität Wien, Austria
- 21) Forschungszentrum Karlsruhe GmbH (FZK), Institut für Kernphysik, Karlsruhe, Germany
- 22) Fakultät für Physik, Universität Wien, Austria
- 23) Dipartimento di Fisica, Università di Bologna, and Sezione INFN di Bologna, Italy
- 24) ENEA, Bologna, Italy
- 25) Physikalisch-Technische Bundesanstalt (PTB), Braunschweig, Germany
- 26) Laboratori Nazionali del Gran Sasso dell'INFN, Assergi (AQ), Italy
- 27) National Technical University of Athens (NTUA), Greece
- 28) Institute of Experimental and Applied Physics (IEAP), Czech Technical University (CTU), Prague, Czech Republic
- 29) Department of Physics, University of Basel, Switzerland

[marco.calviani@cern.ch](mailto:marco.calviani@cern.ch)

**Abstract:** The white spectrum neutron time-of-flight facility n\_TOF is operating at CERN since 2001. A neutron beam with high instantaneous flux and high resolution in energy is delivered in the experimental area located 187 m downstream from the spallation target. The intense neutron fluence per proton burst results in a much enhanced signal to background ratio for neutron capture and fission reactions on radioactive isotopes, thus making the facility well suited for accurate measurement of neutron-induced reaction cross-sections. Combined with state-of-the-art detectors and with advanced data acquisition systems, the innovative characteristics of the n\_TOF neutron beam have allowed collecting data on a variety of stable and radioactive isotopes of interest for nuclear astrophysics and for applications to advanced reactor technologies. After a three-year shutdown, the facility has resumed operations in November 2008 with a new spallation target with an improved engineering design and safety features. In 2009 run the n\_TOF Collaboration has performed the full commissioning of the facility. The physics program of the n\_TOF Phase 2 has started with measurements of neutron capture cross-sections of  $^{56}\text{Fe}$  and  $^{62}\text{Ni}$ . The short and medium term perspectives of the facility are here presented as well.

## Introduction

Accurate neutron cross-section data are of major importance for a wide variety of research fields in basic and applied nuclear physics. In particular, data on neutron reactions are essential in Nuclear Astrophysics for understanding the origin of the heavy elements in the Universe, which are produced mainly through slow and rapid neutron capture processes during the various phases of stellar evolution [1,2]. In the field of nuclear technology, a renewed interest in nuclear energy production has triggered studies aimed at developing future generation systems that would address major safety, proliferation and waste concerns. For these applications the available nuclear data of many nuclides are not sufficiently accurate and sometimes even lacking. In order to improve the evaluated neutron cross-section libraries such as ENDF/B, JEFF and JENDL [4], accurate measurements attainable at advanced neutron sources are of crucial importance. Based on these motivations the neutron time-of-flight facility n\_TOF has been constructed at CERN, Geneva. At the end of 2008 the n\_TOF facility resumed operation after a three-year shutdown for upgrading the spallation target.

## The n\_TOF facility and Phase 2 upgrades

The idea of a new neutron time-of-flight facility at CERN was proposed by C. Rubbia in 1998 [5] as a follow up of the TARC experiment, which had been conducted at CERN before. After the first commissioning phase in 2001, the facility had become fully operational with the start of the scientific program in May 2002. The first measurement campaign (n\_TOF Phase 1) lasted until the end of 2004, when the facility was stopped due to an unexpected radioactivity increase in the filters of the cooling station [6], indicating a degradation of the spallation target. In n\_TOF Phase 1, neutrons were produced by spallation reactions induced by a pulsed, 10 ns wide, 20 GeV/c proton beam with up to  $7 \times 10^{12}$  protons per pulse, impinging on a  $80 \times 80 \times 60 \text{ cm}^3$  lead target, surrounded by a water layer of 5 cm acting both as coolant and moderator of the spectrum. In 2008, the lead target has been substituted and new cooling and ventilation systems were installed.

The n\_TOF neutron energy spectrum spans over nine orders of magnitude, from thermal energy up to approximately 1 GeV [7]. Together with the wide energy range, other important characteristics of the n\_TOF facility are the very high instantaneous flux in the experimental area (around  $10^6$  neutrons/pulse), which makes the facility particularly suited for cross-section measurements on radioactive isotopes, while the very low duty cycle (0.5 Hz) eliminates the problem of bunch wrap around. An evacuated neutron beam line leads to the experimental area located at 187 m from the lead target, which allows one to reach a high resolution in neutron energy. Two collimators exactly define the beam profile in the measuring station, and a very low ambient background is obtained by massive iron and concrete shielding.

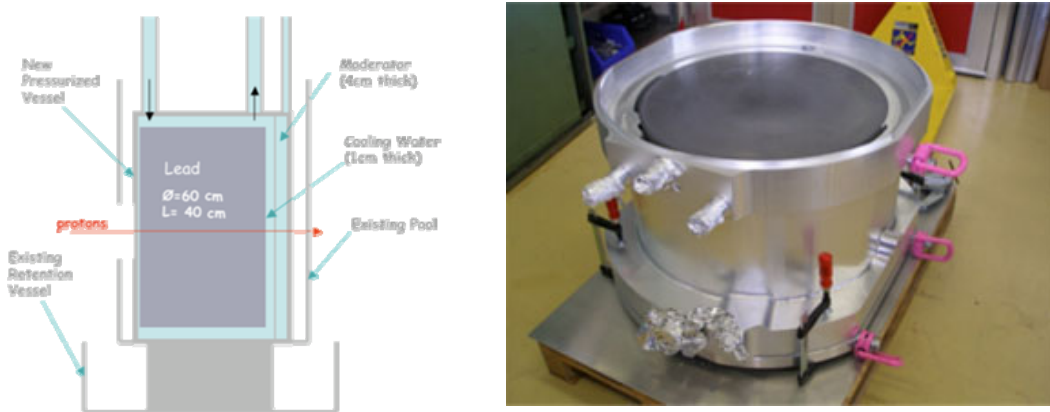


**Figure 1.** Schematics of the new  $n_{\text{TOF}}$  spallation target (left), and the assembly during construction (right), showing the lead block and the pressure vessel.

After a three-year long stop due to activation of the cooling water by spallation products, a new lead target was constructed and new systems according to the safety requirements for the restart of the facility were implemented. In particular, a ventilation system was installed in the primary target area and an optimized cooling system was developed to control and balance the chemical parameters of the water (in particular the oxygen content) and to reliably retain the activation products in the cooling water. An extensive study of the target corrosion mechanism has been performed to improve the long-term stability of the system.

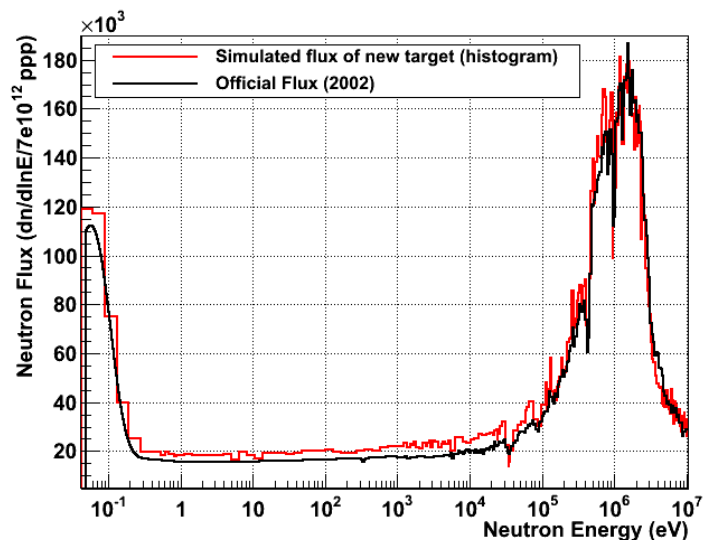


**Figure 2.** Comparison between the expected fluence in the experimental area with the new spallation target and the official flux of  $n_{\text{TOF}}$  Phase 1.

The new lead block was shaped as a cylinder 30 cm in radius and 40 cm in length to efficiently optimize the cooling and the neutron production. The new design avoids also a problem of the previous target due to an insufficient water flow at the proton impact point. Another improvement was achieved by the separation of the target cooling and of the moderator circuit. This enables the use of different moderator materials and provides greater flexibility in choosing the characteristics of the neutron beam. Since the size of the new target and the total amount of moderator are similar compared to the previous version, the neutron flux and spectral shape in Phase 2 is expected to be very close to the one available in the first measurement campaign. This is confirmed by simulations performed with the FLUKA code [8] (see Figure 2), and by the measurements for the commissioning of the new beam [9]. The

larger absorption dips in the 1-100 keV neutron energy range are due to the increased aluminium thickness in the new target with respect to the old one.

In order to decrease the thermal stress on the target, the size of the proton beam spot is now about 9 times larger than in the past. In this way the possibility of pitting corrosion at proton impact is reduced due to the lower energy density.

Part of the 2009 run was dedicated to the commissioning of the new spallation target, both for the analysis of the neutron beam characteristics (fluence, beam profile, resolution function) and for the analysis of the behaviour of the target, cooling and ventilation systems under the new conditions. More details on the beam characteristics could be found in another contribution to this workshop [9].

## The experimental setup

The innovative characteristics of the n\_TOF facility are complemented with the advanced detection and acquisition systems developed by the n\_TOF Collaboration for the first measurement campaign. The neutron flux is monitored with a low mass monitor made of a  ${}^6\text{Li}$  deposit on a thin foil surrounded by an array of silicon detectors outside of the beam [10]. For capture measurements two different devices are typically used: two deuterated benzene ( $\text{C}_6\text{D}_6$ ) liquid scintillator detectors and a  $4\pi$   $\text{BaF}_2$  calorimeter. The first setup is characterized by a very low neutron sensitivity, which was obtained by minimizing the detector by attaching the thin carbon fiber cans for the scintillator directly to the bare photomultiplier [11]. The second system is a total absorption calorimeter (TAC), made of 40  $\text{BaF}_2$  crystals, which is optimized for highly radioactive and fissile isotopes, such as minor actinides. In this case the calorimetric method is used, by which the full  $\gamma$ -ray cascades of a neutron reaction is detected with high efficiency and complete solid angle coverage [12]. A list of capture cross-section measurements performed in n\_TOF Phase 1 with both systems is given in Table 1. Fission cross-section measurements have been performed with two independent detector systems, a Fast Ionization Chamber (FIC) [13] and a stack of Parallel Plate Avalanche Counters (PPACs). The FIC consists of several parallel-plate chambers with 5 mm spacing between electrodes and is operated with a mixture of 90% Ar + 10%  $\text{CF}_4$  at 720 mbar pressure. In the PPACs fission fragments are detected in coincidence, a very efficient method for alpha particle rejection. In both detector systems  ${}^{235}\text{U}$  and  ${}^{238}\text{U}$  samples are included because these cross-sections are considered as standards in the different energy ranges. A list of fission cross-section measurement performed during the first measurement campaign is given in Table 2. Some of the results can be found in Refs. [14] and [15]. Due to stringent radioprotection requirements, the FIC detector will not be used in n\_TOF Phase 2 but will be substituted by new types of detectors, described in the next section.

**Table 1.** Measurements of neutron capture cross-sections performed at n\_TOF in the first experimental campaign. The radioactive isotopes are marked in bold to be distinguishable.

Isotopes	Experimental setup
${}^{197}\text{Au}$ , ${}^{151}\text{Sm}$ , ${}^{204,206,207,208}\text{Pb}$ , ${}^{209}\text{Bi}$ , ${}^{139}\text{La}$ , ${}^{232}\text{Th}$ , ${}^{24,25,26}\text{Mg}$ , ${}^{90,91,92,93,94,96}\text{Zr}$ , ${}^{186,187,188}\text{Os}$	$\text{C}_6\text{D}_6$ – Pulse Height Weighting Technique
${}^{197}\text{Au}$ , ${}^{233,234}\text{U}$ , ${}^{237}\text{Np}$ , ${}^{240}\text{Pu}$ , ${}^{243}\text{Am}$	$\text{BaF}_2$ – Total Absorption Calorimeter

**Table 2.** Neutron-induced fission cross-section measurements performed at n\_TOF Phase 1 with the FIC and PPACs. Radioactive isotopes are indicated in bold to be distinguishable.

Isotopes	Experimental setup
${}^{\text{nat}}\text{Pb}$ , ${}^{209}\text{Bi}$ , ${}^{232}\text{Th}$ , ${}^{237}\text{Np}$ , ${}^{233,234,235,238}\text{U}$	PPAC – Coincidence technique
${}^{232}\text{Th}$ , ${}^{237}\text{Np}$ , ${}^{233,234,235,236,238}\text{U}$ , ${}^{241,243}\text{Am}$ , ${}^{245}\text{Cm}$	FIC – Single fragment detection

### The commissioning run of 2009

The n\_TOF program has been scheduled for  $7.5 \times 10^{18}$  protons on target over the course of the 2009 run. A fraction of the allocated protons ( $2.68 \times 10^{18}$  protons) has been used for the commissioning of the facility. Following the complete characterization of the neutron beam, the collaboration has initiated the approved physics program with the measurement of the  $^{56}\text{Fe}$  and  $^{62}\text{Ni}$  capture cross-sections with the  $\text{C}_6\text{D}_6$  detectors.

During the commissioning the neutron flux has been measured with a calibrated  $^{235}\text{U}$ -based fission chamber from PTB Braunschweig [17], complemented with a Micromegas detector loaded with  $^{10}\text{B}$  and  $^{235}\text{U}$  samples and the standard n\_TOF silicon monitor. In addition the activation technique with two gold foils has been used as well. For the neutron beam profile a Medipix detector [18] with LiF and polyethylene converters and an X-Y Micromegas detector have been used. The last one is an innovative system [19] based on the Bulk technology, capable of producing a 2D image of the neutron beam. Preliminary results are reported in [9]. From the facility point of view, particular attention has been given to the monitoring of the cooling and ventilation systems (see Figure 3). Various detectors are being used to monitor the oxygen content, the pH value and the conductivity of the cooling water, which are the critical parameters for evaluating the corrosion of the target and of the aluminum membranes. The adopted operating condition consists in running the system with a maximum dissolved  $\text{O}_2$  content of 0.08 mg per liter.



**Figure 3.** Picture of the n\_TOF cooling station. In the foreground the four mechanical filters are visible. In the back, beyond the concrete shielding is the ion-exchange cartridge.

To keep the system within this limit a degassing device has been installed, which removes the excessive  $\text{O}_2$  by flushing with nitrogen. An ion-exchange cartridge is used to filter Pb and spallation products out of the cooling water. In order to comply with safety regulations, a ventilation system has been installed to continuously replace the air in the primary target area. A flow rate of about  $\sim 500 \text{ m}^3/\text{h}$  is used to maintain an under pressure of 40 Pa in the  $1200 \text{ m}^3$  area where the spallation target is located. Under these conditions, the released radioactivity remains safely below a limit corresponding to a dose of  $\mu\text{Sv}$  to the public over 1 year of operation.

### Future plans

Presently the n\_TOF collaboration is planning several upgrades in order to improve the characteristics of the facility.

The replacement of the light water moderator by borated water will greatly enhance the measuring capabilities by significantly reducing the present in-beam photon component. These in-beam  $\gamma$ -rays are produced by neutron capture in hydrogen (which give rise to 2.2 MeV photons) and by neutron capture in structural materials such as lead and iron, which produce  $\gamma$ -rays between 7 and 7.5 MeV. Since this photon contribution is emitted with a delay of about  $1 \mu\text{s}$  after the impact of the proton pulse, it results in a background component in the

1-100 keV neutron energy range, which is particularly problematic in measurements performed with  $C_6D_6$  detectors. The use of borated water will reduce the 2.2 MeV photons by a factor of about 10, leaving the neutron fluence unchanged above 1 eV. This option is already in the engineering stage and it will be ready for the 2010 n\_TOF run.

Another upgrade foreseen for the 2010 run is the transformation of the n\_TOF experimental area into a work sector of type A, which will allow us to perform measurement of capture and fission cross-sections by using "unsealed" samples of highly radioactive isotopes, such as  $^{241}\text{Am}$ ,  $^{243}\text{Am}$  and  $^{241}\text{Pu}$ . Since substantial backgrounds from sample cannings can be avoided in this way, a whole new class of experiments will become feasible in the future. This modification, which requires a complete revision of the experimental area and of the related technical services, will start at the end of November 2009.

A longer term project concerns the possibility to construct a second experimental area located above the spallation target pit. The two main advantages over the experimental area at 200 m are the reduced prompt flash and the increased flux, by around a factor 20. The latter factor will allow reducing the mass of the samples, especially in the case of short lived, highly radioactive isotopes, for which the main problem is the cost and the availability in significant amounts. The project is under study and a technical report will be released by summer 2010.

### Acknowledgments

The n\_TOF Collaboration and the CERN EN/STI/EET section would like to thank several CERN groups that contributed with their work to the successful restart and day-to-day operation of the facility. In particular, thanks are due to members of EN/CV for cooling and ventilation, DG/SCR for support on radioprotection issues, EN/MEF and EN/STI for mechanical as well as technical help and BE/OP for optimal beam conditions.

### References

- [1] F. Käppeler, Progr. Particle Nucl. Phys. **43** (1999) 419.
- [2] G. Wallerstein et al., Rev. Mod. Phys. **69** (1997) 995.
- [3] NEA-OECD, Acc. Driven Systems (ADS) and Fast Reactors (FR) in Adv. Nucl. Cyc., 2002.
- [4] see <http://www-nds.iaea.org> for a comprehensive list of nuclear data libraries.
- [5] C. Rubbia et al., Tech. Rep. CERN/LHC/98-02, CERN, 1998.
- [6] T. Otto, Tech. Rep. CERN-SC-2005-034-RP-TN, April 2005.
- [7] U. Abbondando et al., Tech. Rep. CERN-SL-2002-053 ECT, 2003.
- [8] A. Fasso' et al., CERN-2005-10, INFN/TC\_05/11, SLAC-R-773, 2005.
- [9] C. Guerrero et al. (The n\_TOF Collaboration), Characterization of the new neutron beam at n\_TOF-Ph2, Proc. 2nd EFNUDAT Workshop, 23-25 Sept. 2009, Budapest (Hungary).
- [10] S. Marrone et al. (The n\_TOF Collaboration), Nucl. Instr. Meth. **A517** (2004) 389-398.
- [11] R. Plag et al. (The n\_TOF Collaboration), Nucl. Instr. Meth. **A496** (2003) 425-436.
- [12] C. Guerrero et al. (The n\_TOF Collaboration), Nucl. Instr. Meth. **A608** (2009) 424-433.
- [13] M. Calviani et al. (The n\_TOF Collaboration), Nucl. Instr. Meth. **A594** (2008) 220-227.
- [14] M. Calviani et al. (The n\_TOF Collaboration), Phys. Rev. C **80**, 044604 (2009)
- [15] C. Paradela et al. (The n\_TOF Collaboration), submitted to Phys. Rev. C.
- [16] J.L. Tain et al. (The n\_TOF Collaboration), CERN-INTC-2008-035 (2008)
- [17] D.B. Gayther, Metrologia **27**, 221-231 (1990).
- [18] <http://www.cern.ch/medipix>
- [19] S. Andriamonje et al., AccApp '09, 4-8 May 2009, Vienna, Austria.

## Characterization of the new neutron beam at n\_TOF-Ph2

C. Guerrero<sup>1)</sup>, S. Andriamonje<sup>2)</sup>, J. Andrzejewski<sup>3)</sup>, L. Audouin<sup>4)</sup>, V. Bécaries<sup>1)</sup>,  
 F. Bečvář<sup>5)</sup>, F. Belloni<sup>6)</sup>, B. Berthier<sup>4)</sup>, E. Berthoumieux<sup>7)</sup>, M. Brugger<sup>2)</sup>,  
 M. Calviani<sup>2)</sup>, F. Calviño<sup>8)</sup>, D. Cano-Ott<sup>1)</sup>, C. Carrapiço<sup>9)</sup>, P. Cennini<sup>2)</sup>,  
 F. Cerutti<sup>2)</sup>, E. Chiaveri<sup>2)</sup>, M. Chin<sup>2)</sup>, N. Colonna<sup>10)</sup>, G. Cortés<sup>9)</sup>, M. Cortés-  
 Giraldo<sup>11)</sup>, I. Dillmann<sup>12)</sup>, C. Domingo-Pardo<sup>13)</sup>, I. Duran<sup>14)</sup>, M. Fernández-  
 Ordóñez<sup>1)</sup>, A. Ferrar<sup>2)</sup>, S. Ganesan<sup>15)</sup>, I. Giomataris<sup>7)</sup>, G. Giubrone<sup>16)</sup>, M.B.  
 Gómez-Hornillos<sup>8)</sup>, I.F. Gonçalves<sup>9)</sup>, E. González-Romero<sup>1)</sup>, F. Gramegna<sup>17)</sup>,  
 F. Gunsing<sup>7)</sup>, S. Harrisopulos<sup>18)</sup>, M. Heil<sup>13)</sup>, K. Ioannides<sup>19)</sup>, E. Jericha<sup>20)</sup>,  
 Y. Kadř<sup>2)</sup>, F. Käppeler<sup>21)</sup>, D. Karadimos<sup>19)</sup>, M. Krtička<sup>5)</sup>, E. Leebos<sup>2)</sup>,  
 C. Lederer<sup>22)</sup>, H. Leeb<sup>20)</sup>, R. Losito<sup>2)</sup>, M. Lozano<sup>11)</sup>, J. Marganec<sup>3)</sup>,  
 S. Marrone<sup>10)</sup>, T. Martinez<sup>1)</sup>, C. Massimi<sup>23)</sup>, P.F. Mastinu<sup>17)</sup>, M. Meaze<sup>10)</sup>,  
 E. Mendoza<sup>1)</sup>, A. Mengoni<sup>24)</sup>, P.M. Milazzo<sup>6)</sup>, M. Mosconi<sup>25)</sup>, R. Nolte<sup>25)</sup>,  
 M.C. Ovejero<sup>1)</sup>, T. Papaevangelou<sup>7)</sup>, C. Paradela<sup>14)</sup>, A. Pavlik<sup>2)</sup>, J. Perkowski<sup>3)</sup>,  
 R. Plag<sup>13)</sup>, J. Praena<sup>11)</sup>, J.M. Quesada<sup>11)</sup>, R. Reifarth<sup>13)</sup>, C. Rubbia<sup>2,26)</sup>,  
 R. Sarmiento<sup>9)</sup>, G. Tagliente<sup>10)</sup>, J.L. Tain<sup>16)</sup>, D. Tarrío<sup>14)</sup>, L. Tassan-Got<sup>4)</sup>,  
 G. Vannini<sup>23)</sup>, V. Variale<sup>10)</sup>, P. Vaz<sup>9)</sup>, A. Ventura<sup>24)</sup>, V. Vlachoudis<sup>2)</sup>,  
 R. Vlastou<sup>27)</sup>, Z. Vykydal<sup>28)</sup>, A. Wallner<sup>22)</sup>, C. Weiß<sup>20)</sup>  
 (The n\_TOF Collaboration)

- 1) Centro de Investigaciones Energeticas Medioambientales y Tecnologicas (CIEMAT), Madrid, Spain
- 2) European Organization for Nuclear Research (CERN), Geneva, Switzerland
- 3) Uniwersytet łódzki, Lodz, Poland
- 4) Centre National de la Recherche Scientifique/IN2P3 - IPN, Orsay, France
- 5) Charles University, Prague, Czech Republic
- 6) Istituto Nazionale di Fisica Nucleare, Trieste, Italy
- 7) Commissariat à l'Énergie Atomique (CEA) Saclay – Irfu, Gif-sur-Yvette, France
- 8) Universitat Politècnica de Catalunya, Barcelona, Spain
- 9) Instituto Tecnológico e Nuclear (ITN), Lisbon, Portugal
- 10) Istituto Nazionale di Fisica Nucleare, Bari, Italy
- 11) Universidad de Sevilla, Spain
- 12) Physik Department E12 and Excellence Cluster Universe, Technische Universität München, Munich, Germany
- 13) GSI Helmholtzzentrum für Schwerionenforschung GmbH, Darmstadt, Germany
- 14) Universidade de Santiago de Compostela, Spain
- 15) Bhabha Atomic Research Centre (BARC), Mumbai, India
- 16) Instituto de Física Corpuscular, CSIC-Universidad de Valencia, Spain
- 17) Istituto Nazionale di Fisica Nucleare, Laboratori Nazionali di Legnaro, Italy
- 18) National Centre of Scientific Research (NCSR), Demokritos, Greece
- 19) University of Ioannina, Greece
- 20) Atominstytut, Technische Universität Wien, Austria
- 21) Forschungszentrum Karlsruhe GmbH (FZK), Institut für Kernphysik, Karlsruhe, Germany
- 22) Fakultät für Physik, Universität Wien, Austria
- 23) Dipartimento di Fisica, Università di Bologna, and Sezione INFN di Bologna, Italy
- 24) Agenzia nazionale per le nuove tecnologie, l'energia e lo sviluppo economico sostenibile (ENEA), Bologna, Italy
- 25) Physikalisch-Technische Bundesanstalt (PTB), Braunschweig, Germany
- 26) Laboratori Nazionali del Gran Sasso dell'INFN, Assergi (AQ), Italy
- 27) National Technical University of Athens (NTUA), Greece

28) Institute of Experimental and Applied Physics (IEAP), Czech Technical University (CTU), Prague, Czech Republic  
[carlos.guerrero@cern.ch](mailto:carlos.guerrero@cern.ch)

**Abstract:** After a halt of three years and following the construction of a new lead spallation target, the n\_TOF facility has resumed operation in November 2008. After a short commissioning of the new target, the 2009 experimental campaign has been devoted to the full characterization of the neutron beam by means of different and independent detection systems.

The spatial profile of the neutron beam has been measured by position sensitive MicroMegas and MEDIPIX detectors, both providing a 2D profile as a function of neutron energy. The intensity and energy distribution of the neutron beam have been determined from a calibrated fission chamber from PTB with five  $^{235}\text{U}$  deposits, a MicroMegas detector with  $^{10}\text{B}$  and  $^{235}\text{U}$  deposits, and the n\_TOF Silicon Monitor and Total Absorption Calorimeter, as well as from activation of gold foils.

The experimental data from the measurement of the beam profile and neutron fluence are presented for the first time in this work, which contains also a preliminary analysis of the data.

## Introduction

The Neutron Time of Flight facility n\_TOF [1] at CERN has been used since 2001 for the measurement of neutron cross sections relevant for Nuclear Technology and Astrophysics. At n\_TOF neutrons are generated by spallation from a 20 GeV proton beam impinging on a lead target. The initial fast neutron spectrum is shaped into a white spectrum by means of a moderator (demineralised or borated water) preceding a neutron beam line that connects the spallation target with the experimental area where the samples are irradiated. The wide neutron energy range (10 orders of magnitude starting at thermal), the high instantaneous beam intensity ( $10^6$  neutrons/pulse between thermal and 100 MeV) and the long flight path (185 m) are the main advantages of n\_TOF with respect to other facilities. The combination of these with state of the art detection systems and a Data Acquisition System based on flashADC have provided in the first phase of experiments (2001-2004) a large set of high quality capture and fission cross section data.

Following the design and construction of a new spallation target [2], the n\_TOF facility became operative in November 2008. The main improvements with respect to the previous lead target concern the safety and the operational flexibility, since it offers the possibility of using moderators with different thicknesses and compositions, and envisages the possibility of using a new experimental area with a flight path of 20 m in the vertical direction.

The beginning of the 2009 experimental campaign has been devoted to the full characterization of the neutron beam at the irradiation point in the experimental area. This contribution presents the measurements and the data analyses aimed at determining the spatial profile, intensity and energy distribution of the neutron beam.

## Spatial profile of the neutron beam

The neutron beam is shaped along the beam line by means of two collimators placed at 135 m and 175 m from the lead target, the latter being responsible of the shape of the beam in the experimental area. The knowledge of the beam profile and its dependence with neutron energy are crucial in the capture measurements, where the samples are always smaller than the beam and where it is necessary to correct for the beam interception factor.

The beam profile has been measured by means of two position sensitive detectors, the MEDIPIX and the 2D MicroMegas (XY-MGAS):

1) The MEDIPIX [3] detector is  $2.83 \times 2.83 \text{ cm}^2$  in size and consists of  $512 \times 512$  pixels on a 300 mm thick Silicon sensor. Two neutron converters have been used:  $^6\text{Li}$  for slow neutrons (up to 1 keV) and Polyethylene for fast neutrons. The measurements have been performed in four TOF intervals: 0.01-1 eV, 1-103 eV, 0.08-1 MeV and 0.08-200 MeV.

2) The XY-MGAS [4] detector, based on the Bulk principle, has  $6 \times 6 \text{ cm}^2$  active area containing  $106 \times 106$  strips that are read using a Gasiplex card. The detection of the  $\alpha$  particles, produced in a  $^{10}\text{B}$  converter, in two segmented pads allows reconstructing the time-of-flight and position of the neutron interaction. The measured 2D beam profile for thermal neutrons at a flight path of 183.5 m is shown in the left panel of figure 1. The vertical profile in

the right panel illustrates for two energy intervals how the beam becomes narrower with increasing neutron energy.

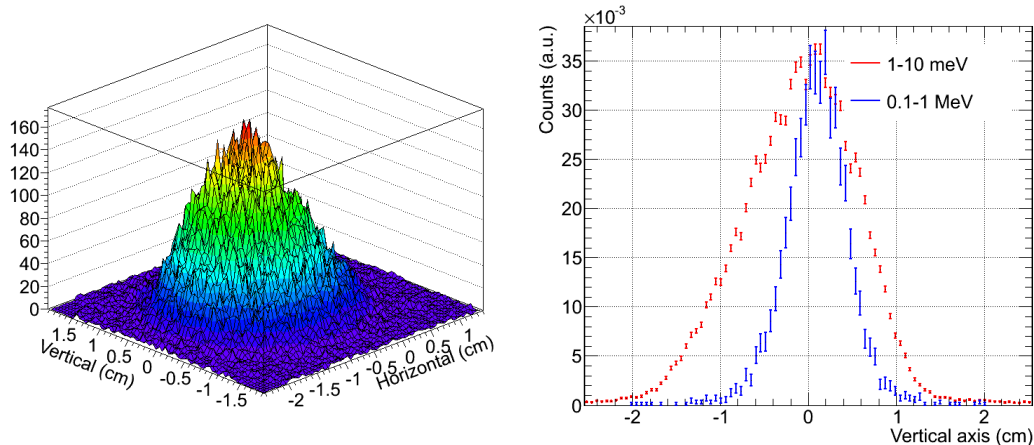


**Figure 1.** Results from the XY-MGAS at 183.5 m time-of-flight distance. Left: Two dimensional spatial profile of the neutron beam at thermal energies. Right: Vertical profile in two neutron energy intervals.

The analysis of data from the MEDIPIX and the XY-MGAS detectors is ongoing. The evaluated beam profile will be obtained by the combination of an analytical fit to the experimental data and the simulations of the optical transport of neutrons from the target to the irradiation point through the collimation system.

### Intensity of the neutron beam

The accurate determination of the neutron beam intensity requires a detector of well known efficiency for detecting reactions with a well known cross section taking place in a sample of well known mass. At n\_TOF we have used a multi plate fission chamber calibrated at PTB [5]. The chamber contains five highly enriched  $^{235}\text{U}$  samples on platinum backings and six tantalum collector plates. The uranium deposits are 76 mm in diameter with a total mass of 201.4(5) mg. The signals from the detectors were connected directly to our flash-ADC (8 bits and 100 MSamples/s) and a total of  $10^{18}$  protons were allocated to the measurement. The resulting pulse height and neutron energy distributions are shown in Figure 2. The dips in the neutron energy spectrum, the largest one around 5 eV, correspond to neutron absorption in strong Ta resonances.

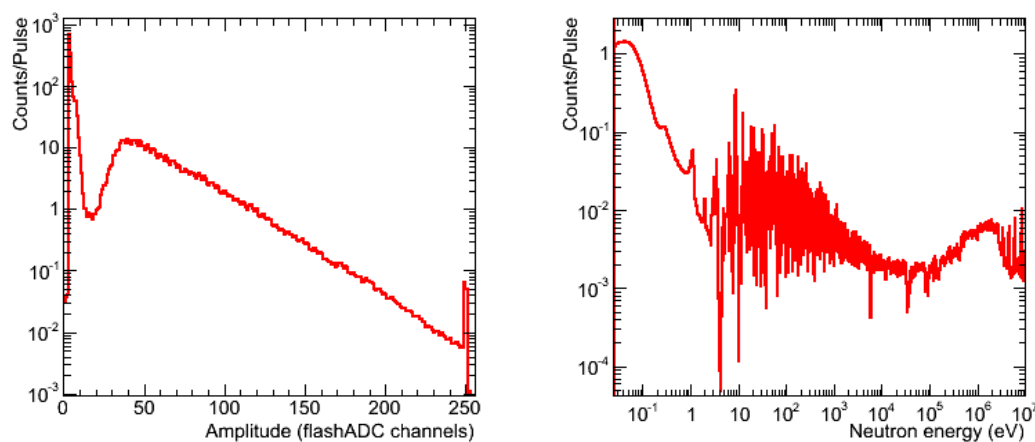


**Figure 2.** Pulse Height (left) and Neutron energy (right) distributions resulting from the measurement with the PTB fission chamber.

The neutron fluence per pulse is calculated from the counting rate  $CR(Counts/Pulse)$ , the efficiency  $\varepsilon(n,f)$  of the detector (95.4% for neutron from thermal up to a several MeV) and the expected fission yield  $Y^{MCNP}$ , calculated from detailed MCNP simulations including the windows, backings and electrodes of the chamber.

The result, expressed in isoethargic units, is shown as a blue line in Figure 3. In the meV and MeV regions one can observe the thermal and evaporation peaks, respectively; while the epithermal range shows a nearly isoethargic energy dependence of the fluence.

A series of additional measurements with other detection systems have been performed in order to validate and complement the results from the PTB fission chamber. The results from such measurements are displayed as colour lines and markers in Figure 3 and are discussed in the following:

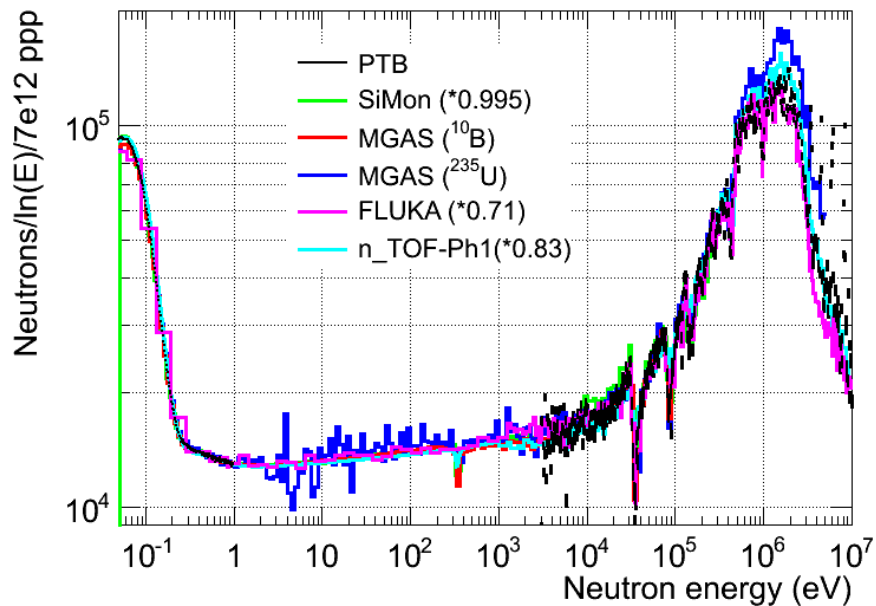


**Figure 3.** Neutron fluence, in isoethargic units, resulting from the analysis of the PTB fission chamber. The complementary measurements of the fluence are also shown: MGAS, SiMon, Activation and TAC.

**The Silicon Monitor (SiMon) [6]:** An assembly of 4 silicon detectors looking at a thin ( $300 \mu\text{g}/\text{cm}^2$ )  $^6\text{Li}$  foil is used for monitoring purposes during the neutron capture measurements at n\_TOF. The corresponding neutron fluence is shown in Figure 3. The overall accuracy of the result is 6%, 5% due to the thickness of the foil and 3% from the calculation of  $\varepsilon^{\text{SiMon}}$  by MC simulations.

**The monitoring MicroMegas (MGAS) [7]:** A new Micromegas detector with an efficiency of 95% has been designed and constructed for on-line monitoring of the neutron beam intensity both at low ( $^{10}\text{B}$  sample with 35 mm diameter) and high ( $^{235}\text{U}$  sample with 20 mm diameter) neutron energies. The results for  $^{10}\text{B}$ , normalized to the  $^{235}\text{U}$  data at thermal, are shown in Figure 3. The accuracy of the results is 7%, which is dominated by the uncertainty in the alignment of the sample and the calculation of the beam interception factor ( $\varnothing_{\text{U-235}}=2 \text{ cm}$ ,  $\varnothing_{\text{beam}}=3.5 \text{ cm}$ ).

**Activation of gold foils:** A pair of gold foils with  $25 \mu\text{m}$  thickness and 45 mm diameter (larger than the beam) were placed back-to-back in the neutron beam. The largest fraction (95%) of the difference in the number of  $^{198}\text{Au}$  produced in the two samples corresponds to neutrons with energies around the 4.9 eV resonance of gold, which saturates in the first sample. This allows one to calculate the neutron fluence around 4.9 eV with an accuracy of 10%, which is dominated by the determination of the activity of the samples.

**Saturated Resonance Method (SRM) with the TAC [8]:** The Total Absorption Calorimeter is an array of 40  $\text{BaF}_2$  crystals used for  $(n,\gamma)$  measurements. The SRM has been applied using a gold sample of 45 mm diameter and  $100 \mu\text{m}$  thickness. The preliminary analysis of the TAC have a large uncertainty of 15%, since it has been performed taking into account the

efficiency of the TAC set-up used in 2004. A more accurate value will follow after the detailed Monte Carlo simulation of the correct geometry used in 2009.

Assuming the detection efficiency calculated for the TAC set-up in 2004 and taking into account that the detector geometry has changed, the accuracy of the result is 15%. This can be improved by means of dedicated MC simulations.

The results from the PTB chamber are shown only below and above the resonance region, where the analysis is still to be improved. The data from MGAS and SiMon are shown up to an energy of 200 keV, above which the results are affected by the prompt gamma-flash for SiMon and the proton recoil from the neutron elastic scattering with the hydrogen contained in the gas filling for MGAS.

**Table 1.** Summary of accuracies in the measurements of the neutron fluence and comparison with respect to the PTB fission chamber.

	PTB	SiMon	MGAS	Activation	TAC
<b>Average Ratio over PTB</b>	1.0	0.96	1.03	1.04	0.88
<b>Accuracy in the absolute value</b>	3%	6%	7%	10%	15%
<b>Accuracy in the energy shape</b>	<3%	<3%	<3%	-	-

Concerning the absolute value of the neutron fluence, the different measurements are in agreement within the associated uncertainties. The intensity of the evaluated neutron fluence will be adopted from the PTB measurement below and above the resonance region. In the resonance region, which is between 1 eV and a few keV, the fluence is better determined from smooth cross sections reactions. Hence, the evaluated fluence in this region will result from the combination of the SiMon and MGAS data normalized to those of PTB below 1 eV.

The absolute value of fluence is however not required for capture measurements, which are usually normalized using the saturated resonance method (SRM) or using a well known cross section at a given energy in the sample itself, or using a well known cross section of a reference sample under identical measurement conditions.

Therefore the important issue about the fluence is not the absolute value but the energy distribution of the neutron fluence. The resulting uncertainty of this distribution depends strongly on the measurement technique and is limited by the uncertainty of the used standard cross sections like  ${}^6\text{Li}(n,t)$ ,  ${}^{10}\text{B}(n,\alpha)$  and  ${}^{235}\text{U}(n,f)$ . At present we estimate the total uncertainty on the energy distribution of the flux at 3%.

## Summary and conclusions

The n\_TOF facility has resumed operation after a halt of three years. The first measurements during the 2009 campaign have aimed at the full characterization of the neutron beam in terms of spatial profile, intensity and neutron energy distribution.

The spatial beam profile has been determined as a function of neutron energy by means of the innovative MEDIPIX and XY-MGAS detectors. The analysis of the results including a simulation of the optical transport on neutrons through the beam line is to be completed.

The intensity of the neutron beam has been determined from the  ${}^{235}\text{U}(n,f)$  reaction using a calibrated fission chamber from PTB. A series of complementary measurements with the SiMon, MGAS, TAC detectors and by activation of gold foils have confirmed the results from the PTB chamber in the full neutron energy range. The evaluated neutron fluence will be determined from a combination of the PTB measurement in the energy regions below and above the resonances, and the SiMon and MGAS data between 1 eV and a few keV. The expected accuracy of the results is 3-4% in the absolute value of the neutron fluence and better than 3% in the energy dependence, which is the important one for capture measurement after normalization.

## Acknowledgements

This work has been partially supported by ENRESA, through the CIEMAT-ENRESA agreements on "Transmutación de residuos radiactivos de alta actividad", the Spanish "Plan Nacional de I+D+i de Física de Partículas (project FPA2005-06918-C03-01)" and the *Spanish Ministerio de Ciencia e Innovación* through the "CONSOLIDER CSD 2007-00042" project.

**References**

- [1] F. Gunsing et al. (The n\_TOF Collaboration), *Status and outlook of the neutron time-of-flight facility n\_TOF at CERN*, Nucl. Instr. and Methods B 261 (2007) 925-929
- [2] M. Calviani et al. (The n\_TOF Collaboration), *Status and Perspectives of the n\_TOF Facility at CERN*, Proc. 2<sup>nd</sup> EFNUDAT Workshop, 23-25 Sept. 2009, Budapest (Hungary).
- [3] [www.cern.ch/MEDIPIX](http://www.cern.ch/MEDIPIX)
- [4] S. Andriamonje et al., *A Low Background Micromegas Detector for Axion Searches*, Nucl. Instr. and Methods A 535 (2004) 309-313.
- [5] D.B. Gayther, *International Intercomparison of Fast Neutron Fluence-Rate Measurements Using Fission Chamber Transfer Instruments*, Metrologia **27** (1990) 221-231.
- [6] S. Marrone et al. (The n\_TOF Collaboration), *A low background neutron flux monitor for the n\_TOF facility at CERN*, Nucl. Instr. and Methods A 517 (2004) 389-398.
- [7] S. Andriamonje et al., *A new detector for neutron beam monitoring*, Int. Top. Meeting on Nuclear Research Applications and Utilization of Accelerators, 4-8 May 2009. Vienna, Austria.
- [8] C. Guerrero et al. (The n\_TOF Collaboration), *The n\_TOF Total Absorption Calorimeter for neutron capture measurements at CERN*, Nucl. Instr. and Methods A 608 (2009) 424-433.

## Preliminary formulation of a nuclear data roadmap for designing the European Spallation Source (ESS)

Mary PW Chin<sup>1,2)</sup>, Francois Plewinski<sup>1)</sup>, Cyril Kharoua<sup>1,2)</sup>, Etam Noah<sup>1,2)</sup>,  
Mats Lindroos<sup>1)</sup>

- 1) European Spallation Source Scandinavia, Lund University, P. O. Box 117, SE-22100 Lund, Sweden
  - 2) CERN (European Organisation for Nuclear Research), CH-1211 Geneva 23, Switzerland
- [mary.chin@esss.se](mailto:mary.chin@esss.se)

**Abstract:** The design of the European Spallation Source (ESS) is in an unprecedented dynamism since the project revival and the recent site decision. A substantial part of the design depends on radiation transport calculation. The consumption of nuclear data is imminent. The task at hand is to identify and quantify issues, as well as to identify and rule out non-issues. In this work, the demands on radiometric calculations will be outlined. The complexity of the radiation phase space will be demonstrated in terms of the broad ranges of isotopes, particle types, particle energy and temperature. Nuclear data requirements will be discussed alongside what is currently available and areas awaiting further development. Recognising the needs for advancement in the field, ESS commits to an active contributory role.

### Specification of needs

The European Spallation Source (ESS) to be built in Lund (Sweden) will feature neutrons of a broad energy spectrum. Twenty two beam ports are envisaged. At each beam port the white spectrum and the pulse structure will be tuned according to the specific experimental and instrumental needs. Versatility is to be a key feature. The complexity of the radiation phase space may be outlined as follows.

#### A variety of isotopes

From the target to the moderator, reflector, guides, shutters, shielding and instruments, particles at different energies will collide with materials of various isotopic compositions. In addition to the isotopes first started off with, additional isotopes are produced in the form of residual nuclei. It is improbable to give an exhaustive list of isotopes involved. Suffice to say that a good coverage of the nuclide chart could be expected. Isotopes even in trace amounts deserve attention, as the reaction rate could mount due to the specific cross sections.

#### A variety of particle types

Protons, by the spallation process, kick off the radiation histories. Neutrons, the spallation product, dominate as the main player of the irradiation field which is in fact populated by secondaries of various other particle types (Fig. 1). This assortment of particle types is further enriched by the decay products (Fig. 2). In addition, a good gauge of residual activities is an essential element of the calculation.

#### A broad energy range

Fig. 3 shows the energy of newborn neutrons produced from the inelastic nuclear collisions of protons with the nuclei of some of the target materials being considered. From multi-GeV energies the calculation code will have to see these neutrons through the intermediate energy range, all the way to cold and ultra-cold energies, from the spallation target, through various components in the beam path, to the instruments. In Monte Carlo simulations this wide energy range causes vulnerability at both ends: effects from thermal motion, crystalline structure and chemical binding, as well as the lack of complete tabulated nuclear levels at low energies, and the lack of measured and evaluated data at high energies. Some aspects of the problem would require free-gas thermal treatment; other aspects would demand the more rigorous  $S(\alpha,\beta)$  treatment (Fig. 4).

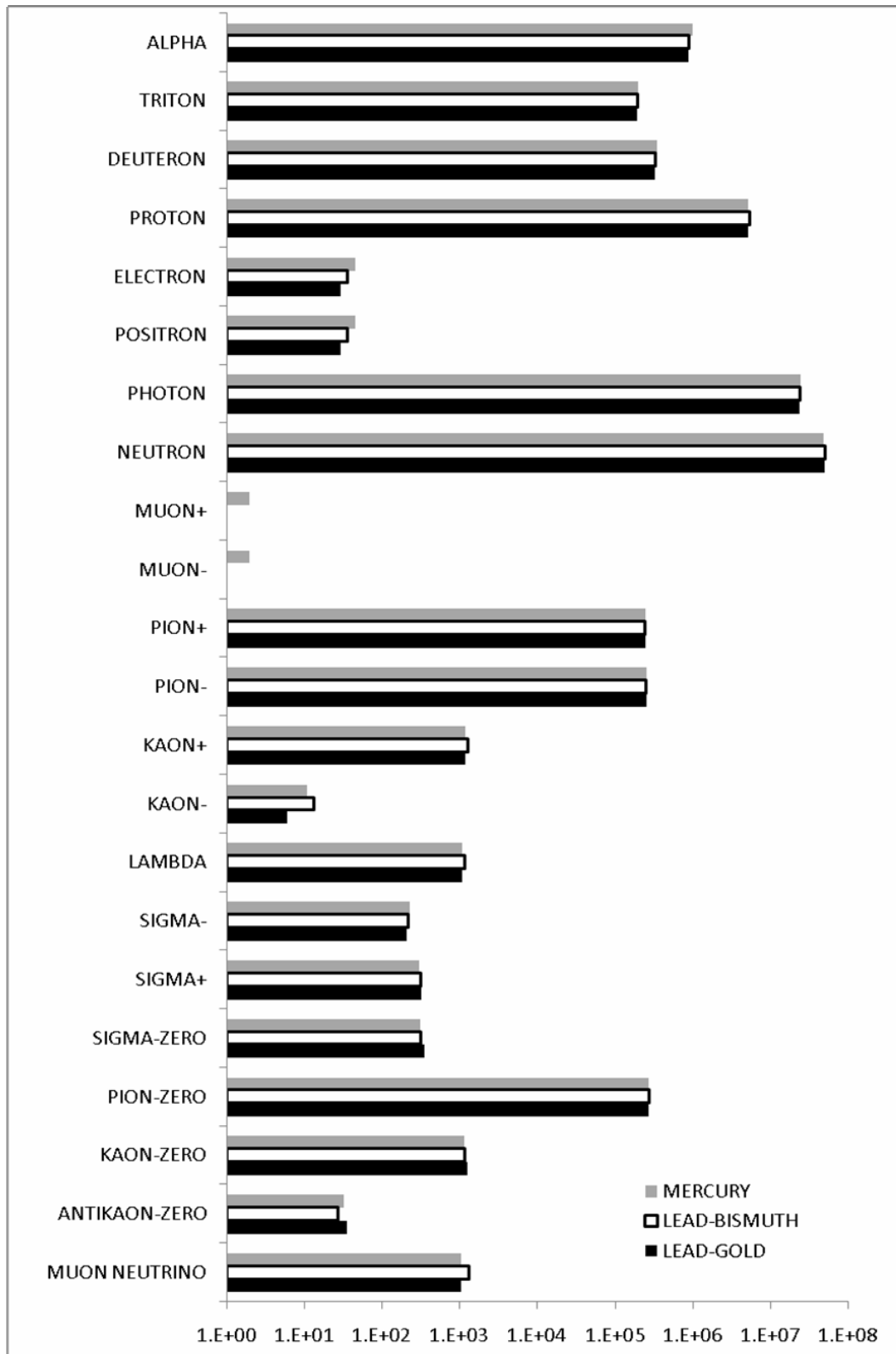


**Figure 1.** Secondary particles produced in a FLUKA 2008.3b simulation of  $5 \times 10^5$  2.5 GeV protons impinging on an effectively infinite homogeneous slab: a count of various particle types.

### The radiation phase space

Within the irradiation phase space, therefore, the problem spans broadly comprising points representing different combinations of energy, projectile, target and ejectile. This is more complex than a typical criticality problem. It is the coverage of this phase space which

challenges the nuclear data needs and subsequent calculations. The coverage of this phase space also explains why it is virtually impossible for a radiation transport code to be completely benchmarked.

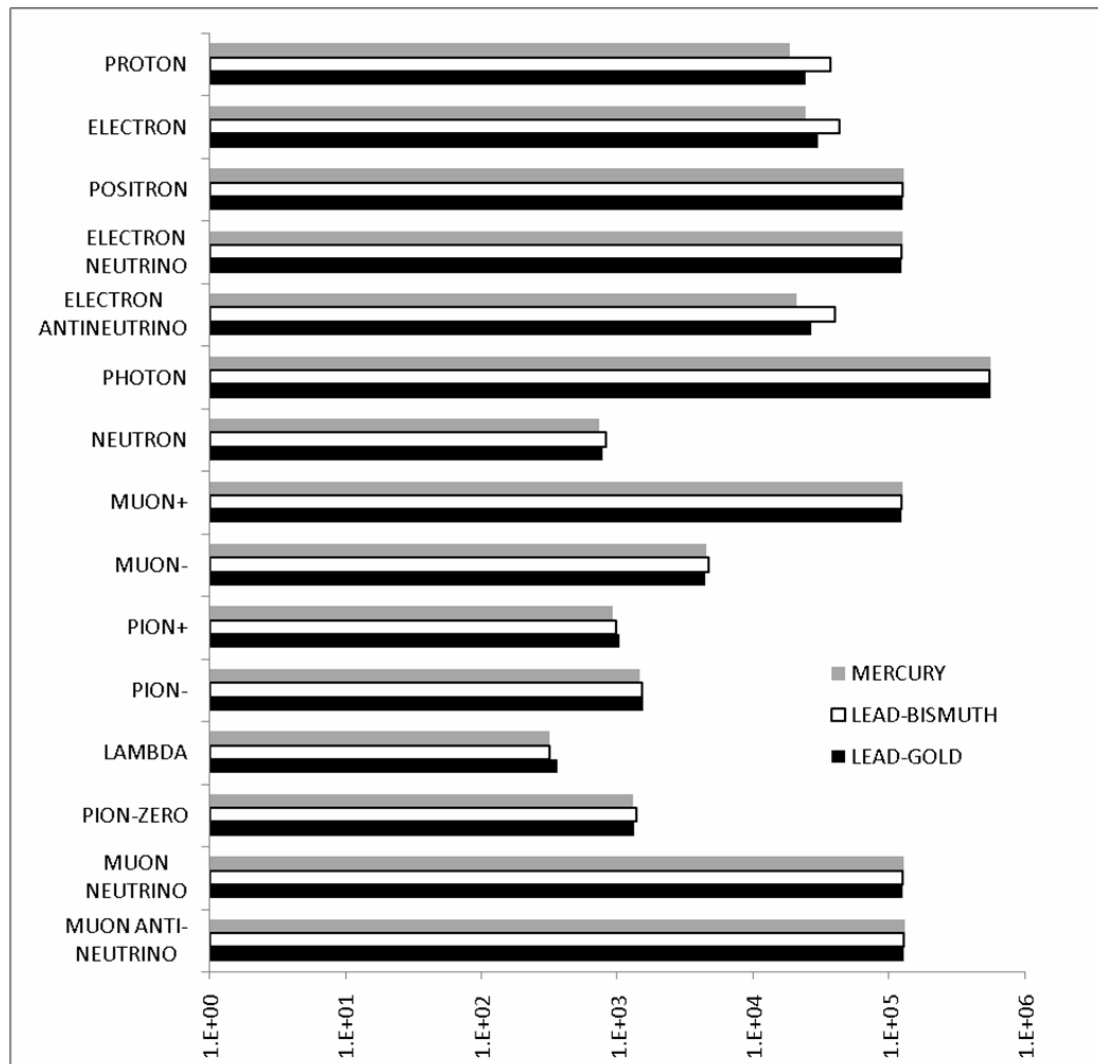


**Figure 2.** Decayed products produced in a FLUKA 2008.3b simulation of  $5 \times 10^5$  2.5 GeV protons impinging an effectively infinite homogeneous slab: a count of various particle types.

### Temperature range

Further demands on the nuclear data processing arise from the temperature range. While the users of the facility will have a comfortable room temperature, the target would probably be operated at hundreds of degree Celsius, which is beyond the temperature(s) available in most data libraries.

In MCNPX2.5.0 [1], for example, except the uranium and the plutonium (which are of no special interest for ESS), most isotopes (including lead, bismuth and mercury) have neutron libraries for only 293.6 K and 300 K. For some other isotopes additional libraries at 0 K, 77.0 K, 587.2 K and 880.8 K, 3000.1 K are available. The 260-group library of FLUKA [2], on the other hand, offers cross sections at 87 K and 296 K for most isotopes, plus additional 4 K data for a few isotopes.

A heavy liquid metal (HLM), if selected to be the material of the target, will have to be operated above melting point, which is 600.6, 544.4 and 397.7 K for lead, bismuth and lead-bismuth eutectic (LBE), respectively. In fact, even higher operating temperatures are often desirable. In the moderators, on the other hand, temperatures below 14 K may be expected, depending on the choice of material (eg. solid H<sub>2</sub>).

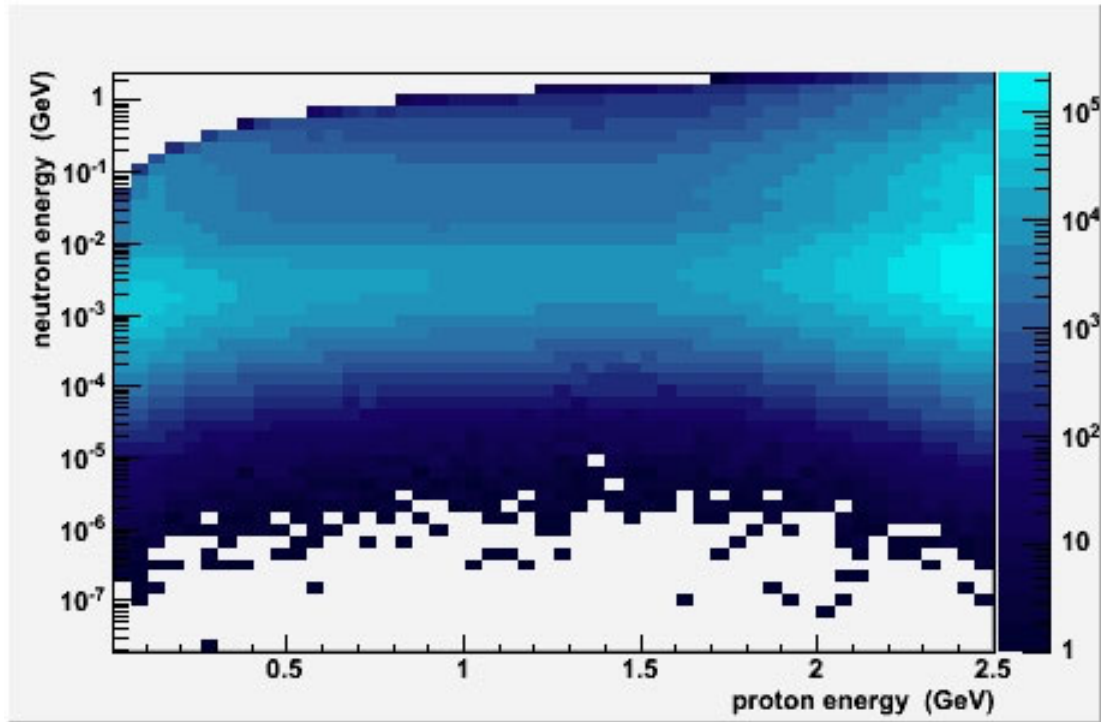


**Figure 3.** Proton energy at the time of neutron production and neutron energy at the time of creation: a double differential plot for the inelastic nuclear collisions of protons with prospective target materials such as mercury, lead-bismuth and lead-gold. Data were obtained by intercepting the subroutine mgdraw in a FLUKA 2008.3b simulation of  $5 \times 10^5$  2.5 GeV protons.

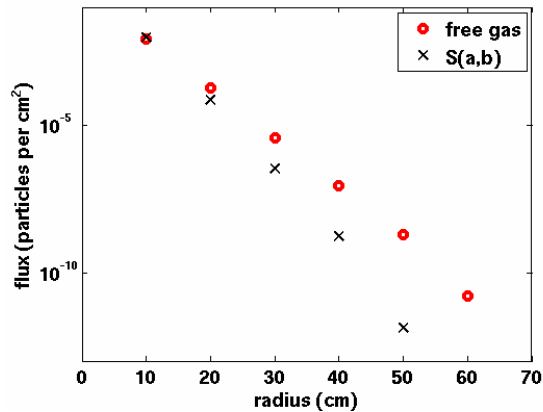


**Figure 4.** Free gas versus  $S(\alpha, \beta)$  thermal treatments as simulated by MCNPX2.5.0. Both simulations were started with a million 5 eV neutrons in concentric spheres of polyethylene, passing all ten statistical tests. Thermal data at 300 K was taken from the tmccs library, which provides scattering data for 1H only; 12C was still represented by the default free-gas treatment.

### Computational demands

While the above drives the nuclear data needs from one direction, additional requirements are imposed by the way the nuclear data is to be consumed for subsequent radiation transport calculations. Knowing the summed flux or averaged energy deposition would not be adequate for the ESS designers, who would need to have at their disposal microscopic quantities and quantities which are differentiated by the particle attributes happening upstream of the radiation history.

ESS is set to draw on the strength of the Monte Carlo technique to its utmost. This includes the capability for 1) analogue transport interaction-by-interaction; 2) full correlation between particles; and 3) pointwise transport. More often than not, both are violated in Monte Carlo simulations [3,4] eg. 1) energy is not conserved at the interaction level but the net flux remains unaffected when averaged over many histories; and 2) progenies from the same particle recognise neither their ancestors nor their siblings. For such studies, FLUKA fares better than MCNP [5] and MCNPX.

## Specific issues

### Models versus tables

Given the high energies at the upper portion of the energy spectra, the availability of tabulated reaction data ceases and therefore nuclear prediction models become indispensable. The upper limit of ENDF/BVII [6] and JEFF3.1 [7], for example, is 200 MeV. Such evaluations themselves contain model-generated data. Reliable models are pertinent. In this respect, significant contribution is expected from the IAEA Benchmark of Spallation Models.

In fact, even when tabulated data do exist, models can be advantageous and preferred. As more and more reaction channels open up at higher energies, exclusive cross sections (where different channels are differentiated) become sparse; models would be required to preserve correlation and energy conservation.

The role of models is not necessarily secondary, and should not be underestimated. This is particularly true for models which have been built bottom-up from microscopic principles. In some cases it is debatable whether a model needs to be benchmarked by measurements, or perhaps vice versa.

### Covariance data

Uncertainty estimation is among the toughest challenges in design modelling. Now that major nuclear data evaluations do provide covariance data for some isotopes, further hurdles persist. Rigorous consumption and general applications are limited. Although there have been efforts in the context of criticality analysis, TSUNAMI [8] and SCALE [9], propagation of the covariance data to the final radiometric estimation is not in the foreseeable horizon of the major Monte Carlo transport codes. Note that the existing PERT card [1] in MCNPX does estimate, based on first and second order differential operator techniques, perturbations due to different cross section datasets, but does not estimate the uncertainty within a solo cross section dataset, which would have covariance data by its own accord.

### Evaluated data and cross section libraries

A direct consequence from the complexity of the phase space is the need to consider special evaluations (eg. FENDL [10] and ADS-ENDF [11]) in addition to the major evaluations (ENDF/B, JEFF, JENDL [12], BROND [13] and CENDL [14]).

While processed nuclear data are often available as ACE libraries ready for use in the MCNP and MCNPX family, the assortment of particle types shown in Fig. 1 and Fig. 2 demands solid high energy physics. Moreover, MCNP and MCNPX are non-analog and it does not honour the correlation between particles [3,4]. Note that ACE is not just a matter of formatting but also the inclusion and exclusion of selected MF-MT combinations tailored to the needs of MCNP and MCNPX, which would not be applicable to some other codes.

Exotic particles aside, the amount of evaluated data for proton, deuteron, triton and  $^3\text{He}$  is drastically impoverished compared to neutrons. In ENDF/BVII, for instance, the number of materials in the corresponding sub-libraries are 48, 5, 3 and 2, respectively, compared to 393 for neutrons. This unbalance does not fulfil the needs depicted in Fig. 1 and Fig. 2. The bias, so far largely driven by military and reactor domains, is set to change in the light of escalating interests in accelerated driven system (ADS) for energy production, waste transmutation, tritium production and fusion technologies (eg. ITER [15] and IFMIF [16]). Such developments are reflected in the HINDAS initiative [17], among others.

ESS benefits from the aforementioned sister technologies, where there is a convergence of needs for experimental, evaluated and processed data at higher energies, higher temperatures and subcritical materials. ESS commits to an active contributory role. Meticulous processing of evaluated data into non-ACE libraries is underway.

## References

- [1] D.B. PELOWITZ, Ed., *MCNPX<sup>TM</sup> USER'S MANUAL Version 2.5.0*, LA-CP-05-0369, Los Alamos (2005).
- [2] A. FERRARI, P.R. SALA, A. FASSO', J. RANFT, *FLUKA: a multi-particle transport code*, CERN 2005-10 INFN/TC\_05/11, SLAC-R-773 (2005).
- [3] S.A. POZZI, E. PADOVANI, M. MARSEGUERRA, *MC'NP-PoliMi: a Monte-Carlo code for correlation measurements*, Nucl Instrum Meth A 513 550 (2003).
- [4] M.P.W. CHIN, N.M. SPYROU, *Event-by-event Monte Carlo tracking of neutron-nucleus collisions in neutron detectors*, T Am Nucl Soc 97 288 (2007).
- [5] X-5 Monte Carlo Team, *MCNP — A General Monte Carlo N-Particle Transport Code Version 5*, LA-UR-03-1987, Los Alamos (2003).
- [6] M.B. CHADWICK et al, *ENDF/B-VII.0: Next Generation Evaluated Nuclear Data Library for Nuclear Science and Technology*, Nuclear Data Sheets 107 2931 (2006).
- [7] A. KONING et al, Ed., *The JEFF-3.1 Nuclear Data Library*, JEFF Report 21, NEA No. 6190, OECD (2006).
- [8] B.T. Rearden, D.E. Mueller, S.M. Bowman, R.D. Busch, and S.J. Emerson, *TSUNAMI Primer: A Primer for Sensitivity/Uncertainty Calculations with SCALE*, ORNL/TM-2009/027, Oak Ridge National Laboratory (2009).
- [9] S.M. Bowman, *Overview of the SCALE code system*, T Am Nucl Soc 97 589 (2007).
- [10] A. TRKOV, R. FORREST, A. MENGONI, Ed., *Summary Report of First RCM of FENDL-3 CRP*, INDC(NDS)-0547, IAEA, Vienna (2008).
- [11] D.L. ALDAMA, A. L. NICHOLS, *ADS-V2.0: A Test Library for Accelerator Driven Systems and New Reactor Designs*, INDC(NDS)-0545, IAEA, Vienna (2008).
- [12] K. SHIBATA et al, *Japanese Evaluated Nuclear Data Library Version 3 Revision-3: JENDL-3.3* J Nucl Sci Technol 39, 1125 (2002).
- [13] A.I. BLOKHIN et al, *Current Status of Russian Evaluated Neutron Data Libraries*, Proc. International Conference on Nuclear Data for Science and Technology 2 695 (1994).
- [14] Chinese Nuclear Data Center, *Communication of Nuclear Data Progress, No. 6, Supplement*, INDC(CPR)-028/L (1992).
- [15] P.H. REBUT, *ITER - the first experimental fusion-reactor*, 8th Symposium on Fusion Technology (SOFT-18), Fusion Engineering and Design 30 1-2 85 (1995).
- [16] K. EHRLICH, A. MOSLANG, *IFMIF - an international fusion materials irradiation facility*, 5th European Conference on Accelerators in Applied Research and Technology (ECAART5), Nucl Instrum Meth B 139 1-4 72 (1998)
- [17] J.P. MEULDERS, A. KONING, S. LERAY, Ed., *HINDAS final report*, EU contract FIKW-CT-2000-00031 (2005).

## Using neutron resonances for non-destructive material analysis: the ANCIENT CHARM project.

*E. Perelli Cippo<sup>1)</sup>, G. Gorini<sup>1,2)</sup>, P. Schillebeeckx<sup>3)</sup>, M. C. Moxon and the ANCIENT CHARM collaboration*

- 1) Università degli Studi di Milano-Bicocca, Piazza della Scienza 3, Milano, Italy 20126
- 2) CNISM, UdR Milano-Bicocca, Piazza della Scienza 3, Milano, Italy 20126
- 3) EC-JRC-IRMM, Neutron Physics Unit, Retieseweg 111, Geel, Belgium 2440  
[Enrico.Perelli@mib.infn.it](mailto:Enrico.Perelli@mib.infn.it)

**Abstract:** The objective of the European-funded Ancient Charm project [1, 2] is to develop complementary neutron-based techniques for non-destructive analysis and imaging of the elemental and phase compositions of samples. Among others, the most promising technique is neutron resonance transmission radiography and tomography (NRT), coupled with neutron resonance capture imaging (NRCI). Both transmission dips and peaks in the capture spectrum can be identified with the time of flight (TOF) technique. Realistic measurement time for imaging require a neutron beam with a high intensity, which can only be realized by spallation sources.

A modular system for NRCI/NRT has been designed and installed at the Italian Neutron Experimental Station (INES) of the ISIS spallation neutron source. Its main components are a gamma detector bank and a neutron transmission detector. The gamma detector bank contains 28 YAP detectors surrounding the sample. The NRT detector head is a 10x10 array of <sup>6</sup>Li-glass crystals mounted on a pitch of 2.5 mm, resulting in a 25x25 mm<sup>2</sup> active area. The analysis methods are based on the measurement of the flight times of epithermal neutrons and intensities of the resonances, and are therefore well exploited at a pulsed spallation source.

The system has been tested and commissioned partly at the time-of-flight facility GELINA and at the INES measurement station of ISIS. In this report, the assessment of the experimental set-up and some preliminary data obtained with reference samples will be reported.

NRCI and NRT are non-destructive techniques; they are useful in many fields where complete integrity of the sample is crucial. In particular, NRT can be used to test homogeneity of metallic samples and distribution of selected nuclides in solids, with possible application to the non-destructive characterisation of nuclear samples and to analysis of archaeological samples and findings.

### Introduction

ANCIENT CHARM [1] is an EU-funded project aimed to the development and application of new non-destructive material analysis based on neutron techniques. Among others, ANCIENT CHARM aims to join the information given by traditional non-destructive methods based on thermal neutrons, like prompt gamma activation analysis (PGAA) and neutron diffraction (ND), with relatively new methods based on neutron resonance absorption in the epithermal region ( $E_n$  up to 1 keV). A new instrumentation aimed to perform neutron radiography in the epithermal energy region has been tested at the ISIS and GELINA spallation neutron sources. This instrumentation makes use of the time-of-flight (TOF) technique available in pulsed neutron sources to measure the resonances occurring in the neutron capture cross sections that are characteristics of different isotopes, and can thus be used as a fingerprint for elemental identification. ANCIENT CHARM instrumentation conjugates two approaches to the neutron resonances analysis, the well-established neutron resonance-capture analysis (NRCA) [2] to the neutron resonance transmission (NRT).

In NRT the neutron beam transmitted through the sample is recorded as a TOF spectrum and the resonances appear as characteristic dips, whose energy position can be identified via the relation:

$$E_n = \left( \frac{72.2985L}{t + t_0} \right)^2$$

where  $E_n$  is the neutron energy in meV,  $L$  is the neutron flight path in meters and  $t$  and  $t_0$  are the time of flight and time offset in ms. An array of 10 x 10 neutron detectors arranged into a position sensitive neutron detector (PSND) allows for a 2D mapping of the sample.

After neutron capture, nuclei are usually left in an excited state and it de-excites through the emission of prompt  $\gamma$ -ray cascades. These  $\gamma$ -rays are thus detected through the NRCA instrumentation, made of an array of  $\gamma$ -ray detectors connected to a fast electronic acquisition. The time stamp of the  $\gamma$  emission is thus recorded, and the emitting nuclei are identified again via the TOF technique. In order to obtain spatial resolution with the NRCA detectors, a suitable neutron collimator with a neutron spot of about 3 mm FWHM at sample position is used. The transmission and capture measurement give a joint indication of the sample content; the higher efficiency of the  $\gamma$ -ray detector bank allows for the determination of trace elements in the sample, while the PSND gives a quick 2D mapping of the major components in the sample.

In this paper, we mainly concentrate on the NRT approach, the instrumentation developed for ANCIENT CHARM and some preliminary results obtained at the ISIS spallation neutron source.

### The neutron resonance transmission (NRT) technique

The neutron resonance transmission technique developed in ANCIENT CHARM is based on a newly developed PSND [3] made of an array of 10 x 10 GS20 scintillator glass (6.6% total lithium of which 95%  $^6\text{Li}$ ) pixels. These pixels are  $1.8 \times 1.8 \times 9 \text{ mm}^3$ , and they are arranged in a 2.5 mm pitch matrix, allowing for an intrinsic spatial resolution of  $2.5 \times 2.5 \text{ mm}^2$ . Individual pixels are coupled via a 0.5 mm thick glass dispenser to a bundle of four 1 mm diameter acrylic optical fibres, which transport the light to 16 channel photomultiplier tubes.

The NRT detector has been designed for epithermal neutron imaging based on the experience of an existing 100-pixel transmission detector designed for cold-neutron Bragg edge transmission on a diffractometer [4]. The most important difference is the requirement for the NRT detector to measure a broad neutron energy range, up to about 1000 eV. The design of the detector has been the subject of careful simulations of the neutron transport performed with GEANT4 code [5] aimed to study the effect of neutron scattering inside the detector and other potential background contributions. Among the different configurations studied, the configuration of choice was boron nitride frame and plastic fibre optics, for which the cross talk among adjacent pixels is kept below 1%. Analysis of the TOF shape of neutron absorption resonances has shown that 1) neutron scattering inside the detector does not induce significant distortion effects on the recorded TOF spectrum and 2) the extended thickness of the pixels, necessary to have a reasonable 25% (4%) efficiency at 10 eV (1 keV), does not induce relevant loss of timing resolution [3].

A prototype PSND has been the object of careful tests both at the INES [6] beamline at ISIS and at GELINA; the final PSND has been tested at the INES beamline in May-June 2009. The main parameters of the ISIS and GELINA beamlines are summarised in table 1.

**Table 1.** parameters of the neutron sources and beamlines at ISIS and GELINA used in ANCIENT CHARM

	GELINA	ISIS (INES beamline)
Average current	65 – 75 $\mu\text{A}$ ( $e^-$ )	150 – 180 $\mu\text{A}$ ( $p$ )
Neutron pulse width	2.5 ns	300 ns
Flight path length	49.3 m	23.0 m
Beam dimensions	45 mm (diam)	50 x 50 mm
Neutron flux at sample pos.	$10^2 \text{ n/eV s cm}^2$ at 10 eV	$10^3 \text{ n/eV s cm}^2$ at 10 eV

In Figure 1 the NRT and NRCA set-up is shown as installed at the INES beamline. The data from the PSND are recorded with the standard ISIS data acquisition electronics (DAE) allowing for a maximum time resolution of 62.5 ns, which is considered adequate for NRT applications at ISIS. Tests have also been conducted for a limited number of channels with a 10 ns fast digitizer CAEN 1728B, that had already given good results at GELINA [7].

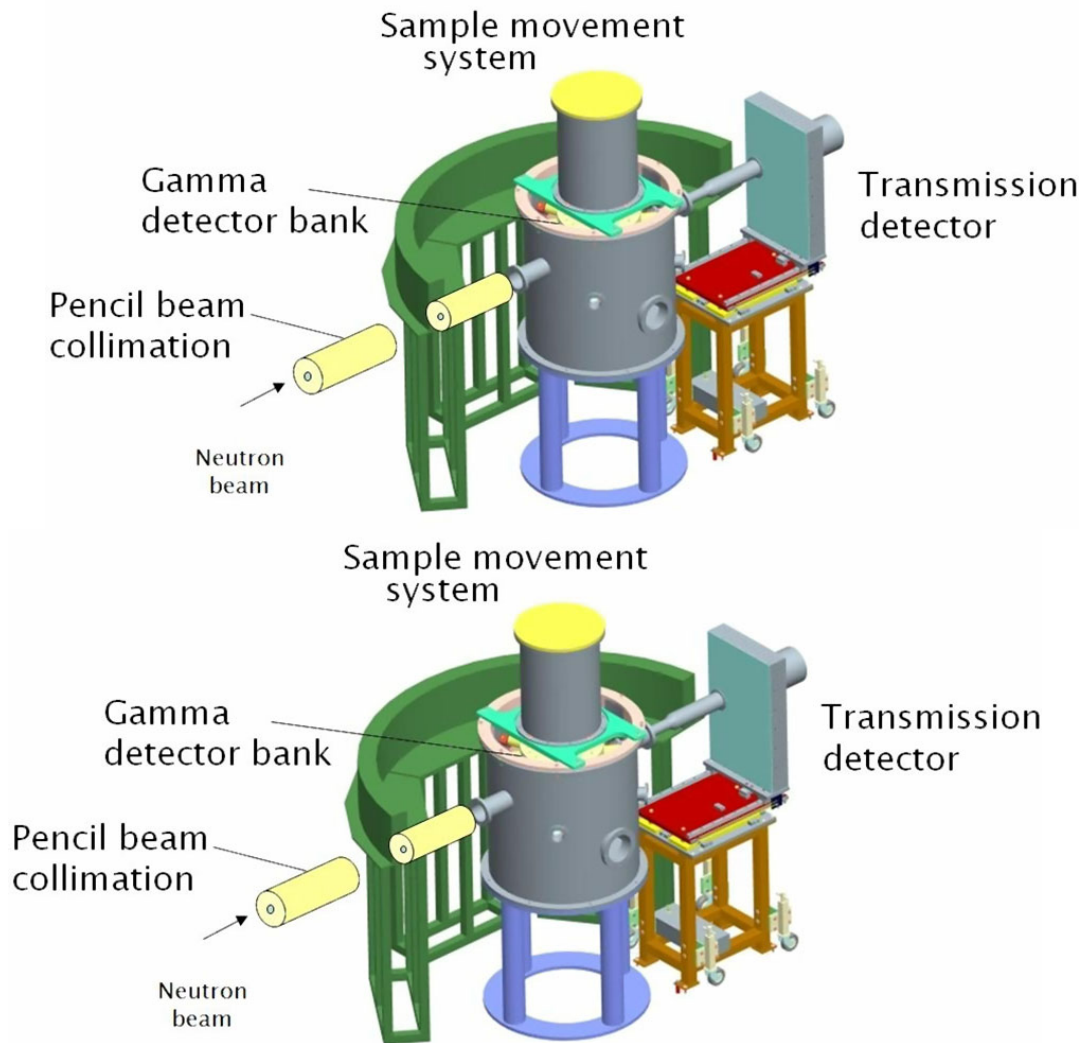


**Figure 1.** The ANCIENT CHARM set-up at the INES beamline at ISIS.

### NRT analysis

The physical quantity measured in NRT is the sample transmission factor:

$$T_{\text{exp}} = \frac{C_{\text{in}}}{C_{\text{out}}} \cong e^{-\sum_x n_x \sigma_{\text{tot}}}$$

where  $C_{\text{in}}$ ,  $C_{\text{out}}$  are the sample transmission spectrum and neutron flux,  $n_x$  is the equivalent thickness and  $\sigma_{\text{tot}}$  the total neutron cross-section of the X isotope. In order to obtain the sample transmission factor from raw TOF spectra, a careful background subtraction is necessary. Possible sources of background are the spallation target itself, neutron scattering and  $\gamma$ -ray emission after neutron absorption in the sample, along the beamline and in the sample tank walls. Background assessment is fundamental in NRT for a correct quantitative analysis, especially in the conditions of the ISIS spallation neutron source. Indeed, while the GELINA facility offers an intrinsic better resolution and lower background, the ISIS facility allows for a very high neutron flux (up to about  $10^6$  neutrons/s  $\text{cm}^2$  in the lower energy region), but this is paid off with a higher background. Theory and details of background subtraction are given in reference [8]: here we just present the basic outlines of the procedure. In order to define background level at selected time positions in the spectra, we used filters made of elements that show “black resonances” in the suitable energy range. A black resonance is a neutron absorption resonance very sharp and intense, so that neutron absorption at the resonance central energy is about 100%. Ideal black resonance filters should have a high contrast ratio, i. e. have a very intense resonance and negligible off-resonance cross-sections. Real filters have a finite scattering cross-section, both in- and off-

resonance, and they constitute a source of background. As a consequence, filters should be positioned as far as possible from the transmission detector. While at GELINA the usual set-up allows for the positioning of the filters at about 20 m from the detector, at the INES beamline, they were positioned only 2 meters away. Detailed analysis of the background components in the case of heavily scattering filters like bismuth will be the subject of future publications.

The elements used as black resonances during ISIS measurements are shown in table 2. A 0.5 mm cadmium filter was used as a fixed filter, in order to provide a flat fixed level for flux normalisation and in order to reduce activation of samples due to thermal neutron absorption.

**Table 2.** Elements used as black resonance filters at the INES beamline.

Element	BR energy (eV)	BR time of flight position at INES beamline ( $\mu\text{s}$ )
Bi	800	59
Co	132	150
W	19	390
Ag	5	750
Cd	0.5	3000

The count rate at the time position of a black resonance defines the background level at this time. In other words, any event detected at that time comes from neutron or gamma background sources, because any neutron of the beam with the resonance energy would be absorbed in the filter. The background points are then fitted with a suitable function in order to obtain the best estimation of the background along the whole TOF spectrum (see Figure 2). The function used for interpolation was:

$$B(t) = a + be^{-ct} + de^{-ft} + gt^h$$

where  $t$  is the TOF position. This function is based on the experience and was revealed adequate for both GELINA and ISIS.

Due to the fact that samples can be in themselves a background source, background estimation has to be provided for both sample-in and sample-out spectra. The experimental transmission factor is thus obtained as:

$$T_{\text{exp}}(t) = N \frac{S_{\text{in}}(t) - B_{\text{in}}(t)}{S_{\text{out}}(t) - B_{\text{out}}(t)}$$

where  $S_{\text{in}, \text{out}}$  are the signal obtained from the sample-in and sample-out (the latter defining the neutron flux), and  $B_{\text{in}, \text{out}}$  are the background levels in the two cases.  $N$  is a normalisation constant accounting for the intensity of the incident neutron beam in the sample-in and -out runs. Because the filters themselves have a small but finite influence on the background, the background level estimated with black resonances has to be adjusted for the “no-filters” case; this can be done with the help of the cadmium, which is used as a fixed filter. The previous operation can be made quicker with the use of the spectra manipulation code AGS [9], that also allows for the dead-time correction [10] and normalisation of the experimental spectra. In figure 3 the transmission factor obtained from the same data shown in figure 2 is presented.

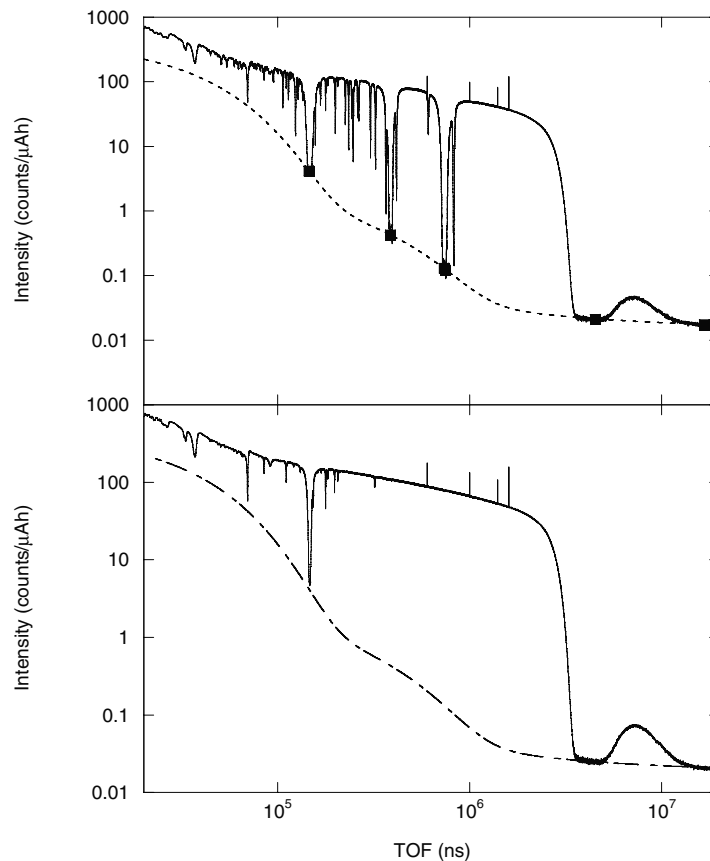


**Figure 2.** Background assessment for NRT measurements at ISIS. Top: a 8-mm thick pure Cu sample-in TOF spectrum with black resonances filters: the black dots show the level of the background over the black resonances, and the dotted line is the interpolation that gives the background estimation. Bottom: the estimated background for sample-in (dashed line) is obtained rescaling the estimated filters background with the sample-in without filters.

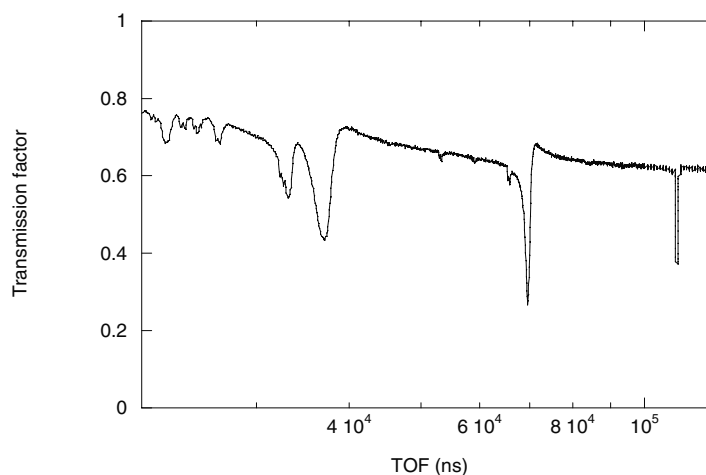


**Figure 3.** Transmission factor of a 8 mm thick Cu sample obtained from the same data presented in figure 2, in the time region 20000 to 120000 ns (corresponding approximately to the energy interval 100 eV to 1200 eV) The dips visible in the spectrum correspond to the most intense Cu absorption resonances.

The NRT spectra analysis is conducted with the help of the REFIT analysis code [11]. REFIT is an analysis code for simulation of nuclear resonance parameters and optimisation with experimental data. It calculates the nuclear cross-sections based on the available resonance parameters, on Doppler broadening and on a Monte Carlo simulated resolution function; the resulting spectra are then compared with experimental data and optimized via a chi-square minimisation procedure. A new version of the REFIT code is being developed

within the ANCIENT CHARM project: this new version (CHARMFIT) will be characterised by a simplified approach, in which only the relevant parameter for composition analysis, i. e. the isotopic concentration, is fitted to the experimental data.

As an example of application, the results of CHARMFIT data fitting to NRT spectra from a reference copper alloy standard BCR-691. The agreement between certified elemental concentrations in the standard and CHARMFIT estimation has to be considered very good. Moreover, the presence of trace elements like silver has been determined, having concentration of the order of some ppm.

**Table 3.** certified and estimated concentration of selected elements in a reference copper alloy.

Element	Certified %wt	Estimated %wt
As	0.194	0.20
Sn	7.2	7.65
Zn	6.02	6.97
Sb	0.5	0.45
Mn	0.2	0.21
Ag	-	12e <sup>-3</sup>

### NRT 2D mapping

The PSND developed for ANCIENT CHARM offers the possibility of obtaining quick (within few minutes at ISIS running power) 2D maps of the isotopic composition of the investigated sample. 2D maps at different angles and positions can be obtained with the use of the sample movement system and then combined via reconstruction algorithms in a 3D tomographic image. As underlined in reference [3] these images give complementary information to standard neutron tomography and prompt gamma activation imaging (PGAI).

Tests conducted at ISIS have shown that the images obtained from thin samples achieve an intrinsic spatial resolution of about 2.5 mm [12], and are not limited by divergence of the neutron beam (resolution can be degraded by neutron scattering inside the sample if the equivalent scattering thickness is longer than some scattering lengths).

An example of 2D images obtained at ISIS with PSND an ancient belt mount from Hungarian National Museum (Budapest) is shown in figure 4, along with an image of its silver inlaying obtained at ISIS with the PSND. This image is based on the intensity of the 5 eV Ag resonance and gives a semi-quantitative indication of the concentration of silver in object.

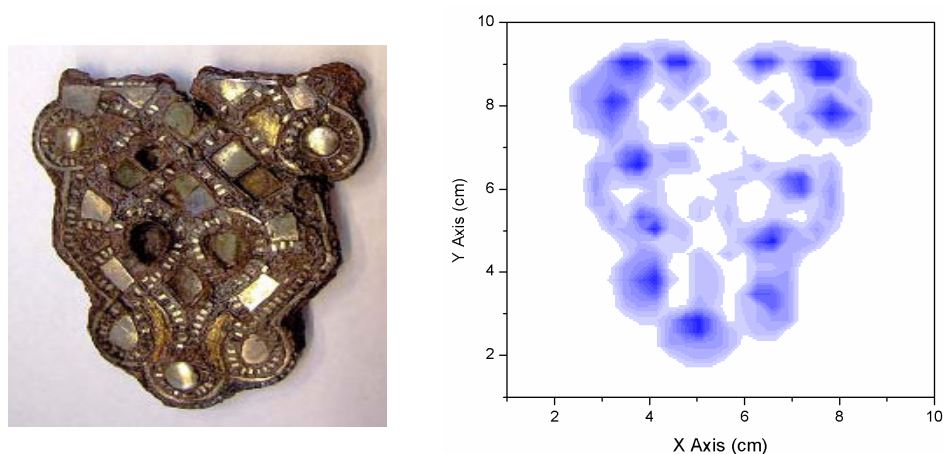


**Figure 4.** Left: an ancient "gegenbeschlag" belt mount from the National Hungarian Museum, with glass and metal inlaying. Right: silver concentration into the inlaying.

### Conclusions

In this paper we have presented the NRT technique that is being developed at ISIS and GELINA pulsed neutron sources within the ANCIENT CHARM project. Despite the project is mainly aimed to the application of neutron-based techniques to the analysis of archaeological objects and artefacts, NRT technique can be proposed for different applications like for instance nuclear target characterisation complementary to Rutherford backscattering and

particle-induced X-ray emission. NRT offers many advantages: it is nondestructive, no sample preparation is needed and produces a negligible residual activation in the sample (especially with the use of Cd filters). Moreover, it quickly provides isotope-resolved images of the sample, which can be used for estimation of homogeneity of nuclear samples. For instance, multivariate statistical analysis methods are available in literature [13] to determine homogeneity and correlation between two or more elements into samples distribution maps [14].

### Acknowledgements

Work performed with financial support by the European Community “New and Emerging Science and Technology” Contract No 15311. The authors acknowledge Consiglio Nazionale delle Ricerche (CNR)-Italy for financial support for the experiment performed at the ISIS pulsed neutron source.

### References

- [1] G. Gorini, *Il Nuovo Cimento C* 30 No.1 47 (2006)
- [2] H. Postma *et al.* *J. Radioanal. Nucl. Chem.* 248 No. 1 115 (2001)
- [3] E. M. Schooneveld *et al.*, *J. Phys. D* 42 No. 15 152003 (2009)
- [4] A. Steuwer *et al.*, *J. Appl. Phys.* 97 074903-1 (2005)
- [5] E. Perelli Cippo *et al.*, *Meas. Sci. Technol.* 19 No. 3 034027 (2008)
- [6] S. Imberti *et al.*, *Meas. Sci. Technol.* 19 034003 (2008)
- [7] L. C. Mihailescu *et al.*, *Nucl. Instr. Meth. A* 600 453 (2009)
- [8] G. Noguere *et al.*, *Nucl. Instr. Meth. A* 575 476 (2007)
- [9] G. Noguere, CEA/DEN Cadarache Report CEA-R-6071 (2005)
- [10] M. S. Moore, *Nucl. Instr. Meth.* 169 245 (1980)
- [11] M. C. Moxon, J. B. Brisland, *Harwell Laboratory Report CBNM/ST/90-131/1* (1990)
- [12] E. M. Schooneveld, “The Neutron Resonance Capture Analysis (NRCA) and Neutron Resonance Transmission (NRT) set-up at ISIS”, presented at the Neuwave2 workshop, Abingdon (UK) July 13 2009
- [13] N. E. G. Lovestam, E. Swietlicki, *Scanning Microscopy* 6 607 (1992)
- [14] F. Munnik *et al.*, *Nucl. Instr. Meth. B* 161-163 348 (2000)



## Neutron resonance-capture analysis and artifacts studied at the GELINA facility

*Hans Postma<sup>1</sup>, P.Schillebeeckx<sup>2</sup> and the Ancient Charm collaboration,*

- 1) RD&M, Faculty of Applied Sciences, Delft University of Technology, Mekelweg 15, 2629 JB Delft, the Netherlands
- 2) EC-JRC IRMM, Retieseweg 111, Geel, B2440, Belgium  
[postma-bosch@dataweb.nl](mailto:postma-bosch@dataweb.nl)

**Abstract:** Neutron resonance-capture analysis (NRCA), as a method to determine bulk elemental compositions of objects, will be discussed and elucidated with the aid of examples from studies of ancient copper-alloy objects. NRCA is non-destructive and does not require treatment of objects and therefore it is very suitable for research of precious ancient artifacts.

### Introduction

There are three closely related analytical methods to determine elemental compositions of materials and objects, which are based on different aspects of the neutron-capture process. These aspects are: i) the activation induced by neutron capture, ii) the prompt gamma radiation emitted during the capture process, and iii) neutron resonance peaks occurring in the capture cross-section as a function of neutron energy. From the physics point of view this is the reversed order of presenting these aspects, but it represents the chronological order in which these analytical methods have been developed. Neutron activation analysis (NAA) is based on the induced activation and is developed as soon as intense low-energy neutron sources from research reactors became available. Now-a-days NAA is based on recognizing gamma emission lines with the aid of high resolution Ge-detectors. Thereafter prompt gamma-ray activation analysis (PGAA), based on recognizing elements by detecting suitable gamma transitions in the capture process, is developed; again using Ge-detectors. The latest, fairly recently developed method is based on observing neutron resonances in the absorption process as a function of neutron energy. This can be done readily with the aid of a time-of-flight system using a pulsed neutron source and a detector that signals capture events. For that purpose a large scintillation detector, not necessarily with a good energy resolution, can be used, however good timing properties are paramount.

Clearly these three analytical methods have different experimental aspects. They should not be considered as competing, but rather as complementary methods. In this paper the third method, neutron resonance capture analysis (NRCA) will be discussed as it has been developed at the pulsed neutron source of the GELINA facility of the EC-JRC Institute for Reference Materials and Measurements (IRMM) in Geel (B) as a joined project with the Delft University of Technology in the Netherlands. In the course of this paper the application of NRCA for ancient bronze objects will be discussed. These objects have often very irregular shapes, which has consequences for the manner the analysis is carried out.

Other applications have been explored at IRMM in the nuclear field and reference materials.

### Some aspects of NRCA experiments at GELINA

Time-of-flight (TOF) systems at the GELINA facility with flight-path lengths of 12.8 and 28.3 m, for most experiments equipped with two  $C_6D_6$ -detectors, are available for NRCA studies of ancient objects, recently as part of the Ancient Charm project.  $C_6D_6$  detectors have excellent timing properties. In addition they have the advantage of being insensitive to neutrons, which is important since neutrons are also scattered from an object placed in the beam and there might be a neutron background from other experiments. The energy resolution of these detectors is rather poor, but this is not a problem since their only purpose is to signal capture events. Together with the machine pulse as start signal the TOF of each capture event can be determined. However, it is important to suppress low-energy neutrons from earlier machine pulses. This requires a so-called overlap filter placed in the beam to cut away neutrons with very low energies. For this purpose either a sheet of Cd or a disk containing  $^{10}B$  are used. Cd has the advantage of a sharp cut-off at about 0.5 eV, but as disadvantage that it produces some dips in the TOF spectrum due to Cd resonances. The

removal of thermal neutrons from the beam by the overlap filter has the additional advantage that activation of objects is very much reduced. Thermal neutrons are not of interest for NRCA. In addition another filter (Bi, Pb or S) is inserted into the beam to reduce the Bremsstrahlung flash from the 150 MV electron accelerator of the GELINA facility to reach the gamma detector, which should otherwise be overloaded for several  $\mu\text{s}$  after each machine burst. Bremsstrahlung, produced by stopping electrons from the accelerator in a uranium target, generates bursts of neutrons by photonuclear reactions in the same target. More details of the GELINA facility can be found in ref. [1].

The TOF data can be transferred into an energy spectrum using the following expression for the neutron energy  $E$ :

$$E = \frac{1}{2}m\left(\frac{L}{t}\right)^2. \quad (1)$$

$L$  is the length of the flight path,  $m$  is the neutron mass, and  $t$  is the time-of-flight. This non-relativistic expression is valid for the low-energy neutrons used in NRCA. Elements are recognized on the basis of energies of one or more of their neutron resonances. Figure 1 shows an example of a neutron resonance spectrum obtained with a bronze artifact, the so-called Buggenum sword from the Bronze Age period. Resonances are broadened by the Doppler-effect and by the resolution function of the TOF-system.

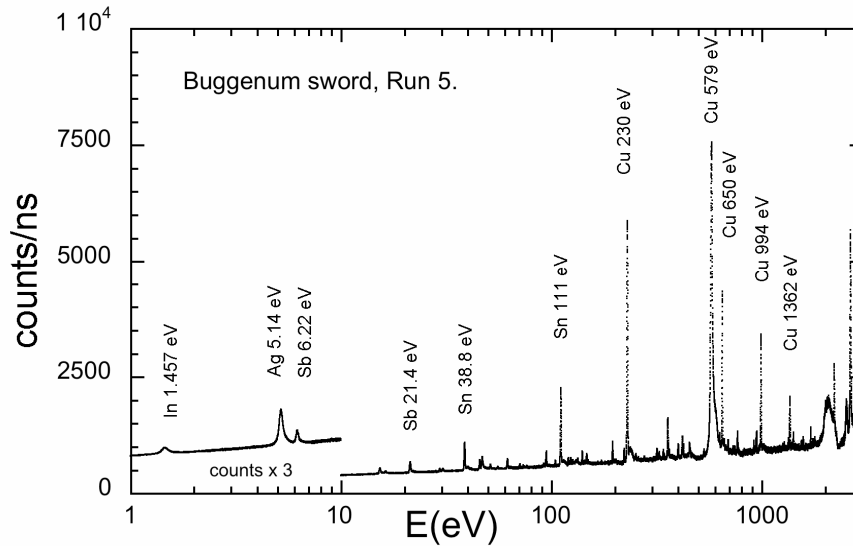


**Figure 1.** Time-of-flight data obtained with the Buggenum sword (on loan from the National Museum of Antiquities in Leiden-NL) plotted versus neutron energy.

The amount of an element can be deduced from the areas of one or more resonance peaks. For a sample of thickness  $D$ , area  $O$ , and number density  $N$  of an element the number of capture events  $N_c$  observed in a resonance can be written as:

$$N_c = OND \cdot \Phi(E_0) \cdot \varepsilon_c \cdot aA_\gamma F. \quad (2)$$

The factor,  $OND$ , relates to the sample size,  $\Phi(E_0)$  is the neutron fluence at the central energy of the resonance,  $\varepsilon_c$  is the efficiency for detecting capture events through the prompt gamma radiation including the solid angle of the sample-detector system. The last factor,  $aA_\gamma F$ , concerns the isotope abundance  $a$ , the area  $A_\gamma$  of the resonance capture cross-section, and  $F$  a factor, that takes into account the reduction of the neutron flux during penetration of the sample. With eq.2 it is possible to derive the number density  $N$  of an element from the experimental number of counts in a resonance if the fluence is monitored, the sample size and the detection efficiency are known, and if  $A_\gamma F$  can be calculated on the basis of resonance parameters. In the practice of analyzing neutron cross-section data at IRMM the REFIT program developed by Moxon is used. [2] This program is based on a complete description of the experimental set-up considering samples of simple shapes.

Archaeological objects have often very irregular shapes and complicated elemental mixtures making the use of REFIT, certainly for the non-expert, difficult for determining elemental quantities. In addition neutron resonance parameters are often not known, or not sufficiently

well. Therefore it is preferred to use calibration samples and to derive ratios of elements instead of absolute amounts. The weight ratio  $W_X/W_Y$  of two elements X and Y is given by:

$$\left\{ \frac{W_X}{W_Y} \right\}_{obj} = K_{\mu,\lambda}^{cal} \frac{F_\lambda}{F_\mu} \cdot \frac{N_\mu(X)}{N_\lambda(Y)} . \quad (3)$$

$K_{\mu,\lambda}^{cal}$  is a calibration factor and  $\mu$  and  $\lambda$  denote resonances of the elements X and Y respectively. The  $F$ -factor, also known as self-shielding factor, is given by:

$$F = \frac{\int_{res} \varphi(E) \left(1 - \exp\left(-n_X D\sigma_{tot}^D(E)\right)\right) dE}{\int_{res} \varphi(E) n_X D\sigma_{tot}^D(E) dE} . \quad (4)$$

It depends on the Doppler-broadened total neutron cross-section  $\sigma_{tot}^D(E)$  and the energy dependence  $\varphi(E)$  of the flux over the integration range. Figure 2 shows the self-shielding factors for a number of copper resonances as a function of copper weight per unit area.

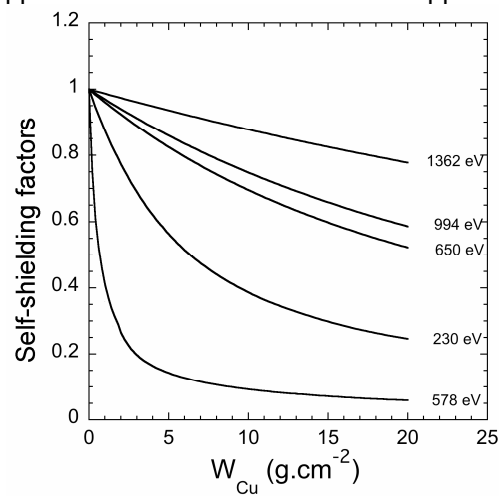


**Figure 2.** Self-shielding factors for some copper resonances.

In fact Eq.(3) contains a double ratio of the count rates of the object and calibration sample for two resonances of two elements, and a correction factor also as a double ratio of self-shielding factors. That is:

$$\left\{ \frac{W_X}{W_Y} \right\}_{obj} = \left[ \frac{\left( \frac{N_\mu}{N_\lambda} \right)_{obj}}{\left( \frac{N_\mu}{N_\lambda} \right)_{cal}} \right] \cdot \left[ \frac{\left( \frac{F_\lambda}{F_\mu} \right)_{obj}}{\left( \frac{F_\lambda}{F_\mu} \right)_{cal}} \right] \cdot \left\{ \frac{W_X}{W_Y} \right\}_{cal} . \quad (5)$$

It is clear that in this approach the detection efficiencies and the energy dependences of the flux, cancel out to a high degree if calibration runs are carried out under the same conditions as the actual measurements. The penalty is that ratios of elements are obtained instead of absolute amounts of the elements. However, if it can be assumed that all elements have been recognized in an object (except may be a few very weak ones) the ratios can be converted into fractions of the elemental composition.

There is still another aspect, which has to be considered with care if one wants to obtain accurate values of weight ratios, especially in the case of thick samples. That concerns that there are events consisting of scattering followed by capture. The scattering cross-section might be potential scattering or resonance scattering. In fact it may become even more complicated due to interference between the two scattering modes and due to multiple scattering. In each scattering event the neutron will loose some of its energy as nuclear recoil energy  $E_{rec}$ :

$$E_{rec} = E \frac{2mM}{(M+m)^2} (1 - \cos \theta) , \quad (6)$$

$M$  is the mass of the recoiling nucleus and  $\theta$  is the scattering angle in the centre-of-mass coordinate system. As a consequence a resonance has an additional structure at its high-energy side. An example is shown in figure 3 for the 230-eV resonance of copper with a scatter-capture (SC) structure due to potential scattering and capture by this resonance. The background and SC-structure are parameterized and thereafter subtracted to get the capture resonance peak. The peak area is obtained by summing channel contents of this peak over a wide enough range. The size of this structure depends on the thickness of the sample. For low-energy resonances the overlap of a capture peak and its SC-structure is large and thus they are more difficult to separate. In such cases simulations become important to estimate the SC-structure underneath a resonance peak. In case of closely lying resonances it becomes necessary to use a fitting algorithm instead of the simple approach sketched above for the 230-eV Cu-resonance.

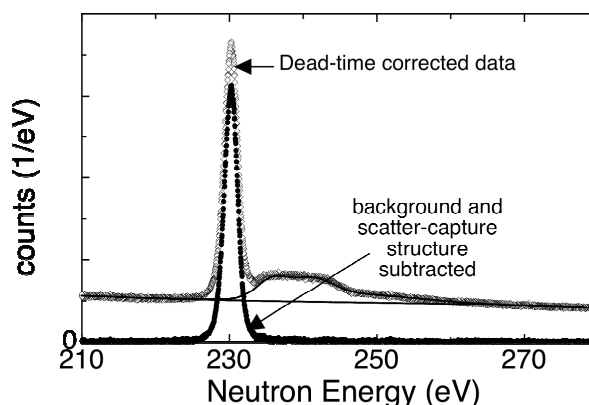


**Figure 3.** The 230-eV Cu-resonance (open dots) obtained with a 14 mm thick flat axe made from native copper (on loan from Kockelmann). The parameterized background and scatter-capture structure are subtracted (black dots) providing the peak used for the analysis.

### Examples of NRCA research

In the course of several years different kinds of ancient objects made from copper alloys have been studied at the GELINA facility: i) Etruscan statuettes, ii) prehistoric axes of various shapes, notably Geistingen socketed axes, iii) Swords and daggers from the Bronze Age, iv) a Roman tabula and four Roman water taps. Most of these objects have irregular shapes making it difficult to estimate self-shielding factors on the basis of their dimensions.

#### Etruscan Statuettes

The National Museum of Antiquities (NMA) in Leiden (NL) owns a collection of Etruscan statuettes, which was assembled by Count Corazzi of Cortona (Italy) in the 18<sup>th</sup> century. Some of these statuettes were recently suspected not to be genuine Etruscan objects, but produced in later times probably from the 16<sup>th</sup> century or later. The elemental compositions of eleven statuettes of this collection and another statuette, offered to the NMA as an ancient statuette, were determined at GELINA. All studied statuettes from the Corazzi collection are tin bronzes, but five of them contain considerable amounts of zinc.

**Table 1.** Elemental compositions of some bronze artifacts

element	“Nijmegen” Roman water tap	Etruscan OC68 (fake)	Geistingen socketed axe (1938/X4)	Jutphaas sword (tip)
Cu	73.56	81.05	94.30	86.07
Sn	8.19	5.81	0.063	13.39
Sb	0.117	0.243	1.63	0.114
As	0.055	0.182	0.67	0.226
Ag	0.053	0.21	0.54	0.0124
In	--	--	0.0005	0.0028
Zn	0.883	5.57	--	0.153
Co	--	--	--	0.033
Pb	15.6	6.7	--	--

With the copper smelting techniques in Etruscan times (7<sup>th</sup> to 2<sup>nd</sup> century BC) it is not possible that large amounts of zinc will dissolve in copper even if the used minerals contain zinc in considerable quantities. The reason is that at the smelting temperature of the copper zinc has a vapor pressure above atmospheric pressure. Hence it will evaporate during the smelting procedure in furnaces used by the Etruscans. At most small amounts of zinc, of order of a fraction of 1%, may dissolve in copper. This is shown in a large study carried out by Craddock of artifacts from the Etruscans and from neighboring regions. The five statuettes with considerable amounts of zinc are therefore believed not to be from Etruscan origin. [3] The composition of one of the Etruscan statuettes is quoted in table 1. The privately owned statuette offered to the NMA turned out to contain 26% of zinc; that is, it is a brass. With other minor elements it may be relatively old, but it is certainly not Etruscan. The Romans developed a technique (the cementation method) from about the 1<sup>st</sup> century BC to make brass with that amount of zinc.

### Roman water taps

For copper-tin alloys it is possible to analyze several pairs of resonances. With four Cu-resonances and three Sn-resonances, 12 pair of resonances of Cu and Sn can be studied, giving 12 values for the Sn/Cu weight ratio. For thick objects like the Roman water taps these ratios are quite different without self-shielding corrections. By varying the effective thickness it is possible to equalize these ratios as is shown for the "Nijmegen" tap in figure 4 and it is thought that this provides the proper Sn/Cu weight ratio. [4] The effective thickness as expressed in gramCu/cm<sup>2</sup> is in fair agreement with the wall thickness of this water tap. In addition other elements are determined for this object; see table 1. All four Roman water taps contain lead, which can be detected by NRCA if Pb/Cu ratios are larger than about 1%. The sensitivity is limited due to the fact that lead has no low-energy resonances. Apparently Romans used leaded tin-bronzes for water taps for technical reasons.

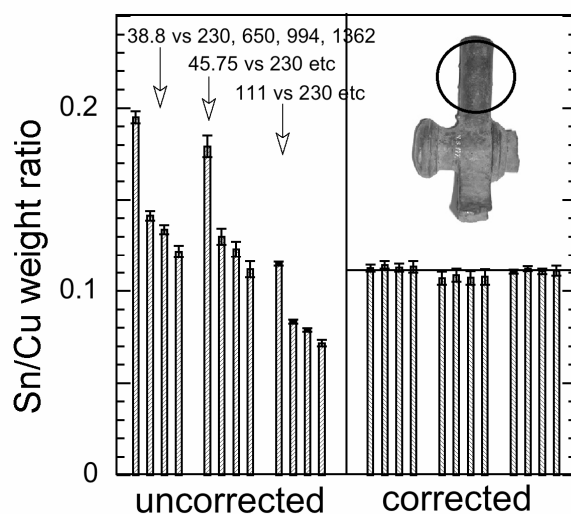


**Figure 4.** The Sn/Cu weight ratio for 12 pairs of resonances of the "Nijmegen" Roman water tap (on loan from the National Museum of Antiquities in Leiden, NL). Left uncorrected and right corrected for self-shielding. The circle indicates the beam size.

### Geistingen socketed axes

Socketed axes are the latest development of bronze axes at the end of the Bronze Age period. One kind socketed axes named after the town Geistingen on the Meuse river are extremely thin-walled, and certainly not suitable for cutting. They may be ceremonial or status objects. Although they look very similar, they have rather different compositions. [5] This may have something to do with the fact that metal trade has become difficult at the end of the Bronze Age period and the start of the Iron Age.

### Swords

Two bronze swords on loan from NMA are studied as part of the Ancient charm project. They are known as the Buggenum and Jutphaas swords named after towns in the Netherlands where they have been excavated. They are both from the middle to late Bronze Age and are

apparently ceremonial or status objects. Both are tin-bronzes with minor elements As, Sb and Ag, which are always found in prehistoric bronze objects; see table 1. In addition both contain cobalt and indium as trace elements. Cobalt is observed quite often in prehistoric objects, but indium is not reported in archeological objects from Europe. However, it occurs in about half of all objects studied by NRCA. The largest amount,  $\approx 100$  ppm, so far observed by us, occurs in the Buggenum sword. Indium is observed on the basis of its 1.457 eV resonance. It is an example of the usefulness of the high sensitivity of NRCA for resonances in the few-eV region. The mineralogical origin of indium is still a question requiring further studies. It may have something to do with early mining activities in Europe and the use of certain ores.

### Concluding remarks

Nearly all of the medium and heavy weight elements and some of the light nuclei (Na, Al, Cl) can be observed with NRCA. However, sensitivities to detect elements depend strongly on the occurrence of low-energy resonances. That is, elements like Ag, Sb, In and others with few-eV resonances can be detected down to a few ppm. Elements like Ni and Pb with resonances of a few keV can only be detected if they occur in the order of 1% or higher. Because of these differences in sensitivity it is of interest to consider complementary methods like PGNA, which has a better sensitivity for light elements, or neutron transmission, which is explored in the Ancient Charm collaboration. So far analyses of resonance spectra is based on a double ratio method using calibration samples for comparison. For more detailed analysis methods it is necessary to have better data concerning resonance parameters. For instance for  $^{63,65}\text{Cu}$ ,  $^{75}\text{As}$  and  $^{157}\text{Gd}$  to mention a few.

The low activation of objects during NRCA runs is a big advantage. A short waiting time (normally less than one day) is sufficient to return an object to its owner.

NRCA is also explored at IRMM for technical research, for nuclear materials and reference materials. An example is the determination of the amount of indium in the mercury cooling system of the GELINA neutron production source. Indium is added to mercury to improve the wettability of the cooling liquid of the neutron production target.

### Acknowledgements

The very skillful and dedicated operation of the GELINA facility by Wim Mondelaers and his staff and the kind hospitality by IRMM are very much appreciated. H.P. likes to memorize the pleasant collaboration at IRMM with Hermann Weigmann and Franco Corvi at the start of this project. Many thanks go to the National Museum of Antiquity, Gallo-Roman Museum, Groningen Institute of Archaeology, Museum het Valkhof, Limburgs Museum, Noord-brabants Museum and Rijksdienst Cultureel Erfgoed for lending artifacts. Part of this research has been carried under the EU FP6 Ancient Charm project funded by the European Commission under contract No. 15311.

### References

- [1] W. Mondelaers and P. Schillebeeckx, NOTIZIARIO, Neutroni e Luce di Sincrotrone, **11**(2) (2006) 19-25.
- [2] M. Moxon, REFIT2: A least Squares Fitting Program for Resonance Analysis in Neutron Transmission and Capture Data, NEA-0914/02 (1989).
- [3] H. Postma, P. Schillebeeckx and R.B. Halbertsma, Archaeometry **46** (2004) 635-646.
- [4] P.A.C. Schut, W. Kockelmann, H. Postma, D. Visser, P. Schillebeeckx, R. Wynants, Journal of Radioanalytical and Nuclear Chemistry **278**(1) (2008) 151-164.
- [5] H. Postma, D. Fontijn, P. Schillebeeckx, R.C. Perego and J.J. Butler, LUNULA, Archaeologia protohistorica **XIII** (2005) 41-46.

## Nuclear data measurements with slow neutrons at Institut Laue Langevin

*Ulli Köster*

Institut Laue Langevin, 6 rue Jules Horowitz, 38042 Grenoble Cedex 9, France

[koester@ill.eu](mailto:koester@ill.eu)

**Abstract:** The 58 MW high flux reactor of Institut Laue Langevin in Grenoble provides slow neutrons for about 40 different instruments. Some of these instruments are used for nuclear data measurements. The recoil separator LOHENGRIN separates by mass and kinetic energy the fission fragments that are produced by thermal neutron induced fission of various actinide targets in a flux of  $5 \times 10^{14} \text{ cm}^{-2} \text{ s}^{-1}$ . Similarly the crystal spectrometers GAMS analyze with extremely high resolution (down to few eV) prompt or delayed gamma rays produced in thermal neutron capture on samples placed in an in-pile position with a neutron flux of  $4 \times 10^{14} \text{ cm}^{-2} \text{ s}^{-1}$ . The high flux irradiation position V4 with a thermal neutron flux of  $1.5 \times 10^{15} \text{ cm}^{-2} \text{ s}^{-1}$  can be used for cross-section measurements and transmutation experiments. Other instruments use extracted neutron beams with neutron energies ranging from few neV to about 1 eV. These beams can either be used as white beams reaching a capture flux up to  $2 \cdot 10^{10} \text{ cm}^{-2} \text{ s}^{-1}$  over areas as large as  $100 \text{ cm}^2$  or as monochromatic beams with the additional options of neutron spin polarization up to >99% and neutron beam chopping for time-of-flight measurements.

### Introduction

Institut Laue Langevin in Grenoble hosts about forty instruments that are served with neutrons by a 58 MW high flux reactor. Most of these instruments use extracted neutron beams for neutron scattering applications. However, some instruments allow performing nuclear data measurements with slow neutrons, either at in-pile positions with neutron fluxes up to  $1.5 \times 10^{15} \text{ cm}^{-2} \text{ s}^{-1}$  or with extracted neutron beams reaching a capture flux up to  $2 \times 10^{10} \text{ cm}^{-2} \text{ s}^{-1}$ . In the following, typical applications of ILL instruments for nuclear data measurements are discussed. This covers nuclear data in a wide sense: cross-sections, branching ratios, half-lives, fission yields, fission product properties, gamma-ray energies, binding energies, scattering lengths, etc. Other ILL instruments that could become useful for future nuclear data measurements as well are presented.

### The fission fragment separator LOHENGRIN

The recoil separator LOHENGRIN [1] at ILL provides mass- and energy-separated fission fragment beams. A fissile or fertile actinide target is placed in an in-pile position at a thermal neutron flux of  $5.5 \times 10^{14} \text{ cm}^{-2} \text{ s}^{-1}$ , see Fig. 1. The fission products are emitted into  $4\pi$  solid angle. When leaving the target with kinetic energies of typically 0.3 to 1.3 MeV per nucleon, several electrons are stripped off and the ions acquire an average equilibrium charge state between 18+ and 25+. Ions emitted into a small solid angle of about  $3 \times 10^{-5}$  sterad reach, after 8 m flight through an evacuated beam tube, a  $45^\circ$  dipole magnet that will deflect and analyze them according to their momentum over ionic charge ratio. Subsequently the ions are deflected vertically by a  $35.5^\circ$  cylindrical condenser. This electrostatic deflector performs an analysis according to kinetic energy over ionic charge. The combination of both magnetic and electric fields results in a separation according to mass over ionic charge and a separation according to kinetic energy in perpendicular direction. For a usual target size of  $7 \times 0.5 \text{ cm}^2$  the mass resolving power is 600 and the energy resolution about 1%. If needed, both values can be further improved by using smaller targets.

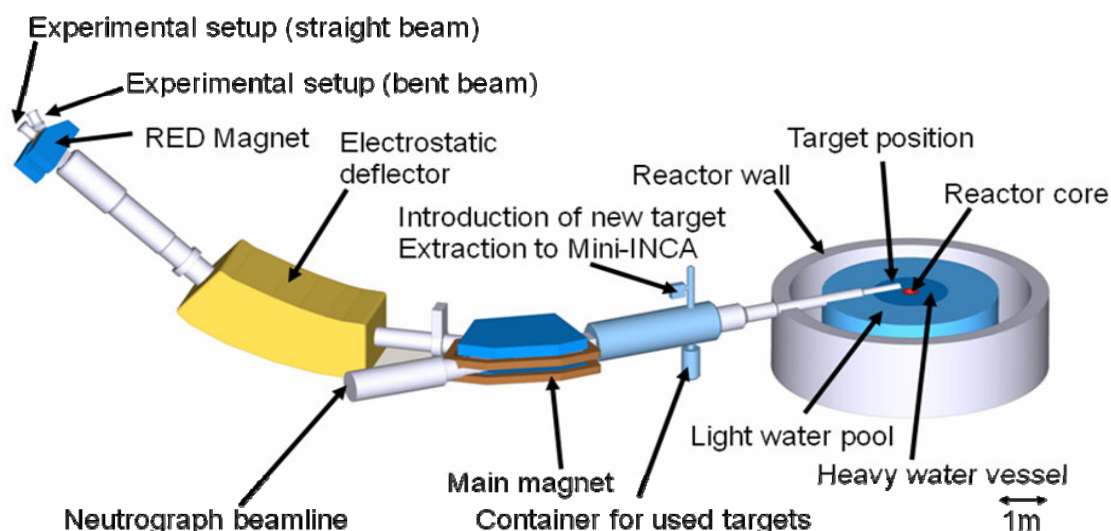


**Figure 1.** Set-up of the LOHENGRIN recoil separator.

### Fission yield measurements

Yields and kinetic energy distributions of fission fragments are determined by scanning mass by mass the distributions in ionic charge state and kinetic energy and counting the ions in the focal plane. The mass yields are readily obtained by integrating over ionic charge and kinetic energy. For light elements ( $Z < 40$ ) an ionization chamber with split anode allows identifying isobars by their specific energy loss. Thus, isotopic yields of light binary and of ternary fission fragments are directly measured by ion counting.

Fission yields and kinetic energy distributions of light binary fission fragments were determined at LOHENGRIN for  $^{229}\text{Th}(n,f)$  [2],  $^{233}\text{U}(n,f)$  [3-5],  $^{235}\text{U}(n,f)$  [3,6-9],  $^{239}\text{Pu}(n,f)$  [10-12],  $^{241}\text{Pu}(n,f)$  [13,14],  $^{242\text{m}}\text{Am}(n,f)$  [15],  $^{243}\text{Cm}(n,f)$  [16],  $^{245}\text{Cm}(n,f)$  [13,14,17-19],  $^{249}\text{Cf}(n,f)$  [20,21],  $^{251}\text{Cf}(n,f)$  [22],  $^{238}\text{Np}(n,f)$  [23,24] and  $^{242\text{g+m}}\text{Am}(n,f)$  [12,21]. For the latter two cases the fissile nuclei were bred in-situ in the high neutron flux from fertile  $^{237}\text{Np}$  and  $^{241}\text{Am}$  targets respectively.

Yields of ternary particles were measured for thermal-neutron induced fission of  $^{229}\text{Th}$  [25],  $^{233}\text{U}$  [25,26],  $^{235}\text{U}$  [26,27],  $^{239}\text{Pu}$  [25,26],  $^{241}\text{Pu}$  [28],  $^{242\text{g+m}}\text{Am}$  [27,29],  $^{245}\text{Cm}$  [26,29],  $^{249}\text{Cf}$  [30,31] and  $^{251}\text{Cf}$  [32]. Even very exotic ternary fission fragments like the halo nuclei  $^{11}\text{Li}$  and  $^{14}\text{Be}$  could be clearly identified with yields as low as  $10^{-10}$  per fission [28].

When the ultimate energy resolution is not needed, the so-called RED (reverse energy dispersion) magnet [33] focuses up to 40 cm of the energy dispersed beam (i.e.  $\Delta E/E=5.5\%$ ) from the focal plane onto a few cm length. This area can be surrounded by an efficient array of radiation detectors. Usually two fourfold clover Ge detectors and one coaxial Ge detector are used for gamma detection. Occasionally additional Ge detectors provided by the users are installed.

Gamma spectroscopy allows identifying isobars also for heavier elements ( $Z > 40$ ). Combining the electro-magnetic mass separation of LOHENGRIN with gamma spectrometry it became recently possible to measure the isotopic fission yields of heavy fragments in  $^{239}\text{Pu}(n,f)$  [34,35]. Similar measurements for other fission systems are planned.

### Nuclear spectroscopy

Apart from fission yield measurements the mass-separated radioactive ion beams can also be used for decay spectroscopy. The setup is particularly efficient for the study of microsecond isomers. Due to the short transport time through the separator (1-2  $\mu\text{s}$ ) even the decay of isomeric states with half-lives down to 0.5  $\mu\text{s}$  can be studied [36]. Isomers in very neutron-rich isotopes (e.g. in  $^{136}\text{Sb}$  with  $N/Z = 1.67$  [36]) and with excitation energies up to 6.6 MeV (17<sup>+</sup> isomer in  $^{98}\text{Zr}$  [37]) have been studied. A review of some LOHENGRIN experiments on microsecond isomers can be found in ref. [38,39].

For conversion electron spectroscopy a  $\text{LN}_2$  cooled Si detector is available and for ultrafast timing measurements several  $\text{LaBr}_3:\text{Ce}$  detectors. Beta-detection for beta-gamma spectroscopy is performed with plastic scintillation detectors. Beta-delayed neutrons are detected with an array of 18  $^3\text{He}$  tubes embedded in a polyethylene matrix [40].

An electrostatic beam chopper allows modulating the continuous fission fragment beam to beam-on/beam-off periods from few milli-seconds to hours. Thus longer-lived isomers and isotopes can be identified by following the grow-in and decay of the respective gamma rays. A tape system serves for removal of long-lived activity.

While fission is usually just exploited as a suitable production mechanism for providing intense beams of neutron-rich nuclei for nuclear spectroscopy, the measured isomeric ratios and their dependence on the kinetic energy of the fragments can also be used to increase our knowledge of the fission process itself [41]. Nanosecond isomers that decay before reaching the focal plane cannot be observed directly, but if they decay with a strongly converted transition they may be identified indirectly via a changed ionic charge state distribution [42,43].

### High-resolution (n, $\alpha$ ) and (n,p) spectroscopy

Usually considered as fission fragment separator, LOHENGRIN is also very suitable for high-resolution spectroscopy of alphas, protons and corresponding recoil nuclei produced in (n, $\alpha$ ) and (n,p) reactions respectively. The high neutron flux at the target position enables to breed radioactive nuclei, which in turn undergo (n, $\alpha$ ) or (n,p) reactions. Examples are  $^{58}\text{Ni}(n,\gamma)^{59}\text{Ni}(n,\alpha)$  see Fig. 2,  $^{151}\text{Eu}(n,\gamma)^{152}\text{Eu}(n,p)$  or  $^{151}\text{Eu}(n,\gamma)^{152}\text{Eu}(\beta^-)^{152}\text{Gd}(n,\gamma)^{153}\text{Gd}(n,\alpha)$ . Due to the electro-magnetic separation protons and alphas do not interfere in the detector. Therefore weak proton lines are detectable even for strong (n, $\alpha$ ) emitters.

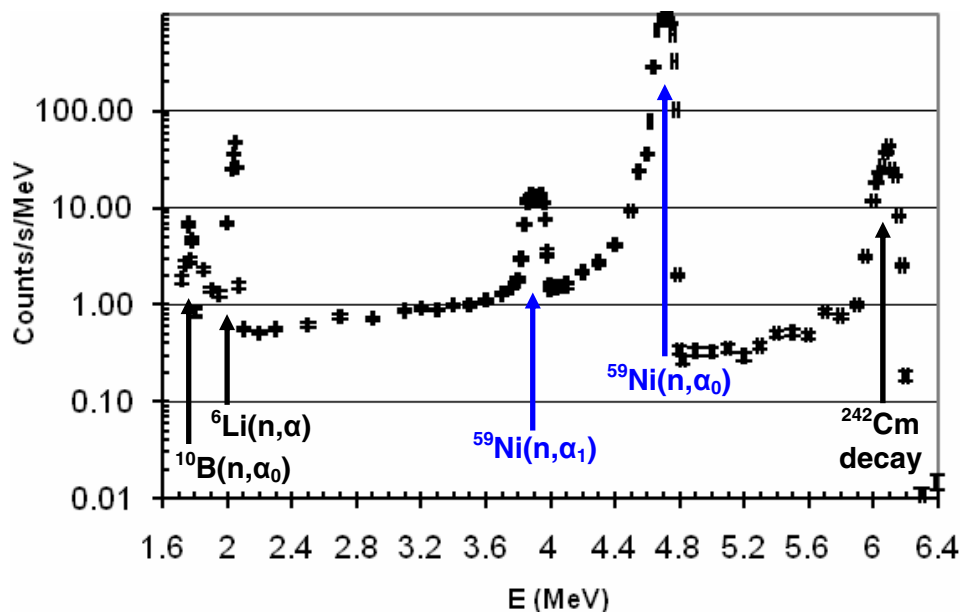


**Figure 2.** Alpha spectrum measured with a  $0.25\ \mu\text{m}$  thick nickel foil with originally natural isotopic composition that had been exposed to a thermal neutron fluence of  $6 \times 10^{21}\ \text{cm}^{-2}$ . Specific background lines are discussed in the text.

Compared to direct measurements at external neutron alpha or proton energies the presence of some LOHENGRIN specific background has to be considered: 6.1 MeV alphas stem from  $^{242}\text{Cm}$  decay. The latter was produced by transmutation of  $^{241}\text{Am}$  targets from which a small amount has been sputtered off by the fission products and deposited on the target holder.  $^{10}\text{B}(n,\alpha)$  background is due to boron diaphragms in the beam tube. Also  $^6\text{Li}(n,\alpha)$  may occur from residues of LiF that were self-sputtered on the target holder from LiF targets used to tune the spectrometer. Finally  $^{40}\text{K}(n,\alpha)$  and  $^{40}\text{K}(n,p)$  background occurs which is bred from traces of natural potassium (“finger prints”) on the target holder. Such background can cover weak lines that fall exactly at the same energies. Protons below 0.6 MeV cannot be detected due to background from  $^{14}\text{N}(n,p)$  in the rest gas of the beam tube.

### Mini-INCA

The Mini-INCA set-up [44] uses the LOHENGRIN target position for irradiations. The neutron energy spectrum is very well thermalized. Less than 2% of the neutrons have epithermal energies  $>1\ \text{eV}$ . After activation the samples are pulled back with the target changer and placed in a shielded measurement setup that is equipped with Si and Ge detectors for high-

rate alpha- and gamma spectroscopy. A detailed discussion of the Mini-INCA set-up and its recent applications for cross-section measurements with thermal neutrons is given in ref. [45].

### The large area thermal neutron beam NEUTROGRAPH

The NEUTROGRAPH beam line is placed in straight prolongation of the LOHENGRIN beam tube, see Fig. 1. This thermal neutron beam with a flux of  $3 \times 10^9 \text{ cm}^{-2} \text{ s}^{-1}$  and low divergence ( $L/D=150$ ) over an area of  $20 \times 20 \text{ cm}^2$  can be used for neutron radiography and neutron tomography [46]. In addition this white neutron beam is also accessible as general purpose intense thermal neutron beam, e.g. for detector tests, instrument development and short activations. Due to the direct view of the inner part of the reactor there is non-negligible background from fast neutrons (approx. 1%) and gamma rays. Therefore experiments with very sensitive detectors as e.g.  $(n,\gamma)$  spectroscopy are better performed at other beam lines.

### The GAMS crystal spectrometers

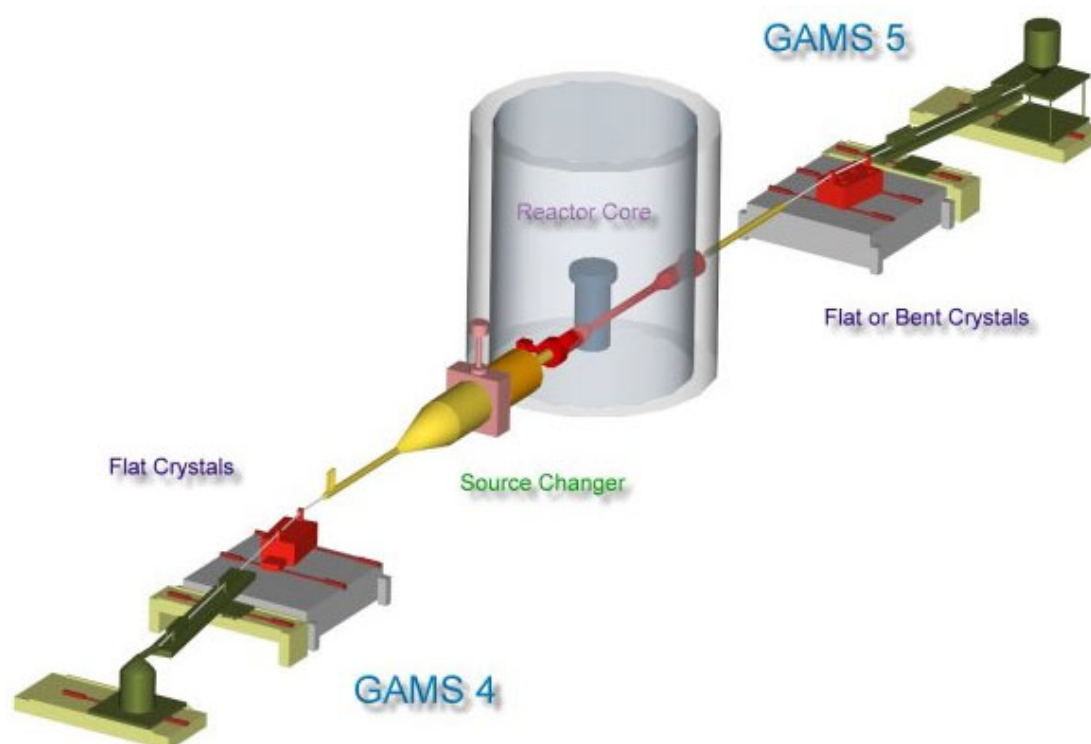


**Figure 3.** Set-up of the GAMS crystal spectrometers for high resolution spectroscopy of capture and decay gamma-rays.

The instrument GAMS has a tangential through-going beam tube, see Fig. 3. Samples are placed in a thermal neutron flux of  $5 \times 10^{14} \text{ cm}^{-2} \text{ s}^{-1}$ . Emitted prompt or delayed capture gamma rays are tightly collimated onto two crystal spectrometers placed at 17 and 21 m respectively from the target. After Bragg diffraction on one or two perfect Si or Ge crystals the gamma-ray intensity is monitored with a Ge detector. Scanning the angle of the diffracting crystal allows measuring with high resolution the energy of the gamma rays. The rotation angle is measured absolutely by laser interferometers providing excellent accuracy for the deduced gamma-ray energies. Therefore most reference energies that are today commonly used in gamma-ray spectroscopy are based on measurements at GAMS. Summing all measured energies of a gamma-ray cascade after thermal neutron capture allows measuring the neutron binding energy [47]. Such measurements provide precision data on nuclear masses, complementary to Penning trap measurements [48]. The flat crystal spectrometer GAMS4 [49] is presently being upgraded to GAMS6 [50] with even higher accuracy.

Not only the centre of a measured gamma-ray energy distribution carries physics information, but also its width: a detailed analysis of the Doppler broadening of the energy distribution of secondary gamma-rays allows deducing the lifetime of intermediate levels in the range of femtoseconds to picoseconds. This so-called GRID (Gamma Ray Induced Doppler

broadening) method [51] has provided important information on transition strengths; see e.g. ref. [52].

### **Bent crystal spectrometer**

Flat crystal spectrometers provide the highest possible resolution, but they suffer from an intrinsically low solid angle acceptance. Therefore samples of several grams are needed and only relatively strong gamma transitions can be used for spectroscopy. An alternative are bent crystal spectrometers in DuMond geometry with a three to four orders of magnitude higher angular acceptance [53]. The GAMS5 spectrometer can be used alternatively with flat or bent crystals [54]. With bent crystals the amount of sample material can be reduced to some ten milligrams, i.e. rare, highly enriched sample material can be used for nuclear spectroscopy. While lower compared to flat crystals, the energy resolution of bent crystals still exceeds by far that of Ge detectors, in particular for low gamma-ray energies of some ten to hundred keV. At 100 keV gamma-ray energy the resolution in first order is about 30 eV, for higher diffraction orders the resolution improves proportional to the order. Depending on the energy and intensity of the line, measurements are possible till about fifth order. Thus doublets or multiplets are usually fully resolved. Due to the high energy resolution, excitation schemes can often be built solely based on the Ritz principle.

### **Multi-neutron capture reactions**

Like at the LOHENGRIN target position, the neutron flux at the GAMS target position is so high that multi-neutron-capture reactions can be used to populate nuclei further from stability. Thus nuclear spectroscopy has been performed e.g. via  $^{150}\text{Sm}(n,\gamma)^{151}\text{Sm}(n,\gamma)^{152}\text{Sm}$  [55], via  $^{169}\text{Tm}(n,\gamma)^{170}\text{Tm}(n,\gamma)^{171}\text{Tm}$  [56], etc.

The capture cross-sections on intermediate unstable isotopes can be deduced from the time dependence of the intensities of the different capture and decay gamma rays. Thus, in addition to nuclear spectroscopy results new cross-sections could as well be derived from several GAMS measurements: for  $^{152g}\text{Eu}(n,\gamma)$  and  $^{152m}\text{Eu}(n,\gamma)$  [57],  $^{193}\text{Os}(n,\gamma)^{194}\text{Os}$  [58], etc.

### **The PF1B intense cold neutron beam with polarization option**

PF1B is a multipurpose beam port where an intense beam of cold neutrons with a capture flux of  $2 \times 10^{10} \text{ cm}^{-2} \text{ s}^{-1}$  on a  $20 \times 6 \text{ cm}^2$  area is available. The thermal neutron energy spectrum of the reactor is shifted by down-moderation in ILL's horizontal cold source, an in-pile vessel filled with 25 K cold liquid deuterium, towards lower neutron energies and longer wavelengths. These so-called cold neutrons are transported by a 72 m long ballistic supermirror neutron guide [59] with little losses to the experimental area while eliminating background of gamma rays or fast neutrons from the reactor completely. Remaining background of fast neutrons (approx.  $10^{-6}$  of the slow neutron flux [60]) and gamma rays is mainly generated locally by the neutron beam collimation system. The average neutron energy of the PF1B beam is 5.4 meV corresponding to a Maxwellian spectrum at 62 K. With the use of super-mirror polarizers, the PF1B neutron beam can be polarized up to 99.7%. For a fully polarized beam, the capture flux is still  $3 \times 10^9 \text{ cm}^{-2} \text{ s}^{-1}$ .

The most frequent application of the polarized PF1B beam is for studies of the free neutron decay. Various standard model parameters can be extracted from a precise measurement of angular distributions and correlations of the electrons and protons emitted in neutron decay, see e.g. [61]. Parity violating asymmetry was also observed in neutron-induced reactions, namely for the tritons emitted in  $^6\text{Li}(n,\alpha)t$  and the gamma rays emitted in  $^{10}\text{B}(n,\alpha\gamma)^7\text{Li}$  reactions induced by polarized cold neutrons [62]. Surprisingly neutron polarization affects the angular distribution of ternary particles emitted in cold neutron induced fission of  $^{235}\text{U}$  too [63].

The unpolarized, intense cold neutron beam serves for cross-section measurements. For example the  $^{39}\text{Ar}(n,\alpha)$  reaction was studied at PF1B [64]. Measurements of fission cross-sections and of yields and energy distributions of ternary fission fragments [65] at PF1B are reviewed in ref. [35]. Due to the excellent stability of the neutron beam intensity it is possible to deduce absolute cross-sections from subsequently performed relative measurements with the sample and a reference sample respectively.

The large area experimental zone ( $3 \times 10 \times 3 \text{ m}^3$ ) permits the installation of complex setups. Fission targets can be surrounded by an array of Ge detectors for spectroscopy of prompt and delayed gamma transitions. The discovery of nanosecond-isomers in fission fragments with such a setup is discussed in ref. [66].

While many experiments use the entire spectrum of the white neutron beam, it is also possible to select individual energies. A Dornier/Astrum velocity selector rotating at up to 28300 rpm allows selecting neutron energies from 0.02 to 13 meV with a transmission above 80% and a velocity resolution of about 10% FWHM [67].

### The S18 neutron interferometer

S18 is a thermal neutron interferometer using perfect Si crystals for beam splitting and merging [68,69]. The incident neutron's wavefunction is split into a transmitted (O) and diffracted (H) component by a first Si lamella protruding out from a Si single crystal. O and H beam pass one or two different samples before being diffracted by a second Si lamella onto a third Si lamella where they are recombined. Downstream of the third Si lamella the interference count rates are monitored as function of phase difference between H and O beam. A turnable Si crystal placed between the second and third Si fin acts as phase shifter. In addition to a multitude of quantum mechanics experiments with neutrons [70], neutron interferometry allows to measure the coherent scattering length with precision. When a sample is placed in one interferometer arm, the neutron path length in the sample induces an additional phase shift that can be measured by scanning the interference pattern with the phase shifter. The measured phase shift is directly proportional to the coherent scattering length of the sample material [71]. The total scattering differential cross-section can be measured by neutron diffraction, e.g. with a hot neutron diffractometer [72]. Combined with the coherent scattering length from neutron interferometry, the incoherent scattering length is deduced.

Note that a precise knowledge of coherent scattering lengths is essential for isotopic substitution techniques in neutron scattering. Therefore such experimental results are not necessarily published in usual nuclear physics journals, but more frequently in solid state physics journals [72].

### The V4 high flux irradiation position

V4 is a vertical beam tube that gives access to an irradiation position at only 15 cm distance from the reactor core. At full reactor power the neutron flux at the bottom of the tube reaches about  $1.5 \times 10^{15} \text{ cm}^{-2}/\text{s}^{-1}$  thermal neutrons,  $3 \times 10^{14} \text{ cm}^{-2}/\text{s}^{-1}$  epithermal neutrons ( $0.625 \text{ eV} < E < 0.82 \text{ MeV}$ ) and  $2 \times 10^{13} \text{ cm}^{-2}/\text{s}^{-1}$  fast neutrons ( $E > 0.82 \text{ MeV}$ ). An irradiation shuttle houses one or several Al capsules filled with quartz ampoules containing the sample material. Irradiations can last from few hours to many weeks. After decay for some days the irradiation shuttle is opened in a hot cell and the samples can be retrieved for nuclear spectroscopy or other investigations.

Miniature fission ionization chambers with on-line current measurement allow following the evolution of the fission rate during an irradiation over several weeks [73].

See ref. [45] for a detailed discussion of transmutation experiments with actinide samples in V4. At present V4 is being used for production of radioisotopes for medical applications [74] and for related cross-section measurements, e.g. for the reactions  $^{187}\text{W}(n,\gamma)$  and  $^{177\text{g}}\text{Lu}(n,\gamma)$ .

### Other instruments

Most other instruments at ILL are devoted to neutron scattering. They can be classified as [75]:

- a) two-axis diffractometers with one- or two-dimensional neutron detectors,
- b) three-axis diffractometers with an energy analyzing crystal between sample and neutron detector to study inelastic processes,
- c) time-of-flight spectrometers with a chopped neutron beam.

All these instruments use monochromatic neutron beams that are provided by Bragg diffraction on a monochromator crystal. Some monochromators focus the neutron beam horizontally and/or vertically onto the sample to increase the flux.

### Hot neutrons

The beam tubes of some of these instruments are pointing at the "hot neutron source" of the ILL reactor, a thermally insulated graphite block that is heated by gamma radiation from the reactor core to about 2000 °C. Thus, the neutron spectrum is shifted towards higher energies and shorter wavelengths compared to thermal neutrons. After crystal diffraction monochromatic "hot" neutrons are available for experiments. At 0.1 eV neutron energy a flux

of  $4 \times 10^7 \text{ cm}^{-2}\text{s}^{-1}$  is available, dropping to  $10^6 \text{ cm}^{-2}\text{s}^{-1}$  at 1 eV. In principle one could temporarily convert such a scattering instrument for measurements of cross-sections with monochromatic hot neutron beams by placing a suitable detector downstream or besides of the sample.

### Very cold and ultracold neutrons at PF2

Still lower neutron energies compared to PF1B are available at the PF2 beam lines. A vertical beam tube extracts neutrons from the vertical cold source. The progressive curvature of the neutron guide eliminates all neutrons but those with the lowest energies. This results in a beam of very cold neutrons with a flux of  $4 \times 10^6 \text{ cm}^{-2}\text{s}^{-1}$  at 8  $\mu\text{eV}$  over an area of  $7 \times 3.4 \text{ cm}^2$ . Very cold neutrons (VCNs) can be “cooled” even further by collisions with a neutron turbine. The produced ultracold neutrons (UCNs) with energies between 0 and 250 neV are totally reflected under all angles from suitable surfaces (e.g. nickel, diamond-like-carbon, beryllium, etc.) and can thus be stored for several minutes in so-called neutron bottles.

A flux of  $3 \times 10^4 \text{ cm}^{-2}\text{s}^{-1}$  UCNs is available over an area up to  $14 \times 10 \text{ cm}^2$ . Due to the  $1/v$  behaviour the cross-sections for VCNs and UCNs are huge, making it possible to achieve significant absorption even for very thin samples, e.g. made from rare enriched or highly radioactive isotopes. For extremely high cross-sections of several ten Mbarn even deviations from the exponential attenuation law are expected [76].

### Actinide samples

Actinide targets can be routinely used at most ILL instruments. At instruments in the neutron guide halls actinide samples with a radiotoxicity equivalent to 20 MBq  $^{239}\text{Pu}$  can be used. This corresponds to 0.3 g  $^{233}\text{U}$ , 1.5 g  $^{235}\text{U}$ , 8 mg  $^{239}\text{Pu}$ , 0.3 mg  $^{241}\text{Pu}$ , 3 mg  $^{245}\text{Cm}$ , 0.2 mg  $^{251}\text{Cf}$ , etc. Due to the high neutron flux such sample quantities are usually sufficient for most applications. Still higher activities (equivalent to 370 MBq  $^{239}\text{Pu}$ ) can be handled at instruments situated in the reactor hall, i.e. at Neutrograph, PF2, the hot neutron instruments, etc. At LOHENGRIN and Mini-INCA samples with activities up to 3.7 GBq activity can be used.

### Conclusion and Outlook

The high flux reactor of ILL is equipped with several unique instruments for nuclear data measurements. LOHENGRIN is the world-leading spectrometer for precise studies of thermal neutron induced fission. The GAMS crystal spectrometers provide on one hand excellent resolution and accuracy for the determination of absolute gamma ray energies, on the other hand they can be used to perform general nuclear spectroscopy or to measure capture cross-sections of in-situ bred isotopes.

PF1B is an intense multi-purpose cold neutron beam with polarization option. The neutron interferometer S18 allows measuring coherent scattering lengths with very high precision.

Another strong point of ILL is the availability of a multitude of external neutron beams with neutron energies ranging from few neV up to about 1 eV. Even after monochromatization by Bragg diffraction on crystals or velocity selectors, the neutron fluxes are sufficiently high for most types of cross-section measurements. There is large potential to use such neutron beams of different energies for solving discrepancies of previous cross-section measurements that might be caused by low-lying resonances or measurements in an imperfect Maxwellian neutron spectrum.

ILL provides not only neutron beams, but also the infrastructure for the sample environment. For example superconducting split pole magnets up to 15 T and cryostats with  $^3\text{He}/^4\text{He}$  dilution inserts reaching temperatures as low as 15 mK are available. Embedding sample atoms into a ferromagnetic host or exposing them to a very high magnetic field allows reaching high degrees of nuclear orientation at low temperatures (Low Temperature Nuclear Orientation). Combining such oriented samples with polarized neutron beams provides full control of the spin distribution in the entrance channel and thus enables the unambiguous assignment of spins and parities in the exit channels. This technique has already been applied for many different neutron-capture reactions, mainly by Hans Postma and coworkers in the 60ties and 70ties, see e.g. ref. [77]. If needed, it could be revived relatively easily at ILL to perform complementary measurements of other specific cases.

Many possible applications of ILL instruments have been presented. It should be reminded that ILL is a user facility. Thus, the physics performed on these instruments depends on the

experiments proposed by the user community. You are very welcome to propose experiments similar to those presented above or even completely different ones if they can profit of the ILL instruments' characteristics.

### References

- [1] P. Armbruster et al., Nucl. Instr. Meth. 139 (1976) 213.
- [2] J.P. Bocquet et al., Z. Phys. A335 (1990) 41.
- [3] D. Belhafaf et al., Z. Phys. A 309 (1983) 253.
- [4] H.G. Clerk et al., Nucl. Phys. A452 (1986) 277.
- [5] U. Quade et al., Nucl. Phys. A487 (1988) 1.
- [6] H.G. Clerk et al., Nucl. Phys. A247 (1975) 74.
- [7] G. Siegert et al., Phys. Rev. C14 (1976) 1864.
- [8] W. Lang et al., Nucl. Phys. A345 (1980) 34.
- [9] J.L. Sida et al., Nucl. Phys. A502 (1989) 233c.
- [10] C. Schmitt et al., Nucl. Phys. A430 (1984) 21.
- [11] W. Ditz, Ph.D. thesis, Univ. Mainz (1991).
- [12] W. Ditz et al., Seminar on Fission "Pont d'Oye II", ed. by Cyriel Wagemans (1991) p. 114.
- [13] T. Friedrichs et al., Second Int. Workshop on Nuclear Fission and Fission-Product Spectroscopy, Seyssins, AIP Conf. Proc. 447 (1998) p. 231.
- [14] T. Friedrichs, PhD, TU Braunschweig, 1998.
- [15] I. Tsekhanovich et al., Nucl. Phys. A 658 (1999) 217.
- [16] I. Tsekhanovich et al., Phys. Rev. C70 (2004) 044610.
- [17] G. Fioni et al., Seminar on Fission "Pont d'Oye III", ed. by Cyriel Wagemans (1995) p. 42.
- [18] D. Rochman et al., Nucl. Phys. A710 (2002) 3.
- [19] D. Rochman et al., Nucl. Phys. A735 (2004) 3.
- [20] M. Djebara et al., Nucl. Phys. A496 (1989) 346.
- [21] R. Hentzschel et al., Nucl. Phys. A571 (1994) 427.
- [22] E. Birgersson et al., Nucl. Phys. A 791 (2007) 1.
- [23] G. Martinez et al., Nucl. Phys. A515 (1990) 433.
- [24] I. Tsekhanovich et al., Nucl. Phys. A688 (2001) 633.
- [25] M. Wöstheinrich et al., Acta Phys. Slovaca 49 (1999) 117.
- [26] U. Köster, Ph.D. thesis, TU München (2000).
- [27] W. Baum et al., Conf. on Nuclei far from Stability, Atomic Masses and Fundamental Constants, IOP Conf. Series 132 (1993) 477.
- [28] U. Köster et al., Nucl. Phys. A652 (1999) 371.
- [29] M. Hesse, Ph.D. thesis., Univ. Tübingen (1997).
- [30] M. Davi, Ph.D. thesis, Univ. Mainz (1997).
- [31] I. Tsekhanovich et al., Phys. Rev. C 67 (2003) 034610.
- [32] S. Oberstedt et al., Nucl. Phys. A761 (2005) 173.
- [33] G. Fioni et al., Nucl. Instr. Meth. A332 (1993) 175.
- [34] A. Bail, Ph.D. thesis, Univ. Bordeaux (2009).
- [35] O. Serot, Proc. of the IAEA Technical Meeting on Specific Applications of Research Reactors: Provision of Nuclear Data, Vienna, 2009.
- [36] G.S. Simpson et al., Phys. Rev. C76 (2007) 041303(R).
- [37] G.S. Simpson et al., Phys. Rev. C74 (2006) 064308.
- [38] J.A. Pinston and J. Genevey, J. Phys. G30 (2004) R57.
- [39] W. Urban et al., CGS13, AIP Conf. Proc. 1090 (2009) p. 494.
- [40] L. Mathieu et al., Fission'2009 Workshop, Cadarache, AIP Conf. Proc., in press.
- [41] F. Gönnerwein et al., Int. J. Mod. Phys. E 16 (2007) 410.
- [42] H. Wohlfarth et al., Z. Phys. A287 (1978) 153.
- [43] T. Materna et al., Fission'2009 Workshop, Cadarache, AIP Conf. Proc., in press.
- [44] F. Marie et al., Nucl. Instr. Meth. A556 (2006) 547.
- [45] A. Letourneau et al., these proceedings.
- [46] A. Hillenbach et al., Nucl. Instr. Meth. A542 (2005) 116.
- [47] M.S. Dewey et al., Phys. Rev. C73 (2006) 044303.
- [48] S. Rainville et al., Nature 438 (2005) 1096.
- [49] E.G. Kessler et al., Nucl. Instr. Meth. A457 (2001) 187.
- [50] J. Krempel et al., CPEM2008 Conf. Digest (2008) 634.
- [51] H. Börner and J. Jolie, J. Phys. G19 (1993) 217.
- [52] H. Börner et al., Phys. Rev. C73 (2006) 034314.
- [53] H.R. Koch et al., Nucl. Instr. Meth. 175 (1980) 401.

- [54] C. Doll et al., J. Res. Natl. Inst. Stand. Technol. 105 (2000) 167.
- [55] N.V. Zamfir et al., Phys. Rev. C65 (2002) 067305.
- [56] W. Schauer et al., Int. J. Mod. Phys. E3 (1994) 793.
- [57] T. von Egidy et al., Z. Phys. A322 (1985) 669.
- [58] R.F. Casten et al., Phys. Lett. 76B (1978) 280.
- [59] H. Abele et al., Nucl. Instr. Meth. A562 (2006) 407.
- [60] M.A. Lone et al., Nucl. Instr. Meth. 174 (1980) 521.
- [61] M. Schumann et al., Phys. Rev. Lett. 99 (2007) 191803.
- [62] V.A. Vesna et al., Nucl. Phys. A827 (2009) 425c.
- [63] F. Gönnenwein et al., Phys. Lett. B652 (2007) 13.
- [64] G. Goeminne et al., Nucl. Instr. Meth. A489 (2002) 577.
- [65] S. Vermote et al., Nucl. Phys. A806 (2008) 1.
- [66] I. Tsekhanovich et al., Phys. Rev. C78 (2008) 011301.
- [67] V. Wagner et al., Physica B180/181 (1992) 938.
- [68] G. Kroupa et al., Nucl. Instr. Meth. A440 (2000) 604.
- [69] M. Zawisky et al., Nucl. Instr. Meth. A481 (2002) 406.
- [70] Neutron Interferometry, Lessons in Experimental Quantum Mechanics, H. Rauch and S.A. Werner, Clarendon Press, Oxford, 1990.
- [71] W. Ketter et al., Eur. Phys. J. A27 (2006) 243.
- [72] H.E. Fischer et al., J. Phys. Condens. Matter. 20 (2008) 045221.
- [73] S. Chabod et al., Nucl. Instr. Meth. A566 (2006) 633.
- [74] U. Köster et al., Eur. J. Nucl. Med. Mol. Imaging 36 (2009) S400.
- [75] The Yellow Book, Guide to Neutron Research Facilities, see: <http://www.ill.eu/>
- [76] H. Rauch et al., Phys. Rev. Lett. 83 (1999) 4955.
- [77] J.J. Bosman and H. Postma, Nucl. Instr. Meth. 148 (1978) 331.



## Slow neutron facilities at the National Physical Laboratory, UK

*N. P. Hawkes<sup>1)</sup>, P. Kolkowski<sup>1)</sup> and D. J. Thomas<sup>1)</sup>*

1) National Physical Laboratory, Hampton Road, Teddington, Middlesex TW11 0LW, UK

[nigel.hawkes@npl.co.uk](mailto:nigel.hawkes@npl.co.uk)

**Abstract:** This paper describes the facilities for generating slow neutron fields at the National Physical Laboratory, and the types of measurement that can be carried out in these fields.

The principal facility is a thermal pile consisting of a large graphite block shielded with an outer layer of paraffin wax. Neutrons are produced by directing a deuteron beam from the Neutron Metrology Group's 3.5 MV Van de Graaff accelerator onto a pair of beryllium targets at separated positions inside the block. Fluence rates of about  $10^7 \cdot \text{cm}^{-2} \cdot \text{s}^{-1}$  can be achieved at the centre, and a servo mechanism keeps the field in the central region uniform and constant. The pile has been used in the past to measure various thermal neutron capture cross sections. It is currently in routine use for detector calibrations and characterisations, and for testing reactor instruments.

The Neutron Group also has a water bath. This is similar to the thermal pile except that the moderator is a cylinder of water, and the neutrons are produced by a single beryllium target at the centre. Compared with the pile, the epithermal neutron field in this facility conforms more closely to the  $1/E$  dependence frequently assumed, but the field is more prone to flux depression when a detector is introduced. The water bath has been used in the past to measure a variety of resonance integrals. It is currently out of use and would need some significant refurbishment before it would be ready for new measurements.

The ability to measure activation cross sections is enhanced by close links to the Radioactivity Group at NPL who can provide access to additional well-characterised gamma and beta measuring equipment.

### Introduction

The National Physical Laboratory (NPL) in south west London is the UK's national standards laboratory. It was founded in 1900 in Bushy House, a former royal residence, and has been developing ever since. It is now largely housed in a custom-built suite of laboratories completed in stages between the years 2000 and 2009 (although the neutron facility, due to its size, remains in the nearby Chadwick Building).

The Neutron Metrology Group can produce well-characterised neutron fields by means of various isotopic neutron sources ( $^{241}\text{Am}$  /  $\text{Be}$ ,  $^{252}\text{Cf}$  and others), or via a 3.5 MV single-ended Van de Graaff accelerator. This machine provides beams of protons, deuterons or alphas at currents of up to 100 microamps. To produce monoenergetic fast neutrons, the beam is directed onto a suitable target at the centre of a low-scatter area, where lightweight floors and low-mass supports keep neutron scattering to a minimum (Figure 1). The standard fields produced here are routinely used for instrument calibrations, and fast neutron activation cross sections have been measured here in the past. The accelerator can optionally deliver the beam in nanosecond pulses, allowing neutron spectra to be measured by the time-of-flight technique.

For the production of slow and thermal neutrons, the beam is instead directed to the thermal pile or the water bath (also shown in Figure 1).

### Thermal Pile

#### Construction

The construction and calibration of the NPL Thermal Pile (Figures 1 and 2) has been detailed by Ryves and Paul [1].

The facility consists of a large graphite moderator with sources of neutrons embedded within it. Access holes are bored into the moderator to allow small devices or activation foils to be exposed to the neutron flux, or to allow a beam of neutrons to be extracted.

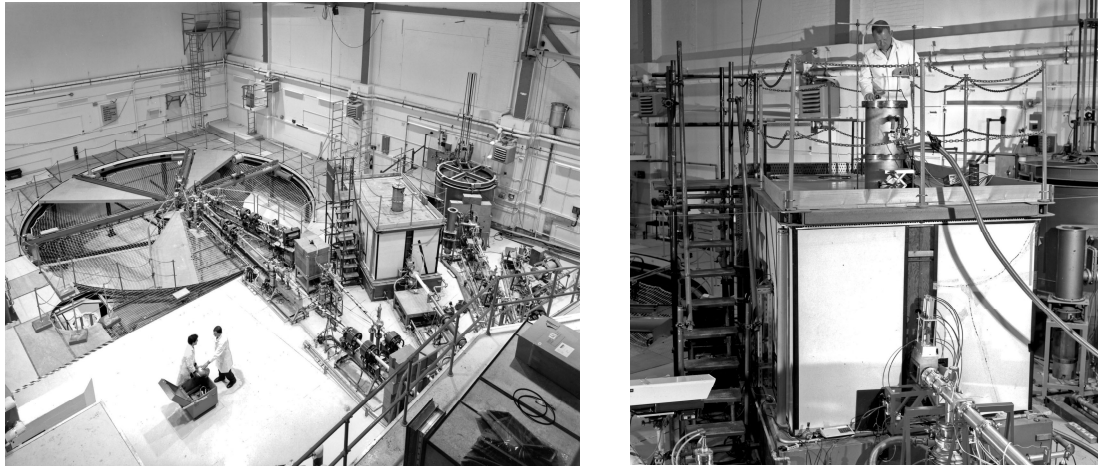


**Figure 1.** The main experimental hall in the neutron building. Left, overall view showing (from left to right) the low scatter area, the thermal pile and the water bath; right, a close-up view of the thermal pile, with a measurement being set up on the thermal column.

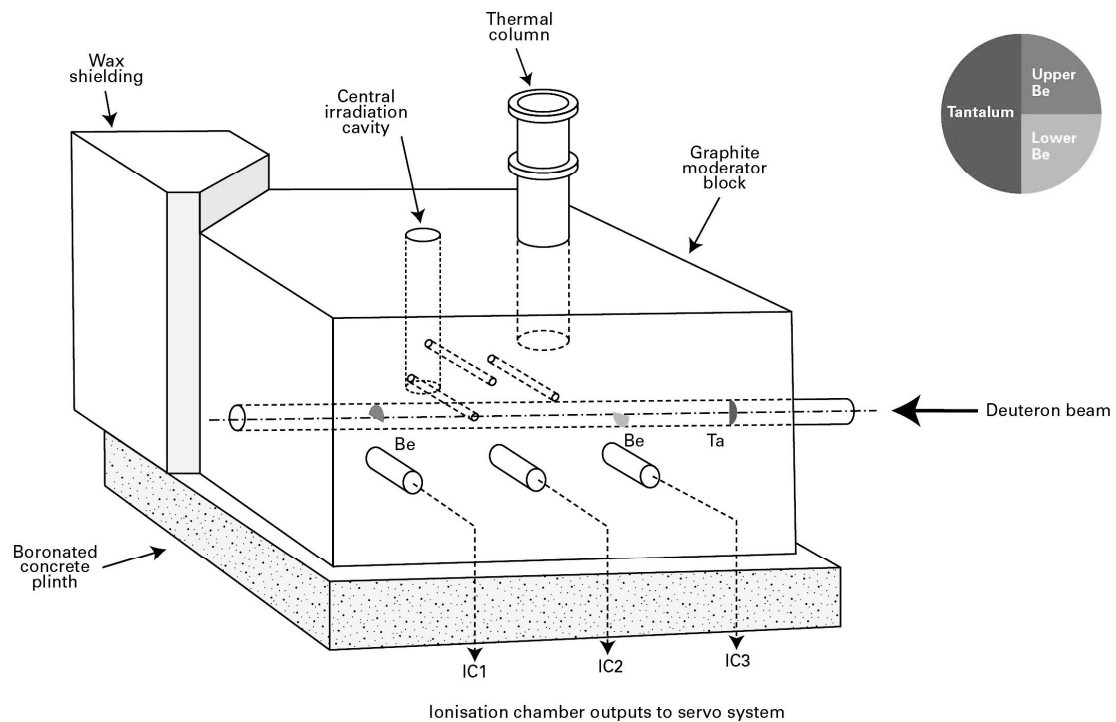


**Figure 2.** Isometric cutaway diagram of thermal pile. Note the arrangement of the three targets, which allows the servo to control the rate and distribution of the neutron production by steering the beam (see inset, top right, showing 'beam's-eye view' of targets).

It can be regarded as similar to a reactor core, except that the source of neutrons is not nuclear fuel but the interaction of deuterons from the accelerator with thick beryllium targets inside the pile. The moderator is built of graphite blocks and is 279 cm long by 144 cm wide and 156 cm high. It rests on a 60 cm thick concrete plinth loaded with boric oxide, and the top and sides of the graphite are shielded with 18 cm of paraffin wax contained in wooden boxes. A 10 cm diameter aluminium tube along the centre line of the moderator block allows the deuteron beam to reach the beryllium targets. There are two of these, one 80 cm upstream of the central point, and the other 80 cm downstream. They are water cooled and are surrounded by 2.5 cm of lead to attenuate gammas.

### Servo control

The neutron production targets are semicircular in shape. One occupies the top half of the beam tube and the other the bottom half. In addition, a tantalum beam stop, which does not produce significant numbers of neutrons, obscures one side of both targets from the incoming beam. (See the inset in Figure 2). This arrangement allows the balance of neutron production to be shifted between the front and back of the block by steering the beam vertically, and the overall production rate to be varied by steering it horizontally on or off the beam stop. The steering is done automatically by a servo circuit. This is controlled by three boron-coated ion chambers positioned as shown under the beam tube, and it drives a set of electrostatic steering plates just upstream of the pile. The servo has been found to keep the neutron flux at the centre reproducible to  $\pm 0.1\%$  over a period of 6 months, and the flux gradient at the same place to less than  $0.2\% \text{ cm}^{-1}$ .

One advantage of the thermal pile over a reactor is that the production of neutrons can be turned off and on almost instantaneously by blocking or admitting the beam. This allows samples to be set up and removed at leisure, with a well-defined irradiation period in between.

### Irradiation locations

Two locations are available for performing irradiations. One is at the bottom of a vertical hole 12 cm in diameter that gives access to a small region near the centre of the pile. Fluence rates over  $10^7 \text{ cm}^{-2}\text{s}^{-1}$  are available here, and the uniformity is good, but only small items can be accommodated. Larger objects can be irradiated in the beam emerging from the thermal column. This arrangement consists of a larger diameter vertical hole, positioned so that it is nearly over one of the beryllium targets. The hole is lined with a stainless steel tube which in turn has a cadmium layer on the curved side so that the only source of thermal neutrons is the graphite under the bottom of the tube. The tube can be evacuated to reduce the attenuation of the neutrons. The beam emerging from the tube is reasonably uniform over a diameter of about 30 cm, but the fluence rate achievable is reduced to  $4 \times 10^4 \text{ cm}^{-2}\text{s}^{-1}$ .

The neutron fluences in the central region and in the thermal column have different directional characteristics. The former is assumed to be isotropic, whereas the latter is essentially unidirectional.

### Neutron spectrum characteristics

The neutron spectrum in a system of this kind is made up of two parts, a thermal (Maxwellian) component with a temperature close to that of the moderator, and an epithermal (slowing down) component that is often assumed to be proportional to  $1/E$  where  $E$  is the neutron energy.

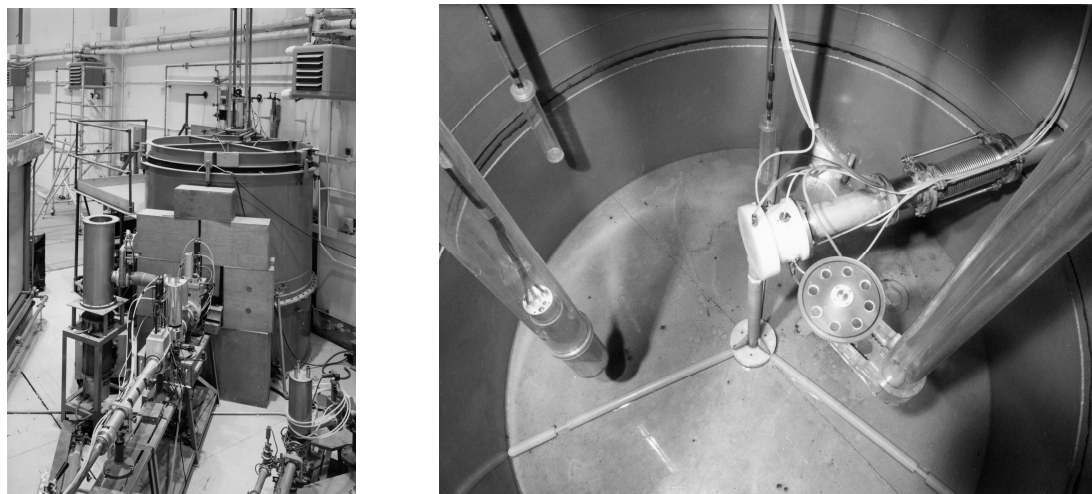
Cadmium absorbs neutrons very effectively below approximately 0.5 eV, so the ratio between the activity induced in a suitable sample (e.g. a thin gold foil) when exposed directly to the neutron field, and that induced when the sample is covered in a cadmium layer, allows an estimate to be made of the relative intensities of the two spectrum components (the higher the cadmium ratio, the smaller the epithermal contribution). Ryves and Paul, in their 1968 characterisation of the newly constructed pile, measured cadmium ratios for a variety of foils with different effective resonance energies, and compared them with measurements in a water moderator where the epithermal spectrum is expected to follow a  $1/E$  dependence closely. From these results they deduced that the epithermal component at the centre of the pile is approximately proportional to  $1/E^{1.05}$ . They also deduced the epithermal fraction, and, using an empirical relationship given by Geiger and van der Zwan [2], estimated the temperature difference between the Maxwellian distribution and the moderator. More recently, Thomas and Souchak [3] carried out gold foil measurements in the thermal column, and deduced corresponding parameters for the spectrum there. Some characteristics of the central and thermal column fields are summarised in Table 1. Note that, in Table 1, the epithermal neutron fraction is given in terms of the number of neutrons, i.e. the number of neutrons associated with the epithermal component divided by the total number. If the epithermal fraction is instead expressed in terms of fluence, the value is much larger because of the difference in average speed between the two components. Kolkowski and Thomas [4] measured an epithermal fluence fraction of 24% for the thermal column, and point out that the fraction in terms of dose equivalent is larger still (about 70%) [5]. The cadmium ratios shown in Table 1 compare favourably with those seen in reactors. The value in the thermal column increases with height, i.e. with distance from the source of neutrons, although with a corresponding decrease in fluence rate.

**Table 1.** Neutron parameters in the central cavity and thermal column of the Thermal Pile.

Parameter	Central cavity	Thermal column (1 m reference position)
Field geometry	Isotropic	Beam
Max. stable fluence rate	$\approx 1.2 \times 10^7 \text{ cm}^{-2} \text{ s}^{-1}$	$\approx 4.0 \times 10^4 \text{ cm}^{-2} \text{ s}^{-1}$
Min. stable fluence rate	$\approx 1.0 \times 10^5 \text{ cm}^{-2} \text{ s}^{-1}$	$\approx 4.5 \times 10^2 \text{ cm}^{-2} \text{ s}^{-1}$
Typical Cd ratio, thin gold foil	33	6.5
Epithermal neutron fraction (typical)	0.8%	2.3%
Maxwellian temp. - moderator temp.	9.5 K approx.	22 K approx.

**Current status of facility**

The thermal pile is currently in routine use for calibrations, irradiations and instrument tests. It has been used in the past to measure thermal neutron capture cross sections (such as  $^{23}\text{Na}$ ,  $^{27}\text{Al}$ ,  $^{37}\text{Cl}$  and  $^{51}\text{V}$  [6]) and neutron capture resonance integrals (such as  $^{69}\text{Ga}$ ,  $^{139}\text{La}$ ,  $^{198}\text{Pt}$  and others [7]).

**Water bath****Figure 3.** Water bath. Left, external view of water tank; right, interior of tank, showing (from left to right) the neutron sensors, the neutron production target, and the sample wheel.**Purpose**

The graphite moderator in the thermal pile has the advantage of being physically stable, and moderators made of graphite typically produce a neutron spectrum with a small difference between the neutron and moderator temperatures. Fluence depression (the drop in fluence rate on introducing an activation foil or a device to be irradiated) is also usually small. However, graphite has the disadvantage that the epithermal component differs significantly from  $1/E$  dependence. The true energy dependence for a given facility needs to be measured. In a water moderator, the  $1/E$  law can be assumed to hold above 1 eV [2], because neutron absorption is negligible over the energy range of interest, and the scattering cross section remains constant. A water bath facility was therefore also constructed at NPL to act as a true  $1/E$  reference.

**Construction**

The water tank (Figure 3) is 2.4 m high and 2 m in diameter, and the neutrons are again produced by directing a deuteron beam from the Van de Graaff accelerator onto a beryllium target. This time there is only one target, located at the centre. A servo controller is employed as before, but this time only to regulate the overall output, as measured by fission and ionisation chambers located in the water towards the edge of the tank.

**Irradiation of activation foils**

The facility is usually used to irradiate foil samples. To ensure that all foils of equal area have equal average irradiation, they are placed at equal intervals around the circumference of a

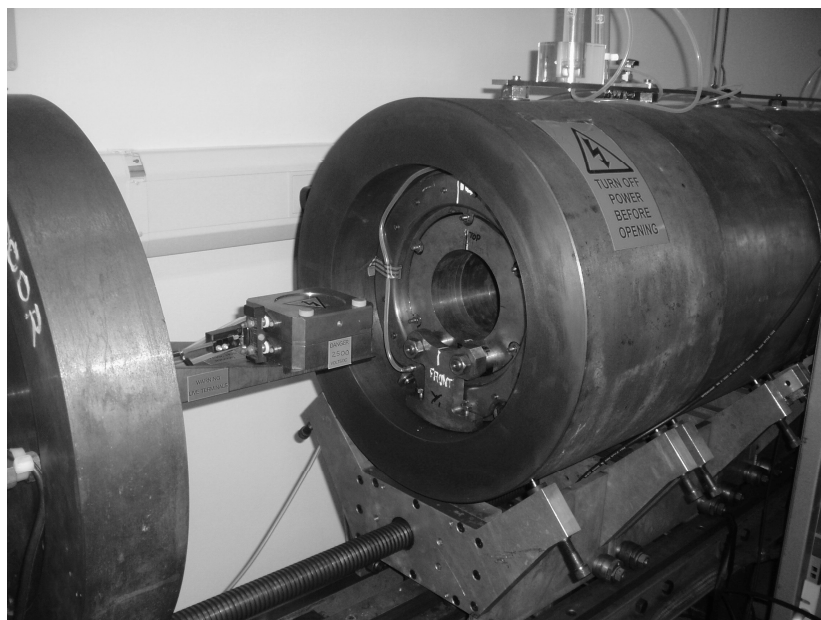
14 cm diameter circle, encased within a thin PMMA wheel that rotates at 150 rpm in a horizontal plane. The centre of the wheel may be located anywhere that is at least 15 cm above the target and 8 cm in front of it.

#### **Current status of facility**

The water bath is currently out of use and would need some significant refurbishment before it could be used for new measurements. For example, the beam line from the accelerator has been partially dismantled to allow access to other facilities. The bath has been used in the past to measure resonance integrals such as those of  $^{63}\text{Cu}$ ,  $^{65}\text{Cu}$ ,  $^{107}\text{Ag}$ ,  $^{159}\text{Tb}$ ,  $^{164}\text{Dy}$  and  $^{165}\text{Ho}$  [8].

#### **Measurement of induced activity in foils**

When the thermal pile is used to test or calibrate an instrument, the fluence delivered is measured by means of the activation of standard gold foils. The activity of the foils is measured as soon as possible after the irradiation is completed. For the standard foils, the beta counting efficiencies are known, and  $4\pi$  counting of the beta emission rate in a low background windowless gas-flow counter (Figure 4) is the preferred method, although  $4\pi\beta\text{-}\gamma$  counting can also be used if the activity is high enough. In experiments where the activity induced in a sample of some material is the quantity of interest, the activity can be measured by beta counting if the efficiency for the sample is known, by  $4\pi\beta\text{-}\gamma$  counting if the induced



activity is sufficiently high, or by gamma counting in NaI, germanium or liquid scintillation counters.

**Figure 4.** Low background beta counter.

Uncertainties of 1 - 2 percent are routinely achievable when fluences are measured with standard gold foils.

The NPL neutron facility is located close to the laboratories of the NPL Radioactivity Group, where various well-characterised detectors are available to help with non-standard or difficult activity measurements. For example, the Radioactivity Group has a beta counter with an automatic sample changer that allows a large number of foils to be processed without manual intervention.

#### **Conclusions**

Facilities are available within the Neutron Metrology Group at NPL for measuring thermal neutron cross sections and resonance integrals. Other groups within the UK's national standards laboratory are located close by and can offer further specialised facilities for solving metrology problems.

**References**

- [1] T.B. Ryves and E.B. Paul, The construction and calibration of a standard thermal neutron flux facility at the National Physical Laboratory, *Journal of Nuclear Energy* 22 (1968) 759 - 775.
- [2] K.W. Geiger and L. van der Zwan, Slowing down spectrum and neutron temperature in a thermal neutron flux density standard, *Metrologia* 2 (1966) 1 - 5.
- [3] D.J. Thomas and N. Soochak, Determination of the  $^3\text{He}$  number density for the proportional counter used in the NPL Bonner sphere system, NPL Report RS(EXT)104, July 1988.
- [4] P. Kolkowski and D.J. Thomas, Measurement of the fast neutron component in the beam of the NPL thermal neutron column using a Bonner sphere spectrometer, NPL Report CIRM 28, May 1999.
- [5] D.J. Thomas and P. Kolkowski, Thermal fluence and dose equivalent standards at NPL, NPL Report DQL RN008, March 2005.
- [6] T.B. Ryves and D.R. Perkins, Thermal neutron capture cross-section measurements for  $^{23}\text{Na}$ ,  $^{27}\text{Al}$ ,  $^{37}\text{Cl}$  and  $^{51}\text{V}$ , *Journal of Nuclear Energy* 24 (1970) 419 - 430.
- [7] T.B. Ryves, Further activation thermal neutron capture cross-sections and resonance integrals, *Journal of Nuclear Energy* 25 (1971) 129 - 131.
- [8] T.B. Ryves and K.J. Zieba, The resonance integrals of  $^{63}\text{Cu}$ ,  $^{65}\text{Cu}$ ,  $^{107}\text{Ag}$ ,  $^{159}\text{Tb}$ ,  $^{164}\text{Dy}$  and  $^{165}\text{Ho}$ , *J. Phys. A: Math., Nucl. Gen.* 7 (1974) 2318 - 2332.

## Cross section measurements for thermal neutron-induced reactions on actinides at the ILL reactor

A. Letourneau<sup>1)</sup>, E. Dupont<sup>1)</sup>, P. Mutti<sup>2)</sup>, S. Panebianco<sup>1)</sup>

1) Irfu/SPhN, CEA-Saclay, 91191 Gif-sur-Yvette, France

2) Institut Laue-Langevin, ILL, 38000 Grenoble, France  
aletourneau@cea.fr

**Abstract:** Within the Mini-INCA project we measured the thermal neutron-induced capture cross section of  $^{232}\text{Th}$ ,  $^{233}\text{Pa}$ ,  $^{234}\text{U}$ ,  $^{237}\text{Np}$ ,  $^{238}\text{Pu}$ ,  $^{242}\text{Pu}$ ,  $^{241}\text{Am}$ ,  $^{242\text{gs-m}}\text{Am}$ ,  $^{243}\text{Am}$ ,  $^{242}\text{Cm}$ ,  $^{244}\text{Cm}$ ,  $^{248}\text{Cm}$ ,  $^{249}\text{Cf}$ ,  $^{250}\text{Cf}$ ,  $^{251}\text{Cf}$  and the neutron-induced fission cross sections of  $^{238}\text{Np}$ ,  $^{242\text{gs-m}}\text{Am}$  and  $^{245}\text{Cm}$ . Experiments were done using two irradiations channels of the High Flux Reactor of ILL: the H9 and the V4 channels. These two channels offer a diversity of neutron fluxes ranging from pure thermal neutrons to about 15% epithermal neutrons with intensities as high as  $1 \cdot 10^{15} \text{ n/cm}^2/\text{s}$ . To determine these cross sections we used activation techniques based on high-counting rate  $\alpha$  and  $\gamma$ -spectroscopy of irradiated samples or mass spectrometry and on-line fission rate measurements with miniature fission-chambers. Thanks to the high neutron fluxes and such techniques it is possible to form short-live isotopes (such as  $^{242\text{gs}}\text{Am}$  or  $^{244\text{m}}\text{Am}$ ) and to study their decay or their neutron capture or fission cross sections.

### Introduction

Facing with the growing of the world power demands, nuclear energy seems to be a conceivable solution for energy production without using remaining limited fossil fuel resources which contribute to the alarming global warming effect. However, public opinion still expresses major concerns about this energy source, mainly due to the residual long-term highly radioactive wastes. In this context, even if the creation of a long-term geological repository seems to be unavoidable, researches and developments about partitioning and transmutation are essentials. In particular, the reduction of uncertainties on nuclear data is one of the fundamental aspects of these researches for systems considered as possible transmuters of transuranic elements or even simply for systems which have to respond to high-level requirements as waste minimization, sustainability, safety and non-proliferation. Most of the nuclear data are available in modern data files, but their accuracies and validation are still a major concern, especially for Minor Actinides (MA).

Within the Mini-INCA project [3], we took benefit of the high neutron fluxes provided by the High Flux Reactor (HFR) of the Laue-Langevin Institut (Grenoble, France) to provide new data for slow neutron-induced reaction on MA and  $\beta$ -decay parameters such as decay half-lives or  $\gamma$ -ray intensities for short-lived isotopes or isomer. High fluxes are very useful but require adapted techniques for the measurements and analysis tools. We present in this paper the experimental approach, the analysis technique and the results obtained on the fission and capture cross sections of the main MA.

### Experimental approach

#### The irradiation facility

We used two channels of the HFR (see Figure 1) for our measurements. The V4 channel which is located very close to the fuel element provides the highest thermal neutron flux in the world accounting for  $10^{15} \text{ n/cm}^2/\text{s}$  in its lowest position. Due to its inclination of  $8^\circ 3'$  with respect to the vertical axis it is possible to irradiate samples into either pure thermal neutron fluxes or with a small component of about 10% of epithermal neutrons (neutrons with energy greater than 1 eV). The H9 channel which is used by the Lohengrin spectrometer is located at about 50 cm from the fuel element and offers a neutron flux with about 2% of epithermal neutrons. The advantage of such high neutron fluxes is the possibility to use small mass samples (few  $\mu\text{g}$ ) which are easier to fabricate and manipulate, especially for neutron emitters like  $^{244}\text{Cm}$  or  $\alpha$ -emitters like  $^{238}\text{Pu}$  and the possibility to explore deeper the transmutation chain of the irradiated sample, especially when short-lived isotopes or isomers are formed.

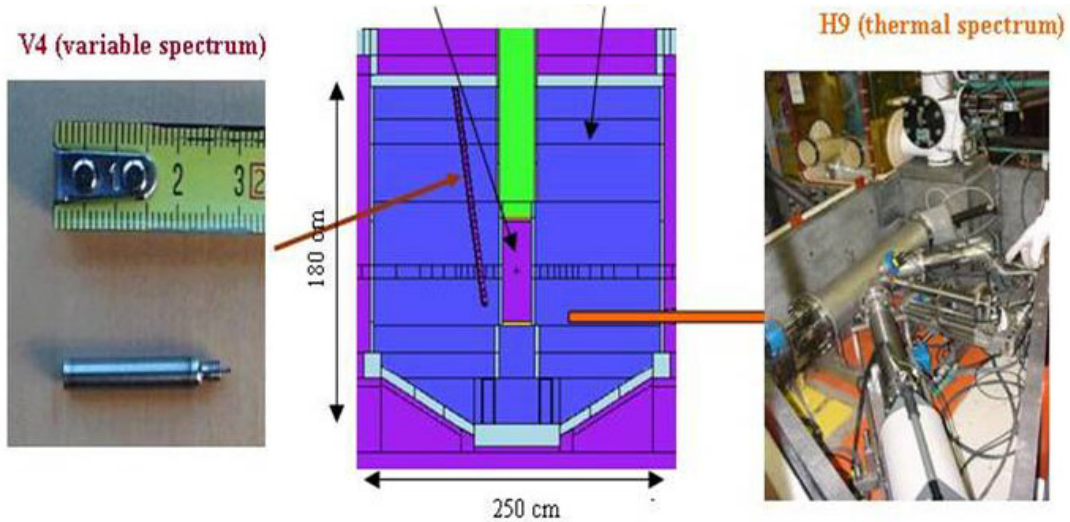


**Figure 1.** The reactor core is sketched with the two irradiation channels used by the Mini-INCA experiments together with the specific instrumentation: the fission chambers in V4 (left) and the  $\alpha$ - and  $\gamma$ -spectroscopy station connected to the Lohengrin target exchanger of H9 (right).

In these in-core irradiation channels the energy of the neutrons cannot be measured so that measurements are integral measurements providing effective or averaged cross sections:

$$\langle \sigma \rangle = \frac{\int_0^{\infty} \sigma(E) \phi(E) dE}{\int_0^{\infty} \phi(E) dE} \quad (1)$$

where  $\sigma(E)$  is the cross section as a function of the neutron energy and  $\phi(E)$  is the neutron energy distribution at the irradiation spot. Instead of using the standard cadmium ratio technique to determine the thermal cross section, we oriented our analysis towards the use of Monte Carlo simulation.

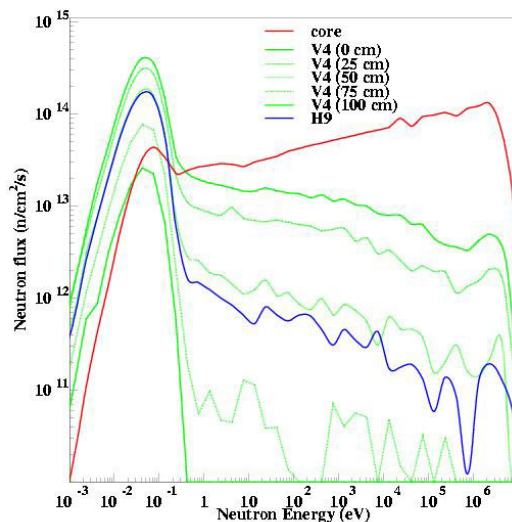


**Figure 2.** Neutron energy spectra simulated with MCNP at different positions of irradiation at the HFR [10].

Then we simulated the reactor core [4] with a precise geometry description of the core including all the beam channels, the hot and the cold sources with the MNCP2.5 code and recently with the TRIPOLI code. Calculations were done for the moderator temperature of 50°C. Results of the calculated neutron fluxes for different positions of irradiation in the V4

and H9 channels are shown on Figure 2. In Table 1. are given the mean neutron flux values measured at different positions of irradiation of the V4 and H9 channels. The calculated thermal contribution is also given showing a strong contribution even in the lowest position of the V4 channel.

For comparison with other experiments we also expressed the neutron flux features in terms of Westcott convention. In this convention the effective cross section is expressed as:

$$\hat{\sigma} = \sigma_0 (g + r \sqrt{\frac{T}{293.53}} s_0) \quad (1)$$

where  $\sigma_0$  is the reaction cross section for 2200 m/s neutrons,  $g$  is the Westcott factor and  $s_0$  is defined by  $s_0 = \frac{2}{\sqrt{\pi}} \cdot \frac{I_0}{\sigma_0}$  and  $I_0 = I_0 - 0.484\sigma_0$  is the reduced resonance integral, i.e., the resonance integral above 0.5 eV after subtracting the  $1/v$  component. From the  $^{59}\text{Co}(n,\gamma)^{60}\text{Co}$  and  $^{197}\text{Au}(n,\gamma)^{198}\text{Au}$  reactions we calculated the epithermal index  $r\sqrt{T/T_0}$  at different irradiation position of the V4 channel (see Table 1).

**Table 1.** Neutron flux characteristics and effective cross sections of the two standard reactions used for the normalisation ( $\sigma_0(^{59}\text{Co})=37.18\pm 0.06$  b,  $\sigma_0(^{235}\text{U})=582.6\pm 1.1$  b [16]).  $\phi$  is the mean neutron flux value as measured in [5] and  $\phi_{th}$  is the calculated thermal component defined with a cut at 1 eV. The  $r\sqrt{323/T_0}$  is the epithermal index defined in Eq.2.

Positions	$\phi$ (n/cm <sup>2</sup> /s)	$\phi_{th}/\phi$	$r\sqrt{323/T_0}$	$^{59}\text{Co}(n,\gamma)^{60}\text{Co}$	$^{235}\text{U}(n,f)$
25 cm	$8 \cdot 10^{14}$	0.898	0.0144	28.33	424.68
50 cm	$7.96 \cdot 10^{14}$	0.966	0.0039	30.74	466.83
75 cm	$4.3 \cdot 10^{14}$	0.997	0.00061	31.66	484.17
100 cm	$5.5 \cdot 10^{13}$	1.000	<0.0006	31.84	487.29
H9	$6 \cdot 10^{14}$	0.981	0.0021	31.10	473.93

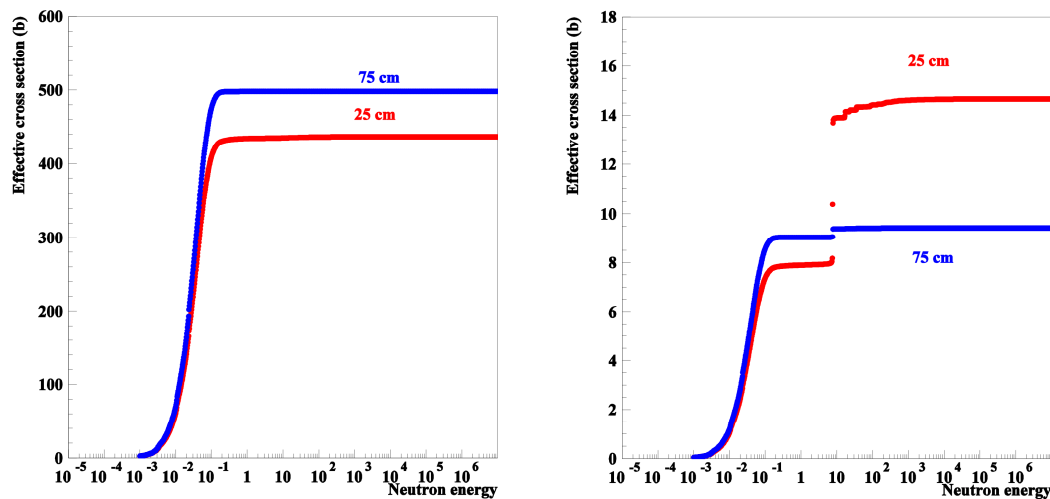


**Figure 3.** Effective cross section as a function of the neutron energy for  $^{235}\text{U}(n,f)$  (left) and  $^{244}\text{Cm}(n,\gamma)^{245}\text{Cm}$  (right) reactions at two irradiation positions in the V4 channel.

We use evaluated resonance parameters to calculate the effective cross section at the irradiation position [6] and to extract the 25.3 meV value ( $\sigma_0$ ) from the calculated ratio  $\sigma_0/\langle\sigma\rangle$ . On Figure 3 is shown the effect of resonances on the effective cross section for two reactions. In the case of the  $^{244}\text{Cm}(n,\gamma)^{245}\text{Cm}$  reaction, about half of the effective cross section measured at 25 cm is due to the huge resonance located at 7.67 eV whereas its effect is much more attenuated when measuring in pure thermal fluxes (75 or 100 cm). Then by measuring the reaction rate in different positions the contribution of such resonance to the total cross section can be estimated. On the other hand, the  $^{235}\text{U}(n,f)$  reaction does not show too much dependence with resonances. Thus for reactions behaving like  $^{235}\text{U}(n,f)$  the correction

procedure does not introduce significant errors especially if resonances are well characterised, whereas for reactions behaving like  $^{244}\text{Cm}(n,\gamma)$  added errors have to be introduced. Nevertheless, the uncertainties on resonance parameters and on neutron flux distribution are fully propagated through the extraction procedure.

### Sample characterisation and analysis

All the samples are characterised prior to their irradiation either by mass spectrometry or/and  $\alpha$ -spectroscopy. After or during irradiation, they are characterized off-line by “standard” activation techniques or on-line by means of dedicated fission chambers. All these techniques have been adapted for high neutron fluxes and minor actinides, the main problem being the counting rate due to the high activity.

Connected to the target exchanger of the Lohengrin spectrometer (H9 channel) we have installed an  $\alpha$  and  $\gamma$  spectroscopy bench [7] which allows a quasi-on-line characterization of the irradiated samples as well as a repeated sequence of irradiation/measurement. The Si- and Ge-detector electronics are able to manage high counting rates (up to 80 kHz for Ge-detector and up to 20 kHz for Si-detector). This set-up is used for  $(n,\gamma)$  cross section measurements but also to measure the life of short-lived isotopes or isomers and the absolute emission probabilities of the  $\gamma$ -rays.

The evolution of actinides can be followed on-line by using dedicated compensated detectors that we will refer as Triple-Deposit Fission-Chambers (TDFC) in the following. They are composed of three microscopic fission-chambers<sup>1</sup> mechanically coupled but electrically isolated and sharing the same gas. They operate in current mode and allow measuring the evolution of the actinide fission current with respect to the evolution of the  $^{235}\text{U}$  fission current. Parasitic currents induced by  $\gamma$ -rays and neutron activation can be subtracted thanks to the third chamber without deposit. Each fission chamber is 2 cm long, has a diameter of 8 mm, and is filled with pure Argon gas. Therefore, these small detectors could be placed one very close to the other, thus reducing systematic errors due to distance. Space charge effects due to high fission rates (high fluxes) are considerably reduced thanks to the thin gap between anode and cathode. Indeed they can be used in high neutron fluxes up to  $8 \cdot 10^{14}$  n/cm<sup>2</sup>/s. Their functioning is detailed in [8] and a description of the different developments can be found in [9].

The mass spectrometry (Thermal Ionisation and Inductive Coupled Plasma Mass Spectrometry) analysis is also used and methods have been developed to measure low mass samples and rare actinides as Protactinium [11] and more recently to measure Berkelium and Californium isotopes.

The data are analysed using a one-group evolution code, named MERCS [10] that we developed. It is based on the ROOT shared libraries and solved numerically the Bateman equations. Its originality lies within its capacity to compute the sensitivity of the experimental observables to the nuclear parameters and properly propagate the uncertainties.

### Recent results

#### Thorium and Protactinium isotopes

The  $^{232}\text{Th}(n,\gamma)^{233}\text{Th}$  and  $^{233}\text{Pa}(n,\gamma)^{234}\text{Pa}$  reaction cross sections were measured by means of a precise mass spectrometry analysis [11]. The analysis was performed few months after 43 days of irradiation in V4. The irradiated sample was a pure 100  $\mu\text{g}$   $^{232}\text{Th}$  sample canned in a quartz container.

**Table 1.** Effective cross sections ( $\langle\sigma\rangle$ ) measured, corrected values to 25.3 meV ( $\sigma_0$ ) and calculated over experimental ratio (C/E) for the main data libraries.

Reactions	$\langle\sigma\rangle$ (b)	$\sigma_0$ (b)	C/E <sub>JEFF3.1</sub>	C/E <sub>ENDF-B7</sub>	C/E <sub>JENDL3.3</sub>
$^{232}\text{Th}(n,\gamma)^{233}\text{Th}$	6.27±0.18	7.34±0.21	1.008±0.029	1.003±0.029	1.008±0.029
$^{233}\text{Pa}(n,\gamma)^{234}\text{Pa}$	34.16±1.54	38.34±1.78	1.085±0.05	1.114±0.05	1.081±0.05
$^{234}\text{U}(n,\gamma)^{235}\text{U}$	87.34±2.75	106.12±3.34	0.94±0.03	0.955±0.03	0.97±0.03
$^{235}\text{U}(n,\gamma)^{236}\text{U}$	79.01±9.05	98±11	1.006±0.11	1.006±0.11	1.006±0.11

<sup>1</sup>Fabricated by Photonis company, France

The irradiation position was chosen to get a significant evolution by multiple captures (i.e. intense flux) and to reduce corrections due to the contribution of resonances (i.e. thermal flux). The neutron fluence, over which thorium evolved, was measured using an Al-0.1%<sup>59</sup>Co monitor. Experimental uranium and thorium isotopic ratios were fitted using the MERCS code with the effective cross section values listed in Table 2. as free parameters. The fit procedure was repeated several times. At each step, all other nuclear parameters (included neutron flux for which we have used the experimental value) were randomly sampled within their Gaussian error distribution. Moreover, every isotopic ratio was chosen to be mainly sensitive to one cross section. By this means, the covariance matrix is closed to a diagonal one and calculated errors could be considered independent. Resulting cross sections are shown in Table 2.

### Neptunium and Plutonium isotopes

The <sup>237</sup>Np(n, γ)<sup>238</sup>Np cross section was measured by α and γ-spectroscopy in the H9 channel. (13.52±0.14) μg of <sup>237</sup>Np were electrodeposited on a Ti backing and irradiated for 2.733 hours in the H9 channel [12]. In this experiment we also measured the absolute γ-ray emission probabilities for the <sup>238</sup>Np β-decay. The <sup>238</sup>Np(n,f) and <sup>238</sup>Pu(n, γ)<sup>239</sup>Pu cross sections were measured in the V4 channel using two TDFCs [13]: one containing (42±1.3) μg of pure <sup>237</sup>Np and the other one containing (42.6±1.6) μg of <sup>238</sup>Pu with 4.978% of <sup>239</sup>Pu. The two detectors were containing also (2.64±0.01) μg and (4.48±0.01) μg of <sup>235</sup>U, respectively. The TDFCs were irradiated separately during one cycle. The nuclear parameters were fitted to the measured currents using the MERCS code. The obtained cross sections in all these experiments are shown in Table 3. The <sup>238</sup>Np and <sup>238</sup>Pu is still in analysis so that the values are still preliminary.

**Table 3.** Effective cross sections (<σ>) measured, corrected values to 25.3 meV (σ<sub>0</sub>) and calculated over experimental ratio (C/E) for the main data libraries. (\*) is for preliminary results.

Reactions	<σ> (b)	σ <sub>0</sub> (b)	C/E <sub>JEFF3.1</sub>	C/E <sub>ENDF-B7</sub>	C/E <sub>JENDL3-3</sub>
<sup>237</sup> Np(n, γ) <sup>238</sup> Np	151±4	182±4.5	0.99±0.03	0.89±0.03	0.89±0.03
<sup>238</sup> Np(n,f)	1611±100*	2050±110*	0.925±0.06	0.955±0.06	0.955±0.06
<sup>238</sup> Pu(n, γ) <sup>239</sup> Pu	411±20*	514±21*	1.05±0.04	1.09±0.04	1.05±0.04

### Americium isotopes

The americium transmutation chain was studied in detail using post-irradiation mass-spectrometry analysis for <sup>241</sup>Am(n, γ)<sup>242m-gs</sup>Am, <sup>242m</sup>Am(n, γ)<sup>243</sup>Am and <sup>242</sup>Cm(n, γ)<sup>243</sup>Cm cross sections, and using fission chambers measurement for <sup>242gs</sup>Am(n,f)<sup>243</sup>Am and <sup>242m</sup>Am(n,f)<sup>243</sup>Am [15]. These cross sections were obtained in a pure Maxwellian neutron flux. They complement previous measurements done on <sup>241</sup>Am [14] and <sup>243</sup>Am [7] capture cross sections. The obtained effective and 25.3 meV cross sections are shown in Table 4. The most striking discrepancy between our results and recent evaluated data libraries concerns the <sup>242</sup>Cm(n, γ)<sup>243</sup>Cm cross section which is underestimated by about 12% in the libraries. For other reactions, discrepancies are below 10%.

**Table 4.** Effective cross sections (<σ>) measured, corrected values to 25.3 meV (σ<sub>0</sub>) and calculated over experimental ratio (C/E) for the main data libraries. (\*) is for preliminary results.

Reactions	<σ> (b)	σ <sub>0</sub> (b)	C/E <sub>JEFF3.1</sub>	C/E <sub>ENDF-B7</sub>	C/E <sub>JENDL3-3</sub>
<sup>241</sup> Am(n, γ) <sup>242</sup> Am	609±20	700±23	0.93±0.03	0.887±0.03	0.913±0.03
Branching ratio		0.8947± 0.0038			
<sup>242m</sup> Am(n, γ) <sup>243</sup> Am	1074±108	1152±112*	1.07±0.1	1.07±0.1	1.07±0.1
<sup>242gs</sup> Am(n,f)	2224±215*	2472±281*		0.85±0.085	
<sup>242m</sup> Am(n,f)	6527±625*	6856±656*	0.936±0.09	0.936±0.09	0.933±0.09
<sup>242</sup> Cm(n, γ) <sup>243</sup> Cm	15.82±1.2*	19.1±1.5*	0.835±0.066	0.887±0.066	0.832±0.066

### Curium, Berkelium and Californium isotopes

The <sup>244</sup>Cm(n, γ) and <sup>245</sup>Cm(n,f) were measured very recently by means of TDFC in the V4 channel. A (39.46 ±0.4) μg mass of curium containing 66.9% of <sup>244</sup>Cm, 3.8% of <sup>245</sup>Cm and 23.6% of <sup>240</sup>Pu was irradiated. The isotopic concentration was determined before irradiation by mass spectrometry with a precision better than 1%. Measured currents were then fitted with the MERCS code taking into account the evolution of <sup>240</sup>Pu and propagating the

associated errors.  $^{240}\text{Pu}$  isotope is the main responsible for the bump in the curium fission current between 10 and 30 days. Preliminary results are given in Table 5.

The  $^{248}\text{Cm}(n,\gamma)^{249}\text{Cm}$ ,  $^{249}\text{Bk}(n,\gamma)^{250}\text{Bk}$  and  $^{249}\text{Cf}(n,\gamma)^{250}\text{Cf}$  have been measured into two different experiments. One of these experiments is reported in [15] but the analysis is still in progress.

**Table 5.** Effective cross sections ( $\langle\sigma\rangle$ ) measured, corrected values to 25.3 meV ( $\sigma_0$ ) and calculated over experimental ratio (C/E) for the main data libraries. (\*) is for preliminary results.

Reactions	$\langle\sigma\rangle$ (b)	$\sigma_0$ (b)	C/E <sub>JEFF3.1</sub>	C/E <sub>ENDF-B7</sub>	C/E <sub>JENDL3-3</sub>
$^{244}\text{Cm}(n,\gamma)^{245}\text{Cm}$	19.11±2.67*	15.81±3*	0.74±0.1	0.96±0.13	0.96±0.13
$^{245}\text{Cm}(n,f)$	1352±23	1979±65*	1.086±0.019	1.086±0.019	1.083±0.019
$^{249}\text{Cf}(n,\gamma)^{250}\text{Cf}$	309±8*	384±10*	1.184±0.03	1.165±0.03	1.18±0.03

## Conclusions

Within the Mini-INCA project, we took benefit of the high fluxes of the ILL reactor to provide new accurate data on slow neutron-induced reaction cross sections for minor actinides. The set-up installed at the ILL High Flux Reactor is proven to be well suited for such studies and allow reducing also uncertainties on the decay parameters for rare short-lived isotopes. The capture and fission cross sections we have measured generally show good agreements with the most recent measurements. However, large discrepancies with evaluated data libraries have been observed in few cases. The analysis of the end of the Curium chain is in progress.

## Acknowledgements

Authors are grateful to ILL technicians for their great help in the preparation of experiments. This work was partially supported by the GDR GEDEPEON (France).

## References

- [1] G. Aliberti et al., Ann. Nucl. Energy **33**, 700 (2006).
- [2] O. Bringer et al., Annals of nuclear energy 35 (2008) 1535.
- [3] G. Fioni et al., J. Nucl. Science and Technol., Supplement, vol.2, issue 2, p.876 (2002).
- [4] D. Ridikas et al., *Proceedings of the 6<sup>th</sup> OECD/NEA Information Exchange Meeting on Actinide and Fission Partitioning and Transmutation*, 11-13 December 2000, Madrid, Spain.
- [5] M. Fadil, Ph.D. thesis, INP Grenoble, 2003 (in French).
- [6] A. Letourneau et al., CEA/DSM/SPhN-03-243 report, 2003 (unpublished).
- [7] F. Marie et al., Nucl. Inst. and Meth. **A556**, 547 (2006).
- [8] S. Chabod et al., Nucl. Inst. and Meth. **A566**, 633 (2006).
- [9] A. Letourneau et al., Proceeding of ANIMMA 2009, IEEE Trans. Nucl. Science, in press.
- [10] see <http://www-dapnia.cea.fr/Sphn/MNM/Modelisation/>
- [11] O. Bringer et al., Nucl. Instr. and Meth **A59** (2008) 510-516
- [12] A. Letourneau et al., submitted to Applied Rad. and Isotopes (2009).
- [13] A. Letourneau et al., to be submitted to Nucl. Phys. A (2009).
- [14] G. Fioni et al., Nucl. Phys. **A693**, 546 (2001).
- [15] O. Bringer, Ph. D. thesis, INP Grenoble, 2007.
- [16] S.F. Mughabghab, Atlas of neutron resonances, 5<sup>th</sup> Ed., Elsevier.

# Measurements of Thermal-Neutron Capture Cross-Sections for Radioactive Nuclides

Shoji NAKAMURA

JAEA, 2-4 Shirane, Shirakata, Tokai-mura, Naka-gun, Ibaraki, 319-1195, JAPAN  
[nakamura.shoji@jaea.go.jp](mailto:nakamura.shoji@jaea.go.jp)

**Abstract:** The social acceptability of nuclear power reactors is related to the waste management of long-lived fission products (FP's) and minor actinides (MA's) existing in spent nuclear fuels. The FP's (ex., Cs-137, Sr-90, Tc-99, I-129, Cs-135, Pd-107 and so on) and MA's (ex., Np-237, Am-241, Am-243) are important in the nuclear waste management, because the presence of these nuclides induces long-term radiotoxicity because of their extremely long half-lives. The transmutation is one of the solutions to reduce the radiotoxicity of nuclear wastes. In the transmutation study of FP's and MA's, the accurate data of neutron capture cross-sections are necessary to evaluate reaction rates. However, there are discrepancies among the reported data for the thermal-neutron capture cross-sections for those nuclides. The discrepancies reach to 10-20%. Therefore, our concern was focused to re-measure the cross-sections of those FP's and MA's. This paper describes JAEA's activities for the cross-section measurements of FP's and MA's by an activation method and a prompt gamma-ray spectroscopic method.

## Cross-section measurements by activation method

### Motivation

Associated with a social acceptability of nuclear power reactors, it would be desired to solve the problems of nuclear waste managements of FP's and MA's existing in spent nuclear fuels. In nuclear waste management, the major 29 FP's shown in **Table 1** are important nuclides as the objectives for transmutation.

**Table 1.** Major 29 fission product nuclides for the nuclear waste management

Nuclide	Half-Life (yr)	Nuclide	Half-Life(yr)	Nuclide	Half-Life(yr)
I-129	$1.57 \cdot 10^7$	Ag-108m	418	Eu-155	4.7611
Pd-107	$6.5 \cdot 10^6$	Sm-151	90	Rh-102	2.9
Cs-135	$2.3 \cdot 10^6$	Sn-121m	55	Sb-125	2.7582
Zr-93	$1.53 \cdot 10^6$	Cs-137	30.07	Pm-147	2.6234
Tc-99	$2.1 \cdot 10^5$	Sr-90	28.78	Cs-134	2.062
Sn-126	$1.0 \cdot 10^5$	Cd-113m	14.1	Tm-171	1.92
Se-79	$6.5 \cdot 10^4$	Eu-152	13.542	Cd-109	1.270
Nb-94	$2.03 \cdot 10^4$	Nb-93m	16.13	Ru-106	1.007
Ho-166m	$1.2 \cdot 10^3$	Kr-85	10.756	( C-14)	5730
Tb-158	$1.8 \cdot 10^2$	Eu-154	8.593		
		Pm-146	5.53		

For the study of transmutation by using reactor neutrons, the accurate data are needed on neutron capture cross-sections ( $\sigma_0$ ) and resonance integrals ( $I_0$ ) in order to estimate the

accurate reaction rates of those FP's. However, there are few cross-section data on those FP's. If any, most of the data have large errors. By using the recently developed measuring equipments and the accurate gamma-ray emission probability data, one could obtain more accurate cross-section data than that measured previously. Accordingly, my group had started to measure the cross-sections of FP's to obtain the accurate ones. In the beginning five nuclides, Cs-137 [1], Sr-90 [2], Tc-99 [3], I-129 [4] and Cs-135 [5], were chosen from the nuclides listed in Table 1 because of their large fission yields and long half-lives, and then the cross-sections of these nuclides were measured by the activation and gamma-ray spectroscopic methods. Nuclear wastes sometimes contain a large amount of stable nuclei having the same atomic number as that of long-lived FP. These stable nuclei absorb thermal neutrons during the neutron irradiation of the nuclear wastes, and affect the neutron economics; the reaction rate of the target nuclei is reduced. Moreover, some of stable nuclei breed more radioactive nuclei by the neutron capture process. In this point, it is also necessary to pay attention to these influences caused by stable nuclei involved in the FP's. The cross-sections of the stable nuclei, such as I-127 [6] and Cs-133 [7], were also measured. Moreover, MA's (ex., Np-237 [8,9], Am-241 [10], Am-243 [11], etc.) are of importance in nuclear waste managements, because the presence of these nuclides induces long-term radiotoxicity on account of their extremely long half-lives. Thus this work was aimed to measure the thermal-neutron capture cross-sections for radioactive FP's and MA's.

### Brief outline of analysis

Since the details of Westcott's convention [12] that we used to determine the cross sections and neutron fluxes were described elsewhere [1-7], here we present only a brief outline of the analysis. Equations based on Westcott's convention can be rewritten by using simplified flux notation as follows:

$$R/\sigma_0 = \phi_1 + \phi_2 s_0, \quad (1)$$

for irradiation without a Cd or Gd shield capsule,

$$R'/\sigma_0 = \phi_1' + \phi_2' s_0, \quad (2)$$

for irradiation with a Cd or Gd shield capsule. Here, the R (or R') is the reaction rate and  $\sigma_0$  the thermal-neutron (2,200 m/s neutron) capture cross-section;  $\phi_1$  and  $\phi_1'$  are neutron flux components in the thermal energy region, and  $\phi_2$  and  $\phi_2'$  are those in the epithermal energy region. The  $s_0$  is the parameter defined by

$$s_0 = \frac{2}{\sqrt{\pi}} \frac{I_0'}{\sigma_0}, \quad (3)$$

where  $I_0'$  is the reduced resonance integral, i.e. the resonance integral after subtracting the  $1/v$  components. The resonance integral  $I_0$  is calculated as follows:

$$I_0 = I_0' + 0.45\sigma_0, \quad (4)$$

where  $0.45\sigma_0$  is the  $1/v$  contribution given by assuming the Cd cut-off energy to be 0.5eV [13]. Eqs.(1) and (2) give the relation,

$$s_0 = -\frac{\phi_1 - \phi_1'(R/R')}{\phi_2 - \phi_2'(R/R')}, \quad (5)$$

so that the value of  $s_0$  is obtained from R/R' value of each irradiated target. The  $\sigma_0$  is derived by substituting the  $s_0$  into Eq.(1), and then the values of  $I_0'$  and  $I_0$  are calculated from Eqs.(3) and (4).

## Results

The cross-sections were determined on the basis of the Westcott's convention and simple flux notations. The results for MA' are listed in Table 2, and for FP's in Table 3 together with previously reported values.

**Table 2.** Results of  $\sigma_0$  and  $I_0$  for MA nuclides

Nuclide	Half-Life [14]	Previous Data (Author, Year)	JAEA Data
Np-237	$2.14 \cdot 10^6$ yr	$\sigma_0=158 \pm 3$ b $I_0=652 \pm 24$ b (Kobayashi 1994) [15]	$\sigma_0=141.7 \pm 5.4$ b $I_0=862 \pm 51$ b (2003) [8] $\sigma_0=169 \pm 6$ b (2006) [9]
Np-238	2.1 d	No Data	$\sigma_{\text{eff}}=479 \pm 24$ b (2004) [18]
Am-241	432 yr	$\sigma_{0g}=768 \pm 58$ b $I_{0g}=1694 \pm 14$ b (Shinohara 1997) [16]	$\sigma_{0g}=628 \pm 22$ b $I_{0g}=3.5 \pm 2.5$ kb (2007) [10]
Am-243	7370 yr	$\sigma_0=80$ b, $\sigma_{0g}=4.3$ $\sigma_{0m+g}=84.3$ b (Ice 1966) [17]	$\sigma_{\text{eff}}=174.0 \pm 5.3$ b (2006) [11]

**Table 3.** Results of  $\sigma_0$  and  $I_0$  for FP nuclides

Nuclide	Half-Life	Previous Data (Author, Year)	JAEA Data
Cs-137	30 yr	$\sigma_{\text{eff}}=0.11 \pm 0.03$ b (Stupegia 1960) [19]	$\sigma_0=0.25 \pm 0.02$ b $I_0=0.36 \pm 0.07$ b (1990, 1993, 2000) [20-22]
Sr-90	29 yr	$\sigma_{\text{eff}}=0.8 \pm 0.5$ b (Zeisel 1966) [23]	$\sigma_0=15.3 \pm 1.3/4.2$ mb $I_0 < 0.16$ b (1994) [24] $\sigma_0=10.1 \pm 1.3$ mb $I_0=104 \pm 16$ mb (2001) [25]
Tc-99	$2.1 \cdot 10^4$ yr	$\sigma_0=20 \pm 2$ b $I_0=186 \pm 16$ b (Lucas 1977) [26]	$\sigma_0=22.9 \pm 1.3$ b $I_0=398 \pm 38$ b (1995) [27]
I-129	$1.6 \cdot 10^7$ yr	$\sigma_0=27 \pm 2$ b $I_0=36 \pm 4$ b (Eastwood 1958) [28]	$\sigma_0=30.3 \pm 1.2$ b $I_0=33.8 \pm 1.4$ b (1996) [29]
I-127	Stable	$\sigma_0=4.7 \pm 0.2$ b $I_0=109 \pm 5$ b (Friedmann 1983) [30]	$\sigma_0=6.40 \pm 0.29$ b $I_0=162 \pm 8$ b (1999) [31]

Cs-135	$3 \cdot 10^6$ yr	$\sigma_0 = 8.7 \pm 0.5$ b $I_0 = 61.7 \pm 2.3$ b (Baerg 1958) [32]	$\sigma_0 = 8.3 \pm 0.3$ b $I_0 = 38.1 \pm 2.6$ b (1997) [33]
Cs-134	2 yr	$\sigma_{\text{eff}} = 134 \pm 12$ b (Bayly 1958) [34]	$\sigma_{\text{eff}} = 141 \pm 9$ b (1999) [35]
Cs-133	Stable	$\sigma_0 = 30.4 \pm 0.8$ b $I_0 = 461 \pm 25$ b (Baerg 1960) [36]	$\sigma_0 = 29.0 \pm 1.0$ b $I_0 = 298 \pm 16$ b (1999) [37]
Ho-166m	$1.2 \cdot 10^3$ yr	$\sigma_0 = 9140 \pm 650$ b $I_0 = 1140 \pm 90$ b (Masyanov 1993) [38]	$\sigma_{\text{eff}} = 3 \pm 1$ kb (2000) [39] $\sigma_0 = 3.11 \pm 0.82$ kb $I_0 = 10.0 \pm 2.7$ kb (2002) [40]

### Cross-section measurements by prompt gamma-ray method

#### Motivation

The long half-life ( $6.5 \cdot 10^6$  yr [14]) and fission yield (3% for Pu-239) of Pd-107 make it an important FP in studies of nuclear transmutation. In the case of Pd-107, no direct measurement of the thermal-neutron capture cross-section ( $\sigma_0$ ) has been reported. Because the Pd-107( $n, \gamma$ ) reaction leads to the stable nuclide Pd-108, it is impossible to measure this cross section using an activation method. The technique of measuring intensities of prompt gamma-rays following thermal-neutron capture reaction can be employed to determine  $\sigma_0$ . Therefore, this work was undertaken to obtain  $\sigma_0$  for the Pd-107 ( $n, \gamma$ ) Pd-108 reaction by prompt gamma-ray spectroscopy.

#### Brief Outline of Experiment and Analysis

The experiments were performed using the internal target facility at the 8-MW Los Alamos Omega West Reactor. The target position was at the center of the graphite thermal column, of which thermal neutron flux was about  $6 \cdot 10^{11}$  n/cm<sup>2</sup> and the Cd(In) ratio was about 2000. The gamma-rays emitted in the ( $n, \gamma$ ) reaction were measured with a 26-cm<sup>3</sup> coaxial Ge(Li) detector positioned inside a 20 cm-outer-diameter  $\times$  30 cm-long NaI(Tl) annulus. The Pd sample weighed  $201.4 \pm 0.1$  mg and contained  $15.54 \pm 0.05$  % of Pd-107. A  $100.0 \pm 0.1$  mg sample of (CH<sub>2</sub>)<sub>n</sub> was placed at the target position together with the Pd sample in the thermal column. The capture cross-sections obtained in this work are determined on the basis of standard cross-section of  $332.6 \pm 0.7$  mb for Hydrogen. **Figure 1** shows an example of the prompt gamma-ray spectrum for the combined Pd and (CH<sub>2</sub>)<sub>n</sub> samples. Prominent gamma-rays due to the Pd-105,107,108( $n, \gamma$ ) reactions were observed. The gamma-rays feeding the ground states were identified using the known level information. Summation of their intensities yields a lower limit for  $\sigma_0$ , *i.e.*,  $\sum I\gamma(1+\alpha) = \sigma_0$ . Here, the quantity  $\alpha$  is an internal conversion coefficient. To test the effectiveness of the analysis method,  $\sigma_0$  also was determined for Pd-105. Because  $\sigma_0$  for <sup>105</sup>Pd-105 is large ( $20.0 \pm 0.3$  b), and because this isotope made up a large fraction of the Pd sample, prompt gamma-rays due to the Pd-105( $n, \gamma$ )Pd-106 reaction were easily observed as shown in Fig.1.

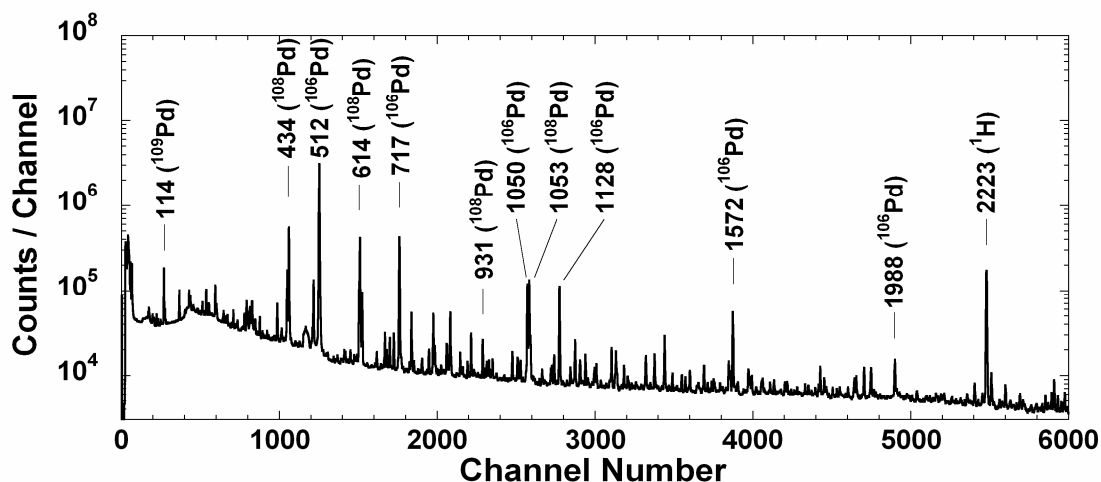


**Figure 1.** Prompt gamma-ray spectrum from thermal-neutron capture by the Pd-107

### Results

The present results are tabulated in **Table 4** together with the previous measurement and evaluations. The intensities of prompt gamma-ray transitions feeding the ground state of Pd-108 were summed to determine a lower limit of  $9.16 \pm 0.27$  b for thermal neutron capture cross-section. The present result is about five times larger than current evaluations.

**Table 4.** Experimental and evaluated data for Pd-107 and Pd-105 cross-sections

References		$\sigma_0$ (b) for Pd-107	$\sigma_0$ (b) for Pd-105
Mughabghab <i>et al.</i> [41]	1981	$1.8 \pm 0.2$	$21.0 \pm 1.5$
Table of Isotopes 8ed. [14]	1998	$1.8 \pm 0.2$	$20.0 \pm 3.0$
JENDL-3.3 [42]	2002	2.0071	20.25
Firestone <i>et al.</i> [43]	2005	—	$21.1 \pm 1.5$ *
<b>Present Result</b> [44]	2007	<b><math>9.16 \pm 0.27</math>*</b>	<b><math>19.1 \pm 0.5</math>*</b>

\* Prompt gamma-ray analysis

### Acknowledgements

The authors wish to acknowledge their indebtedness to the crew of the Rikkyo Research Reactor, Kyoto University Reactor (KUR) and JRR-3 reactor at JAEA for their cooperation.

### References

- [1] T.Sekine *et al.*: *J. Nucl. Sci. Technol.*, 30, No.11, 1099 (1993).
- [2] H.Harada *et al.*: *J. Nucl. Sci. Technol.*, 31, No.3, 173 (1994).
- [3] H.Harada *et al.*: *J. Nucl. Sci. Technol.*, 32, No.5, 395 (1995).
- [4] S.Nakamura *et al.*: *J. Nucl. Sci. Technol.*, 33, No.4, 283 (1996).
- [5] T.Katoh *et al.*: *J. Nucl. Sci. Technol.*, 34, No.5, 431 (1997).
- [6] T.Katoh *et al.*: *J. Nucl. Sci. Technol.*, 36, No.3, 223 (1999).
- [7] S.Nakamura *et al.*: *J. Nucl. Sci. Technol.*, 36, No.10, 847 (1999).
- [8] T.Katoh *et al.*: *J. Nucl. Sci. Technol.*, 40, No.8, 559(2003).
- [9] H.Harada *et al.*: *J. Nucl. Sci. Technol.*, 43, No.11, 1289(2006).
- [10] S.Nakamura *et al.*: *J. Nucl. Sci. Technol.*, 44, No.12, 1500 (2007).
- [11] M.Ohta *et al.*: *J. Nucl. Sci. Technol.*, 43, No.12, 1441 (2006).
- [12] C.H.Westcott *et al.*: “*Proc. 2nd Int. Conf. Peaceful Uses of Atomic Energy, Geneva*”, United Nations, New York, 16, 70(1958).
- [13] K.H.Beckurts and K.Wirtz: “*Neutron Physics*”, Springer-Verlang, New York, (1964).
- [14] R.B.Firestone, V.S.Shirley, *Table of Isotopes, 8th Ed.*, John Wiley & Sons, New York (1996).

- [15] K.Kobayashi *et al.* : *J. Nucl. Sci. Technol.*, 31, No.12, 1239(1994).
- [16] N.Shinohara *et al.* : *J. Nucl. Sci. Technol.*, 34, No.7, 613(1997).
- [17] C.H.Ice : *Du Pont, Savannah River Reports*, 66, 69(1966).
- [18] H.Harada *et al.* : *J. Nucl. Sci. Technol.*, 41, No.1, 1(2004).
- [19] D.C.Stupegia: *J. Nucl. Energy*, A12, 16 (1960).
- [20] H.Harada *et al.* : *J. Nucl. Sci. Technol.*, 27, No.6, 577(1990).
- [21] T.Sekine *et al.* : *J. Nucl. Sci. Technol.*, 30, No.11, 1099(1993).
- [22] H.WADA *et al.* : *J. Nucl. Sci. Technol.*, 37, No.10, 827(2000).
- [23] G.Zeisel: *Acta. Phys. Austr.*, 23, 5223 (1966).
- [24] H.Harada *et al.* : *J. Nucl. Sci. Technol.*, 31, No.3, 173(1994).
- [25] S.Nakamura *et al.* : *J. Nucl. Sci. Technol.*, 38, No.12, 1029(2001).
- [26] M.Lucas *et al.*: *IAEA-TC-119/14*, 407 (1977).
- [27] H.Harada *et al.* : *J. Nucl. Sci. Technol.*, 32, No.5, 395(1995).
- [28] Eastwood, T.A. *et al.*: "*Proc. 2nd Int. Conf. Peaceful Uses of Atomic Energy, Geneva*", United Nations, New York, 16, 54 (1958).
- [29] S.Nakamura *et al.*: *J. Nucl. Sci. Technol.*, 33, No.4, 283(1996).
- [30] L.Friedmann *et al.*: *Radiochemica Acta*, 33, 182 (1983).
- [31] S.Nakamura *et al.*: *J. Nucl. Sci. Technol.*, 36, No.3, 223(1999).
- [32] A.P.Baerg *et al.* : *Can. J. Phys.*, 36, 863, (1958).
- [33] T.Katoh *et al.* : *J. Nucl. Sci. Technol.*, 34, No.5, 431(1997).
- [34] J.G.Bayly *et al.* : *Inorg. Nucl. Chem.*, 5, 259(1958).
- [35] T.Katoh *et al.* : *J. Nucl. Sci. Technol.*, 36, No.8, 635(1999).
- [36] A.P.Baerg *et al.* : *Can. J. Chem.*, 38, 2528, (1960).
- [37] S.Nakamura *et al.* : *J. Nucl. Sci. Technol.*, 36, No.10, 847(1999).
- [38] S.M.Masyanov *et al.* : *At. Energy*, 73, 673(1993).
- [39] H.Harada *et al.*, *J. Nucl. Sci. Technol.*, 37, No.9, 821(2000).
- [40] T.Katoh *et al.* : *J. Nucl. Sci. Technol.*, 39, No.7, 705(2002).
- [41] S.F.Mughabghab *et al.*: *Neutron Cross Section*, Vol.1, Academic Press, NewYork(1981).
- [42] K.Shibata *et al.*: *J. Nucl. Sci. Technol.*, 39, 1125(2002).
- [43] R.B.Firestone *et al.* : *Proc. 12th Int. Symp. Capture Gamma-Ray Spectroscopy and Related Topics*, 389(2006).
- [44] S.Nakamura *et al.*: *J. Nucl. Sci. Technol.*, 44, No.2, 103(2007).

## Photon strength in heavy nuclei in correlation to the number of valence nucleons

*Eckart Grosse<sup>1,2)</sup>, Arnd R. Junghans<sup>2)</sup>,  
and the transmutation research team of FZD*

- 1) Institute of Radiation Physics, Forschungszentrum Dresden -Rossendorf, 01314 Dresden,  
2) Institute of Nuclear and Particle Physics, Technische Universität Dresden, 01069 Dresden,  
Germany  
[e.grosse@fzd.de](mailto:e.grosse@fzd.de)

### Introduction

A nuclear process of special importance for projects aiming for the transmutation of radioactive waste is the radiative neutron capture. It has a very large cross section at low energies, but it also competes especially to fission also at higher energies. Respective calculations are performed on the basis of the Hauser-Feshbach formalism for compound nuclear processes. For the incoming neutron channel information is needed about the nuclear mean field acting as optical potential for the free neutron and as origin of the neutron binding in the capture. The other important ingredient for these calculations is the photon strength function governing the  $\gamma$ -decay to low lying final states down from the capturing resonances in the continuum. Here neutron reemission and fission may compete thus reducing the capture cross section. As far as the relevant spins allow, this decay is mainly of electric dipole type, and a parameterization for the dipole strength in heavy nuclei, developed recently [1], will be discussed in relation to nuclear spectroscopy data.

### Broken spherical and axial symmetry

Non-spherical nuclei are the predominant standard and many different theoretical schemes have been proposed to predict details of their shapes – with not always conforming results. Attempts to obtain a reasonable knowledge on non-spherical or even tri-axial nuclei from just counting the number of valence nucleons outside the magic shells have been rather promising, as will be shown below. In contrast, calculations starting from the nucleon-nucleon force to arrive at a microscopic theory for the macroscopic nuclear shape do not arrive at consistent results. Calculations with the ETFSI method [2] (Thomas-Fermi plus Strutinsky integral) indicate a widespread (more than 30% ) occurrence of triaxiality whereas the droplet model (FRDM, [3]) predicts only a few % of the heavy nuclei to be triaxially deformed; among the even Mo-isotopes discussed in this work these are <sup>96-100</sup>Mo. As shown in Fig. 1, Nilsson-Strutinski calculations performed at FZD [4] on the deformation dependence of ground state energies show triaxiality only for <sup>98</sup>Mo and <sup>100</sup>Mo.

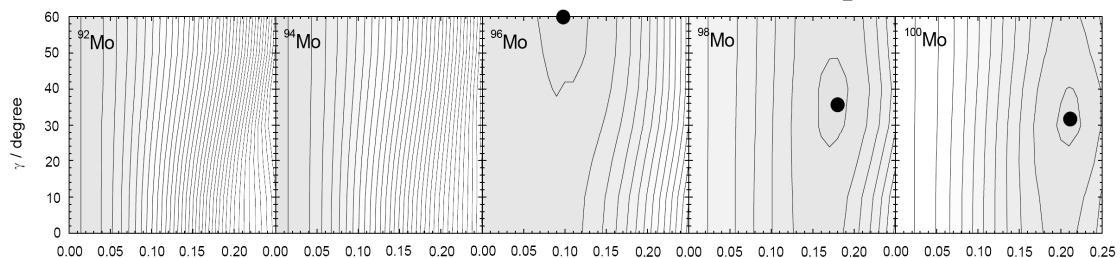


**Figure 1.** Calculated ground state energies of <sup>92-100</sup>Mo in dependence of deformation  $\beta$  and  $\gamma$ .

A systematic investigation [5] employing various experimental observables of relevance for the triaxial deformation of heavy nuclei shows an interesting correlation between the quadrupole deformation  $\beta$  and the triaxiality  $\gamma$ ; it comes to a slightly different conclusion, with

<sup>94,96</sup>Mo also being triaxial with  $\gamma$  near  $30^\circ$ . As will be discussed below, the triaxiality influences the form of the peak of the GDR, the isovector giant resonance: It plays a non-negligible role when the shape is regarded with respect to the extraction of information on the GDR spreading width.

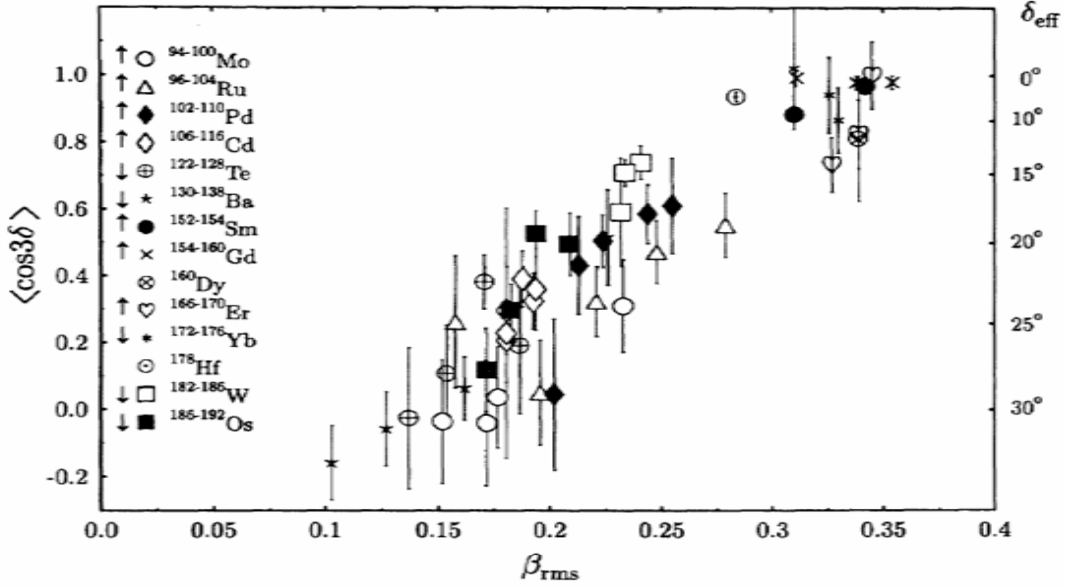


**Figure 2.** Result of a systematic study [5] of experimental observables showing a correlation between the triaxiality  $\gamma_{rms} = \delta_{eff}$  and the quadrupolar deformation  $\beta_{rms}$  for heavy nuclei.

Since this systematic uses experimental information the results have to be considered as root mean square (rms) values [6], *i.e.* zero point fluctuations are included. The extracted values for  $\beta$  are in satisfactory agreement to the tables of Raman et al. [7], where the E2-transition strength from the ground state to the first  $2^+$ -state is used to derive an ‘experimental’ deformation  $\beta$ . We use these results for our investigation of the influence of nuclear non-sphericity on the GDR for Mo and Sm-isotopes, for which data were recently obtained at our superconducting electron linac ELBE [8-10].

### Rotation invariants and root mean square shape parameters

We thus start from rotation invariants [6] and not from model dependent deformation parameters. Rotation invariant electromagnetic quantities (*e.g.* rms quadrupole moment and triaxiality) are observables, and they have been extracted from measurements for more than 70 heavy nuclei. Information about the GDR oscillation frequencies along the three orthogonal nuclear axes can be directly deduced from these by only assuming nuclear incompressibility, implying identical distributions of mass and charge, *i.e.*, neutrons and protons [6].

The procedure [1] used here to determine the GDR energies and widths before calculating the photon strength functions is valid for a static triaxial deformation. A fully adiabatic coupling of the fast GDR motion to the low-frequency collective excitations, responsible for the dynamics of the ground state deformation, may cause differences. Often these are assumed to be only small, and the root mean squares (rms) of the deformation parameters are treated as static values. To implement a less simplified coupling of the GDR to the quadrupole dynamics of the nuclear body, it is interesting to study the effect of the variance of the deformation parameters. It has been proposed recently [11], how a description of such dynamics can be derived within the interacting boson model (IBA). This procedure allows introducing an instantaneous shape sampling (ISS), and this requires to calculate the three GDR components at each sampling point and to form the time averaged cross section. To quantify the change introduced by the ISS this average has to be compared to the cross section obtained in a ‘single shot’ with the average deformations from the ISS. Such a comparison was performed using the time dependent shape parameters, and the corresponding result is shown in Fig 3. ISS causes some change near the GDR peak for the

triaxial  $^{100}\text{Mo}$  but its impact in the region of photon scattering data [8, 10] is of minor importance. An explicit variation of the GDR width with  $E_\gamma$ , also depicted in Fig. 3, leads to a severe disagreement to the low energy data [1, 10].

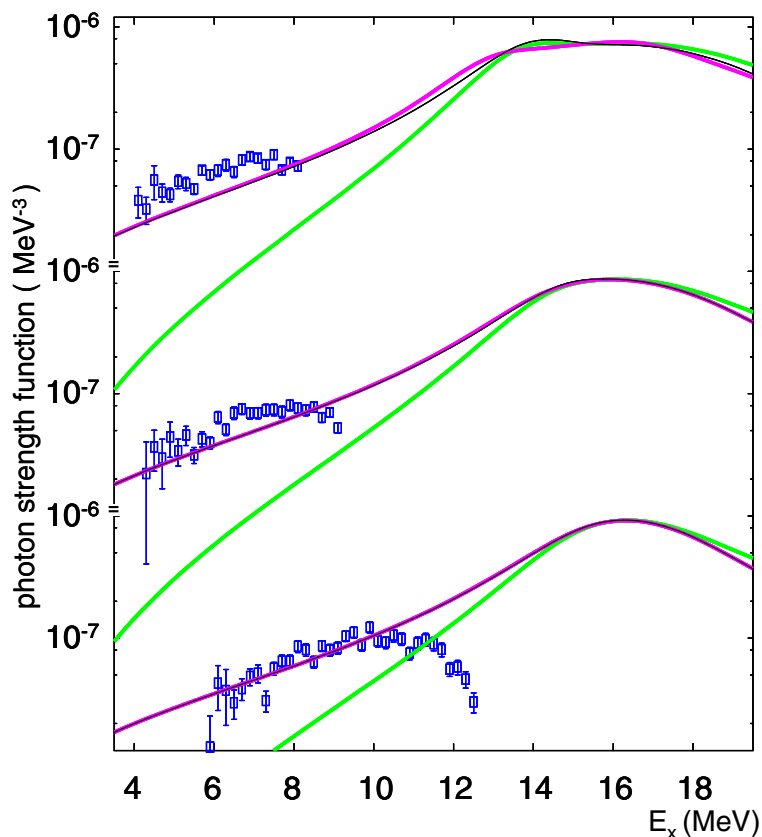


**Figure 3.** Dipole strength functions  $f_1$  for  $^{92,96,100}\text{Mo}$  calculated from the parameterization for the GDR. An agreement with  $f_1$  as determined from ELBE data [10] (blue squares with error bars) is only found for the curves calculated without photon energy dependence. Thick pink line: Weighted sum of Lorentzians with deformation parameters as derived [11] by instantaneous shape sampling (ISS). Black thin line: The deformation parameters were first averaged and then used in the Lorentzian description of the dipole strength. The lower thick green line shows the Lorentzian parameterization with an explicitly introduced quadratic dependence on  $E_\gamma$ ; for  $^{94}\text{Mo}$  and  $^{98}\text{Mo}$  respective comparisons are presented in [1].

### Giant resonances and e.m. radiation

As has been shown from a recent study [1] involving many heavy nuclei with  $A > 80$  the electric dipole strength determining the radiative neutron capture is well parameterized as the low energy tail of the isovector giant dipole resonance (GDR). Its resonance integral, which determines the overall absolute photo-neutron cross section, is in accordance to the dipole sum rule and its spreading width is a function of its resonance energy. Whereas the centroid energy is predictable using parameters of the FRDM [3, 12], a splitting of the GDR induced by the deviation of the nuclear shape from spherical symmetry has to be considered. It is important especially for exact calculations in dependence of the photon energy, as applied to photo-nuclear and radiative capture cross sections.

### Electric dipole strength in the GDR tail

The ground state deformations shift the lowest of the three GDR resonance energies away from the centroid by up to 2 MeV and subsequently [14] they also modify their widths by up to 22 %. As seen in Fig. 4 this results in a shape different from, albeit quite similar to, a Lorentz curve, and explains why past attempts [15] to use a fit with a single Lorentzian are apt to lead to unreasonably large width values. These were eventually interpreted incorrectly as a

spreading width and this resulted in a false extrapolation for the low energy tail. The cross section in that tail region depends linearly on the GDR width. In our parameterization the rather good description of the data below the neutron threshold is the result of a shift of one component of the GDR to lower excitation energy, and thus an increase of the strength there. No explicit photon energy dependence of the resonance width is needed and all parameters entering (except the deformations) are resulting from a procedure [1] considering globally all heavy nuclei. It may be stressed here again, that we have not performed a local fit to the data to obtain the quite appealing agreement with the experiments.

The deformation independent global parameters [1] – valid for all  $A > 80$  – are:

1. an effective nucleon mass of 874 MeV together with the symmetry-energy  $J = 32.7$  MeV and the effective surface-stiffness constant  $Q = 29.2$  MeV, which are already fixed by a fit to ground state masses [3, 12];
2. the proportionality factor in Eq. 10 of Ref. [1], which is used together with the exponent 1.6 already fixed by a hydrodynamic calculation [15], incorporating one body dissipation.

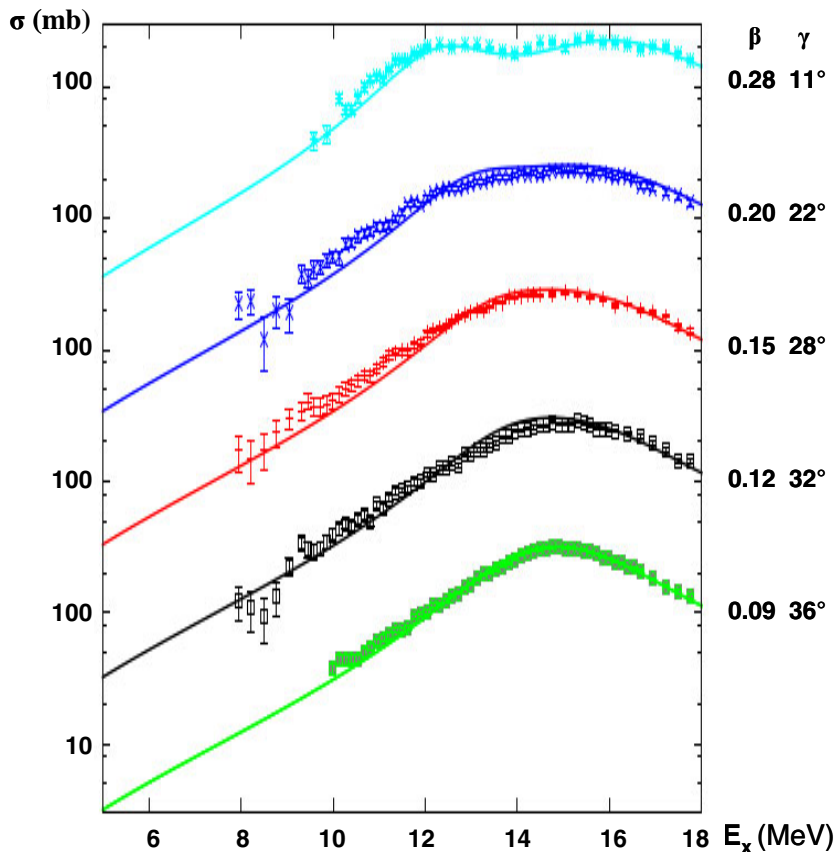


**Figure 4.** Comparison of photo-neutron data [13] for the even Nd isotopes  $^{142-150}\text{Nd}$  [13] in comparison to the parameterization [1], using the deformation parameters listed. These were determined from [7] and the systematics are shown in Fig. 2. Apparently the resonance integral is in a surprisingly good agreement to the Thomas-Reiche-Kuhn sum rule.

The good overall agreement between the cross sections from different experiments with the ones calculated by TALYS on the basis of the E1-parameterization [1] and a reasonable selection of deformation parameters is remarkable. Although in  $^{98}\text{Mo}$  and especially in  $^{100}\text{Mo}$ , the apparent width of the GDR reaches or even exceeds 6 MeV, three overlapping Lorentzians of smaller width, but shifted by the proper amount lead to a very good description of the resonance and to the tail region (*cf.* Figs. 3 and 5). The latter is especially sensitive to the width  $\Gamma$  and its possible energy dependence. The ansatz allows the use of a GDR spreading width depending smoothly on the energy of the GDR component, and thus only weakly on  $A$  and  $Z$ . Additionally, the resonance integrals are in agreement with the Thomas-Reiche-Kuhn (TRK) sum rule, which we find fully respected at the excitation energies studied. This sum rule makes very much the same predictions as the GGT sum rule, which is based on very general considerations [18]. This surprisingly good agreement does not exclude a

possible violation at higher energies where, *e.g.*, pionic degrees of freedom may come into play. We have to mention that the accurate yield normalization, obtained at ELBE by an activation technique for various photo effect channels [8, 9, 19], disprove older absolute cross section measurements [13, 16, 20] and confirm the need for a correction factor proposed earlier [21]. These new data agree much better to the sum rule and thus indicate that previous statements about breaking it have to be questioned. Nevertheless also our data indicate some excess of the ‘pygmy resonance’ type which has attracted some attention recently – albeit constituting a few % of the integral GDR strength only.

The extrapolation into the tail region of the GDR not only constitutes a good reference for the eventual enhancement in pygmy resonances, it is important particularly with regard to the E1-strength near and below the neutron thresholds. This is why another example is shown for the misinterpretation of the GDR data, occurring when the ground state deformation is not well accounted for. Hg is close to the magic Pb-shell, but it is not close enough thus it has a small quadrupole deformation [7]. The fact, that a small deformation is, according to Fig. 2, correlated with a considerable triaxiality, results in a single peak and not a double humped structure.

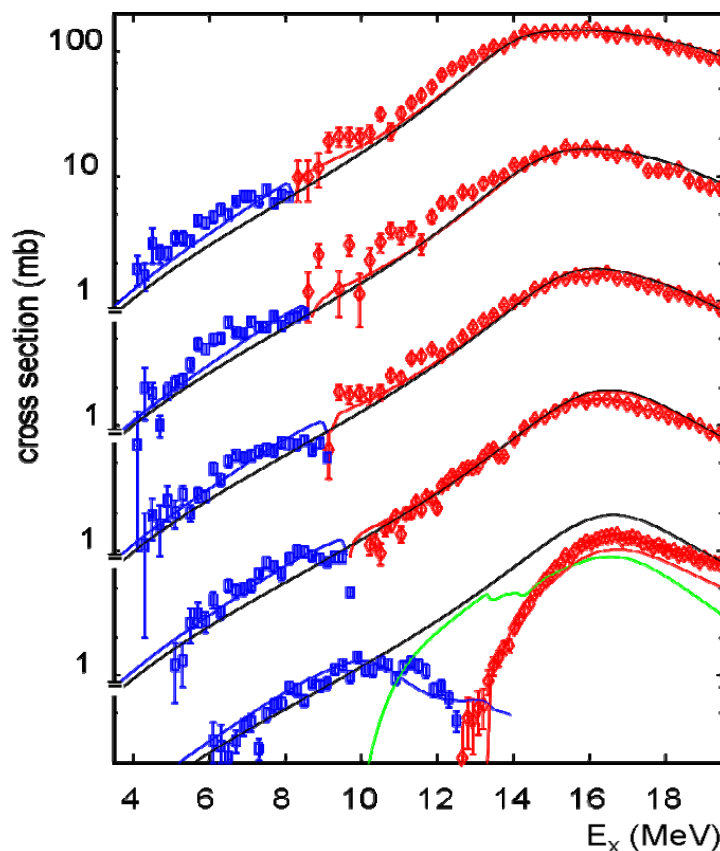


**Figure 5.** Experimental cross sections for photon induced processes in  $^{92,94,96,98,100}\text{Mo}$  (from bottom). The data at low  $E_x$  from the present scattering experiment (blue  $\square$ ) are shown together with  $(\gamma, n)$ -data (red  $\diamond$ ) [16] rescaled as described in the text. The thin lines depict the results of Hauser-Feshbach calculations performed [8] with the code TALYS [17] (blue:  $(\gamma, \gamma)$ ; red:  $(\gamma, n)$ ; green:  $(\gamma, p)$ ; only shown as long as their contribution exceeds 10%). These calculations use the parameterization [1] for the absorption cross section  $\sigma_\gamma(E1)$ , represented by the thick solid line, which is based on the deformations as given in Fig. 2. A cross section overshooting this line may indicate contributions from M1 or E2 as included in TALYS [17].

The 3 respective Lorentzians in Fig. 6 (right part, with  $\Gamma \sim 3.2$  MeV and assuming  $A=200$ ) clearly demonstrate this point, and the red curve shows the perfect agreement of their sum to the data [19]. The black curve is a reproduction of the fit with a single resonance with  $\Gamma = 4.4$  MeV, as performed previously [15], and also shown in the left part of Fig. 6. The overshoot of this curve at small energies is obvious in the Figure.

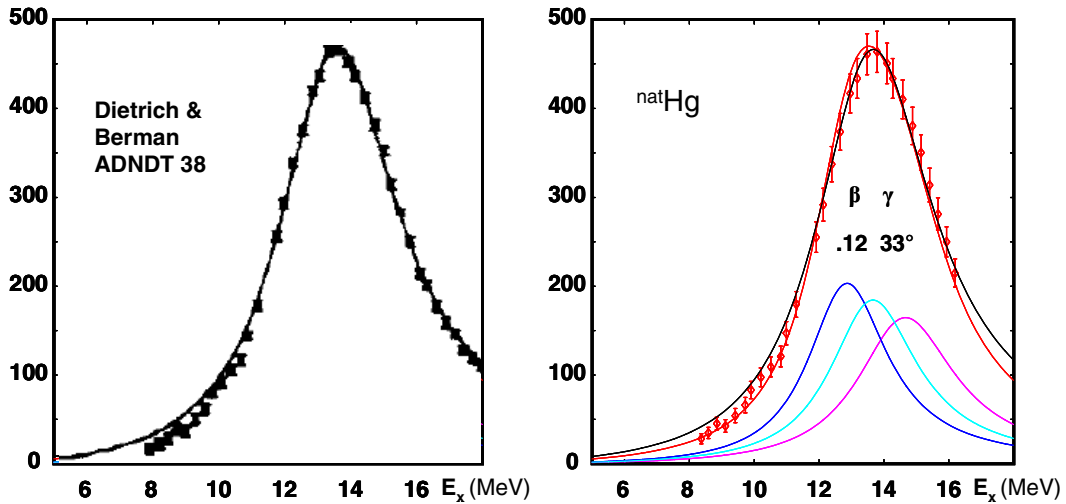


**Figure 6.** Experimental cross sections for photon induced neutron emission with a Hg target of natural isotopic abundances. A Lorentzian fit as obtained previously ([15], black curve) is compared to the results of our parameterization shown in colour ; details are given in the text.

### Valence nucleon systematics

Comparison of excitation energies and electric quadrupole transition strengths to the number of valence nucleons in various regions outside of closed shells have been presented previously, and a recent review [22] on this matter shows results encouraging further work in that direction. An application of this approach, combined to the systematics shown in Fig. 2, promises a reasonably accurate prediction of a dipole strength function obtainable without any knowledge of deformation parameters. In Fig. 7 one attempt to find an expression covering all heavy nuclei from  $A = 70$  to  $A = 240$  is shown.

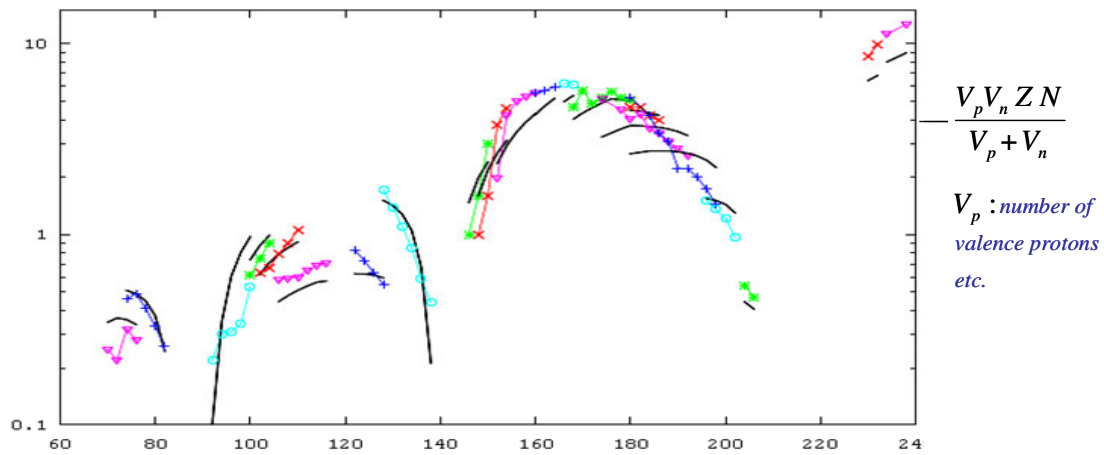


**Figure 7.** Dependence of the parameter  $K_2$ , which is a measure of the quadrupole deformation of the nuclear ground state on the mass of the nuclei; different isotopic chains from Ge to U are shown in different colours. The black curves depict the expression shown, which contain  $Z$  and  $N$  of the nuclei as well as the numbers of valence protons and neutrons.

The agreement of the experimental  $K_2 = \sum_i B(E2, 0_1^+ \rightarrow 2_i^+)$  to an expression containing nucleon numbers only is accurate up to 60 %, corresponding to a deviation of 30 % in the deformation parameter  $\beta$ . Here the number of valence nucleons corresponds to the nearest closed shell for neutrons or protons, respectively. To obtain better predictions the different areas of the nuclide chart have to be considered separately.

### Acknowledgements

We acknowledge the support by the 6<sup>th</sup> EU framework programme through the EFNUDAT project as well as funding by the DFG. Thanks are due to colleagues from the institute's divisions for the Radiation Source ELBE and for Nuclear Physics, who helped considerably to make the experiments mentioned a success.

### References

- [1] A. Junghans et al., Phys. Lett. B 670 (2008) 200.
- [2] A. K. Dutta et al., Phys. Rev. C 61 (2000) 054303.
- [3] P. Möller et al., At.Data Nucl. Data Tables 94 (2008) 758
- [4] G. Rusev et al., Phys. Rev. C 73 (2006) 044308.
- [5] W. Andrejtscheff and P. Petkov, Phys. Rev. C 48 (1993) 2531.
- [6] K. Kumar, Phys. Rev. Lett. 28 (1972) 249.
- [7] S. Raman et al., At. Data Nucl. Data Tables 78 (2001) 1.
- [8] M. Erhard et al., submitted to Phys. Rev. C (2009).
- [9] C. Nair et al., to be published.
- [10] G. Rusev, et al., Phys. Rev. C 77 (2008) 064321; *id.*, PoS (PSF07, 2008) 022;
- [11] S.Q. Zhang et al., Phys. Rev. C 80 (2009) 021307.
- [12] W. D. Myers et al., Phys. Rev C 15 (1977) 2032.
- [13] P. Carlos et al., NP A172 (1971) 437
- [14] B. Bush and Y. Alhassid, Nucl. Phys. A 531 (1991) 27.
- [15] S. S. Dietrich and B. L. Berman, At. Data Nucl. Data Tables 38 (1989) 199.
- [16] H. Beil et al., Nucl. Phys. A227 (1974) 427.
- [17] A. J. Koning et al., Proc. Int. Conf. on Nucl. Data, ND 2007, Nice/F (2008).
- [18] M. Gell-Mann et al., Phys. Rev. 95 (1954) 1612.
- [19] C. Nair et al., Phys. Rev. C78 (2008) 055802.
- [20] A. Veyssiere et al., Journal de Physique, 36 (1975) L 267.
- [21] B. L. Berman et al., Phys. Rev. C 36 (1987) 1286.
- [22] R. Casten et al., Journal of Physics G 34 (2007) R 285.



## Preparation and characterization of thin film nuclear targets by vacuum evaporation

*D. Sapundjiev<sup>1)</sup>, G. Sibbens<sup>1)</sup>, A. Moens<sup>1)</sup>, K. Luyckx<sup>1)</sup>, M. Peeters<sup>1)</sup>,  
R. Eykens<sup>1)</sup>, Y. Aregbe<sup>1)</sup>*

1) Institute for Reference Materials and Measurements (IRMM), European Commission, Joint Research Center, Retieseweg 111, Geel, Belgium, B-2440  
[danislav.SAPUNDJIEV@ec.europa.eu](mailto:danislav.SAPUNDJIEV@ec.europa.eu)

**Abstract:** Among the many different techniques to prepare thin uniform deposits for nuclear experiments, physical vacuum deposition is the most widely applied. After several years of standstill, the preparation of thin deposited layers restarted in the Target Preparation Laboratory at IRMM. At present the laboratory is producing thin layers of  ${}^6\text{LiF}$ ,  $\text{LiF}$ ,  $\text{Au}$ ,  ${}^{10}\text{B}$  and  ${}^{235}\text{UF}_4$ . Knowing that the nuclear experimental results depend among other things on the uniformity and areal characteristics of the deposited layer, the deposition parameters have been optimized and investigation started to improve the characterization. Besides photospectrometry for thickness monitoring, other techniques are presented and compared. Experiments on the deposition of pure lithium are under investigation. This article reviews the available equipment and methods on the preparation of thin uniform deposits and reports on the progress in the characterization of thin layers produced by physical vapour deposition.

### Target preparation at IRMM

At the Institute of Reference Materials and Measurements (IRMM) targets for nuclear data measurements are mainly fabricated for internal research in support of the nuclear physics unit. Different preparation techniques are used: from simple mechanical shaping (wire drawing, punching, pressing and cutting) [1,2], and electro deposition [3] to vacuum evaporation techniques [4]. A variety of metallic foils, wires and discs, homogeneous powder compacts that are not available commercially are manufactured [5]. Small ingots of alloys with specific composition and high melting point are prepared by arc-melting. Besides the production of assorted target types additional reference materials like reactor melt-wire temperature monitors and reactor neutron fission dosimeters are fabricated.

After long period of inactivity the physical vapour deposition (PVD) lab of at IRMM resumed operation. The target preparation lab is able to produce thin films non active  $\text{LiF}$ ,  ${}^6\text{LiF}$ ,  ${}^{10}\text{B}$  targets and active actinide targets (e.g.  ${}^{235}\text{UF}_4$ ).

In this article we describe the PVD lab of the IRMM and the current status in target fabrication, thin film characterization and other activities related to thin film targets (like the fabrication of thin polyimide (PI) foils as backings for  $\text{LiF}$ ,  $\text{Au}$  and  ${}^{10}\text{B}$ ).

### The physical vapour deposition laboratory at IRMM

High vacuum evaporation is the most generally employed technique for preparation of thin film targets. In principle it consists in heating the source material to be evaporated to high temperature in an evacuated vacuum chamber. The so evaporated material is transported as a vapour through the chamber and is allowed to condense on a suitable substrate (backing).

The heating of the source material is selected on the basis of its properties (chemical and physical). In most cases a simple resistive heating can be utilized while in other cases alternative methods have to be sought. Materials which are highly reactive at high temperature (B, Si) or which form alloys with the heating crucible (e.g. Al, Ni, Fe, etc) and dissolve most of the refractive metals, have to be heated by other methods. Such heating can be done by electron bombardment sources [6].

The PVD laboratory is equipped with a bent e-beam evaporator, and resistance evaporation installations - of which some are placed in the controlled zone for the evaporation of actinides. In this article we will focus on the installations outside the controlled area. The reported procedures and results of thin film analyses can be applied in the cases of evaporation and deposition of active materials.

### LiF and $^6\text{LiF}$ vapour deposition set-up

The LiF deposition set-up uses resistive heating to sublimate LiF powder. The latter is placed into tantalum crucible and the substrate is fixed into a specially designed substrate holder which is attached to a holder disk by a flange (Fig. 1). The disk is rotated through a gearbox allowing uniform distribution of the condensing vapours. Typical evaporation rates fall between 0.03 - 0.22 nm/sec. During evaporation the thickness of the LiF deposit is controlled by a thickness monitor (see below).



**Figure 1.** Overview of the LiF and  $^6\text{LiF}$  vapour deposition set-up.

### Gold vapour deposition set-up

The vapour deposition set-up for gold uses also resistance heating to melt and volatilize the gold material. The positioning of the substrate and the thickness monitor are somehow different as for the LiF vapour deposition set-up. The gold set-up is designed with a universal substrate holder which is rotated with the help of the built in carousel. Typical deposition rates range from 0.03 - 0.25 nm/sec.

### Bent beam e-gun for deposition of $^{10}\text{B}$

For the evaporation of  $^{10}\text{B}$ , a bent beam electron bombardment source is used for the heating of the charge material (the material to be evaporated). It has excellent beam quality and optimal beam deflection. What is more important it allows evaporation of materials with high meltingpoint. High evaporation rates can be obtained through vertical beam impingement. Other properties include x,y - beam deflection and all-round evaporation at an angle of  $110^\circ$ .



**Figure 2.** Bent beam e-gun and crucible for deposition of  $^{10}\text{B}$

## Evaporation procedure

The target substrate (backings) is placed at a fixed position fixed into the substrate holder. The source charge (the material to evaporate) is added into the crucible. Small chunks of  $^{10}\text{B}$  are placed into the crucible of the e-gun (see Fig. 2). During evaporation it will retain its shape and will only melt partially at the point of beam impact. The chamber is evacuated to pressures of about  $3 \cdot 10^{-8}$  Pa. Low vacuum ensures sufficient mean free path of the volatilized particles and reduces the contamination. The evaporation is carried at low and moderate rates to reduce the chance of backscattering of particles within the vapour flux and rapid nucleation and grain growths on the substrate. The film growth is also monitored with an acoustic impedance thickness monitor.

## Thickness control during deposition

The deposition process is controlled by a quartz crystal resonator (QCR) thickness monitor. The quartz crystal oscillates in a thickness shear mode (TSM). The sensor consists of a thin AT - cut quartz with metal electrodes on both sides. It is an electro-mechanical device that can be used to characterize materials bound to its surface. The crystal is used as the frequency determining element of an electronic oscillator whose output frequency equals one of the crystal proper frequencies - preferably the fundamental. The alternating electric field applied to the electrodes produces a bulk acoustic wave in the crystal (and the material bound on its surface). The frequency of the wave is modulated by the amount of the material and can give information on the amount of material bound to the crystal.

The sensor is placed as near as possible to the substrate. It "measures" the thickness indirectly and therefore its reading needs to be corrected by three parameters (Fig. 3):

- Tooling Factor - compensates for geometrical factors (Fig. 3) coming from the relative position of the sensor and the substrate with respect to the source charge
- Acoustic impedance - correction for acoustic impedance mismatch between the crystal and the condensing material
- The third parameter required to measure the thickness by the acoustic impedance sensor is the density of the evaporated material

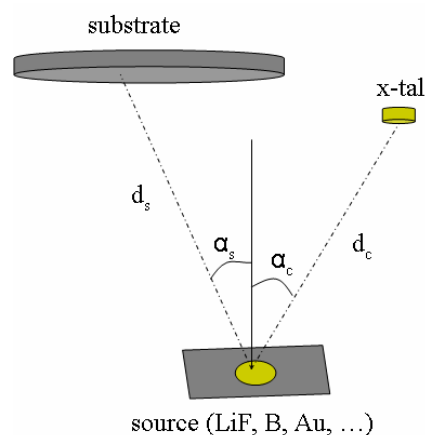


**Figure 3.** Parameters entering the calculation of the tooling factor - compensating for the relative positions of substrate, source and sensor crystal (x-tal).

The acoustic impedance and the density of the deposited material can be found in reference tables. The tooling factor is calculated from the relative position of the vapour source, the substrate and the sensor. The uncertainty of the thickness determined by the thickness monitor is most affected by the tooling factor and therefore the relative positions of the source, substrate and sensor should be known with significant precision.

Provided that no other effects affect the deposition process and that the flux of vapour particles is uniform, the uncertainty of the thickness monitor reading is of the order of  $\pm 5$  nm.

## Targets characterization

It was already mentioned that the thickness is monitored by indirect measurement - calculated from the deposition rate at the vicinity of the substrate. The deposited thickness is corrected for material density and relative position. Such a measurement can only be used to control the deposition process and not to characterize the resulting thin film.

Various characterization techniques are used: from simple weighing, and dimensional measurement of the larger targets to more sophisticated micro - probe and optical methods. Universal method for film thickness measurement is not available. The particular characterization method is selected with respect to the physical and chemical properties of the thin film.

In the cases where the sample is the limiting factor for the resolution of the nuclear measurement the thickness and the area of the target can introduce a significant uncertainty. To a first approximation the uncertainty of the cross section is proportional to the uncertainty of the thickness and/or the area of the target. The important parameter is the amount of particles per unit target material; when the particles are those which take part in the nuclear reaction the, impurity of the material should be known.

### Spectrophotometry

For optically transparent materials spectrophotometric measurements can be used to determine the thickness of the backing and the deposited layers. The principle is based on reflection and transmission through thin layers and observing the resulting interference picture. The thickness is derived from the difference in the optical path between the reflected and refracted ray of light passing through the film. The necessary input data are the spectral refractive indices of the materials through which the rays are propagating. If there are not available, a calibration of the system is made [7].

The thickness of the LiF, polyimide foils and the boron films is determined by spectrophotometric measurements. For non optical materials (gold) and to verify the thickness values obtained by spectrophotometric measurements and by the quartz crystal thickness monitor alternative *direct* methods have to be used. For example the thickness values for LiF obtained by the thickness monitor and the spectrophotometric measurements (Table 1) differ significantly (more than the experimental uncertainty) which indicates that the UV Vis spectrometer has to be recalibrated for LiF thickness measurements. The thickness was calculated using the empirical value of the spectral refractive index of LiF  $n(\lambda)$ .

### $\alpha$ -particles spectroscopy thickness measurements

The measurement of the energy lost by  $\alpha$  - particles on passing through a thin layer is an accurate method for thin film thickness measurements [8], [9]. The important condition here is that the thickness of the film and/or the backing has to be smaller than the range of the  $\alpha$ -particles in the respective materials. Another limiting factor of the method is the minimal thickness that can be measured which depends on the width of the  $\alpha$  - peak. Typical energy spectra of  $\alpha$  - particles are given on Fig. 4. The method can be used to map or scan the thickness distribution of the film and the backing. An important condition for achieving high thin film thickness accuracy is good stability of the measurement system and good energy resolution.

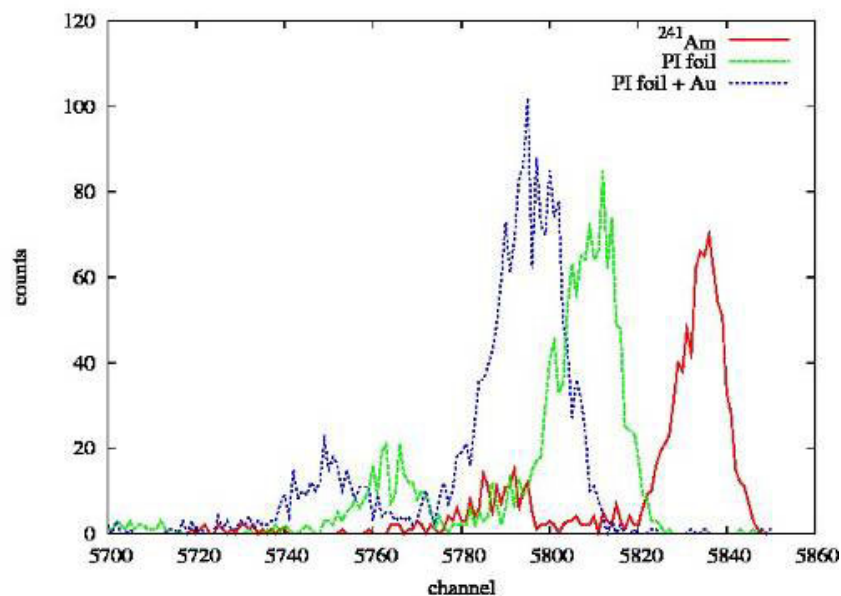


**Figure 4.** Thickness measurements by  $\alpha$ -particles energy loss.

## Comparison of the results

Thin film measurements of gold layers, polyimide foils and LiF films are compared. The results are reported in Table 1. The values obtained by the different methods for the LiF layers are significantly different. This discrepancy has been explained with the nature of the operation of the thickness monitor (i.e. it determines the film thickness by indirect calculation of the deposited material) and the difference in the calibration of the spectrophotometric thickness measurement. The  $\alpha$  - particles energy loss was measured with low counting statistics. The experiment was performed as first feasibility study of its applicability to film thickness measurement.

**Table 1.** Thin film thickness measurements by various methods,  $\mu\text{g}/\text{cm}^2$  (\*thickness calculated using the spectral refractive index of LiF  $n(\lambda)$ ).

sample	thickness monitor	photospectrometry	$\alpha$ -spectroscopy
LiF on Al	$50 \pm 2\%$	$11.1 \pm 2\%$ (or $66 \pm 2\%$ )*	n.a.
PI foil	n.a.	$32.1 \pm 2\%$	$31.3 \pm 1\%$
Au on PI foil	$50 \pm 2\%$	n.a.	$54.8 \pm 1\%$

## Effect of surface roughness on the LiF film thickness measurements

To explain the large difference between the LiF thickness value from the thickness monitor and the measurements with the spectrophotometer the influence of the substrate (backings) surface roughness on the spectrophotometric thickness measurement was studied. Five Al backings were polished to different surface roughness - 6, 8.4, 15.3, 18.3, 21.8  $\mu\text{m}$ , and as received. The results showed unambiguously that the thickness measurements by spectrophotometry do not depend on the surface conditions regarding the roughness (Fig. 5). The accuracy however depends on the reflectivity of the backing. The wavelength of the interference fringes might not be detectable if the reflectivity is small (high surface roughness leads to scattering of the incident light).

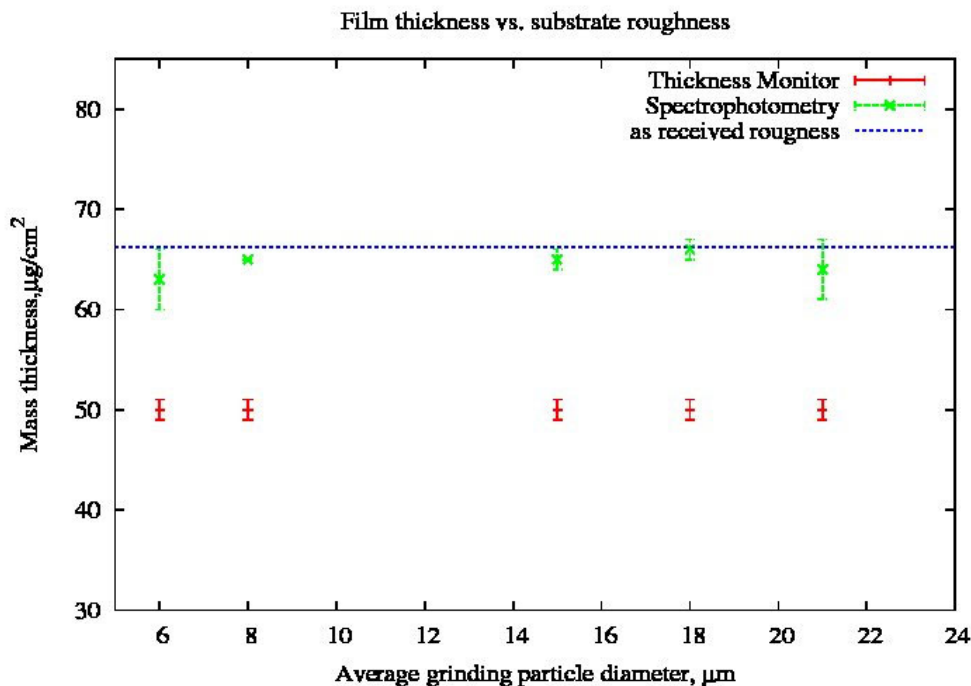


**Figure 5.** LiF film thickness measurement by spectrophotometry as a function of the substrate roughness.

## Thickness measurements with atomic force microscopy

The absence of any large observable effects of surface conditions on the thickness measurement reduces the problem of accurate thickness measurement to calibration of the thickness monitors, and the spectrophotometer. Simple and highly accurate procedure is to measure the thickness with an atomic force microscope (AFM). AFM measurements can produce thickness values with an accuracy approaching 0.1 nm and can be used to measure the thickness of optical, non optical, conductive and non conductive materials. The selected procedure of calibration is the following: using focused ion beam (FIB) a thin narrow channel is made into the film by sputtering (milling) the film down to the substrate material. The accuracy of milling using FIB can easily approach one atomic layer. A transverse scan(s) of the groove is carried out with the probe of the AFM and the depth of the layer can be determined. The uniformity of the layer can be investigated by making several grooves into the thin film layer.

Film thickness measurement with atomic force microscope (AFM) - a thin microscopic groove is milled using focused ion beam (FIB) down to the substrate material. The depth of the groove is measured by atomic force microscope (AFM) as shown in the illustration.

Although FIB may sputter grooves with microscopic sizes, it is a destructive technique. In addition some of the impact ions are captured into the target material/film and remain implanted which produces changes in the target composition.

## Ongoing and future work

### Alternative methods for film thickness measurements

- ellipsometry - uses the change in the polarization of light upon reflection (or less commonly transmission) from material [10]. Analysis of the reflected light, knowing the properties of the incident light allows for determination of the refractive index,  $n(\lambda)$ , and also the thickness(es) of the material. Additionally, it is also possible to characterize more complex multilayered films. Measurements are carried out at a range of incidence angles and wave lengths. The properties of the investigated film are determined by modeling the film and comparing (fitting) the measured and the calculated data. Ellipsometry is accurate measurement technique which does not require initial calibration as ratios between the incident and the refracted/transmitted light are calculated. It is non destructive but only suitable for optical films;
- $\alpha$ -particles spectroscopy - it was shown that  $\alpha$ -particles may be used for measurement of the film thickness. At present an experimental set-up for  $\alpha$  - spectroscopic film thickness measurement is available mainly for the measurement of PI foils and thin film deposits on PI films, especially gold and  $^{10}\text{B}$ , which cannot be measured by optical methods.
- prism film coupling method (also known as m-line spectrometry) - the film is placed in contact with the prism; light is guided by the prism onto the film which selects only those modes which are inclined at the correct coupling angles for guiding. An image is projected on a screen and contains several dark lines corresponding to guide mode of the film and are called *m-lines* from where the name of the technique [11] [12]. The angle between the m-line and the central position of the non refracted ray is measured and used to calibrate the coupling angles from which is calculated the thickness of the film. The main advantage of the technique is that films with significant absorption or scattering losses can be analyzed. A disadvantage is that the contact may "damage" the thin layer.

### Preparation and analysis of lithium metallic targets

In the literature - preparation by pressing (thick targets) and vacuum deposition [13] or even more advanced sputtering deposition technique [14] are reported. The major problems arise from the chemical activity of pure lithium.  $\text{Li}_2\text{O}$  has the highest affinity to oxygen among the alkali metals, reacts with nitrogen and diffuses in metals. The metallic state lithium is highly flammable.

Post test analyzes - XRD to study the evolution of the Lithium layer - test the stability and fractions of  $\text{Li-Li}_2\text{O}$ ; XRD tests at few time intervals after deposition to measure the evolution of the  $\text{Li-LiO}$  ratio.

Alternatives comprise the deposition/application of protective sealing cladding of material/element with suitable nuclear properties (e.g. Zr clad on Li layer, polyimide foils, etc). Experiments of using stainless steel protective cladding [14] provided short term protection but subsequently diffusion and oxidation of Li has been observed. Another possibility is

immersion in Si oil or cooling down to liquid nitrogen temperatures in order to reduce the reaction rates. Post deposition handling of the sample is crucial for its stability.

### Theoretical calculation of film thickness distribution

This work intends to support the film characterization and help better understand film growth and thickness distribution from point and real source charge. Given the specific geometry and test parameters of the vapour deposition experiment theoretical calculation of the resulting film thickness are underway using Monte-Carlo techniques. The simulation uses as a starting point equations based on the Hertz-Knudsen vaporization equation. Parameters such as source and substrate diameter, type of evaporation species, melting temperature, source-substrate distance, ambient and partial vacuum pressure are currently used in the calculations. The measured thickness is used to compare, verify the theoretical calculations, and to improve and develop the theoretical model.

### PI films preparation and analysis

For high accuracy fission fragment and  $\alpha$ -particles spectroscopy thin substrate foils are necessary to keep the energy loss of the fission fragment minimum. Polyimide foils have number of advantages and are used as substrate foils for targets. The target preparation group has long experience in producing the polyimide foils and is still working on the optimization of their fabrication and properties.

### Conclusions

At the target preparation the PVD lab has successfully resumed its operation. Thin LiF,  $^{10}\text{B}$ , Au, and actinide film targets can be readily prepared. The deposition monitoring has been improved by optimising the design of the deposition system and by precise determination of the deposition parameters. In this article we have shown that the use of only the thickness monitor for the characterization of the thin film thickness is insufficient to characterize the resulting deposits. The challenges to face for the thin film target preparation lab are improvement in the characterization of the deposited films and of the in-house produced backings (i.e. the PI foils). New methods like ellipsometry and m-line spectroscopy for thickness measurements are being tested and investigated. Calibration of the acoustic impedance thickness monitors is underway for better in-situ deposition control. In addition theoretical calculations are carried out to better understand the effect of various deposition parameters on the film growth and properties.

### References

- [1] J. Van Audenhove and J. Joyeux. Sample preparation by metallurgical methods. *Nuclear Instruments and Methods*, 102(3):409 – 415, 1972.
- [2] C. Ingelbrecht. Metallurgical sample preparation at the institute of reference materials and measurements. *Nuclear Instruments and Methods in Physics Research Section B: Beam Interactions with Materials and Atoms*, 99(1-4):790 – 793, 1995. Application of Accelerators in Research and Industry '94.
- [3] C. Ingelbrecht, A. Moens, R. Eykens, and A. Dean. Improved electrodeposited actinide layers. *Nuclear Instruments and Methods in Physics Research Section A: Accelerators, Spectrometers, Detectors and Associated Equipment*, 397(1):34 – 38, 1997. Proceedings of the 18th World Conference of the International Nuclear Target Development Society on Nuclear Targets: Theory, Practice, Behavior, Studies.
- [4] H.L. Eschbach. Preparation of standard layers by vacuum evaporation. *Nuclear Instruments and Methods*, 102(3):469 – 475, 1972.
- [5] J. Van Audenhove, P. De Bievre, J. Pauwels, F. Peetermans, M. Gallet, and A. Verbruggen. The preparation and characterisation of reference fission foils. *Nuclear Instruments and Methods*, 167(1):61 – 63, 1979.
- [6] A.H.F. Muggleton. Deposition techniques for the preparation of thin film nuclear targets. *Vacuum*, 37(11-12):785 – 817, 1987.
- [7] M. Pauwels J. Van Gestel J. Pauwels, J. Wesenbeek. The use of a visible light spectrophotometer for nuclear target production control. Technical Report EUR 7985, Institute for Reference Materials and Measurements, Retieseweg 111, 2440 Geel, Belgium, June 1982. This is a full TECHREPORT entry.
- [8] W. C. Barber. Foil uniformity measurement by alpha-particle transmission. *Review of Scientific Instruments*, 24(6):469–470, 1953.

- [9] I.V.Mitchell H.L.Eschbach, R.Werz and P.Rietveld. Highly accurate thickness determination of thin self-supporting foils by the  $\alpha$ -absorption method. In *Proceedings of the eighth International Vacuum Congress Cannes, France, April 22-26*, volume 1, pages 267–270, 1980.
- [10] M. Fried, T. Lohner, and P. Petrik. Ellipsometric characterization of thin films. In Hari Singh Nalwa, M.Sc, and Ph.D., editors, *Handbook of Surfaces and Interfaces of Materials*, pages 335 – 367. Academic Press, Burlington, 2001.
- [11] John S. Wei and W. D. Westwood. A new method for determining thin-film refractive index and thickness using guided optical waves. *Applied Physics Letters*, 32(12):819–821, 1978.
- [12] P C Jaussaud and G H Chartier. A quick method for the determination of refractive index profiles for diffused optical waveguides. *Journal of Physics D: Applied Physics*, 10(5):645–654, 1977.
- [13] Aslam, W. V. Prestwich, and F. E. McNeill. Lithium target performance evaluation for low-energy accelerator-based in vivo measurements using gamma spectroscopy. *Applied Radiation and Isotopes*, 58(3):321 – 331, 2003.
- [14] C. Rigaux, R. Vigneron, F. Bodart, Y. Jongen, A. Cambriani, and S. Lucas. Rnra and neutron threshold analyses of thick lithium coatings deposited by sputter evaporation. *Nuclear Instruments and Methods in Physics Research Section B: Beam Interactions with Materials and Atoms*, 266(10):2446 – 2449, 2008. Accelerators in Applied Research and Technology - Proceedings of the 9th European Conference on Accelerators in Applied Research and Technology, 9th European Conference on Accelerators in Applied Research and Technology.

## Model defects for nuclear data evaluation

St. Gundacker<sup>1)</sup>, H. Leeb<sup>1)</sup>

1) Atominstitut, TU Wien, Vienna, Austria, 1040 Vienna  
[e0325764@student.tuwien.ac.at](mailto:e0325764@student.tuwien.ac.at)

**Abstract:** A consistent procedure for the determination of the covariance matrix due to model defects is presented. The method relies on a comparison of nuclear model calculations with corresponding experimental data at neighbouring nuclei for which one expects a description of similar quality. The method was successfully applied to the most important neutron-induced reaction channels of <sup>55</sup>Mn. The model defects were determined for a nuclear model based on TALYS calculations, where the latter were performed with a specific optical potential.

### Introduction

The development of novel nuclear technologies and radioactive waste incineration methods require an extension of the energy range beyond the standard of 20 MeV as well as inclusion of uncertainty information in evaluated nuclear data files. In principle nuclear data evaluation is a statistical process which is performed by means of Bayesian statistics. Unfortunately above an incident neutron energy of about 20 MeV there is a scarcity of experimental data. Therefore the evaluations at energies beyond 20 MeV depend strongly on the used priors, which are usually generated via nuclear models. Most of the current methods for the generation of priors account only for parameter uncertainties to evaluate the covariance matrices. However, there are additional uncertainties due to model defects, because in general nuclear models cannot reproduce all experimental reaction data, even exploiting their full parameter range. It is therefore important to include the uncertainties due to model defects into the prior. In the absence of a strict mathematical basis one aims at an almost unbiased procedure which extracts model defects from experimental data. Only recently, a procedure for a reliable estimate of model defects has been proposed [1].

In this contribution we extend this procedure and apply it to a larger data set. In the second section the basics of the method are outlined in detail. In the section "Results", as a first example, the method was successfully applied to determine covariance matrices due to model defects of TALYS calculations [2] for neutron-induced cross sections of <sup>55</sup>Mn. Conclusions and an outlook are given in the final section.

### Formulation of model defects

The formulation of model defects is hampered by the fact that failures are of non-statistical nature and cannot be determined via theoretical considerations within the considered nuclear model. It is therefore required to involve experimental data in the procedure, keeping in mind that double counting has to be avoided, e.g. by considering only corresponding data from neighbouring nuclei, which are not used in the evaluation (see [1]). In the following we apply the concept of [1] restricting ourselves to the so-called *scaling procedure*. This has the advantage that not only we can deal with scarce experimental data sets, but it also directly reflects the deficiencies of the underlying nuclear model.

We can start the procedure assuming that we can use experimental data from  $N$  neighbouring isotopes,  $n=1, \dots, N$  for which it is believed that the nuclear model works for the included reaction channels,  $c$ , equally well as for the considered nucleus. The energy region is divided into  $M$  bins with energy  $E_m$ ,  $m=1, \dots, M$  at the centre of the  $m^{\text{th}}$  bin. A bin width of 0.5 MeV was used by default. However, the bin width is widened if in this energy bin there are experimental data for less than a certain number of isotopes, e.g. 5, available. Within the procedure an overall scaling factor  $D^{(c)}$  for the channel  $c$  is defined by averaging over the isotopes,

$$D^{(c)} = \frac{1}{N^{(c)}} \sum_{n=1}^{N^{(c)}} \langle D_n^{(c)} \rangle, \quad (1)$$

where the scaling factor per isotope averaged over all energy bins  $1, \dots, M$  is given by

$$\langle D_n^{(c)} \rangle = \sum_{m=1}^M w_m^{(c,n)} \langle D_n^{(c)}(E_m) \rangle. \quad (2)$$

Due to the chosen weights,

$$w_m^{(c,n)} = \frac{\sigma_{th}^{(c,n)}(E_m)}{\sum_{m=1}^M \sigma_{th}^{(c,n)}(E_m)}, \quad (3)$$

the overall scaling factor is dominated by those with the highest values of the cross section. The quantity

$$\langle D_n^{(c)}(E_m) \rangle = \sum_{j \in Ebin(E_m)} w_j^{(c,E_m,n)} \frac{\sigma_{ex}^{(c,n)}(E_j)}{\sigma_{th}^{(c,n)}(E_j)} \quad (4)$$

is the scaling factor in the energy bin characterised by  $E_m$ . The index  $j$  refers to the  $j$ -th experimental point in the energy bin  $m$  for the isotope  $n$  and channel  $c$ . The abbreviations 'ex' and 'th' refer to experimental and theoretical (model) cross sections, respectively. The chosen weight,

$$w_j^{(c,E_m,n)} = \frac{\sigma_{th}^{(c,n)}(E_j)}{\sum_{j' \in Ebin(E_m)} \sigma_{th}^{(c,n)}(E_{j'})}, \quad (5)$$

is in accordance with Eq. (3) and is defined for each experimental data point. Thus the covariance matrix for model defects can be defined in the following way,

$$\begin{aligned} \langle \Delta \sigma^{(c)}(E_m) \Delta \sigma^{(c)}(E_{m'}) \rangle &= \sigma_{th}^{(c)}(E_m) \sigma_{th}^{(c)}(E_{m'}) \times \\ &\times \frac{1}{\sqrt{N^{(c)}(E_m)} \sqrt{N^{(c)}(E_{m'})}} \sum_n \left\{ \left[ \langle D_n^{(c)}(E_m) \rangle - D^{(c)} \right] \left[ \langle D_n^{(c)}(E_{m'}) \rangle - D^{(c)} \right] + \right. \\ &\quad \left. + \delta_{cc'} \delta_{mm'} \left[ \langle (D_n^{(c)}(E_m))^2 \rangle - \left( \langle D_n^{(c)}(E_m) \rangle \right)^2 \right] \right\} \end{aligned} \quad (6)$$

Here  $N^{(c)}(E_m)$  is the number of isotopes for which sufficient experimental data are available to evaluate  $\langle D_n^{(c)}(E_m) \rangle$ . The first term in the sum is due to the defect of the model and represents systematical errors, whereas the second term accounts for the uncertainties in the scaling factor as a result of the fluctuating experimental data. The second term is the variance of the scaling factor in a certain energy bin  $m$  and channel  $c$  with,

$$\langle (D_n^{(c)}(E_m))^2 \rangle = \sum_{j \in Ebin(E_m)} w_j^{(c,E_m,n)} \left( \frac{\sigma_{ex}^{(c,n)}(E_j)}{\sigma_{th}^{(c,n)}(E_j)} \right)^2 \quad (7)$$

The corresponding correlation is defined as usual,

$$C^{(cc')} (E_m, E_n) = \frac{\langle \Delta \sigma^{(c)}(E_m) \Delta \sigma^{(c')}(E_n) \rangle}{\sqrt{\Delta^2 \sigma^{(c)}(E_m)} \sqrt{\Delta^2 \sigma^{(c')}(E_n)}}. \quad (8)$$

In the denominator of the correlation matrix the square root of the two diagonal covariance matrix elements for the bin  $m$  and  $n$  appear. The number  $N^{(c)}(E_m)$  can be different for each energy bin. Therefore we approximate the normalisation of the covariance matrix as in Eq. (6). This normalisation accounts for the non-statistical nature of this formulation. However we know that the cross-correlations between two reaction channels and off-diagonal elements in the correlation can be slightly under-predicted.

## Results

In a first actual application of the method outlined above we estimated the model defects of TALYS-1.0 calculations of neutron-induced cross sections of  $^{55}\text{Mn}$  in the energy range 1-150MeV. For the estimate we use all cross section data of isotopes between  $^{40}\text{Ca}$  and  $^{65}\text{Cu}$  (excluding those of  $^{55}\text{Mn}$ ), Fig. 1, which are available in the EXFOR Data Library [3]. In addition we used

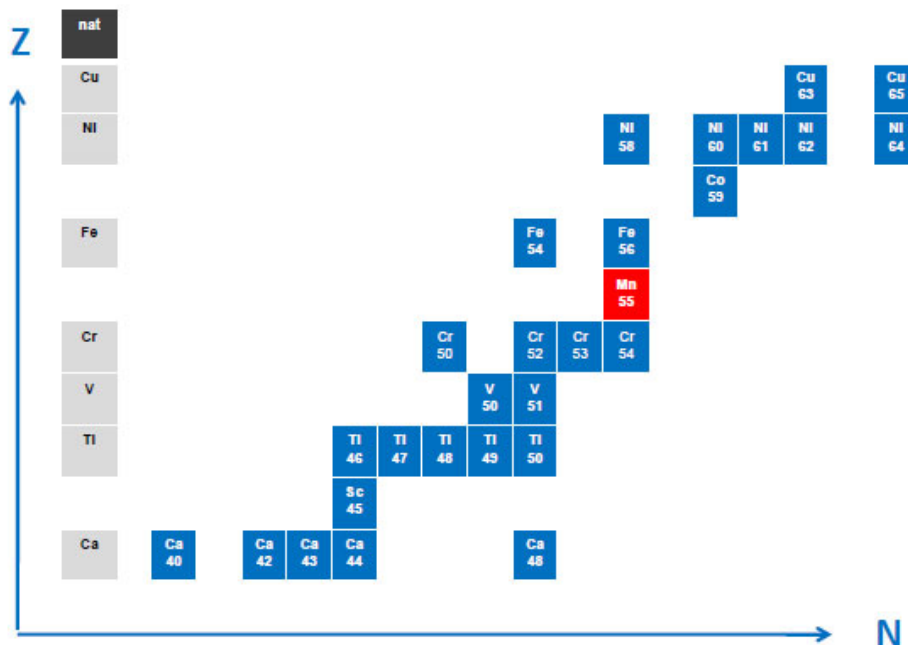


**Figure 1.** Isotopes used for the estimate of the model defects of  $^{55}\text{Mn}$  (blue squares). Used natural elements are also shown (grey squares).

these data to optimise the optical potential and level density parameters for this isotope region. Using the same parametrisation as Koning and Delaroche [4] and a global parametrisation for the level densities in the constant temperature model (CTM) and adjustment factors for the alpha optical model as in TALYS [2] we obtained slightly different values of the parameters, which are given in Tab. 1.

**Table 1.** Optical model and level density parameters for Sc-Ni region

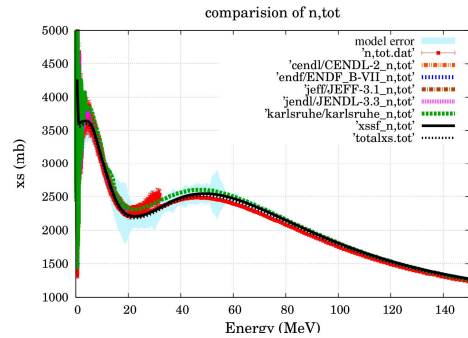
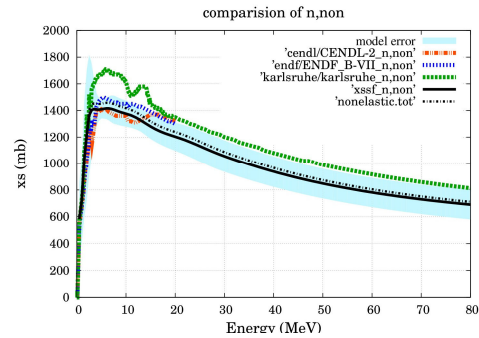
global neutron optical model parametrisation:					
$r_v = 1.295 - 0.3814 \cdot A^{-1/3}$	$a_v = 0.661 - 0.3940 \cdot 10^{-3} A^{-1/3}$	$v_1 = 64.41 - 20.23(N - Z) / A - 0.113A$			
$v_2 = 0.00715$	$v_3 = 0.000020$	$w_1 = 11.6$			
$w_2 = 80$	$r_{vd} = 1.414 - 0.0389 \cdot A^{1/3}$	$a_{vd} = 0.351 + 3.2452 \cdot 10^{-3} A^{-1/3}$			
$d_1 = 19.59 - 64.95 \frac{N - Z}{A}$	$d_2 = 0.0318 - 0.149 \cdot 10^{-3} A$	$d_3 = 24.91 - 0.270 \cdot A$			
$r_{vso} = 1.000$	$a_{vso} = 0.665$	$v_{so1} = 7.375$			
$v_{so2} = 0.0038$	$w_{so1} = -3.5$	$w_{so2} = 160.0$			
global alpha optical adjustment factors					
$r_v = 0.9578$	$a_v = 1.1625$	$v_1 = 0.9320$	$v_2 = 1.0024$	$v_3 = 1.0104$	$v_4 = 1.0236$
$w_1 = 1.1273$	$w_2 = 0.9738$	$r_{vd} = 1.0327$	$a_{vd} = 1.0641$	$d_1 = 1.1254$	$d_2 = 0.9992$
$d_3 = 0.9809$	$r_c = 1.0178$				
global level density parametrisation:					
$\alpha = 0.026220$	$\beta = 0.270416$	$\gamma_1 = 0.456296$	$P_{\text{shift}}(\delta) = 0$		

For the covariance matrices due to model defects cross section data of 34 isotopes in the vicinity of  $^{55}\text{Mn}$  were used. An overview of included reaction channels in the considered energy range is given in Tab. 2.

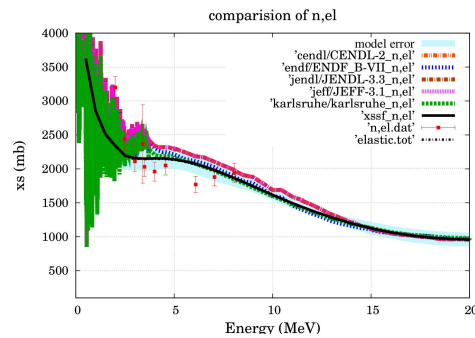
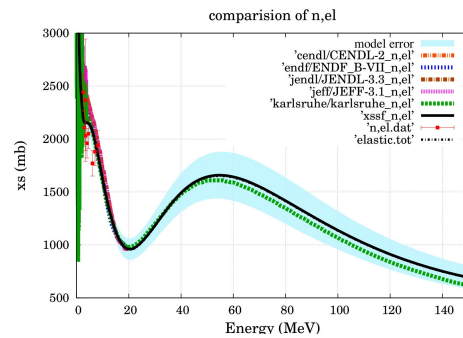
**Table 2.** Number of isotopes and data points per reaction channel

channel:	n,tot	n,non	n,el	n,inl	n,2n	n,p	n, $\alpha$
Nr. of isotopes	23	8	21	15	14	24	15
Nr. of data points	200162	173	2151	1666	1259	2498	772

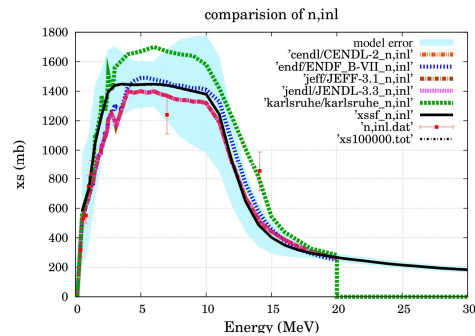
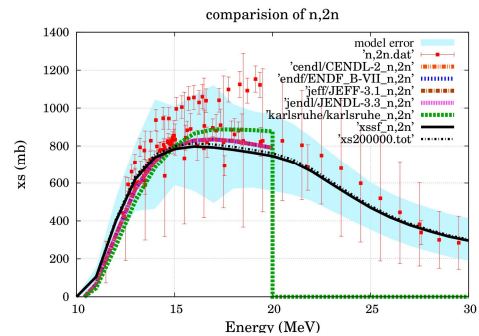
The square root of the diagonal elements of the covariance matrix, Eq. 6, yields the uncertainties due to model defects shown as blue error-bands. The reaction cross sections, Fig. 2-9, obtained with TALYS (Tab. 1) are shown by black dotted lines and multiplied with the scaling factor by black solid lines. In addition data from different evaluated libraries and experimental data (red points) of  $^{55}\text{Mn}$  are also shown.

**Figure 2.** ( $n,tot$ ) with scaling factor = 1.013**Figure 3.** ( $n,non$ ) with scaling factor = 0.971

The uncertainty for the total cross section ( $n,tot$ ) is about 7% up to 60 MeV and goes down to about 1.5% for higher energies. For the ( $n,non$ ) reaction model defects uncertainties are about 10% and for energies above 30 MeV about 17% estimated from 3 isotopes contributing.

**Figure 4.** ( $n,el$ ) with scaling factor = 1.004**Figure 5.** ( $n,el$ ) with scaling factor = 1.004

The elastic reaction channel ( $n,el$ ) shows a relative error of about 7% up to an energy of 20 MeV. One can see that the JEFF-3.1 and a recent evaluation of Karlsruhe [5] are within the uncertainties. Above 20 MeV the error goes up to 15% whereas only one isotope, i.e. natural copper at 136 MeV, contributes to the calculation.

**Figure 6.** ( $n,inl$ ) with scaling factor = 1.002**Figure 7.** ( $n,2n$ ) with scaling factor = 0.980

For the inelastic cross section channel ( $n, inl$ ) the mean relative error is about 12% and for the ( $n, 2n$ ) reaction channel about 25%.

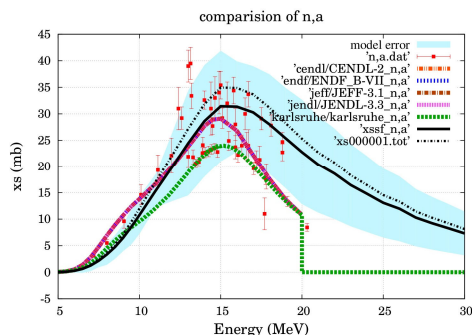


Figure 8. ( $n, \alpha$ ) with scaling factor = 0.899

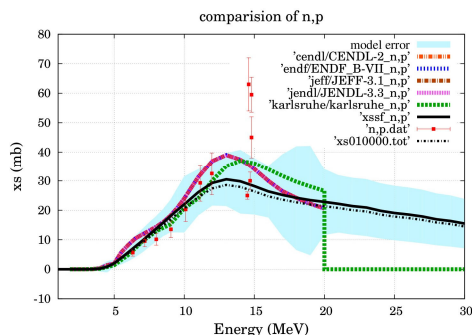


Figure 9. ( $n, p$ ) with scaling factor = 1.068

Both the ( $n, \alpha$ ) and ( $n, p$ ) reaction channels show a mean uncertainty of about 40%. With regard to the global ansatz for the model defects and the number of near by isotopes used for the calculation a relative error of 40% for the ( $n, \alpha$ ) and ( $n, p$ ) reaction is not large. In general the total and the elastic cross sections are described very well by the model. Also the inelastic scattering and ( $n, 2n$ ) reactions are well reproduced by TALYS. The evaluated files like JEFF-3.1 and Karlsruhe evaluation [5], which was based on calculations with the code GNASH, are within the error bands of our estimate.

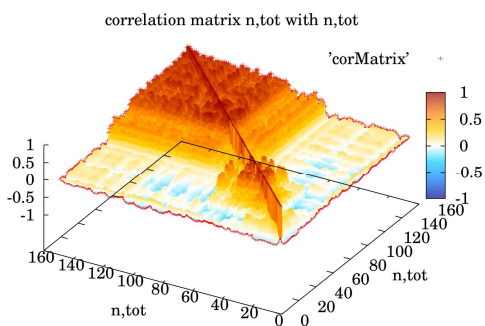


Figure 8. correlation ( $n, tot$ ) with ( $n, tot$ )

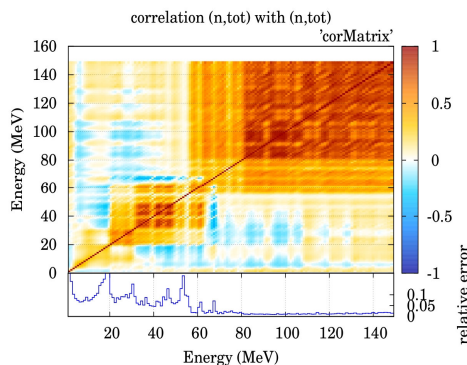


Figure 9. correlation ( $n, tot$ ) with ( $n, tot$ )

Figs. 8 and 9 show the correlation matrix of the total cross section. A systematic failure, i.e. a slight underestimation, above 60 MeV can be seen. However, the uncertainty is only about 1.5%. Between 20 and 60 MeV a sizeable correlation is obtained due to an underestimation.

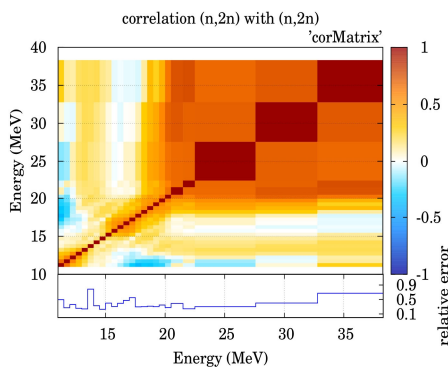


Figure 10. correlation ( $n, 2n$ ) with ( $n, 2n$ )

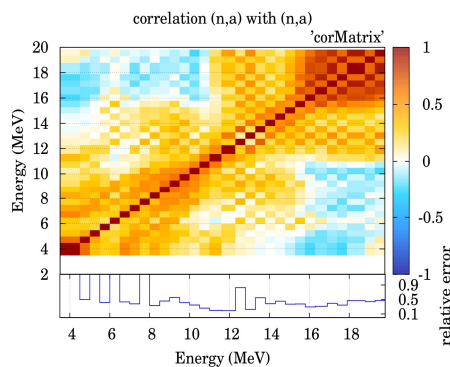
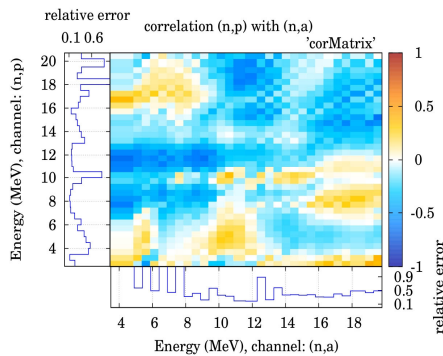


Figure 11. correlation ( $n, \alpha$ ) with ( $n, \alpha$ )

In the correlation matrix of the ( $n, 2n$ ) reaction, Fig. 10, at about 20 MeV a significant correlation is seen which is the consequence of a systematic overestimate of the calculated cross section. The peak of the ( $n, 2n$ ) reaction cross section at about 17 MeV does not show any correlation with higher energies. At about 13 MeV the rising slope of the ( $n, 2n$ ) reaction

cross section is weakly correlated with higher energies due to a global overestimation in the model.

For the  $(n,\alpha)$  reaction channel, Fig. 11, an anti-correlation of high and low energies is obtained as a result of an underestimation at lower and an overestimation at higher energies.



**Figure 12.** correlation  $(n,p)$  with  $(n,\alpha)$

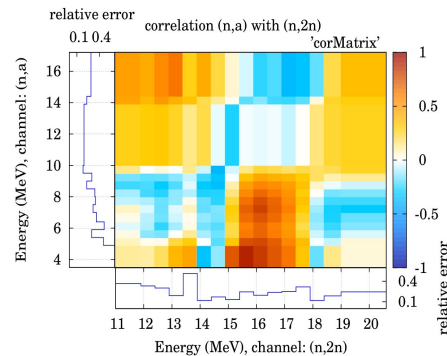


**Figure 13.** correlation  $(n,\alpha)$  with  $(n,2n)$

All correlations and cross-correlations between different reaction channels, Tab. 2, have been evaluated. In Fig. 12 we show the cross-correlation of the  $(n,p)$  and  $(n,\alpha)$  channels which are almost complete anti-correlated. Additionally the cross-correlation of  $(n,\alpha)$  and  $(n,2n)$  is shown in Fig. 13.

## Conclusions

We have slightly modified the recent formulation of model defects [1] and applied to an actual evaluation problem of neutron-induced cross sections of  $^{55}\text{Mn}$ . The comparison of the model uncertainties with several evaluated nuclear data files demonstrate that our formulation leads indeed to reasonable estimates of the model defects. The situation is expected to improve for those nuclei, where more experimental cross section data are available. Further applications to oxygen and lead isotopes are in progress.

## Acknowledgements

Work supported by the EC under the Fusion for Energy Grant F4E-2008-GRT-014.

## References

- [1] H. Leeb, D. Neudecker, Th. Srdinko, Nucl. Data Sheets 109 (2008) 2762.
- [2] A.J. Koning, S. Hilaire and M.C. Duijvestijn, TALYS: Comprehensive nuclear reaction modeling, Proceedings of the International Conference on Nuclear Data for Science and Technology - ND2004, AIP vol. 769, eds. R.C. Haight, M.B. Chadwick, T. Kawano, and P. Talou, Sep. 26 - Oct. 1, 2004, Santa Fe, USA, p. 1154 (2005).
- [3] Exfor data library, <http://www.nndc.bnl.gov/exfor/exfor00.htm>
- [4] A.J. Koning, J.-P. Delaroche, Nucl. Phys. A 713 (2003) 231.
- [5] P.Pereslavl'tsev, U.Fischer, private communication

## Determination of thermal radiative capture cross section

*Tamás Belgya*

Institute of Isotopes, HAS, P.O. Box 77, Budapest, H-1525 Hungary  
[belgya@iki.kfki.hu](mailto:belgya@iki.kfki.hu)

**Abstract:** The PGAA-NIPS facilities operated by the Institute of Isotopes at the Budapest Research Reactor's cold neutron guide are major sources of high quality radiative thermal neutron capture data. The ingredients of our methodology determining radiative neutron capture cross sections will be presented, including the sources of their uncertainties and the limitations of the applied methods. The methods worked out for separated isotope samples will also be described. Limitations due to the complex gamma-ray spectra are shown through an example of the  $^{101}\text{Ru}(n,\gamma)^{102}\text{Ru}$  reaction measured on an enriched sample at our facilities.

### Introduction

Neutron capture cross sections play an important role in several fields of application. Specifically, thermal neutron cross sections are anchor points for broad energy range differential cross section measurements. They help to decide on the existence and magnitude of negative resonances, to calculate the direct neutron capture contribution to the total capture, and in discovering systematic uncertainties in differential experiments. Detailed gamma spectroscopic information with partial gamma-ray production cross sections can be used to calculate gamma heat in power reactors and in accelerator driven systems for nuclear waste transmutation. Furthermore, it also helps to improve nuclear model calculations for nuclear astrophysics [1].

The PGAA-NIPS facilities operated by the Institute of Isotopes at the Budapest Research Reactor's cold neutron guide are major sources of high quality radiative thermal neutron capture data, and are continuously improved. In this article we will present the ingredients of our methodology in determining capture cross sections, the sources of their uncertainties and the limitations of the applied methods. We are extending our measurements of library reference spectra from elemental samples to separated isotope samples to improve the precision for the weaker  $\gamma$ -rays of a given isotope.

### Experimental facility

Our experimental facility has been already described many times [2], so we will give here only a brief summary. The neutron beam is transported by a super-mirror neutron guide from the liquid hydrogen cooled neutron source of the Budapest Research Reactor to the experimental area and it is split at the end of our guide to serve the two measuring stations. The facility is dual-purpose: neutron induced prompt gamma ray spectroscopy or NIPS, and its application, namely prompt gamma activation analysis or PGAA.

The NIPS facility has been designed for a large variety of experiments, for example studying nuclear reaction-induced prompt and delayed gamma radiation,  $\gamma$ - $\gamma$ -coincidences, and in-beam imaging of samples or following catalytic processes. The thermal equivalent neutron fluxes are  $1.5 \times 10^8 \text{ n}\cdot\text{cm}^{-2}\cdot\text{s}^{-1}$  and  $5 \times 10^7 \text{ n}\cdot\text{cm}^{-2}\cdot\text{s}^{-1}$  at the PGAA and NIPS sample positions, respectively. The new 27% efficiency PGAA main detector has an active BGO shield, which is used in Compton-suppression mode and a new 16-stage sample changer is available for elemental analysis of samples. Three other HPGe detectors are available to experiments with the NIPS station. Cross section measurements can be done on both stations depending on the nature of the experiments. We prefer to use the PGAA station for high quality prompt gamma experiments. For activation, however, the NIPS station is favoured. The sample preparation methods for the experiments were discussed earlier [3].

## Isotopic cross section determination methods and their uncertainties

Our main starting point in measuring unknown sample cross sections is the data base of elemental partial gamma-ray production cross sections that has been measured since 1995 for PGAA applications at our laboratory [4-7]. The basic comparator equations [8, 9] for the cross section evaluation of elements are

$$\sigma_{\gamma x} = \sigma_{\gamma c} \frac{n_c}{n_x} \frac{A_{\gamma x}}{A_{\gamma c}} \frac{\varepsilon(E_{\gamma c})}{\varepsilon(E_{\gamma x})} \frac{f(E_{\gamma c})}{f(E_{\gamma x})}; \quad \sigma_{\gamma} = \theta P_{\gamma} \sigma_{th} \quad (1a, 1b)$$

where  $\sigma_{\gamma}$  is the elemental partial  $\gamma$ -ray production cross section,  $n$  is the number of atoms of the element,  $A$  is the measured peak area at energy  $E_{\gamma}$ ,  $\varepsilon$  is the detector efficiency and  $f$  is a correction factor for neutron and  $\gamma$ -ray attenuations in the sample. The indexes  $c$  and  $x$  stands for the comparator and unknown, respectively. The second equation defines the elemental partial  $\gamma$ -ray production cross section with measurable nuclear constants, where  $\theta$  is the isotopic abundance and  $\sigma_{th}$  is the thermal capture cross section of the progenitor isotope of the element, while  $P_{\gamma}$  is the absolute  $\gamma$ -ray emission probability of the daughter. If the  $\sigma_{\gamma}$  is used for natural abundance elemental PGA analysis then the  $\sigma_{\gamma}$  is unique for the element and it is not necessary to know which isotope it belongs to. Isotopic identifications in our elemental library were made by R. Firestone [4, 6], which makes it possible to use it for isotopic analysis as well.

We have recently started to measure enriched sample cross sections and compositions within the EFNUDAT project. They enable to increase the precision of the partial  $\gamma$ -ray cross measurements by suppressing the presence of  $\gamma$ -rays from other isotopes and enhance weak transitions of the isotope under study. Since enriched samples are usually not available in the desired compound or mixture form for using the comparator method, other ways have to be used for the determination of partial  $\gamma$ -ray cross sections. For this purpose, we introduce the partial  $\gamma$ -ray production cross section for a mono-isotopic sample  $\sigma_{isotope-\gamma}$ . If the  $\gamma$ -ray of the isotope is observed in the elemental spectrum, it is easy to calculate the isotopic cross section  $\sigma_{isotope-\gamma}$  using the Eq. (1b).

$$\sigma_{isotope-\gamma} = \sigma_{\gamma} / \theta = P_{\gamma} \sigma_{th} \quad (2)$$

The partial  $\gamma$ -ray cross sections of other  $\gamma$ -rays in the enriched isotope spectrum can then be obtained from the following comparator equation

$$\sigma_{\gamma x} = \sigma_{\gamma c} \frac{A_{\gamma x}}{A_{\gamma c}} \frac{\varepsilon(E_{\gamma c})}{\varepsilon(E_{\gamma x})} \frac{f(E_{\gamma c})}{f(E_{\gamma x})}; \quad \sigma_{\gamma c} = \sigma_{isotope-\gamma} \quad (3)$$



Achievable uncertainties using Eq. (3) are shown in Table 1.

**Table 1.** Origin, type and estimate of uncertainties in Eq. (3).

Factor number	Type of error
1. Derived from primary (H) or secondary (Cl, N...) standards (table or dedicated experiment)	Systematic (~ 1%)
2. Uncertainty can be decreased by time or by count rate	Statistical
3. Uncertainty can be decreased to systematic level (This can be minimized by improving standards)	Statistical + [systematic, 0 at pivot ( $\equiv E_{\gamma c}$ ) point], (~ 1%)
4. Can be measured or calculated using attenuation models (Thin sample minimizes the uncertainty)	Statistical + systematic or systematic (~ 1%)

To improve the precision of the partial cross sections we have put a large effort into reducing uncertainties in the  $\gamma$ -ray intensity data for calibration sources to minimize the uncertainty of the detector efficiency ratio (3<sup>rd</sup> term in Eq. (3)).

### Improvement of data from calibration sources

The  $\gamma$ -ray detection efficiency can be determined using radioactive and high energy reaction standards. The detector efficiency in the range of few keV to 5 MeV can be measured comfortably with a set of well selected radioactive calibration sources. A recent effort coordinated by the International Atomic Energy Agency (IAEA) [10, 11] summarized those works on which we have concentrated for the higher energy radioactive sources such as <sup>56</sup>Co

[12],  $^{66}\text{Ga}$  [12] and  $^{226}\text{Ra}$  [13]. For even higher energies up to 11 MeV, radiative neutron capture reactions provide standards. The most useful standards are the  $^{14}\text{N}(n,\gamma)$ ,  $^{35}\text{Cl}(n,\gamma)$ ,  $^{48}\text{Ti}(n,\gamma)$ , and  $^{51,53,54}\text{Cr}(n,\gamma)$  reactions that have been measured with high precision at our laboratory [11]. An even newer effort was made to provide new intensities for the primary  $^{14}\text{N}(n,\gamma)$  standard reaction, which was based solely on basic principles [9, 14].

We have also put a great deal of effort in the description of detector efficiency by analytical functions for HPGe detectors [15, 16] and for the description of efficiency ratios as it appears in Eq. (1) or (3) [17, 18].

### Total capture cross sections

In the majority of the neutron capture cases the compound nucleus loses its excitation energy by releasing a series of  $\gamma$ -rays after neutron capture. In this case the cross section can be determined by the detection of  $\gamma$ -rays. In this section the methods used to do this in our laboratory are reviewed. Table 2 summarizes these methods.

**Table 2.** Methods for determination of radiative capture cross sections.

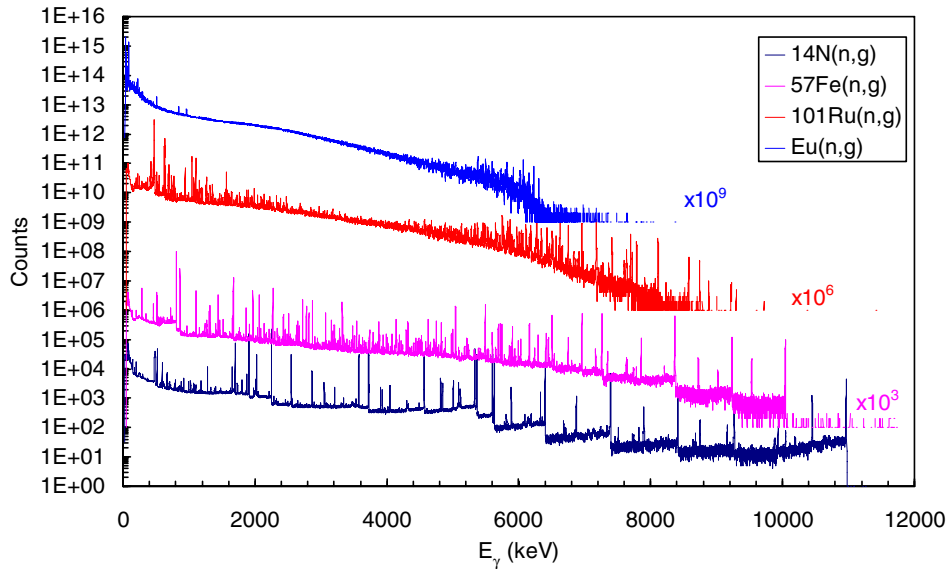
Method	Equation	Notes
1	$\sigma_{th} = \frac{\sigma_{\gamma}}{\theta P_{\gamma}}$	$P_{\gamma}$ must be known, for example from beta decay if the captured nucleus is unstable.
2	$\sigma_{th} = \sum_{f=1}^{n-1} \sigma_{\gamma C \rightarrow f} (1 + \alpha_f) (1 + PCC_f)$	The sum of all primary transitions from the capture state can be used for nuclei with a relatively simple decay scheme. Conversion $\alpha$ and pair conversion PCC coefficients must be known for methods 2-5.
3	$\sigma_{th} = \sum_{i=2}^n \sigma_{\gamma i \rightarrow g.s.} (1 + \alpha_i) (1 + PCC_i)$	The sum of all ground state transitions can be used for nuclei with a relatively simple decay scheme.
4	$Q = \min \left( \sum_{\substack{1 \leq f \leq n-1 \\ 1 \leq s \leq n-1}} (T_f - \sigma_{th}) w_{f,s} (T_s - \sigma_{th}) \right)$	Well balanced and relatively simple decay scheme. See Ref. [9, 14] for definition of $T$ and $w$ .
5	$\sigma_{th} = \sum_i E_i \sigma_{\gamma i} (1 + \alpha_i) (1 + PCC_i) / B_n$	The energy weighted sum can be used for any nuclei with resolved gamma-transitions. $E_i$ is the energy of the transition, $B_n$ is the binding energy.

These methods have already been explained in the NEMEA4 workshop [19], except method 4, which can be found in Refs. [9, 14]. The question arises: for which nuclei can these methods be applied. Before we try to explain it let us review, from a spectroscopy point of view, examples for spectra of various complexities. In Figure 1 four spectra of different complexity can be seen.

The spectrum of  $^{14}\text{N}(n,\gamma)$  is considered to be simple with about 80 transitions. The highly enriched (99.5%)  $^{57}\text{Fe}(n,\gamma)$ -spectrum is manageable with about 600 transitions. The similarly highly enriched (93.9%)  $^{101}\text{Ru}(n,\gamma)$ -spectrum is already very complex with about 1200 resolvable transitions, while the natural  $\text{Eu}(n,\gamma)$  is extremely complex, though the number of resolvable peaks is smaller than in the case of  $^{101}\text{Ru}$ .

Method 1 (activation) can be applied for any spectral complexity provided the final nucleus is not stable and after its decay it releases measurable  $\gamma$ - or X-rays. Its precision for cross section determination depends on the precision of the  $P_{\gamma}$  value. Methods 2-4 are only applicable for nuclei with a manageable decay scheme (up to ~500  $\gamma$ -rays). A limitation can be the unobserved conversion electron intensities. Method 5 is applicable for spectra with resolvable  $\gamma$ -lines (up to ~700-800  $\gamma$ -rays). An example for the  $^{58}\text{Ni}(n,\gamma)$  reaction was shown by Zoltán Kis during this workshop. Again the limitation can be the unobserved conversion electron intensities. We have to mention that this method is similar to the weighting function method used with  $\text{C}_6\text{D}_6$  detectors [20].

In more complex cases a quasi continuum of  $\gamma$ -rays appears in the spectra as seen in  $\text{Eu}(n,\gamma)$ . A possible approach is stripping or deconvolution of the spectra with a few-percent accuracy.

**Figure 1.** Spectra of various complexities.

Alternatively, measurements with  $C_6D_6$  detectors or total absorption detector are needed with a highly enriched sample.

### Completeness and Example

The Q-value test, equivalent to method 5, is used to test completeness of level schemes. The test requires a good knowledge of the total radiative capture cross section. However we can use equally well the inverse Q-value or energy weighted partial cross section sum to estimate the completeness by comparing it to a well known cross section. Let us consider now a problematic case of  $^{101}\text{Ru}(n,\gamma)$  which M. Jentsel from the ILL suggested to investigate. In the ENSDF file there are no  $\gamma$ -rays for this reaction. In the EXFOR database we can find the following data sets for thermal neutron capture (see Table 3).

Table 3. Thermal capture cross section of  $^{101}\text{Ru}$  from the EXFOR database.

$\sigma_{\text{th}}$ (b)	Facility	Method	Author	Year
3.1(9)	Reactor Oakridge	Activation	Halperin <i>et al.</i> [21]	1964
5.5(1.4)	Reactor Oakridge	Mass spectrometry	Halperin <i>et al.</i> [22]	1965

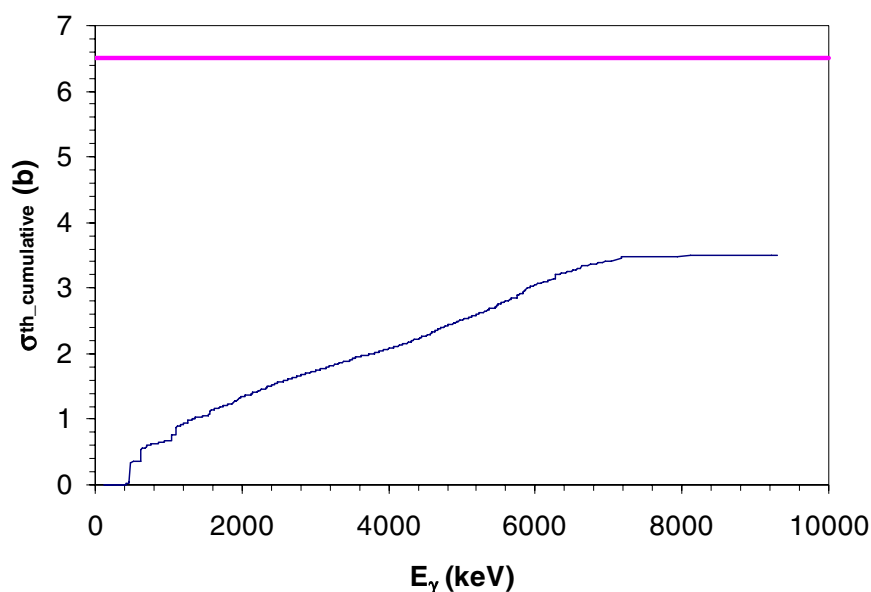
The  $^{101}\text{Ru}(n,\gamma)$  reaction was also recently measured in our laboratory. The  $\sigma_{\text{isotope}_\gamma}$  value for the transition from the first excited state to the ground state is 5.7(5) b [6, 10]. This means that due to method 3 the total thermal neutron capture cross section must be higher. In fact with the few known ground state transitions observed in the present work it is higher than 6.5(6) b, which is still in agreement with the mass spectrometry value of Halperin *et al.* [22].

We can use method 5 to calculate the cumulative sum of the energy weighted partial  $\gamma$ -ray cross sections as a function of the energies for the observed  $\gamma$ -rays ordered in increasing energy.

$$\sigma_{\text{th\_cumulative}}(E_{\gamma,i}) = \sum_{k \leq i} \frac{E_{\gamma,k} \sigma_{\gamma,k}}{B_n} \quad (4)$$

where we have used our measured  $\sigma_{\text{isotope}_\gamma}$  values. This cumulative plot, which neglects the possible internal conversion corrections, can be seen in Fig. 2 together with a horizontal line which represents the method 3 sum of partial  $\gamma$ -ray cross sections of the known ground state transitions in  $^{102}\text{Ru}$ . This latter value is much higher than the energy weighted cumulative sum (3.5(5) b), which in turn seems to be rather close to Halperin's activation value. We have to note that some weaker  $\gamma$ -rays could not be identified in our spectrum. As a summary, the nuclear decay scheme of  $^{101}\text{Ru}(n,\gamma)^{102}\text{Ru}$  reaction is rather incomplete. Its completeness is only about 50% based on the 3.5/6.5 ratio. The unresolved  $\gamma$ -rays should be located in the 2-5 MeV region and they make up a quasi continuum. To estimate their possible contribution one has to use modeling of the decay scheme such as DICEBOX, which is presented by Becvar and Krticka during this workshop [23] and also was presented in Ref. [24].

**Figure 2.** Cumulative sum of the energy-weighted partial  $\gamma$ -ray cross sections as a function of the energies for the observed  $\gamma$ -rays ordered in increasing energy for the  $^{101}\text{Ru}(n,\gamma)^{102}\text{Ru}$  reaction.



## Conclusion

Gamma ray spectrometry with a high resolution germanium detector provides powerful methods for the determination of thermal neutron radiative capture cross sections. While the activation method (method 1) is applicable for any isotopes which result in unstable daughter nuclei, the prompt  $\gamma$ -ray spectroscopy (method 2-5) is presently only useful for isotopes that yield not very complex  $\gamma$ -ray spectra. In the case of complex spectra, modeling of the decay scheme may provide a solution for the estimation of the contribution of the quasi continuum of  $\gamma$ -ray spectra.

## Acknowledgement

Support by the EFNUDAT (No. FP6-036434) and by the NAP VENEUS05 (No. OMFB/00184/2006) projects are acknowledged.

## References

- [1] Belgya, T., E. Uberseder, D. Petrich, and F. Kappeler. *Thermal Neutron Capture Cross Section of  $^{22}\text{Ne}$* . in *13th Int. Symposium on Capture Gamma-Ray Spectroscopy and Related Topics*. Cologne, Germany 25-29 August 2008: AIP Conf. Proc., 367-371(2009).
- [2] Révay, Z., T. Belgya, Z. Kasztovszky, J.L. Weil, and G.L. Molnár, *Cold neutron PGAA facility at Budapest*. Nuclear Instruments & Methods in Physics Research Section B-Beam Interactions with Materials and Atoms, **213**, 385-388(2004).
- [3] Belgya, T. *Target preparation for in-beam thermal neutron capture experiments*. in *EFNUDAT Fast Neutrons, Scientific Workshop on Neutron Measurements, Theory and Applications Nuclear Data for Sustainable Nuclear Energy*. Geel, Belgium, 28 – 30 April, 2009, 21-26(2010).
- [4] Choi, H.D., R.B. Firestone, R.M. Lindstrom, G.L. Molnár, S.F. Mughabghab, R. Paviotti-Corcuera, Z. Révay, A. Trkov, V. Zerkov, and C. Zhou, *DATABASE OF PROMPT GAMMA RAYS FROM SLOW NEUTRON CAPTURE FOR ELEMENTAL ANALYSIS: INTERNATIONAL ATOMIC ENERGY AGENCY*, VIENNA, 2007. 1-251(2007).
- [5] Molnár, G.L., Z. Révay, T. Belgya, and R.B. Firestone, *New catalog of Neutron Capture  $\gamma$  rays for Prompt Gamma Activation Analysis*. Journal of Nuclear Science And Technology, supplement, **2**, 1338-1343(2002).
- [6] Révay, Z., R.B. Firestone, T. Belgya, and G.L. Molnár, *Prompt Gamma-Ray Spectrum Catalog*, in *Handbook of Prompt Gamma Activation Analysis with Neutron Beams*, G.L. Molnár, Editor. Kluwer Academic Publishers, Dordrecht, Boston, London. 173-366(2004).

- [7] Révay, Z. and G.L. Molnár, *Standardisation of the prompt gamma activation analysis method*. Radiochimica Acta, **91**(6), 361-369(2003).
- [8] Révay, Z., *Determining Elemental Composition Using Prompt,gamma Activation Analysis*. Analytical Chemistry, **81**, 6851-6859(2009).
- [9] Belgya, T., *New gamma-ray intensities for the N-14(n,gamma)N-15 high energy standard and its influence on PGAA and on nuclear quantities*. Journal of Radioanalytical and Nuclear Chemistry, **276**(3), 609-614(2008).
- [10] Bé, M.M., V.P. Chechev, R. Dersch, O.A.M. Helene, R.G. Helmer, M. Herman, S. Hlavac, A. Marcinkowski, G.L. Molnár, A.L. Nichols, E. Schönfeld, V.R. Vanin, and M.J. Woods, *Update of X-ray and gamma ray decay data standards for detector calibrations and other applications*. Vol. I and II. Vienna: IAEA(2007).
- [11] Molnár, G.L., Z. Révay, and T. Belgya, *Precise determination of gamma-ray intensities for high-energy calibration standards*, Summary report of the third research co-ordination meeting on Update of X- and gamma-ray decay data standards for detector calibration and other applications, IAEA, INDC(NDS)-437, 23-36(2002).
- [12] Baglin, C.M., E. Browne, E.B. Norman, G.L. Molnár, T. Belgya, Z. Révay, and F. Szelecsényi, *Ga-66: a standard for high-energy calibration of Ge detectors*. Nuclear Instruments & Methods in Physics Research Section a- Accelerators Spectrometers Detectors and Associated Equipment, **481**(1-3), 365-377(2002).
- [13] Molnár, G.L., Z. Révay, and T. Belgya. *New intensities of high energy gamma-ray standards*. in *11th International Symposium on Capture Gamma-Ray Spectroscopy and Related Topics*. Pruhonice near Prague, Czech republic: World Scientific, New Jersey, London, Singapore, Hong Kong, 522-530(2003).
- [14] Belgya, T., *Improved accuracy of gamma-ray intensities from basic principles for the calibration reaction  $^{14}\text{N}(n,g)^{15}\text{N}$* . Physical Review C, **74**, 024603-1-8(2006).
- [15] Kis, Z., B. Fazekas, J. Östör, Z. Révay, T. Belgya, G.L. Molnár, and L. Koltay, *Comparison of efficiency functions for Ge gamma-ray detectors in a wide energy range*. Nuclear Instruments & Methods in Physics Research Section A, **418**(2-3), 374-386(1998).
- [16] Molnar, G.L., Z. Revay, and T. Belgya, *Wide energy range efficiency calibration method for Ge detectors*. Nuclear Instruments & Methods in Physics Research Section a- Accelerators Spectrometers Detectors and Associated Equipment, **489**(1-3), 140-159(2002).
- [17] Révay, Z., *Calculation of uncertainties in prompt gamma activation analysis*. Nuclear Instruments & Methods in Physics Research Section a- Accelerators Spectrometers Detectors and Associated Equipment, **A 564**(4-6), 688-697(2006).
- [18] Kis, Z., T. Belgya, L. Szentmiklósi, and F. Gunsing. *Determination of the total neutron capture cross section for  $^{58}\text{Ni}(n,g)^{59}\text{Ni}$  reaction*. in *in this proceeding*, (2010).
- [19] Belgya, T., P. Schillebeeckx, and A. Plompen. *Thermal neutron capture cross section measurements using a cold neutron beam*. in *Neutron Measurements, Evaluations and Applications*. Prague, Czech Republic, 16-18 October 2007, JRC Scientific and Technical Reports, EUR 23235 EN: European Communities, 2008, 31-34(2008).
- [20] Borella, A., G. Aerts, F. Gunsing, M. Moxon, P. Schillebeeckx, and R. Wynants, *The use of  $^{6}\text{D}6$  detectors for neutron induced capture cross-section measurements in the resonance region*. Nuclear Instruments & Methods in Physics Research Section A, **577**, 626-640(2007).
- [21] Halperin, J., C.R. Baldock, and J.H. Oliver, Oak Ridge National Lab. Reports, 3679, 12(1964).
- [22] Halperin, J., C.R. Baldock, and J.H. Oliver, Oak Ridge National Lab. Reports, 3832, 4(1965).
- [23] Becvar, F. and M. Krlicka. *Slow-Neutron Capture: Present Status and Outlook*. in *EFNUDAT Slow and Resonance Neutrons, a Scientific Workshop on Nuclear Data Measurements, Theory and Applications*. Budapest, Hungary, 23-25 September 2009 (2009).
- [24] Krlicka, M., R.B. Firestone, D.P. McNabb, B. Sleaford, U. Agvaanluvsan, T. Belgya, and Z.S. Revay, *Thermal neutron capture cross sections of the palladium isotopes*. Physical Review C, **77**(5), 054615(2008).

## Determination of the total neutron capture cross section for $^{58}\text{Ni}(n,\gamma)^{59}\text{Ni}$ reaction

Z. Kis<sup>1)</sup>, T. Belgya<sup>1)</sup>, L. Szentmiklósi<sup>1)</sup>, F. Gunsing<sup>2)</sup>

- 1) Institute of Isotopes, Hungarian Academy of Sciences, 29-33 Konkoly-Thege Miklós u., Budapest, Hungary, H-1121  
 2) CEA/Saclay, Gif-sur-Yvette, France, F-91191  
[zkis@iki.kfki.hu](mailto:zkis@iki.kfki.hu)

**Abstract:** The thermal neutron capture cross section of  $^{58}\text{Ni}$  ( $\sigma_{th}$ ) has been determined from the radiative neutron capture reaction using a beam of cold neutrons at the PGAA facility of the Institute of Isotopes, Budapest, Hungary. The new experimental value is in agreement with the recommended value (Mughabghab) but higher than the most precise and most recent value of Raman. A detailed description of the analysis is given, which includes a) the calculation of relative efficiency of the detector system based on new calibration intensities from  $^{14}\text{N}(n,\gamma)^{15}\text{N}$  reaction; b) details of the  $^{58}\text{Ni}(n,\gamma)^{59}\text{Ni}$  measurement and the evaluation of the partial  $\gamma$ -ray production and total capture cross sections; and c) the comparison of results with former measurements. The higher intensities from the  $^{14}\text{N}(n,\gamma)^{15}\text{N}$  reaction used for efficiency calibration yielded significantly lower efficiency values in the energy range  $\sim 2$  MeV – 11 MeV. As an inherent effect, the partial  $\gamma$ -ray production cross sections,  $\sigma_{\gamma i}$  for  $^{58}\text{Ni}(n,\gamma)^{59}\text{Ni}$  reaction came out larger, and hence the total capture cross-section is also higher than Raman's value. The measured values for  $\sigma_{th}$  determined from  $\Sigma\sigma_{\gamma i}$  (primary),  $\Sigma E_{\gamma} \sigma_{\gamma i} / S_n$ , and  $\Sigma\sigma_{\gamma i}$  (ground state) are lower limits because the detection conditions make practically impossible to detect all of the possible  $\gamma$ -transitions. Estimation for the missing fraction could only be given based on theoretical considerations.

### Introduction

The precise determination of the thermal neutron capture cross sections finds its importance in various fields of applications and theories, which include reactor design, nuclear waste transmutation, astrophysics and medicine. In this paper the thermal neutron capture cross section of  $^{58}\text{Ni}$  ( $\sigma_{th}$ ) determined from radiative neutron capture reaction using cold neutron beam at the PGAA facility of the Institute of Isotopes, Budapest is presented.

### Methods for determining the total neutron capture cross section

The cross section of the neutron capture can be obtained in several ways using the prompt gamma radiation emerging during the irradiation of the material with a neutron beam [1]. Theoretically, the sum of all the transitions depopulating the capture state (PM – primaries) or populating the ground state (GS) are good measures of the total capture cross sections. Other possibility is the use of the energy weighted sum of all transitions in the level scheme (we call it inverse  $Q$ -value formula).

However, in practical cases there are issues to be addressed. If PM and GS transitions are used, the knowledge of the level scheme of the nucleus is necessary. For a nucleus with complicated level scheme this identification is far not obvious or impossible. Applying the inverse  $Q$ -value method the binding energy of the neutron must be precisely known. Moreover, there are cases when alternative decay processes are to be known, such as electron conversion and pair conversion to be able to obtain meaningful results from the above formulas. In Table 1 the equations and the summary of the methods are given.

As one can see the calculations are based on key quantities called partial  $\gamma$ -ray production cross sections ( $\sigma_{\gamma i}$ ). These are the quantities we can measure during the experiments [2]. In general,  $\sigma_{\gamma i}$  is a combination of atomic and nuclear constants, and equals to

$$\sigma_{\gamma i} = \Theta P_{\gamma i} \sigma_{th} \quad (1)$$

for chemical elements, where  $\Theta$  is the *isotopic* abundance,  $P_{\gamma i}$  is the absolute gamma emission probability and  $\sigma_{th}$  is the total capture cross section of the *isotope*. For highly enriched materials,  $\Theta$  reduces to 1.

**Table 1.** Overview of the methods which can be used to obtain the total neutron capture cross sections via the detection of prompt gamma rays emitted from the compound nucleus

Method	Equation	Notes
PM	$\sigma_{th} = \sum_{i=1}^{n-1} (1 + \alpha_i)(1 + PCC_i) \cdot \sigma_{\gamma(CS \rightarrow f)}$	The sum of all primary transitions from the capture state can be used for nuclei with relative simple decay scheme. Knowledge of conversion coefficients is not important.
GS	$\sigma_{th} = \sum_{i=2}^n (1 + \alpha_i)(1 + PCC_i) \cdot \sigma_{\gamma(i \rightarrow GS)}$	The sum of all ground state transitions can be used for nuclei with relative simple decay scheme. Conversion coefficients must be known.
Inv-Q	$\sigma_{th} = \sum_i \frac{E_i}{B_n} \cdot (1 + \alpha_i)(1 + PCC_i) \cdot \sigma_{\gamma_i}$	The energy weighted sum can be used for any nuclei with resolved gamma-transitions. $E_i$ is the energy of the transition, $B_n$ is the binding energy. Knowledge of conversion coefficients is not so important, it is weighted out.

### Determining the partial $\gamma$ -ray production cross sections

The best way to obtain the value of any unknown partial  $\gamma$ -ray production cross section,  $\sigma_{\gamma X}$ , is the use of the so-called internal comparator technique [2]. In this calculation the unknown  $\sigma_{\gamma X}$  at energy  $E_{\gamma X}$  is determined relative to a well known partial  $\gamma$ -ray production cross section,  $\sigma_{\gamma C}$ , of the comparator material at energy  $E_{\gamma C}$  according to the following equation:

$$\sigma_{\gamma X} = \sigma_{\gamma C} \cdot \frac{A_{\gamma X}}{A_{\gamma C}} \cdot \frac{n_C}{n_X} \cdot \frac{\varepsilon(E_{\gamma C})}{\varepsilon(E_{\gamma X})} \cdot \frac{f(E_{\gamma C})}{f(E_{\gamma X})}, \quad (2)$$

where  $C$  and  $X$  denote the comparator and unknown, respectively. The ratios on the right side stand for count rates ( $A_{\gamma X}$  and  $A_{\gamma C}$ ), for number of atoms of the elements irradiated ( $n_X$  and  $n_C$ ), for detector efficiency values at the different energies ( $\varepsilon(E_{\gamma X})$  and  $\varepsilon(E_{\gamma C})$ ), and for gamma self-absorption and neutron self-shielding corrections ( $f(E_{\gamma X})$  and  $f(E_{\gamma C})$ ).

The most effective use of the comparator technique is if the irradiated material is a homogeneous chemical compound with precisely known stoichiometry, because in such cases the atomic ratio is assumed to be an exact integer, and hence the result could be given with smaller uncertainty. The proper choice of the comparator peak, for which the partial  $\gamma$ -ray cross section,  $\sigma_{\gamma C}$  is very well known, helps to keep the uncertainty of  $\sigma_{\gamma X}$  low. The statistical uncertainties of the peak count rates can be lowered by increasing the acquisition time. Instead of measuring absolute efficiency it is sufficient to obtain the relative efficiency, which can be accurate at the level of 1% over most of the 11-MeV energy range. Moreover, the effect of neutron self-shielding is smaller because the local neutron flux is the same for both components of the material.

### Calculation of relative efficiency based on new intensities of $^{14}\text{N}(n,\gamma)^{15}\text{N}$ reaction

One of the most important factors affecting the uncertainty of the partial  $\gamma$ -ray production cross sections is the uncertainty of relative efficiency. To keep it as low as possible we need well known intensity standards for a range of energy extending from  $\sim 50$  keV up to  $\sim 11$  MeV. This wide range can only be covered by the joint use of radioactive sources and  $(n,\gamma)$  reactions. Among the suitable reactions the most important is the  $^{14}\text{N}(n,\gamma)^{15}\text{N}$ , because of its 16 transitions with well known intensities ranging quite evenly from 1678 keV to 10829 keV [3,4]. As the range covered by radioactive sources extends up to  $\sim 3$  MeV, there is an overlap between the two datasets. This is a basic requirement of our efficiency-calculation procedure. The recommended intensity values for  $^{14}\text{N}(n,\gamma)^{15}\text{N}$  reaction are published by Journey et al. [4]. Recently a new measurement and its evaluation were published by Belgya [5], who showed that there are deficiencies among the recommended values. Using the CIS (Cross Intensity Sum) method it was pointed out that for the energy range above  $\sim 3$  MeV the transitions should have higher intensities than assumed earlier. The plot of the ratio between Journey's and Belgya's values is presented in Figure 1. One can readily see the effect of the higher intensities on detector efficiency if using the new set: we will get higher values for ranges

where the ratio is above 1; and, in contrast to this we will obtain lower values for ranges where the ratio is below 1.

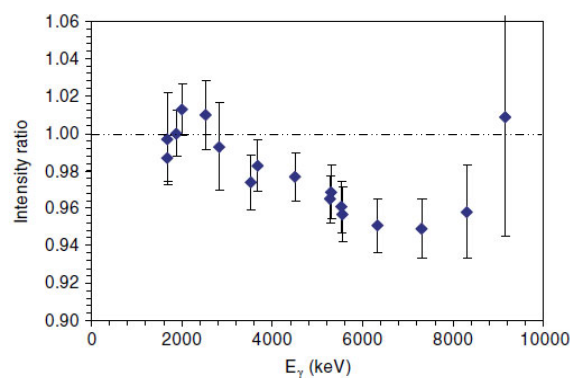


**Figure 1.** Ratios between transition intensities in  $^{14}\text{N}(n,\gamma)^{15}\text{N}$  reaction (calculated as Jurney's values / Belgya's values)

This change will alter the relative efficiencies according to the choosing of the pivot energy, to which all the other efficiency values are compared.

## Experiments

### Sample description

Our measured sample was a pressed metal target enriched in  $^{58}\text{Ni}$  up to 99.5%. Its weight was 2.0679 g, and had a diameter of 20 mm and a thickness between 0.77-0.78 mm (because of some surface depression as one can see in Figure 2.).

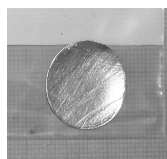


**Figure 2.** Photo of the pressed metal target enriched in  $^{58}\text{Ni}$  up to 99.5%.

### Experimental conditions

Samples were irradiated at the Budapest PGAA facility [6,7,8]. The aperture of the neutron beam was set to  $10\text{ mm}^2$  during the measurement because of the count rate limitations of the electronics. The thermal-equivalent neutron flux at the target position was  $\sim 1.2 \times 10^8\text{ cm}^{-2}\text{ s}^{-1}$ . The vacuum in the target chamber was 2 mbar. As a  $\gamma$ -ray detector an n-type coaxial HPGe was used, together with BGO shielding annulus in Compton-suppression mode. The Compton-suppressed HPGe detector has been precisely calibrated [9].

### Internal comparator method for enriched isotopes

In the case of  $^{58}\text{Ni}(n,\gamma)^{59}\text{Ni}$  reaction we applied a slightly modified internal comparator method. As internal comparator we have chosen the same material, i.e.  $^{58}\text{Ni}$ , because partial  $\gamma$ -ray production cross sections are well known from standardization measurements on natural Ni element. Spectroscopic data libraries for the stable elements were developed at our laboratory [10].

The  $\sigma_{\gamma C}$  of the enriched  $^{58}\text{Ni}$  at the comparator energy ( $E_{\gamma C} = 464.9\text{ keV}$ ) can be calculated using Eq. (1) from the elemental  $\sigma_{\gamma C}(\text{Ni})$  and the isotopic abundance of  $^{58}\text{Ni}$  as  $\sigma_{\gamma C}(^{58}\text{Ni}) = 0.843 \pm 0.013\text{ b} / 0.68077 = 1.238 \pm 0.013\text{ b}$ . Then the internal comparator method, Eq. (2) can be applied with  $\sigma_{\gamma C}(^{58}\text{Ni}) = 1.238\text{ b}$  as a comparator value for the enriched isotope data to obtain partial gamma ray cross sections for weak transitions that could not be observed in the elemental spectrum. In this comparison the number of irradiated atoms are the same ( $n_C = n_X$ ), therefore its ratio cancels from the further calculations.

### Relative efficiency

In Figure 3 the relative efficiency curve and its uncertainty are shown for the energy range 50 keV to 9 MeV, which fully covers the energy range of the transitions from the  $^{58}\text{Ni}(n,\gamma)^{59}\text{Ni}$  reaction. The uncertainty of the relative efficiency is below 1% for a wide range (85 keV – 7.5

MeV). Since there are correlations between the efficiency points, the uncertainty becomes small if two close-lying peaks are considered, and is exactly zero [11] at the pivot energy. The pivot energy was chosen to be equal to the comparator energy of 464.9 keV in our case. This is illustrated in Figure 3.

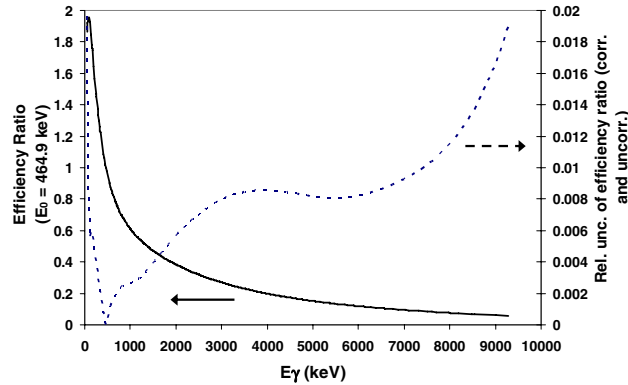


**Figure 3.** Relative efficiency function normalized to 464.9 keV, and its uncertainty for the energy range 50 - 9000 keV

### Identification of peaks and attenuation correction

The gamma-ray spectra were evaluated using the Hypermet-PC program [12]. From the resulting peak list the single and double escape peaks were first eliminated based on their 511-keV or 1022-keV energy offsets. In case of interference, the contribution of the escape peak was subtracted from the net peak area. Dedicated measurement was accomplished to find the background peaks. If present in the  $^{58}\text{Ni}(n,\gamma)^{59}\text{Ni}$  spectrum, they were discarded again. Since the enrichment was not 100% we were looking for peaks from other isotopes of Ni and from impurities. The only such isotope was found to be  $^{60}\text{Ni}$ , but only in a low amount ( $\sim 0.4$  n%).

As pointed out above we had to correct the peak areas for self-absorption of gammas and absorption of neutrons. It was carried out taking into consideration the sample geometry and the energy dependence of the attenuation.

### Results

In a very thorough paper, Raman *et al.* [13] identified the majority of the lines from the  $^{58}\text{Ni}(n,\gamma)^{59}\text{Ni}$  reaction. Based on their identification we found 55 of 57 primaries, and 42 of 44 ground state transitions. The lines not found in our work could be considered negligible, because the sum of their partial  $\gamma$ -ray production cross sections are 1.13 mb and 1.01 mb for PM and GS transitions, respectively. The number of transitions, which could be ascribed to the  $^{58}\text{Ni}(n,\gamma)^{59}\text{Ni}$  reaction is 430 ( $> 414$  from Raman's work). It was not the scope of the present work to place them into the level scheme.

The results of the calculations for the thermal neutron capture cross section are summarized in Table 2. To make the calculations comparable, the same transitions were involved into the calculations from the  $^{58}\text{Ni}(n,\gamma)^{59}\text{Ni}$  reaction for PM, GS and inverse Q methods, respectively; i.e. 55 primary, 42 ground state and altogether 430 transitions. The conversion coefficients were considered negligible. The uncertainties of the results ( $1\sigma$ ) are about 1%.

**Table 2.** Overview of the results obtained for the thermal neutron capture cross section using different ways of calculation. Two sets of data are presented according to the two sets of intensity standards from  $^{14}\text{N}(n,\gamma)^{15}\text{N}$  reaction.

$^{58}\text{Ni}(n,\gamma)^{59}\text{Ni}$	$\sigma_{th}$ (b)	
	Jurney $^{14}\text{N}$	Belgysa $^{14}\text{N}$
Primary	$4.08 \pm 0.05$	$4.26 \pm 0.05$
Ground state	$4.23 \pm 0.04$	$4.33 \pm 0.05$
Inverse Q	$4.12 \pm 0.05$	$4.29 \pm 0.05$

## Discussion

Based on the data in Table 2 the following conclusions can be drawn for the thermal neutron capture cross section values of the  $^{58}\text{Ni}(n,\gamma)^{59}\text{Ni}$  reaction:

- The obtained values are higher if the new set of intensity standards from  $^{14}\text{N}(n,\gamma)^{15}\text{N}$  reaction are used for the detector efficiency calibration. It readily comes from the fact that new intensity values are higher compared to values from Journey et al. [4], which implies a lower efficiency for almost the entire energy range.
- For PM and GS transitions, the knowledge of the level scheme is essential so that due value could be obtained. As the cross sections in Table 2 are different for both sets of older [4] and newer [5] intensity standards we can conclude that there are some discrepancies in the level scheme. In order to use the inverse Q method, however, one has to find all transitions, but the knowledge of the level scheme is not necessary (if the conversion coefficients are negligible). Therefore the difference between the cross section values could be ascribed purely to the different intensity standard sets.
- The energy sampling of the methods is different along the energy range. The PM, the GS and the inverse Q method sample more in the *higher*, more in *lower* and more *uniformly* the energy range, respectively (Figures 4a and 4b). Therefore the energy domain, where the intensity standard transitions tend to differ, will determine the biases of the methods. The calculation based on the PM transitions suffers most from this fact, because the older set of nitrogen standard is different in the higher energy range [5]. It is shown in Figure 4c, where the differences between the cumulative cross sections are presented for the older and newer intensity standard sets applying the different methods. It turns out that the distortion comes mainly from differences at the energies of 8533.8 and 8998.6 keV.

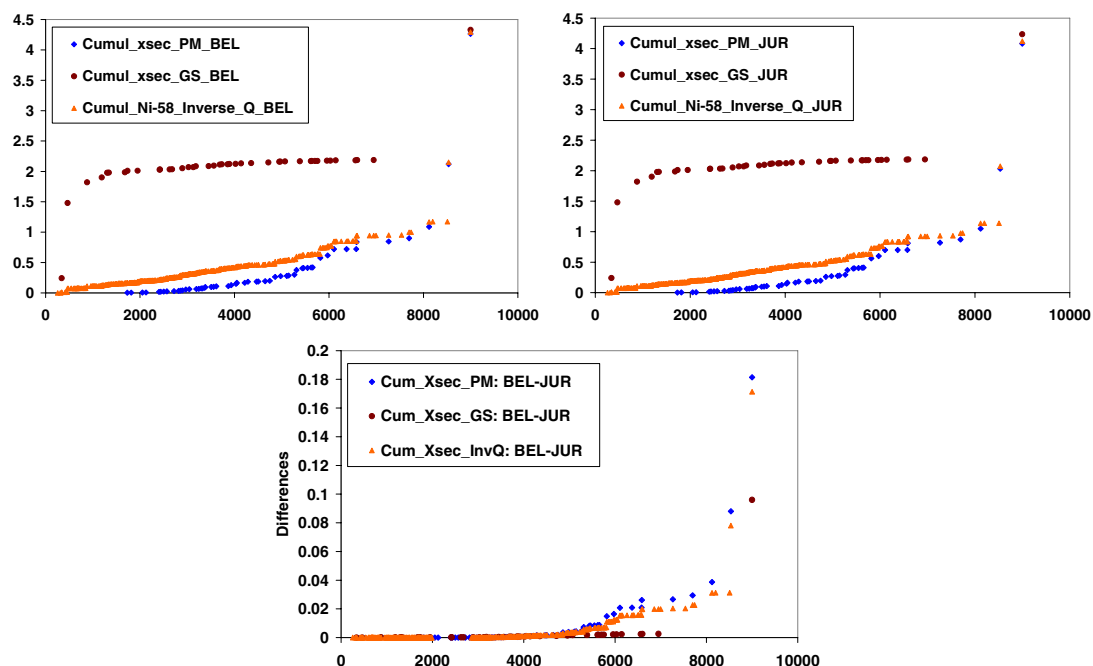


**Figure 4.** a) and b) Cumulative cross sections as a function of  $^{59}\text{Ni}$  gamma energy for the three different methods (PM, GS and Inv Q) using Journey's and Belgya's sets of  $^{14}\text{N}(n,\gamma)^{15}\text{N}$  intensities to obtain detector efficiency function; c) Differences between the cumulative cross sections using the two sets of nitrogen intensities for the three methods.

### Comparison with former results

A summary of the former measurements is shown in Table 3. The recently adopted cross section evaluated by Mughabghab [14] is  $4.37 \pm 0.1$  b, but results from Raman et al. [13], which would decrease the value, were not involved in this evaluation. Our new cross section value is in agreement with all former ones [15-20] but with considerable lower uncertainty ( $\sim 1\%$ ). Most results were based on  $^{14}\text{N}(n,\gamma)^{15}\text{N}$  intensities, but only Raman [13] and Venturini [15] used the recently recommended values of Journey et al.. Weselka [16] and Pomerance [20] applied independent methods: activation and pile oscillator.

**Table 3.** Summary of the former measurements for the thermal neutron capture cross section values of the  $^{58}\text{Ni}(n,\gamma)^{59}\text{Ni}$  reaction. (MXW means Maxwellian energy distribution of neutrons.)

Xsec (b)	Err (b)	Author	Source	Sample	Monitor
4.13	0.05	Raman, 2004	MXW th n flux: 6E11	99.93% enriched $^{58}\text{NiO}$	en. cal.: melamine ( $\text{C}_3\text{H}_6\text{N}_6$ ) int. cal.: rad sources and $^{14}\text{N}(n,\gamma)^{15}\text{N}$
4.4	0.2	Venturini, 1997	MXW th n flux: 5E11	melanine + natural Ni	en. cal.: melamine ( $\text{C}_3\text{H}_6\text{N}_6$ ) int. cal.: rad. sources and $^{14}\text{N}(n,\gamma)^{15}\text{N}$
4.6	0.3	Weselka, 1991	MXW th n flux: 4E17	Foil of 4.8 mg/cm <sup>2</sup>	Activation: Ni-58 and Fe-54
4.52	0.1	Carbonari, 1988	MXW th n flux: 5E11	melanine + natural Ni	en. and int. cal.: $^{14}\text{N}(n,\gamma)^{15}\text{N}$ and $^{35}\text{Cl}(n,\gamma)^{36}\text{Cl}$
4.5	-	Ishaq, 1977	MXW th n flux: 5E12		en. and int. cal: $^{14}\text{N}(n,\gamma)^{15}\text{N}$
4.4	-	Gippner, 1971	Th beam. No details	natural Ni	-
4.2	0.34	Pomerance, 1952	Pile oscillator	enriched NiO	Activation: Au-197

## Conclusion

The  $\sigma_{th}$  obtained is a lower limit because it can not be stated that all possible  $\gamma$ -transitions have been detected. Based on theoretical considerations the contribution of the not measurable weak transitions should be estimated and added to get to the final cross section.

## Acknowledgements

This work was supported by the EFNUDAT (No. FP6-036434) and by the NAP VENEUS05 (No. OMFB/00184/2006) projects.

## References

- [1] T. Belgya, P. Schillebeeckx, and A. Plomen, Thermal neutron capture cross section measurements using a cold neutron beam, Proc. CANDIDE workshop, NEMEA-4, Neutron Measurements, Evaluations and Applications, 2008, **EUR 23235EN**, pp. 31–34.
- [2] Zs. Révay and G.L. Molnár, Standardisation of the prompt gamma activation analysis method, *Radiochim. Acta*, **91**, 361–369 (2003).
- [3] T.J. Kennett, W.V. Prestwich, and J.S. Tsai, *Nucl. Instrum. Meth. A* **249**, 366–378 (1986).
- [4] E.T. Journey, J.W. Starner, J.E. Lynn, and S. Raman, *Phys. Rev. C* **56**, 118–134 (1997).
- [5] T. Belgya, *J. Radioanal. Nucl. Chem.* **276(3)**, 609–614 (2008).
- [6] Zs. Révay, T. Belgya: *Principles of PGAA method*, in: Handbook of Prompt Gamma Activation Analysis with Neutron Beams, (G.L. Molnár ed.), Kluwer Academic Publishers, Dordrecht/Boston/New York, 2004, pp.1–30.
- [7] Zs. Révay, T. Belgya, Zs. Kasztovszky, J.L. Weil, and G.L. Molnár, *Nucl. Instrum. Meth. B* **213**, 385–388 (2004).
- [8] Zs. Révay, T. Belgya, L. Szentmiklósi, and Z. Kis, *J. Radioanal. Nucl. Chem.* **278**, 643–646 (2008).
- [9] G.L. Molnár, Z. Révay, T. Belgya, *Nucl. Instrum. Meth. A* **489**, 140–159 (2002).
- [10] H.D. Choi et al.: Database of prompt gamma rays from slow neutron capture for elemental analysis, International Atomic Energy Agency, Vienna, 2007.
- [11] Zs. Révay, *Nucl. Instrum. Meth A* **564**, 688–697 (2006).
- [12] Zs. Révay, T. Belgya, and G.L. Molnár, *J. Radioanal. Nucl. Chem.* **265**, 261–265 (2005).
- [13] S. Raman et al., *Phys. Rev. C* **70**, 044318 (2004).
- [14] S.F. Mughabghab, Thermal Neutron Capture Cross Sections, Resonance Integrals and G-Factors, International Atomic Energy Agency INDC(NDS)-440, Vienna, 2003.
- [15] L. Venturini and B.R.S. Pecequilo, *Appl. Radiat. Isot.* **48(4)**, 493–496 (1997).
- [16] D. Weselka, B. Schneck, W. Ruehm, L. Zerle, G. Korschinek, E. Nolte, and H. Vonach, Conf.on Nucl.Data for Sci. and Technol., Juelich, p.559 (1991).
- [17] A.W. Carbonari and B.R. Pecequilo, Conf. on Nucl. Data for Sci. and Technol., Mito, p.133 (1988).
- [18] A.F.M. Ishaq, A. Robertson, W.V. Prestwich, T.J. Kennett, *Z. Phys. A* **281**, 365 (1977).
- [19] P.Gippner, H.Jaeger, W.Rudolph, Kernforschung Rossendorf Reports, No. **215** (1971).
- [20] H. Pomerance, *Phys. Rev.* **88(2)**, 412–413 (1952).

## Preparatory experiments for cold-neutron induced fission studies at IKI

*A. Oberstedt<sup>1)</sup>, S. Oberstedt<sup>2)</sup>, R. Billnert<sup>1)</sup>, J. Karlsson<sup>1)</sup>, X. Ledoux<sup>3)</sup>,  
J.-G. Marmouget<sup>3)</sup>, and F.-J. Hamsch<sup>2)</sup>*

- 1) School of Science and Technology, Örebro University, Fakultetsgatan 1, 70182 Örebro, Sweden
  - 2) European Commission, Joint Research Centre, Institute for Reference Materials and Measurements, Retieseweg 111, 2440 Geel, Belgium
  - 3) CEA/DAM Ile-de-France, 91297 Arpajon Cedex, France
- [andreas.oberstedt@oru.se](mailto:andreas.oberstedt@oru.se)

**Abstract:** Prior to an experiment at the 10 MW research reactor of IKI in Budapest, dedicated to the simultaneous measurement of the fission-fragment mass and kinetic energy distribution as well as prompt fission  $\gamma$ -rays from thermal (cold) neutrons on  $^{235}\text{U}$  and scheduled for the beginning of the year 2010, we have performed several preparatory studies. First we have characterized three coaxial  $1.5'' \times 1.5''$   $\text{LaCl}_3:\text{Ce}$  detectors in terms of energy conversion and resolution, linearity, dynamical range, intrinsic efficiency, timing resolution and intrinsic radioactivity. These detectors were then recently tested in a fast-neutron environment with the 4 MV Van de Graaff accelerator at CEA/DAM Ile-de-France in order to investigate a possible built-up of background components in the detector material due to neutron capture as well as their neutron/ $\gamma$  separation properties by means of the time-of-flight technique. Below we report on the results that have been obtained so far.

### Introduction

About ten percent of the total energy release in the core of a standard nuclear reactor is accounted for by the  $\gamma$ -ray energy released in fission, of which 40% or 8 MeV result from the prompt  $\gamma$ -decay of fission products [1]. Although the characteristics of the  $\gamma$ -ray emission, e.g. multiplicity, total energy and energy distribution, are fairly well known for neutron capture and inelastic neutron scattering, fission  $\gamma$ -rays are the major source of uncertainty in the modelling of  $\gamma$ -heating. Since four out of six nuclear systems identified by the Generation-IV international forum are fast reactors, a very innovative core design is required in order to respond to the high performance expected of those future systems.

One particular challenge in modelling new generation reactor neutron kinetics is to calculate the  $\gamma$ -heat deposition in e.g. steel and ceramic reflectors without  $\text{UO}_2$  blankets. According to Ref. [2] those modern designs require  $\gamma$ -heating to be known with an uncertainty as low as 7.5% ( $1\sigma$ ). The comparison of various benchmark experiments with calculated  $\gamma$ -heating shows a systematic underestimate ranging from 10 to 28% for the main fuel isotopes  $^{235}\text{U}$  and  $^{239}\text{Pu}$ . This is attributed to deficiencies in  $\gamma$ -ray production data in evaluated nuclear data files [3]. Data found in modern nuclear-data libraries all date back to experiments performed in the early 1970's [4–6]. In those experiments NaI scintillation detectors were used as  $\gamma$ -ray spectrometer with an ionization chamber as fission trigger. However,  $\text{LaCl}_3$  detectors are today proven to be inferior with respect to both energy and timing resolution as well as efficiency.

Therefore, requests for new measurements on prompt  $\gamma$ -ray emission in the reactions  $^{235}\text{U}(n,f)$  and  $^{239}\text{Pu}(n,f)$  have been formulated and included in the Nuclear Data High Priority Request List of the Nuclear Energy Agency (NEA, Req. ID: H.3, H.4) [7]. In a recent modelling exercise of neutron emission from fission fragments by means of a Monte-Carlo approach [8] the authors achieved a reasonably good description of the average  $\gamma$ -energy released in fission, but they were unable to reproduce the experimentally obtained dependence as a function of the fission fragment mass. They recommended putting more work in clarifying the competition between neutron and  $\gamma$ -ray emission during fission fragment de-excitation.

A major difficulty in such measurements is, beside the need to obtain a sufficient mass resolution for fission fragments, the clear suppression of background  $\gamma$ -rays induced by prompt fission neutrons in the  $\gamma$ -detector. A usual method here is to discriminate  $\gamma$ -rays and

neutrons by their different time-of-flight. The quality of discrimination is strongly coupled to the timing resolution of the detector, which is for NaI detectors usually not better than 5 ns. A promising step towards better data might be achieved by using the recently developed Cerium-doped Lanthanum Chloride ( $\text{LaCl}_3:\text{Ce}$ ) crystal scintillation detectors, which provide a timing resolution around 500 ps [9,10] together with a 40% better energy resolution compared to NaI, i.e. less than 4% (FWHM) compared to 6.5% at 662 keV ( $^{137}\text{Cs}$ ) [11]. For this purpose three coaxial 1.5" x 1.5" (38 mm in diameter and 38 mm in thickness)  $\text{LaCl}_3:\text{Ce}$  detectors [12] were purchased at EC-JRC IRMM in Geel, Belgium.

So far the detectors have been characterized and tested in strong neutron fields. Below we present the properties of these detectors and discuss their capability with respect to the intended fission  $\gamma$ -ray studies. We start, however, with a brief description of the planned experiments at the 10-MW research reactor at IKI Budapest.

### Fission-fragment and $\gamma$ -spectrometry at IKI

Post-neutron fission fragment distributions will be measured by means of time-of-flight in conjunction with a kinetic energy measurement. From both quantities the fission fragment mass may be calculated. The kinetic energy will be measured by one of the 19 silicon detectors, with an area of  $450 \text{ mm}^2$ , placed at a distance of 50 cm from the fission target. For this purpose the fission-fragment spectrometer VERDI [13] will be employed, with polycrystalline chemical vapour-deposited (pcCVD) diamond detectors as fission trigger. The corresponding time-of-flight is determined by the difference between the time of arrival of a fission fragment in an energy detector and the time stamp created by the corresponding fragment in a diamond detector, where the fission target is practically placed on top. The effective mass of the  $^{235}\text{U}$  sample covered by the time pick-up detector will be  $113 \mu\text{g}$ . The thermal neutron flux of  $7 \times 10^7 \text{ cm}^{-2} \text{ s}^{-1}$  will provide a fission rate of  $1.18 \times 10^4 \text{ s}^{-1}$ . Taking into account the geometrical efficiency of the spectrometer we expect a count rate of about  $12 \text{ s}^{-1}$ . During the granted 10 days of beam-time the total number of fission fragments will be around  $8.5 \times 10^6$ , i.e. about 8500 at an emission yield of 0.1 % corresponding mass number,  $A$ , around 85.

In a parallel experiment  $\gamma$ -rays will be measured in coincidence with the fission time stamp provided by the diamond detector. As  $\gamma$ -ray detectors we will use 3  $\text{LaCl}_3:\text{Ce}$  scintillation detectors placed at a distance of 50 cm from the fission sample. The detectors will be shielded against thermal neutrons by a cadmium layer and a  $^6\text{Li}$  cap. The intrinsic background of this particular scintillation material will be efficiently suppressed by applying the coincidence condition with the fission trigger detector. With an effective efficiency of  $1.45 \times 10^{-4}$  of the  $\gamma$ -ray detectors and a fission  $\gamma$ -ray multiplicity of about 7, one obtains a count rate of approximately 10  $\gamma$ -rays/s. Thus, during the granted beam-time we expect to collect a total number of about  $10^7$  detected  $\gamma$ -rays per detector.

Both parts of the proposed experiment, which is scheduled for February 2010, will be performed with two separate data acquisition systems using the same fission event trigger.

### Characterization of $\text{LaCl}_3:\text{Ce}$ detectors

The cylindrical  $\text{LaCl}_3$  crystals are glued to photomultiplier tubes (PMT) of type Photonis XP2500/FB. To its base only one signal output is connected, in addition to the connector for applying the high voltage. Therefore, the output signal had to be split for a simultaneous measurement of time and energy. During the study of the detector performances the bias voltage, amplification of the signals and the shaping time were varied. Different radioactive sources ( $^{22}\text{Na}$ ,  $^{54}\text{Mn}$ ,  $^{57}\text{Co}$ ,  $^{60}\text{Co}$ ,  $^{133}\text{Ba}$ ,  $^{137}\text{Cs}$  and  $^{232}\text{Th}$ ) as well as  $\gamma$ -rays from the reaction  $^{19}\text{F}(n,\alpha)^{16}\text{O}^*$  were used to determine detector characteristics at  $\gamma$ -energies from 81 keV to 6919 keV. The results of the measurements are presented below. This part of our work was carried out at EC-JRC IRMM.

As known from previous studies  $\text{LaCl}_3:\text{Ce}$  detectors suffer from a large intrinsic activity component [14]. This activity arises basically from the decay of the radioactive  $^{138}\text{La}$  (0.09% relative abundance in naturally occurring lanthanum) and because of the contamination with the chemically similar actinium isotope  $^{227}\text{Ac}$  (and the daughters of its  $\alpha$ -decay chain). The common result for all three detectors is an intrinsic activity of about  $1.3 \text{ Bq cm}^{-3}$ , where the  $\alpha$ -particles account for  $1.2 \text{ Bq cm}^{-3}$  and the decay of  $^{138}\text{La}$  together with  $^{40}\text{K}$  from the environment stands for about  $0.055 \text{ Bq cm}^{-3}$ . The  $\beta$ -continuum around 800 keV, however, has

not been taken into account. This result is in reasonable agreement with previously reported values of about  $0.9 \text{ Bq cm}^{-3}$  for the  $\alpha$ -activity only [15,16]. However, the background activity may be tackled by either subtracting it from measured spectra or by imposing a coincidence condition.

In terms of both energy resolution and intrinsic peak efficiency the superiority of  $\text{LaCl}_3:\text{Ce}$  over  $\text{NaI}:\text{TI}$  detectors was confirmed, in this work with about 40% and 50% better, respectively. The energy resolution was determined for several bias PMT voltages by recording spectra of different radio-nuclides. A fit of Gaussians to the  $\gamma$ -peaks revealed the widths of the peaks, which is a measure for the energy resolution. Experimentally we obtain an energy resolution between 3.8 and 4.2% at 662 keV, which is in accordance with the manufacturer. Figure 1 shows the measured energy resolution as a function of  $\gamma$ -energy.

The intrinsic full peak efficiency of the detectors was determined for different point sources at a distance of  $(25.0 \pm 0.3) \text{ cm}$  between source and detector. The number of detected photons in the photo-peak was calculated by dividing the areas under the detected  $\gamma$ -peaks in the spectra, determined by fitting Gaussians plus a linear background function, with the time of measurement. With the known activity of the source the efficiencies were then given by the ratio between the number of detected photons and the number of photons hitting the detector. Our results were found to be in good agreement with efficiency values for  $\text{LaCl}_3$  detectors of size  $1'' \times 1''$  and  $2'' \times 2''$  [17], respectively, obtained by interpolation to the size of our detectors. The results from both this work and Ref. [17] are depicted in Figure 2, together with corresponding values for a  $\text{NaI}:\text{TI}$  of the same size [18].

The timing resolution was determined by exposing two detectors to a  $^{22}\text{Na}$  and  $^{60}\text{Co}$  source at the same time. The best coincidence timing resolution in this experiment over the entire energy region was found to be about 890 ps (FWHM), corresponding to an intrinsic timing resolution of 630 ps (cf. Figure 3), which is not that good compared to other values previously published for lanthanum halide detectors. For instance, an intrinsic timing resolution of 181 ps was reported for  $\text{LaCl}_3:\text{Ce}$  detectors in Ref. [9], but for much smaller detectors, with a volume of about  $1 \text{ cm}^3$ , compared to  $43 \text{ cm}^3$  in this study. 350 ps was reported for  $1'' \times 1''$   $\text{LaCl}_3:\text{Ce}$  detectors with  $^{60}\text{Co}$ , and  $\text{LaBr}_3:\text{Ce}$  detectors provided an even faster coincidence resolving time (less than 300 ps), but also for smaller volumes [10]. By putting a threshold just below the  $^{60}\text{Co}$ -peaks, i.e. around 1000 keV, we also succeeded to achieve an intrinsic timing resolution of 441 ps as indicated in Figure 3.

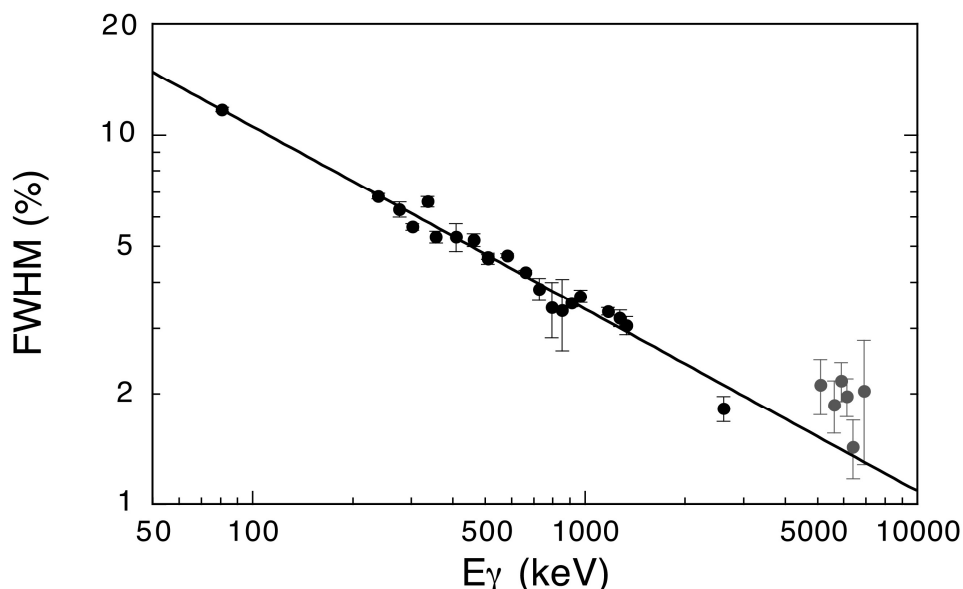


**Figure 1.** Measured energy resolution for  $\gamma$ -rays in the energy range between 81 and 6919 keV. The full drawn line describes the expected  $E^{-1/2}$  behaviour.

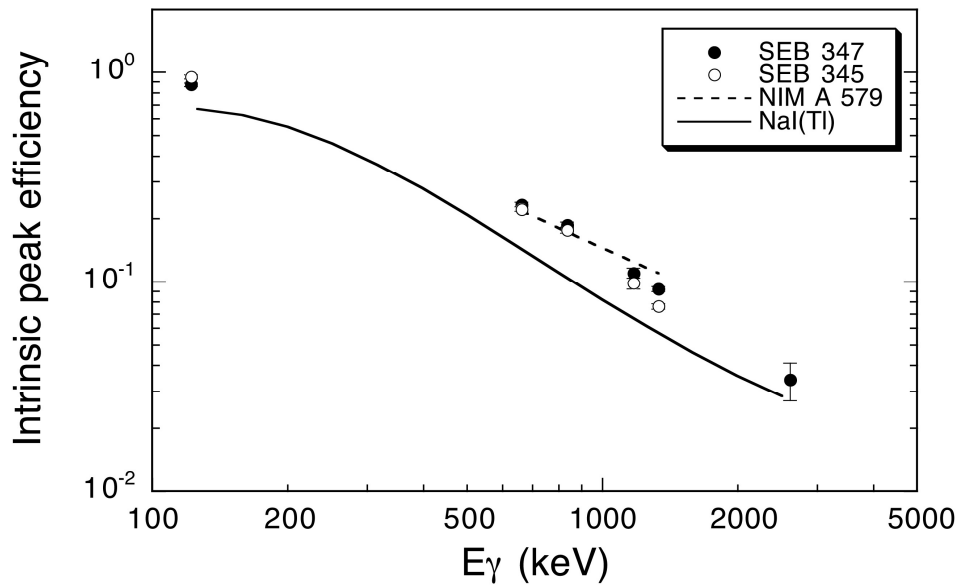


**Figure 2.** Intrinsic full peak efficiency vs.  $\gamma$ -energy from this work (full and open circles for two different detectors) together with estimates (dashed line) from values in Ref. [17]. For comparison corresponding values for NaI:Tl detectors of same size [18] are shown as full drawn line.

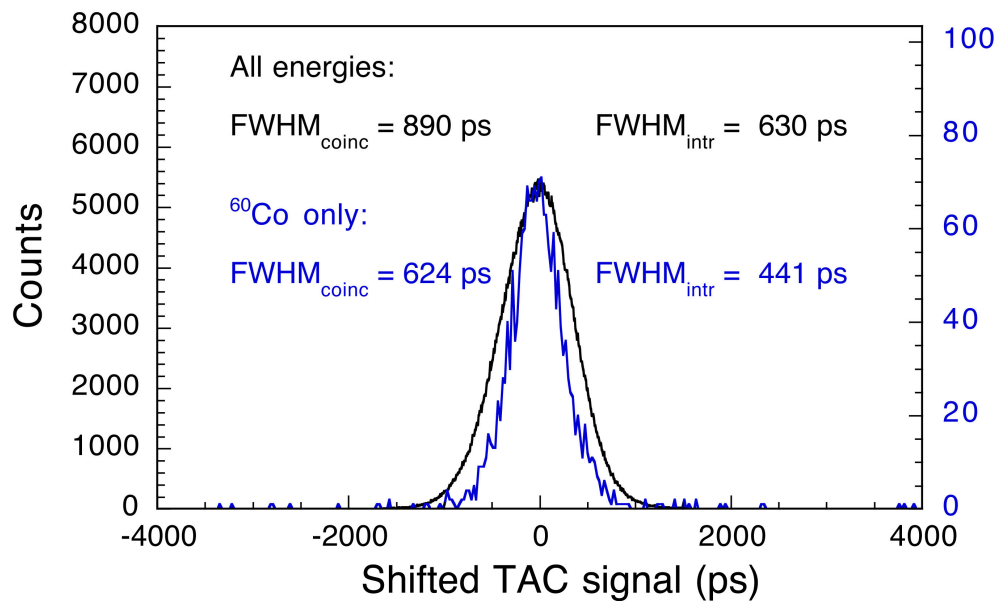


**Figure 3.** TAC spectra obtained in a coincident measurement of two  $\gamma$ -rays from  $^{22}\text{Na}$  and  $^{60}\text{Co}$  sources with two virtually identical  $\text{LaCl}_3:\text{Ce}$  detectors. The intrinsic timing resolution is given for both the entire energy region and for the  $^{60}\text{Co}$   $\gamma$ -rays only.

### LaCl<sub>3</sub>:Ce detectors in strong neutron fields

As a next step these detectors were tested in a fast-neutron environment with the 4 MV Van de Graaff accelerator at CEA/DAM Ile-de-France in Bruyères-le-Châtel in June 2009. The goal was to characterize the neutron-gamma separation by means of the time-of-flight technique and to investigate the possible built-up of background components due to neutron

capture in the scintillation material as well as the influence of the  $\gamma$ -rays due to the intrinsic  $\beta/\gamma$ -activity of the detector crystals. Three different targets (30 g  $^{238}\text{U}$ , 90 g  $^{197}\text{Au}$  and 240 g  $^{209}\text{Bi}$ ) were irradiated by a neutron beam of 5 MeV incident energy, produced in the reaction  $\text{D}(\text{d},\text{n})^3\text{He}$ . The neutron production target was solid TiD of thickness  $1\text{ mg/cm}^2$ , the pulsed deuteron beam had an energy of 1.86 MeV, a current of  $1.8\text{ }\mu\text{A}$  and a pulse structure of 3 ns width and 400 ns in distance. During the beam time of two weeks the position of the detectors was varied as well as the amount of shielding material, consisting of copper and lead. A photograph of the experimental setup is shown in Figure 4, in that case without any shielding material. Although the data analysis is still pending, we have already observed that detected events could be unambiguously identified by their time-of-flight in terms of particle kind as well as distance between their origin of production and the detectors. For instance,  $\gamma$ -rays scattered off the beam line or resulting from the prompt  $\gamma$ -flash from the neutron production target were easily separated from  $\gamma$ -rays of our interest, i.e. from the target in use. Neutrons hitting the detector and inducing reactions there were distinguished by their time signature corresponding to their kinetic energy and did not interfere with the  $\gamma$ -rays from the target. Of course, the good n/ $\gamma$ -separation properties of these detectors by measuring the time-of-flight of particles is owed to their timing resolution well below 1 ns. In this sense, the  $\text{LaCl}_3:\text{Ce}$  detectors tested in this work have shown to be sensitive to neutrons. However, spectra of measurements without beam and taken right after preceding irradiation with 5 MeV neutrons did not exhibit any  $\gamma$ -rays indicating activation of the crystals by fast neutrons. This is obviously in contrast to observations in  $\text{LaBr}_3:\text{Ce}$  detectors [19]. One of the intentions with the upcoming experiment at IKI Budapest is to investigate the corresponding behaviour in a thermal neutron field.



**Figure 4.** Picture of the experiment site in the 4-MV Van de Graaff accelerator laboratory at CEA/DAM Ile-de-France. Two detectors may be seen in the foreground, while the beam comes from the left and the transparent bag with the sample is located in the middle of the picture.

### Summary and conclusions

In this paper we have presented the results of measurements performed in order to characterize  $1.5'' \times 1.5''$   $\text{LaCl}_3:\text{Ce}$  detectors, in which they were exposed to  $\gamma$ -radiation with energies between 81 and 6919 keV. From those results we may conclude that these

detectors indeed do have properties almost as promising as reported for other lanthanum halide scintillation detectors studied prior to our investigations.

In terms of both energy resolution and intrinsic peak efficiency the superiority of  $\text{LaCl}_3:\text{Ce}$  over  $\text{NaI:Tl}$  detectors was confirmed, in this work with about 40% and 50% better, respectively. The dynamical range was determined to reach  $\gamma$ -energies up to 17 MeV and an excellent linearity was observed. The observed intrinsic timing resolution was 630 ps and 441 ps, respectively, which is definitely good enough for their intended purpose, i.e. the study of neutron-induced prompt fission  $\gamma$ -rays. Considering a timing resolution of about 1 ns of the ionization chamber for fission fragment detection and a typical neutron pulse width of about 1.5 ns, any intrinsic timing resolution less than 1 ns for a  $\gamma$ -detector is sufficient. During the envisaged experiment at the 10 MW research reactor of IKI Budapest the employment of the fission-fragment spectrometer VERDI and its pcCVD diamond detectors as fission trigger will provide an even better coincidence timing resolution [13]. Since this experiment aims at the coincident measurement of fission fragments and  $\gamma$ -rays, the intrinsic activity of these crystals will be effectively suppressed. The risk of activation of the detector crystals by fast neutrons may be excluded.

### Acknowledgements

The authors would like to gratefully acknowledge the support for this project, obtained within the EFNUDAT programme of the European Commission (agreement number 31027).

### References

- [1] K. S. Krane, *Introductory Nuclear Physics*, John Wiley & Sons, ISBN 0-471-80553-X (1987).
- [2] G. Rimpault, *Proc. Workshop on Nuclear Data Needs for Generation IV*, April 2005 (Editor: P. Rullhusen) Antwerp, Belgium, World Scientific, ISBN 981-256-830-1 (2006) 46.
- [3] G. Rimpault, A. Courcelle and D. Blanchet, *Comment to the HPRL: ID H.3 and H.4*.
- [4] R. W. Peelle and F. C. Maienschein, *Phys. Rev. C* 3 (1971) 373.
- [5] F. Pleasonton, R. L. Ferguson and H. W. Schmitt, *Phys. Rev. C* 6 (1972) 1023.
- [6] V. V. Verbinski, H. Weber and R. E. Sund, *Phys. Rev. C* 7 (1973) 1173.
- [7] Nuclear Data High Priority Request List of the NEA (Req. ID: H.3, H.4), <http://www.nea.fr/html/dbdata/hprl/hprlview.pl?ID=421> and <http://www.nea.fr/html/dbdata/hprl/hprlview.pl?ID=422>.
- [8] S. Lemaire, P. Talou, T. Kawano, M. B. Chadwick, and D. G. Madland, *Phys. Rev. C* 72, 024601 (2005).
- [9] K. S. Shah, J. Glodo, M. Klugerman, L. Cirignano, W. W. Moses, S. E. Derenzo, M. J. Weber, *Nucl. Instr. Meth. A* 505 (2003) 76.
- [10] A. Iltis, M. R. Mayhugh, P. Menge, C. M. Rozsa, O. Selles, V. Solovyeu, *Nucl. Instr. Meth. A* 563 (2006) 359.
- [11] B. D. Milbrath, B. J. Choate, J. E. Fast, W. K. Hensley, R. T. Kouzes, J. E. Schweppe, *Nucl. Instr. Meth. A* 572 (2007) 774.
- [12] SCIONIX Holland bv, P.O. Box 143, 3980 CC Bunnik, The Netherlands.
- [13] S. Oberstedt et al., contribution to this workshop.
- [14] A. Owens, A. J. J. Bos, S. Brandeburg, C. Dathy, P. Dorenbos, S. Kraft, R. W. Ostendorf, V. Ouspenski, F. Quarati, *Nucl. Instr. Meth. A* 574, 110 (2007).
- [15] M. Balcerzyk, M. Moszynski, M. Kapusta, *Nucl. Instr. Meth. A* 537, 50 (2005).
- [16] R. Nicolini, F. Camera, N. Blasi, S. Brambilla, R. Bassini, C. Boiano, A. Bracco, F. C. L. Crespi, O. Wieland, G. Benzoni, S. Leoni, B. Million, D. Montanati, A. Zalite, *Nucl. Instr. Meth. A* 582, 554 (2007).
- [17] B. Ayaz-Maierhafer and T. A. DeVol, *Nucl. Instr. Meth. A* 579, 410 (2007).
- [18] G. Gilmore, *Practical Gamma-ray Spectroscopy*, John Wiley & Sons, ISBN 978-0-470-86196-7 (2008).
- [19] J.-M. Laborie, private communication.

## VERDI – a double (v, E) fission fragment spectrometer

*S. Oberstedt<sup>1)</sup>, R. Borcea<sup>1)</sup>, Th. Gamboni<sup>1)</sup>, W. Geerts<sup>1)</sup>, F.-J. Hamsch<sup>1)</sup>,  
R. Jaime Tornin<sup>1)</sup>, A. Oberstedt<sup>2)</sup>, M. Vidali<sup>1)</sup>,*

1) European Commission Joint Research Centre IRMM, Geel, Belgium, 2440

2) School of Science and Technology, Örebro University, Örebro, Sweden, 70182  
[stephan.oberstedt@ec.europa.eu](mailto:stephan.oberstedt@ec.europa.eu)

**Abstract:** The investigation of neutron-induced fission characteristics like fragment mass and kinetic energy is usually based on the double-energy technique using twin Frisch-grid ionization chambers (IC). The main feature of an IC is its insensitivity to radiation damage, which makes it most suitable for measurements in a strong neutron environment. Providing the existence of prompt neutron emission data, the pre-neutron fission fragment mass and energy distributions may be obtained in an iterative process. However, those input data do exist only for the main isotopes of uranium and plutonium with sufficient precision and extrapolation methods have to be applied when analyzing neighbouring compound nuclear systems. With the construction of the double (v, E) spectrometer VERDI we aim at measuring pre- and post-neutron masses directly and simultaneously, avoiding prompt neutron corrections. In order to achieve a mass resolution  $\Delta A < 2$ , ultra-fast time pick-up detectors based on artificial diamond material are under investigation. From the simultaneous measurement of pre- and post-neutron fission-fragment data prompt neutron emission data may then be inferred as a function of fragment mass and total kinetic energy. In its final state VERDI is supposed to be coupled to particle detectors to measure delayed decay channels from fission fragments as for example beta-delayed neutron emission.

### Introduction

In nuclear fission pairs of fission fragments with different mass and kinetic energy are produced [1]. This process is accompanied by the emission of prompt neutrons and  $\gamma$ -rays from the highly excited fission fragments (FF). The knowledge of the FF yield distribution as a function of mass ( $A$ ) and kinetic energy ( $E_k$ ),  $Y(A, E_k)$ , is a key input to fission models and important data to better understand the fission process as such. This information may be obtained by means of different techniques. First, chemical separation of fission fragments give the mass yield after the FF has decayed to stable isotopes (cumulative yield) [2]. Next, by measuring with a recoil mass separator [3] or measuring the time-of-flight together with the kinetic energy [4] single fission fragment yields after prompt neutron emission may be obtained. Employing the double-energy (2E) method fission-fragment yields prior to neutron emission, the so-called pre-neutron masses  $A^*$ , can be obtained provided prompt neutron emission data are available for the iterative determination of the fragment mass [5, 6].

For a 2E measurement two different detector systems are generally used: first, a pair of silicon detectors, with which the two fission fragments, emitted in opposite direction, are measured simultaneously; and second, double Frisch-grid ionization chambers, where each pulse height of the two fragments is detected in one of the decoupled sections. The use of a Frisch grid additionally allows measuring the emission angle, leading to a correct treatment of the angular dependent energy loss of the emitted FF in the target [5]. Whereas the latter does not suffer from radiation damage, both 2E-measurement techniques require the introduction of the neutron emission data leaving the determination of the FF yield data to an iterative process. Since from many isotopes, even for uranium and plutonium, no or very limited neutron data are available, inter- or even extrapolation from the few cases, where those data exist, may severely affect the quality of the obtained FF yield data.

For example, in the early 1990s a very successful interpretation of FF distributions in terms of fission modes was introduced [7]. This model was based on the picture of a multi-dimensional fission barrier, including not only double humped, but also suggesting different barriers for symmetric and asymmetric fission configurations. Even asymmetric fission was supposed to occur by passing different outer fission barriers [8]. In an attempt to combine the fission modes into neutron-induced fission cross-section calculations the prediction of FF yields at energies not accessible experimentally was tested [9]. Calculations for the reactions  $^{238}\text{U}(n, f)$

and  $^{237}\text{Np}(n, f)$  suggested strong fluctuations of FF yields in the vicinity of the vibrational resonances close to the fission barrier [10, 11].

In order to verify the results emerging from model calculations and to prove experimentally the existence of such a multi-dimensional nuclear energy landscape close to the fission barrier fission fragment distributions from the reaction  $^{238}\text{U}(n, f)$  were measured around  $E_n = 0.9$  and  $1.2$  MeV with the 2E method using a double Frisch-grid IC [12]. As a result no significant variations in FF yields could be observed and the question arose whether such an effect may have been masked by the limited knowledge of neutron evaporation and the generally iterative character of the mass/energy determination.

### VERDI – the concept

One way to avoid such ambiguities in the data analysis is to measure not only the two fragment kinetic energies, but simultaneously the fragment velocities as well. Theoretically, from a double-velocity ( $2v$ ) measurement both fragment masses before prompt-neutron evaporation may be obtained provided the compound nuclear mass,  $A_{\text{CN}}$ , is known. This is assured at excitation energies below the onset of the second chance fission, i.e. fission after evaporation of a neutron from the compound nucleus prior to fission. The subsequent measurement of the fragment velocity provides the information of the fission fragment after prompt-neutron evaporation. The difference of pre- and post-neutron masses is just the number of evaporated prompt neutrons. In such a way those important neutron data need no longer to be introduced in the data analysis. Moreover, they may be directly deduced as a function of fragment mass and total kinetic energy, i.e. total excitation energy,  $Y(A, \text{TXE})$ . Such a double time-of-flight and energy spectrometer had already been realized in the 1980s at Institute Laue Langevin and was called Cosi-Fan-Tutte [4]. The spectrometer was based on micro-channel plate detectors as start and stop trigger devices and ionization chambers to measure fission fragment kinetic energies. With an impressive mass resolution  $\Delta A$  well below 1 mass unit it suffered from a very small geometrical efficiency of about  $4 \times 10^{-5}$  [13]. Therefore, FF yield measurements were affected by the non co-linearity of FF emission due to prompt neutron emission. The spectrometer does no longer exist.

Presently, a double ( $v, E$ ) spectrometer is being built at the JRC-IRMM, which aims at a FF mass resolution  $\Delta A < 2$  in conjunction with a geometrical efficiency of at least 0.5%, i. e. about 100 times more efficient than Cosi-Fan-Tutte. In the following we present work performed to investigate the different detector types that are going to be used in the single ( $v, E$ ) spectrometer version of VERDI, which is designated to determine the characteristics in terms of fission-fragment mass resolution.

#### A) VERDI – the energy side

The kinetic energy of fission fragments may be best measured with an ionization chamber (IC). Ionization chambers are easy to construct and to operate without suffering from radiation damage. They have a very good intrinsic energy resolution, but their timing characteristics are usually limited to a resolution not much better than 1 ns. In addition, one has to consider thin entrance foils to separate the IC from the vacuum of the time-of-flight section of the spectrometer. Those foils are difficult to make at large sizes, limiting the geometrical efficiency, and usually suffer from inhomogeneity, which considerably limits the accuracy of energy loss corrections.

In view of achieving a high geometrical efficiency silicon detectors are chosen as energy detectors, which are relatively cheap, allowing building up a detector array. Silicon detectors show both an excellent pulse height resolution and signal stability and have promising timing characteristics [14]. Since the energy detectors are well outside the neutron beam, their lifetime will be determined by the fission fragment dose. For a typical fission experiment this does not entail a severe problem.

#### B) VERDI – the timing side

In general, micro-channel plate detectors are used when aiming at a high timing resolution as it was done in Cosi-Fan-Tutte [4]. However, back then those detectors have been placed outside the neutron beam to avoid radiation damage and, therefore, limited strongly the geometrical efficiency. In order to allow a larger opening angle the time pick-up devices should be placed as close as possible to the target under investigation. Since this means that

such devices would have to be placed directly in the neutron beam, they have to be radiation hard. Therefore, an artificial polycrystalline chemical vapor deposited (pcCVD) diamond film is considered as detector material for the fission event trigger.

In nuclear physics diamond detectors are used mainly in high-energy experiments as beam monitors and tracking devices, replacing traditionally employed silicon detectors, because they survive in high radiation environments, have low leakage current and do not need cooling [15-18]. In particular the timing properties of artificial diamonds are remarkable and an intrinsic timing resolution better than 30 ps has been achieved for a mono-energetic  $^{52}\text{Cr}$ -beam at incident energy of 650 MeV/u [19]. In view of the properties of this surprising material it is tempting to see whether a similar timing resolution may be obtained with low energy fission fragments with energies typically between 0.5 and 2.0 MeV/u.

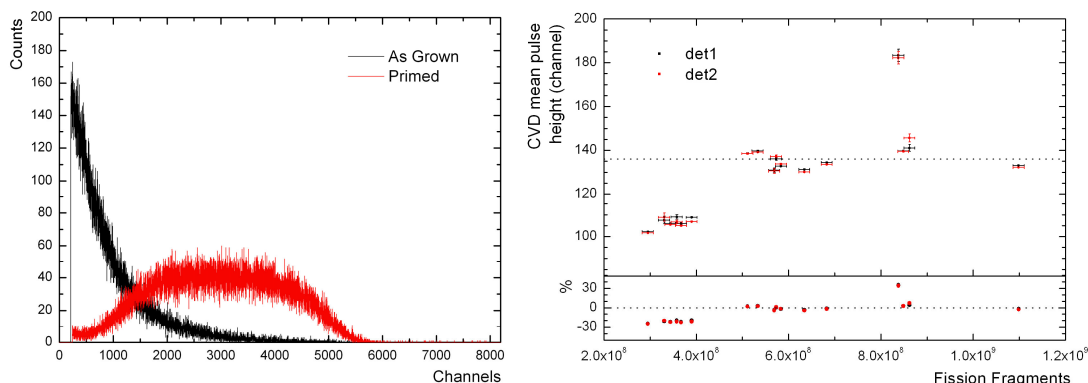


**Figure 1.** Left part: pulse height distribution of a mixed  $\alpha$ -particle source taken with a primed and with a not primed pcCVD diamond detector, the latter denoted “as grown”. Right part: mean pulse height of fission fragments as a function of absorbed fission-fragment dose taken with two different primed pcCVD diamond detectors.

The thickness of the diamond film is 100  $\mu\text{m}$  and its active area is 10 mm  $\times$  10 mm. Electrical contact is made by 150 nm thick gold layers deposited on the diamond film. Polycrystalline diamond material has very limited charge collection efficiency, typically around 30% [17], which deteriorates further when irradiated with strongly ionizing particles with a stopping range much smaller than the film thickness. This is due to polarization caused by electric charges trapped within a layer characteristic for the range of the particles. Experimentally, it was observed that the charge collection efficiency may be stabilized and even slightly improved if the material is irradiated with long-ranging electrons prior to use (see Fig. 1). This procedure is called “priming” [20, 21]. The priming effect is due to an increase of carrier lifetime caused by saturation of deep traps with electrons (holes) produced by radiation. This saturation has been demonstrated to be very effective and very stable in time under irradiation with  $\alpha$ -particles [21], provided the sample is not exposed to ambient light.

The timing properties of a pcCVD diamond detector were investigated with a symmetric configuration consisting of two identical diamond detectors with a spontaneous fission source ( $^{252}\text{Cf}$  evaporated on a 250 nm Al-backing) placed on top of one detector. The time-of-flight distance was 9.5 cm. Using pre-amplifiers built at the Technical University of Darmstadt [22] and standard timing filter amplifiers and constant fraction discriminators the time-of-flight was registered event by event. The time-of-flight spectrum is shown in the lower left part Fig. 2. Since the time-of-flight spectrum is composed of a large variety of particles, with different energies and masses, timing properties had to be deduced from simulations. For that purpose Monte-Carlo simulations have been performed on the basis of experimental mass and kinetic-energy yield data [23-25] and taking the geometry of the set-up into account. The free parameter in such a simulation is the width of the total resolution function, which was varied until the best description of the experimental time-of-flight spectrum was achieved. The result of those simulations is shown in the lower left part of Fig. 2 as open circles (connected with a solid line). The intrinsic timing resolution of a single pcCVD diamond detector is then obtained from the resolution parameter divided by  $\sqrt{2}$ . In this way the intrinsic timing resolution of a 100  $\mu\text{m}$  thick and 1  $\text{cm}^2$  large pcCVD diamond detector was determined to  $(285 \pm 15)$  ps. This

result appears to be considerably worse than what might be expected from high-energy heavy-ion experiments.

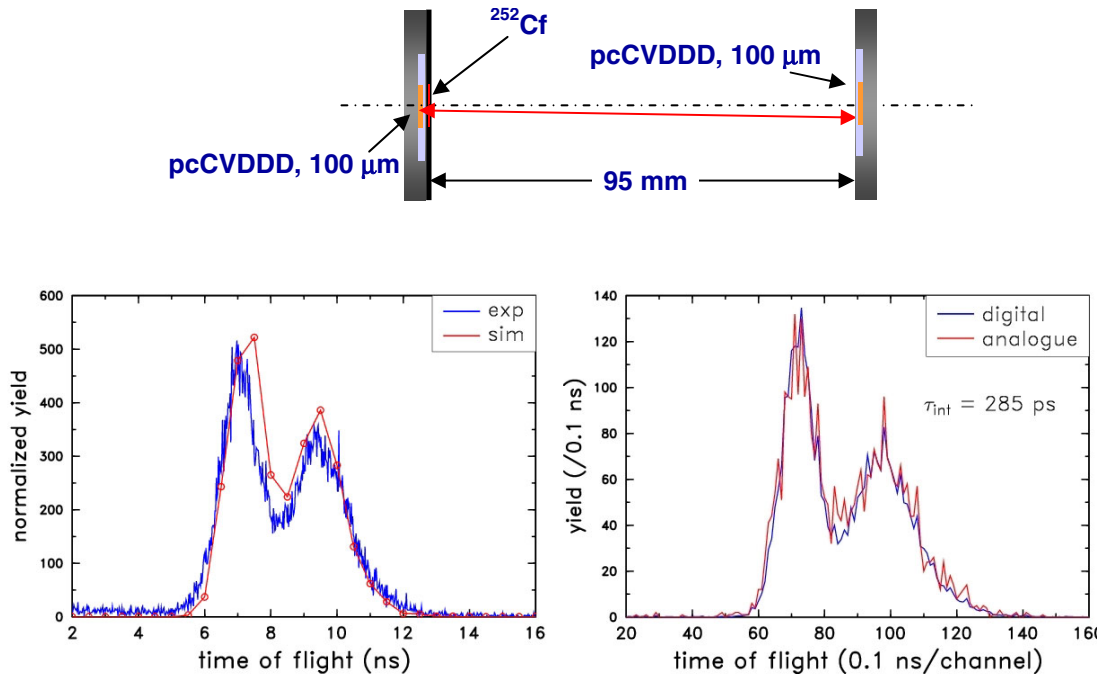


**Figure 2.** Upper part: Sketch of the symmetric set-up used to determine the intrinsic timing resolution of pcCVD diamond detectors (see text). Lower part (left): fission-fragment time-of-flight spectrum (solid line) together with a Monte-Carlo simulation (circles). Lower part (right): fission-fragment time-of-flight spectrum taken with both analogue electronics and a wave-form digitizer. The obtained intrinsic timing resolution of a 100  $\mu\text{m}$  thick pcCVD diamond detector of size  $1 \times 1 \text{ cm}^2$  is determined to  $(285 \pm 15) \text{ ps}$ .

However, one should not forget that we here are dealing with a mixed "particle beam", leading to a great variety of pulse heights and rise times.

### C) VERDI – first measurements

With the above tested fission-event trigger and a silicon detector with the best timing resolution (Eurisys, size =  $25 \text{ mm}^2$ ) a first test measurement of fission fragments from the reaction  $^{252}\text{Cf}(\text{SF})$  was performed. The obtained time-of-flight spectrum for a distance of 33 cm is shown in the left part of Fig. 3. From our Monte-Carlo simulations a coincidence timing resolution of 600 ps was inferred. The time-of-flight was calibrated by extrapolating experimental data obtained for  $^{233,235}\text{U}$  and  $^{239}\text{Pu}$  [26]. The energy calibration was based on published post-neutron data. The pulse-height defect (PHD) correction in the silicon detector was performed according to the Schmitt procedure [27, 28].

The post-neutron fission fragment mass was calculated from measured time-of-flight and kinetic energy according to

$$A = E/\xi (t/L)^2,$$

where  $\xi = 0.5175 \text{ MeV (ns/fm)}^2$  and  $A$  is in mass units. Since the true energy is only known after correcting for the PHD, the final masses must be obtained by iteration, which converges quickly. The obtained post-neutron mass distribution is shown in the right part of Fig. 3 (full circles). The data compare very well with those measured with the LOHENGRIN spectrometer (triangles) and with data obtained with the 2E technique (squares).

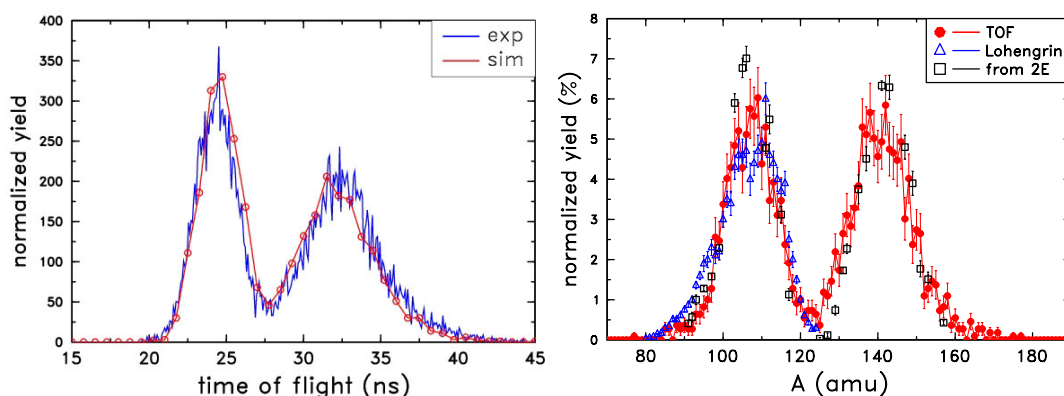


**Figure 3.** Left part: time-of-flight spectrum from the spontaneous fission of  $^{252}\text{Cf}$  together with a Monte-Carlo simulation. The timing resolution is estimated to 600 ps. Right part: Post-neutron fission fragment mass distribution from this work (circles) compared to data from the reaction  $^{251}\text{Cf}(n, f)$  measured with the LOHENGRIN spectrometer (triangles) and data obtained with the 2E technique (squares).

### Summary and conclusions

The VERDI double time-of-flight and double energy spectrometer for fission fragments is being constructed at the JRC-IRMM. Presently, a single ( $v, E$ ) version of VERDI is ready to be tested. Polycrystalline CVD diamond detectors have been employed successfully as fission event triggers. These devices were proven to be radiation hard against neutron and charged-particle doses typical in fission experiments. The intrinsic timing resolution for fission fragments has been determined to be better than 300 ps. This value has to be considered as an average over all masses and kinetic energies. For a segmented (transmission) detector even better figures may be expected.

In conjunction with a high energy resolution, small size PIPS detector a coincidence timing resolution of 600 ps has been determined by means of Monte-Carlo simulations. The obtained post-neutron mass distribution from the reaction  $^{252}\text{Cf}(\text{SF})$  compares well with data measured directly with the LOHENGRIN spectrometer and obtained from a double energy measurement. With the present timing resolution and a flight path length of 50 cm, a mass resolution  $\Delta A < 3$  amu may be estimated for the final version of the VERDI spectrometer. In early 2010 a dedicated experiment at the Budapest Research Reactor will be performed.

In conclusion, further effort will have to be focused on the improvement of the timing resolution of the silicon-based energy detectors of larger sizes in order to reach the contemplated geometrical efficiency. Then, we may expect to achieve a mass resolution of  $\Delta A < 2$  with VERDI. This will allow measuring consistent pre- and post-neutron fission-fragment data and to obtain information on prompt fission-neutron emission as a function of fragment pairs and total excitation energy with unprecedented accuracy.

### References

- [1] *The Nuclear fission process*, editor C. Wagemans, CRC Press, ISBN 0-8493-5434-X (1991)
- [2] G. Herrmann and N. Trautmann, *Ann. Rev. Nucl. Part. Sci.* 32 (1982) 117
- [3] E. Moll, H. Schrader, G. Siegert, H. Hammers, M. Asghar, J.P. Bocquet, P. Armbruster, H. Ewald and H. Wollnik, *Kerntechnik* 8 (1977) 374
- [4] A. Oed, P. Geltenbort, R. Brissot, F. Gönnerwein, P. Perrin, E. Aker, D. Engelhardt, *Nucl. Inst. Meth. in Phys. Res.* 219 (1984) 569
- [5] C. Budtz-Jørgensen, H. -H. Knitter, Ch. Straede, F. -J. Hamsch, R. Vogt, *Nucl. Inst. Meth. A*258 (1987) 209
- [6] F. Vives, F. -J. Hamsch, H. Bax, S. Oberstedt, *Nucl. Phys. A*662 (2000) 63
- [7] U. Brosa, S. Grossmann, A. Müller, *Phys. Rep.* 197 (1990) 167
- [8] S. Oberstedt, F. -J. Hamsch, F. Vivès, *Nucl. Phys. A*644 (1998) 289
- [9] F.-J. Hamsch, G. Vladuca, A. Tudora, S. Oberstedt, I. Ruskov, *Ann. Nucl. Energy* 32 (2005) 1297

- [10] G. Vladuca, A. Tudora, F.-J. Hamsch, S. Oberstedt, Internal report GE/R/NP/03/2001 (2001)
- [11] G. Vladuca, Anabella Tudora, F. -J. Hamsch, S. Oberstedt, Nucl. Phys. A 707 (2002) 32
- [12] E. Birgersson, A. Oberstedt, S. Oberstedt, F.-J. Hamsch, Nucl. Phys. A817 (2009) 1
- [13] N. Boucheneb, M. Ashgar, G. Barreau, T. P. Doan, B. Leroux, A. Sicre, P. Geltenbort and A. Oed, Nucl. Phys. A535 (1991) 77
- [14] PIPS® (Silicon) Detectors, TMPD series, CANBERRA Industries, [http://www.canberra.com/pdf/Products/Detectors\\_pdf/C36115-PIPS-SS.pdf](http://www.canberra.com/pdf/Products/Detectors_pdf/C36115-PIPS-SS.pdf)
- [15] P. Weilhammer et al., Nucl. Inst. Meth. A 409 (1998) 264
- [16] D. Meier et al., Nuc. Inst. Meth. A 426 (1999) 173
- [17] E. Berdermann, K. Blasche, P. Moritz, H. Stelzer, "Diamond Detectors for Heavy-Ion Measurements", XXXVI Int. Winter Meeting on Nuclear Physics, Bormio 1998
- [18] E. Berdermann, K. Blasche, P. Moritz, H. Stelzer, B. Voss, F. Zeytouni, Nucl. Phys. B (Proc. Suppl.) 78 (1999) 533-539
- [19] E. Berdermann, K. Blasche, P. Moritz, H. Stelzer, B. Voss, Diamond and Related Materials 10 (2001) 1770-1777
- [20] M. Marinelli, E. Milani, A. Paoletti, A. Tucciarone, and G. Verona Rinati, App. Phys. Lett. 75 (1999) 3216-3218
- [21] M. Marinelli, E. Milani, A. Paoletti, A. Tucciarone, G. Verona Rinati, M. Angelone, M. Pillon, Nucl. Inst. Meth. A 476 (2002) 701-705
- [22] U. Bonnes and M. Mutterer (1999) private communication
- [23] F.-J. Hamsch and S. Oberstedt, Nucl. Phys. A617 (1997) 347-355
- [24] F.-J. Hamsch, 2004, private communication
- [25] E. Birgersson, S. Oberstedt, A. Oberstedt, F.-J. Hamsch, D. Rochman, I. Tsekhanovich, S. Raman, Nucl. Phys. A 791 (2007) 1-23
- [26] P. Geltenbort, "*Fragmentgeschwindigkeiten, Energien und Massen für die durch thermische Neutronen induzierte Spaltung von  $^{233}\text{U}$ ,  $^{235}\text{U}$ ,  $^{239}\text{Pu}$* ", Dissertation, Eberhardt-Karls-Universität zu Tübingen (1985) private communication
- [27] H. W. Schmitt, W. M. Gibson, J. H. Neiler, F. J. Walter, T. D. Thomas, Proc. Symp. Physics and Chemistry of fission, Vol. 1, IAEA, Vienna (1965) 531
- [28] S. B. Kaufman, E. P. Steinbeg, B. D. Wilkins, J. Unik, A. J. Gorski, Nucl. Inst. and Meth. 36 (1965) 61

## The effect of pulse pile-up from proton recoils

*E. Birgersson<sup>1,2)</sup>, F.-J. Hamsch<sup>2)</sup>, A. Oberstedt<sup>3)</sup>, S. Oberstedt<sup>2)</sup>*

- 1) Institut für Strahlenphysik, Forschungszentrum Dresden-Rossendorf, 01314 Dresden, Germany
- 2) European Commission, Joint Research Centre, Institute for Reference Materials and Measurements, Retieseweg 111, 2440 Geel, Belgium
- 3) Akademin för naturvetenskap och teknik, Örebro universitet, 701 82 Örebro, Sweden

[e.birgersson@fzd.de](mailto:e.birgersson@fzd.de)

**Abstract:** The total kinetic energy (TKE) release in fission depends on the excitation of the compound nucleus and might indicate a change in the fission fragment mass distribution. The TKE is therefore an important observable when studying fission and when trying to model e.g. prompt neutron evaporation.

The kinetic energy of the two fission fragments can be measured with a double Frisch grid ionization chamber. Such chambers are especially suitable to investigate changes in the fission fragment distributions and TKE as a function of the incident neutron energy. However, if the counting gas of the chamber contains hydrogen and the chamber is put in a high flux neutron field, pulse pile-up from the ionization created by recoiled protons will occur. This will cause an increase in the detected pulse height from the fission fragments and has to be taken into account.

Signals from a pulse generator connected to the preamplifiers of the chamber will be affected by the same pile-up from the recoiled protons as the signals from fission fragments. A calculation of the spectral shape of the pulse signal clearly showed for several orders of magnitude that the recoiled protons may cause a significant increase of the detected fission fragment pulse heights.

### Introduction

Although fission of the nucleus was discovered 70 years ago, the process is still not fully understood. Predictions of mass distributions as well as total kinetic energy release in fission are needed for minor actinides. With the future Generation IV nuclear reactors [1] the minor actinides will be a part of the nuclear fuel. Knowledge of the fission fragment mass distribution as well as prompt neutron yield is important for the safety of the nuclear reactor. The number of prompt neutrons has a direct influence on the reactivity of a nuclear reactor, while the number of delayed neutrons, which are emitted by some fission fragments, is important in order to safely maintain the criticality of the reactor.

The fissioning nucleus does not arbitrarily deform, instead a few pathways in the potential energy landscape can be identified. For example, the pathway leading to symmetric fission fragment masses has an increasing probability as the incident neutron energy increases. The probability for specific pathways depends on the incident neutron energy, which is the reason for changes in the mass distribution of the fission. Pathways leading to high excitation of the fission fragments will also imply a higher prompt neutron yield.

### Double side Frisch grid ionization chamber

The double side Frisch grid ionization chamber is a fission fragment (FF) detector, which suffers almost no radiation damage. It is very useful for observing changes in the FF mass and kinetic energy distributions as a function of excitation of the fissioning system. The target is put on a common cathode in the middle of the chamber. Grids are shielding the anodes in each chamber half. The emission angle and energy of both fission fragments are detected. The emission angle is used when the detected signals are corrected for energy loss in the target material. More details on fission fragment analyses can be found in Refs. [2-4]. An energy calibration has also to be performed. This is normally done by measuring the TKE at known incident neutron energy or by measuring a different isotope in the chamber. Relative to the reference measurement even a small change of 0.2 MeV in the TKE of the fission fragments can be observed. The current paper deals with the correction for pulse pile-up. The

experimental data come from the work in Refs. [2,3], where  $^{238}\text{U}(n, f)$  was studied at  $E_n = 0.9 - 2.0$  MeV. The ionization chamber was put only a few centimetres from the neutron source. The distance from the cathode to the grid was 3 cm and from the grid to the anode 0.7 cm. The radius of the grid was 4.5 cm and the whole ionization chamber has cylindrical symmetry. The counting gas was P10 (10%  $\text{CH}_4 + 90\%$  Ar) slightly above atmospheric pressure. The neutron fields were created using  $^7\text{Li}(p, n)$  and  $^3\text{H}(p, n)^3\text{He}$  reactions. The protons were accelerated using the 7 MV Van de Graaff accelerator at EC-JRC IRMM in Geel, Belgium. Pulse generator signals were put to the preamplifiers to monitor electronic drifts. This offers an opportunity to study and observe the pulse pile-up as well. The fission fragment signals and the pulse generator signals will have the same probability for pile-up, since the count rate is low [5,6].

### Pulse pile-up between proton recoils and fission fragments

In Ref. [6] the effect of alpha-particle pulse pile-up on fission fragments from the reaction  $^{239}\text{Pu}(n, f)$  was studied. A separation of detected fission fragments with and without alpha pile-up was performed. Both sets were subject to different energy calibrations. The same changes in fission fragment mass distributions as well as TKE were seen for different incident neutron energies. As the calibration energy suffers from the same pulse pile-up, the only effect was a reduced energy resolution. However, if the pulse pile-up is not constant or not present for the calibration energy, pile-up has to be treated more carefully. This may happen, if a target material is changing in alpha-activity. A similar effect could also occur because of proton recoils. If the counting gas in the chamber contains hydrogen, the incident neutrons might undergo elastic scattering off these protons. The recoiled protons will then ionize the gas. If this happens in coincidence with a fission fragment being emitted, pulse pile-up from the recoiled proton and the fission fragment signal will occur. Since the cross section for neutron-proton scattering is energy dependent, different contributions are expected depending on both intensity and energy of the neutron field.

Thus, the probability for pulse pile-up from recoiled protons depends on the amount of protons in the ionization chamber, the neutron flux, the elastic scattering cross section, the neutron energy and the width of the coincidence time window.

An electric signal is created only when the recoiled proton ionizes the counting gas in the region, where an electric field exists. This region is called the sensitive volume. The increase in pulse height due to pile-up from a recoiling proton also depends on its time relative to the signal from the fission fragment.

### Calculation of pulse generator peak

In order to confirm that the observed pulse pile-up originates from proton recoils, the pulse generator peak was calculated for several different neutron fields. For the work presented in Refs. [2,3] part of the measurements could not be corrected with the pulse generator signal spectrum due to a broken pulse generator. Thus, these calculations offered an alternative way to correct the fission fragment signals.

The calculations were performed in two steps. The recoiled protons deposit energy in the sensitive volume of the chamber and first these energy spectra were estimated. The second part includes Monte Carlo simulations of the pulse generator peak including pile-up effects due to proton recoils.

### Ionization by recoiled protons

The calculation of the energy spectrum from the recoiled protons in the sensitive volume in each chamber half was performed by dividing the chamber in a few segments. Although an electric field was present also between grid and anode, this region was not considered as the sensitive volume here, because of the smaller volume of this region and the smaller signals created there compared to the region between cathode and grid. Both neutron flux and energy depend on the neutron production reaction, but also on the emission angle. By using the computer code EnergySet [7], the average neutron energy,  $E_{ns}$ , and the neutron flux,  $\Phi_{ns}$ , were determined in each segment. The number of proton recoils per seconds in each segment is given by  $C_s = N_s \Phi_{ns} \sigma(E_{ns})$ , where  $N_s$  is the number of protons in the segment. The elastic neutron scattering cross section  $\sigma(E_{ns})$  is depicted in Figure 1 and was in this energy region approximated by  $\sigma(E_n) = 4.2723 E_n^{-0.4992}$ , in accordance with data found in one of the evaluated libraries [8]. Once the count rate of proton recoils from each segment is

known, the proton emission angle relative to the incident neutron was randomized. The angular distribution was assumed to be isotropic in the centre-of-mass (CM) system and a conversion to the laboratory system could be performed according to  $\tan \theta = \sin \theta^{\text{CM}} / (1 + \cos \theta^{\text{CM}})$ , by assuming that neutrons and protons have equal masses. By using the same assumption, the energy of the proton in the laboratory system is given by  $E_p = E_n \cos 2\theta$ . A SRIM [9] simulation for 1.8 MeV protons was performed to find the energy loss as a function of distance in the counting gas, see Figure 1. For different energies  $E_p'$  the energy loss of protons was estimated by integrating the Bragg curve in Figure 1 until the result amounts  $E_p - E_p'$ . To obtain the Bragg curve for the new proton energy, its origin was shifted to the upper limit for the integration. The amount of energy deposited by the proton in the sensitive volume was found by integrating this Bragg curve until the edge of the sensitive volume was reached. It is also possible that the proton passes the thin layer with the fission target in the middle of the cathode. In this case the energy of the proton was deposited in both chamber halves, but with different contributions. The contribution from each segment was used to obtain the normalized deposited energy spectrum, which can be seen for each chamber half in Figure 2.

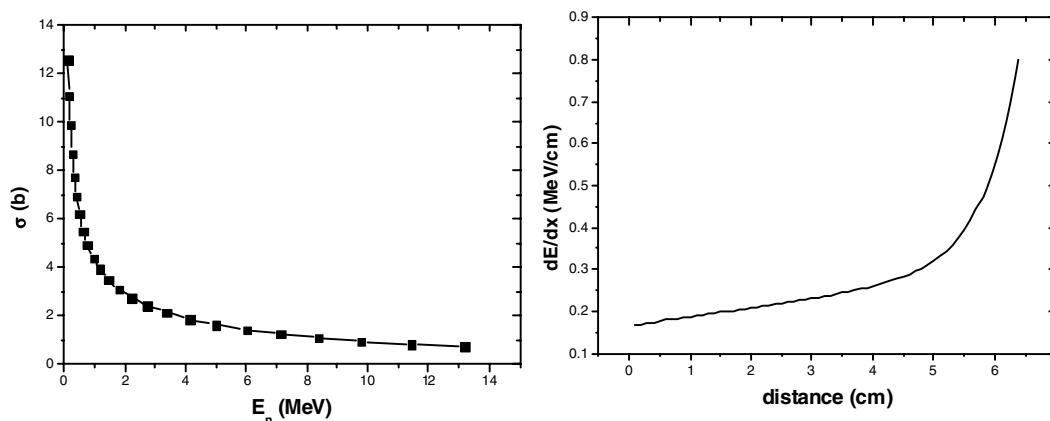


**Figure 1.** The elastic neutron scattering cross section is from JEFF [8] with its corresponding fit (left). The calculated energy loss as a function of distance (Bragg curve) for 1.8 MeV protons (right).

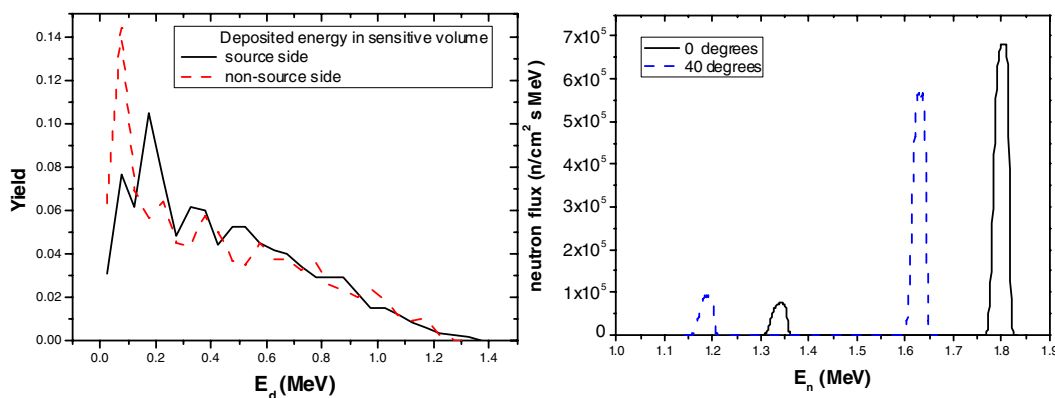


**Figure 2.** Normalized spectra for energy deposited by the recoiled protons in each chamber half. The neutron energy in forward direction was 1.8 MeV (left). Calculated neutron spectrum [10] at two emission angles. A small contribution from the reaction  ${}^7\text{Li}(p,n){}^7\text{Be}^*$  at lower neutron energies is also seen (right). The neutrons were created in the reaction  ${}^7\text{Li}(p,n){}^7\text{Be}$  using a  $445 \mu\text{g}/\text{cm}^2$  LiF target.

Since the chamber is divided in segments an artificial structure appears. The spectra for both chamber-halves exhibit a maximum at low energies, with this maximum shifted towards higher energies for the chamber half closest to the neutron source. There, neutrons hitting

protons close to the edges of the chamber half have lower energy than in the corresponding location on the other side. If the protons do not deposit their entire energy in the sensitive volume, the amount of deposited energy,  $E_d$ , is higher, when the initial proton energy is lower. This is a consequence of the Bragg peak shown in Figure 1. Since a 1.8 MeV proton has a track length of 6 cm, the chamber is too short for all kinetic energy to be deposited.

When using a Li target for the quasi-mono energetic neutron production at higher energies, also a contribution of low energy neutrons from the reaction  ${}^7\text{Li}(p, n){}^7\text{Be}^*$  appears. Simulated neutron spectra [10] for two emission angles are shown in Figure 2. In the calculations of the deposited energy spectrum, these low-energetic neutrons, which amount only around 10% of the total flux, were not taken into account.

### Monte Carlo method to simulate pulse generator signal spectrum

In Figure 3, pulse generator peaks are shown without a neutron field being present. They are well described by Gaussians, except for the alpha pile-up, which also can be seen by the tail. The increase in pulse height of a signal due to pile-up depends on the relative time difference between the two events. In the experiment a spectroscopic amplifier with a Gaussian shaping time of 3  $\mu\text{s}$  was used. The width of the signal after the spectroscopic amplifier at the baseline was 12  $\mu\text{s}$ . To confirm that the coincidence time window also was 12  $\mu\text{s}$ , a separate experiment with two pulse generators was performed. A 3000 Hz low amplitude (0.1 V) signal was added to a 10 Hz large (0.2 V) signal. The result is seen in Figure 3. The main peak at channel number 2375 exhibits a squared pile-up contribution up to channel number 2500, which is consistent with the sum of the amplitude of both pulse generator signals. The coincidence count rate can be approximated by  $C_r = \Delta T \cdot C_1 \cdot C_2$  [11], where  $C_1$  and  $C_2$  are the count rates for the two pulse generator signals. The result from Figure 3 gives a coincidence time window  $\Delta T = (11.3 \pm 0.4) \mu\text{s}$ , which is only slightly lower than the 12  $\mu\text{s}$  coincidence time window, which was used later in these calculations.

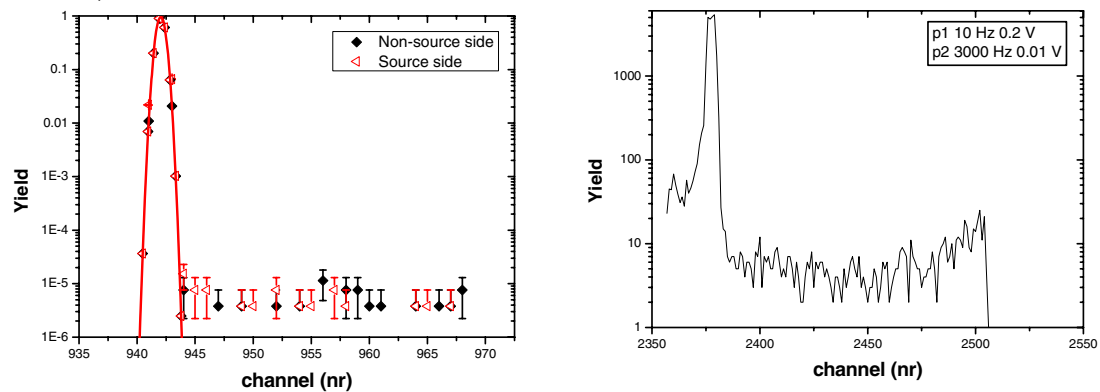


**Figure 3.** Pulse generator peaks from both chamber halves without neutron field. The pulse pile-up from alpha particles is seen as high-energy tail (left). A similar spectrum was generated from the sum of two pulse generator signals (right). The increase in pulse height due to pile-up follows a square distribution.

The probability that a low count rate signal and  $r$  pulses from proton recoils will occur in coincidence is given by the Poisson probability [11]

$$P(r) = \frac{(C_r \Delta T)^r \exp(-C_r \Delta T)}{r!}, \quad (1)$$

where  $C_r$  denotes the proton recoil count rate and  $\Delta T$  the coincidence time window. The calculation of the pulse generator peak was performed by randomising the channel number for  $10^6$  pulse signals. The number of pulse generator signals with  $r$  pile-ups is given by  $P(r) \cdot 10^6$  and multiple pile-up was considered as long as this number was larger than 1. For  $r = 0$ , no pile-up occurs and the channel number for these signals were randomized with a Gaussian,  $G(s1)$ . Both width and peak position of the Gaussian were found by manual adjustment. The pulse generator signal channel number with  $r$  pulse piled up signals was simulated by

$$Ch = G(s1) + \sum_{x=1}^r E_x(s2) \cdot F(s3) \frac{1}{Ch2MeV}, \quad (2)$$

where the second part of the equation (2) is a sum of the contribution from multiple piled up events. The function  $E_x(s_2)$  describes the deposited energy, which was randomized from the deposited energy spectrum. The function  $F(s_3)$  gives a random value between 0 and 1 to simulate the relative position in the coincidence time window. The expression  $Ch2MeV$  is simply the energy calibration factor. The spectrum from the  $10^6$  simulated pulse generator signals is normalized and can be compared to the normalized experimental pulse generator signal spectrum.

## Results

In Table 1 results of the simulations are listed for different neutron energies and intensities. For a high intensity neutron field, the increase in detected pulse height (or energy,  $\Delta E$ ) would correspond to an increase in total kinetic energy of fission fragments  $\Delta TKE \approx 0.7$  MeV or more. The results of the simulations of the pulse generator peak, which are depicted as lines in Figures 4 and 5, are in excellent agreement with the experimental peaks, shown as different symbols depending on chamber half and neutron energy. In both figures the alpha pile-up is visible as well, however causing a negligible increase to the detected average fission fragment energy in this case. As expected, the chamber half closest to neutron source (“source side”) exhibits more pile-up due to the higher neutron flux.

**Table 1.** Summary of input parameters and results. Neutron energy and flux are angular dependent and here only given for forward direction and in the middle of the chamber. The neutrons were produced in the reactions  ${}^7\text{Li}(p, n){}^7\text{Be}$  and  ${}^3\text{H}(p, n){}^3\text{He}$ , respectively.

$E_n$ forward (MeV)	Target	Target thickness ( $\mu\text{g}/\text{cm}^2$ )	Ion current ( $\mu\text{A}$ )	Neutron flux at centre ( $\text{cm}^{-2} \text{s}^{-1}$ )	Recoil rate non source side (recoils/s)	Recoil rate source side (recoils/s)	$\Delta E$ non source side (MeV)	$\Delta E$ source side (MeV)	$\Delta TKE$ (MeV)
0.9	LiF	445	45	4.84E4	18300	43200	0.036	0.089	0.13
1.2	LiF	445	36	3.0E4	18300	43000	0.041	0.11	0.15
1.8	LiF	445	11	7.71E3	4200	9300	0.011	0.025	0.036
1.8	TiT	2083	33	2.1E5	90400	167300	0.26	0.46	0.72
2.0	TiT	2083	30	2.05E5	81200	150000	0.22	0.40	0.63

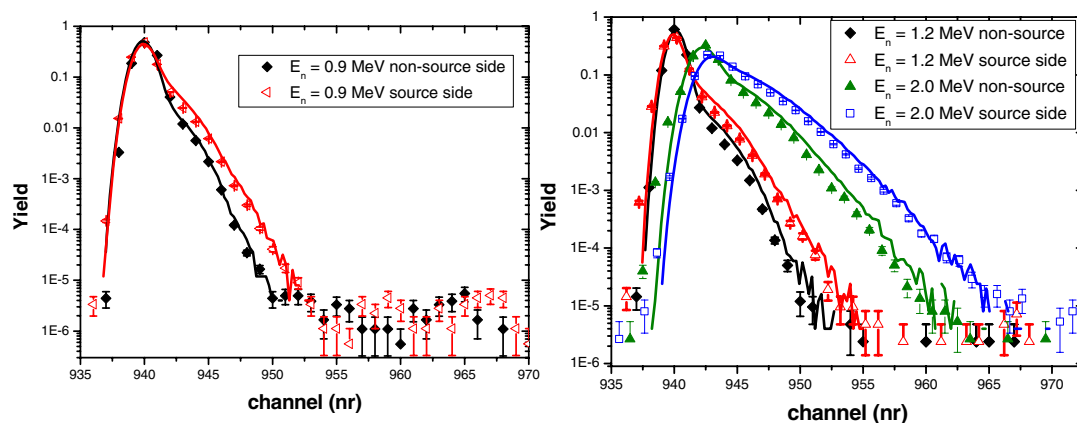


**Figure 4.** Measured and simulated pulse generator peaks for neutron fields with  $E_n = 0.9$  MeV using a LiF target (left) and for  $E_n = 1.2$  and  $2.0$  MeV in the forward direction using LiF and TiT targets, respectively (right). The calculations, shown as lines, describe very well the experimental data for several orders of magnitude. The side of the ionization chamber closer to the neutron source exhibits as a consequence more pile-up.

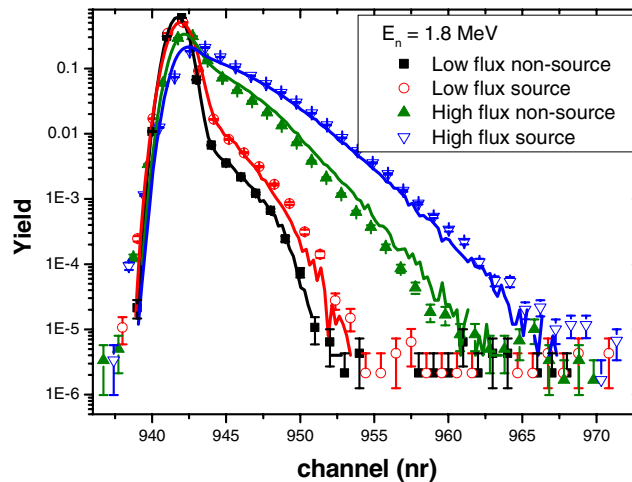


**Figure 5.** Measured and simulated pulse generator peak for neutron fields with  $E_n = 1.8$  MeV. The use of LiF and TiT targets for neutron production results in low and high neutron flux, respectively. Again, the calculations, shown as lines, describe very well the pulse pile-up contribution for several orders of magnitude.

## Summary

In this work we have studied the effect of pile-up of signals from proton recoils and fission fragments on the total kinetic energy of the fragments, measured with ionization chambers. When measuring fission fragments with a double side Frisch grid ionization chamber, pulse generator signals can be fed into the preamplifiers in order to monitor electronic drift in the system. Since the count rates of both fission fragments and the pulse generator signals are low, they both will be subject to the same amount of pile-up rate. Simulations of pulse generator signal spectra were performed and compared to experimental results. It could be shown that an excellent agreement was achieved for different neutron energies and intensities. Within the frame of our investigations the effect of pulse pile-up was shown to cause an increase in total kinetic energy as high as 0.7 MeV. From that we may conclude that the observed effect of proton recoils indeed needs to be taken into account when studying neutron-induced fission with an ionization chamber, especially for high neutron energies and fluxes and if the counting gas contains hydrogen atoms.

## References

- [1] A technology roadmap for generation IV nuclear energy systems, GIF-002-00, US Department of Energy (2002)
- [2] E. Birgersson, A. Oberstedt, A. Oberstedt, F.-J. Hamsch, Properties of the reaction  $^{238}\text{U}(n, f)$  at the vibrational resonances, Nucl. Phys. A 817 (2009) 1-34
- [3] E. Birgersson, Doctoral thesis, Determination of binary fission-fragment yields in the reaction  $^{251}\text{Cf}(n_{\text{th}}, f)$  and Verification of nuclear reaction theory predictions of fission-fragment distributions in the reaction  $^{238}\text{U}(n, f)$ , Örebro ISBN 978-91-7668-548-8 (2007)
- [4] C. Budtz-Jørgensen, H.-H. Knitter, C. Straede, F.-J Hamsch and R. Vogt, Nucl. Instr. And Meth. A258, 209 (1987)
- [5] L. Demattè, F.-J. Hamsch, H. Bax, NIM A 480 (2002) 706-712
- [6] G. F. Knoll, Radiation Detection and Measurement, 2<sup>nd</sup> Edition, Wiley, New York (1989) 8
- [7] G. Lövestam, Computer Code EnergySet, Internal report No. Ge/NP/2/2002/2/06/20 (2002)
- [8] A. König, R. Forrest, M. Kellett, H. Henriksson and Y. Rugama, editors, The JEFF-3.1 Nuclear Data Library, JEFF report 21, NEA (2006)
- [9] J.F. Ziegler and J. P. Biersack, Computer code SRIM2003.26 (2003)
- [10] E. Birgersson, G. Lövestam, Computer Code NeuSDesc available from irmm.jrc.ec.europa.eu, (2009)
- [11] W. R. Leo, Techniques for Nuclear and Particle Physics Experiments 2<sup>nd</sup> edition, Springer-Verlag New York, ISBN 0-387-57280-5 (1994)

## MCNPX simulation for optimization of efficiency of a $4\pi$ neutron detector for beta delayed neutron emission measurements

*V. Gorlychev<sup>1)</sup>, M. B. Gómez Hornillos<sup>1)</sup>, G. Cortés<sup>1)</sup>, R. Caballero-Folch<sup>1)</sup>, A. Poch<sup>1)</sup>, C. Pretel<sup>1)</sup>, J. L. Taín<sup>2)</sup>, D. Cano-Ott<sup>3)</sup>, F. Calviño<sup>1)</sup>, T. Martínez<sup>3)</sup>*

1) UPC, Departament de Física i Enginyeria Nuclear, 08028 Barcelona, Spain.

2) IFIC, CSIC-Univ. Valencia, 46980 Paterna (Valencia), Spain.

3) CIEMAT, Grupo de Innovación Nuclear, 28040 Madrid, Spain.

[vitaly.gorlychev@upc.edu](mailto:vitaly.gorlychev@upc.edu)

**Abstract:** This work presents the Monte Carlo simulations carried out to design a moderation based  $4\pi$  neutron detector. This neutron detector will be used to study beta delayed neutron emission. Monte Carlo simulations with the MCNPX [1] code have been performed to find the optimal neutron detector structure that achieves the maximum neutron detection efficiency while keeping the efficiency curve flat for the range of energies of interest (0.01 MeV-5 MeV). This detector will be part of the DESPEC [2] experiment at FAIR [3]. Also a campaign of measurements with a detector of this type will be performed at JYFL.

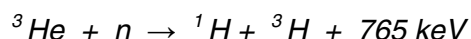
### Motivation

One of the important objectives of this work is to design a neutron detector in order to study the beta delayed neutron emission. The study of the decay properties of neutron rich nuclei far from the region of beta stability provides the opportunity to obtain valuable information about the structure of atomic nuclei. For example the study of beta delayed neutron emission allows us to understand the rapid neutron capture nucleosynthesis process [4] and it is very important for nuclear engineering for the safe design of nuclear reactors. In the fission reaction chain there are many fission products (approximately 270) which can be considered emitters of delayed neutrons [5]. Even though the delayed neutron emission could be less than 1% of the total neutrons from fission, they are very important in the accident analysis and in the conversion of period into reactivity. The nuclear chain reaction can be controlled by using neutron poisons and neutron moderators to change the fraction of neutrons that will go on to cause more fission. As the delayed neutron emission can be produced much latter, these neutrons can play an important role in the security at nuclear plants. In order not to increase the criticality of the nuclear reactor the delayed neutron should be well studied.

### General features of the neutron detector

There were different criteria in the design of the optimal configuration of the neutron detector. The main requirements for the neutron detector were a high efficiency in order to detect the neutrons from isotopes with low production rates and to achieve an efficiency curve as flat as possible for the range of energies of interest (0.01MeV-5MeV).

The neutron detector consists of a block of polyethylene with a beam hole in the centre. The beam hole will be used to deliver radioactive isotopes inside the detector. A  $\beta$ -detector will be installed inside the neutron detector beam-hole in order to be able to correlate the  $\beta$ -decay and the subsequent neutron emission on the experiment. Two rings of proportional counters filled with  $^3\text{He}$  detection gas will be placed around the beam hole. This construction of the detector covers a solid angle of almost  $4\pi$ . The reaction which provides neutron detection is



The detection of the neutrons with the proportional gas-filled counters will be possible due to large cross-section of  $^3\text{He}$  detection gas for neutrons at thermal energy (0.025 eV) [6]. In order to decrease the neutron energy the polyethylene block around the beam hole moderates them from their initial energy of source (up to a few MeV) to thermal energy.

The detector will be shielded in order to protect the measurement from background neutrons. Background can be of two origins. The first one is cosmic radiation and the second origin is the laboratory installation and the accelerator.

### Simulation in MCNPX of the design

The simulations were done on the cluster ARGOS at UPC-SEN with the MCNPX 2.5.0 simulation code. The flat efficiency is achieved by placing the proportional counters on two rings at different radii from the neutron source.

The first simulations had the objectives of determining the length of the counters and the total number of counters for the detector. During the simulations a neutron point source with energy 1 MeV was placed in the centre of the beam hole. The simulation was made for  $10^5$  neutrons. The proportional counters used in the simulation were manufactured by LND Inc. and their main characteristics are presented in *Table 1*.

**Table 1.** The main characteristics of proportional counters.

Counter	Gas	Maximum length (mm)	Effective length (mm)	Maximum diameter (mm)	Effective diameter (mm)	Gas pressure (torr)	Cathode material
2527 LND Inc.	$^3\text{He}$	686.84	604.8	25.4	24.38	15200	Stainless Steel

According to the preliminary simulation the detection gas in the counters was chosen to be  $^3\text{He}$ . The effective length of counters obtained in the simulation was 60 cm and the gas pressure 15200 torr. The optimal number of counters obtained during the simulation was 20 and these counters should be distributed between two rings with 8 and 12 counters around the beam hole. The diameter of the beam hole was set to 10 cm so that it is able to accommodate other detectors inside (such as beta detector, Ge detector).

Based on the first results of the preliminary simulations, further simulations were performed in order to find the optimal radial position of the two rings of  $^3\text{He}$  counters (see Figure 1).

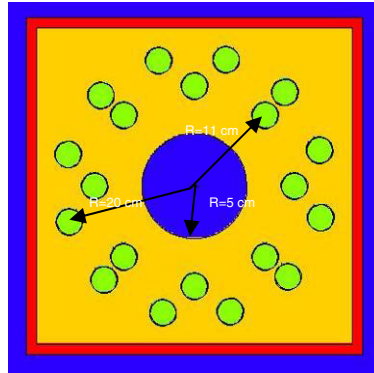


**Figure 1.** The detector construction with 8  $^3\text{He}$  counters in the first ring and 12  $^3\text{He}$  counters in the second ring.

In order to find optimal configuration of the neutron detector a range of possible radii for the rings of counters in the polyethylene block was checked. Input files were generated with different ring radii and different source energies. The range of radii for the ring of counters was wide in order to find the optimal configuration that gives an efficiency as flat as possible. The range of radii for ring A was from 8 cm to 15 cm and for ring B from 11 cm to 24 cm. The neutron energy range in the simulations was from 0.01 MeV to 10 MeV. The neutron source was monoenergetic in each simulation. After these simulations the output files from MCNPX were analyzed to find the radii combinations that provided the flattest efficiency curve for the energy range of interest (0.01MeV-5MeV). According to the simulations the optimal radii of the proportional counter rings were set to 11 cm and 20 cm. The front view of the detector is presented in Figure 1. The efficiency curve is presented in Figure 2, The curve was calculated for two different neutron propagation times. The first simulation was made for infinite propagation time and the second one was made for propagation time 200  $\mu\text{s}$ . The variation between maximum and minimum efficiency for 200  $\mu\text{s}$  propagation time is about 5 percent. As the setup will detect all the neutrons including those from the background it is important to limit the correlation time in order to avoid the detection of background neutrons. This time can be used as trigger window or offline correlation time after each  $\beta$ -disintegration on the

experiment. For the 200  $\mu$ s propagation time the efficiency decreases by 5 percent with respect to the infinite propagation time.

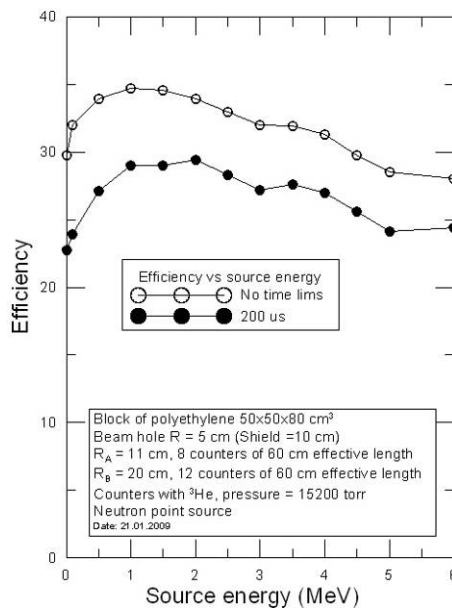


**Figure 2.** Neutron detection efficiency for the neutron detector.

### Background and shielding.

In order to protect the detector from the background a shielding cover was designed. The background on the experiment can be of two origins. The first one is cosmic background and the second one is a background originating from the laboratory installations such as the accelerator. The flux of background is unknown and in the next simulation we suppose it have the same energy range as the neutron source. The background neutrons in this simulation were emitted inwards from the surface of a sphere surrounding the neutron detector (see Figure 3). During the simulation the block of polyethylene was covered by a polyethylene layer from the sides parallel to the beam direction. The source energies were from 0.01 MeV to 5 MeV and the neutron propagation time was set to infinite. The efficiency of background detection ranged from 5% (for source energy 0.01 MeV) to 19% (for source energy 5 MeV) when there was no shielding in the simulation. When adding the polyethylene shielding the number of neutrons detected in the counters decreased. Different thicknesses of the shielding layers (5, 10, 15 and 20 cm) were studied during the simulations. The calculations were repeated for the same layers but with an additional layer of Cd of 0.5 mm between the shielding polyethylene and one from the detection block.

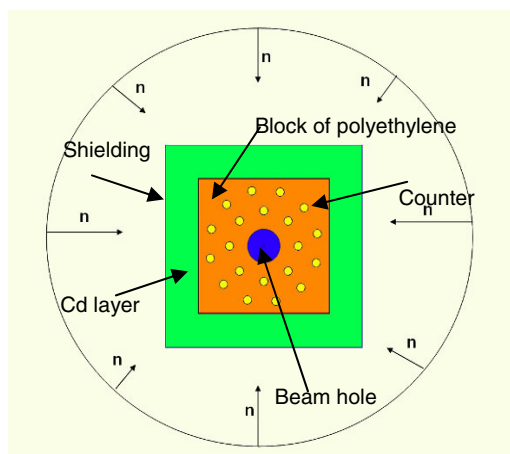


**Figure 3.** Scheme of background simulation.

The result about the detection of the background can be seen in Figure 4. The thicker the layer of polyethylene, the better the shielding from the background it provides, however no significant difference was observed when adding the Cd layer. The final design of the shielding is a 20 cm layer of polyethylene without any Cd layer. The background detection decreases to about 0% for neutron background energy of 0.01 MeV and to about 4% for neutron background energy of 5 MeV.

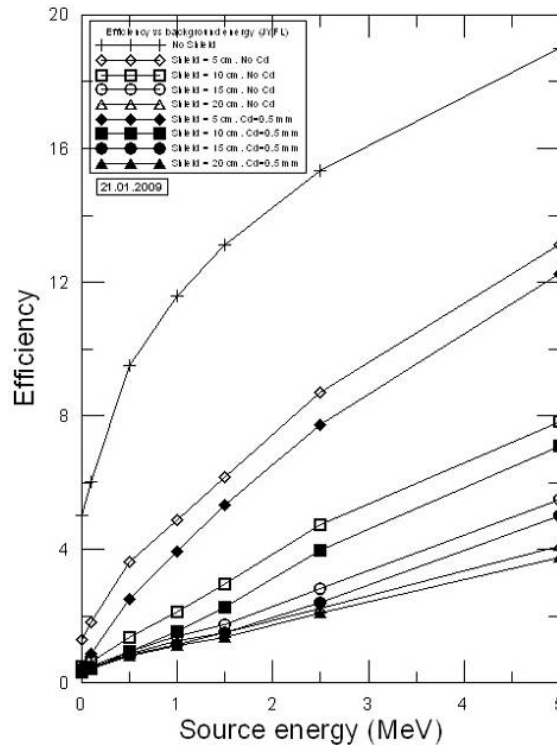


**Figure 4.** Efficiency of background detection.

## Summary

The optimal characteristics of the  $4\pi$  neutron detector have been studied using MCNPX simulations in order to obtain a high and flat efficiency for energy range from 0.1 MeV to 5 MeV. The total number of counters obtained in the simulation is 20. These counters are placed in two rings; ring A contains 8 counters at a radius of 11 cm and ring B contains 12 counters at a radius 20 cm. The effective length of the counters is 60 cm. These counters are filled with  $^3\text{He}$  as a detection gas at a pressure of 15200 torr.

This construction has an efficiency of about 28% for the energy range from 0.5 MeV to 4.5 MeV when the neutron propagation time in the simulation was limited to 200  $\mu\text{s}$ .

According to the study of background shielding in the final setup, the dimensions of the polyethylene block were found to be  $50 \times 50 \times 80 \text{ cm}^3$  with a 20 cm of polyethylene layer, therefore the total dimensions of the detector are  $90 \times 90 \times 80 \text{ cm}^3$ .

## References

- [1] MCNPX user's manual.
- [2] Technical Proposal for the Design, Construction, commissioning and Operation of the HISPEC/DESPEC experiment at the Low-Energy Branch of the Super-FRS facility. [http://www-linux.gsi.de/~wwwnusta/tech\\_report/09-hispec\\_despec.pdf](http://www-linux.gsi.de/~wwwnusta/tech_report/09-hispec_despec.pdf)
- [3] <http://www.gsi.de/fair/>
- [4] K.-L. Kratz, K. Farouqi, B. Pfeiffer, Nuclear physics far from stability and r-process nucleosynthesis, *Progress in Particle and Nuclear Physics* 59 (2007) 147–155.
- [5] Adimir dos Santos, The application of the multiple transient technique for the experimental determination of the relative abundances and decay constants of delayed neutrons of the IPEN/MB-01 reactor, *Annals of Nuclear Energy* 33 (2006) 917–923.
- [6] Knoll, G.F. "Radiation detection and measurement", Wiley Ed. 2<sup>nd</sup> edition (1988).

## Characterization of neutron detectors for nuclear technology applications

*T. Martinez<sup>1)</sup>, J. Agramunt<sup>2)</sup>, A. Algora<sup>2)</sup>, A. Aprahamian<sup>3)</sup>, D. Cano-Ott<sup>1)</sup>,  
L.M. Fraile<sup>4)</sup>, A.R. Garcia<sup>1)</sup>, A. Gottardo<sup>5)</sup>, C. Guerrero<sup>1)</sup>, M.D. Jordan<sup>2)</sup>,  
H. Mach<sup>3)</sup>, E. Mendoza<sup>1)</sup>, M. Mosconi<sup>6)</sup>, R. Nolte<sup>6)</sup>, M.C. Ovejero<sup>1)</sup>,  
E. Reillo<sup>1)</sup>, J.L. Tain<sup>2)</sup>, J.J. Valiente<sup>5)</sup>, D. Villamarin<sup>1)</sup>*

- 1) Centro de Investigaciones Energéticas, Medioambientales y Tecnológicas (CIEMAT) Avda. Complutense, 22, E-28040 Madrid, Spain
- 2) Instituto de Física Corpuscular (IFIC) Edificio de Institutos de Paterna, Apdo. Correos 22085, E-46071 Valencia, Spain
- 3) University of Notre-Dame, Notre Dame, IN-46556 Indiana, USA
- 4) Universidad Complutense de Madrid, Ciudad universitaria, E-28040, Madrid, Spain
- 5) Laboratori Nazionali di Legnaro (LNL-INFN) Viale dell'Università, 2, I-35020 Legnaro, Italy
- 6) Physikalisch-Technische Bundesanstalt (PTB) Bundesallee, 100, D-38116 Braunschweig, Germany

[trino.martinez@ciemat.es](mailto:trino.martinez@ciemat.es)

**Abstract:** The development of neutron detector systems contributes greatly to improve nuclear data relevant to nuclear technologies for radioactive waste transmutation and management. A time-of-flight spectrometer based on BC501A liquid scintillator has been proposed to measure beta delayed neutron data. Characterization of prototype detector at known irradiation fields and relevant energies is mandatory for a complete knowledge of the response function.

### Introduction

Improvement on nuclear data has received a special attention in the last decades within the framework of "Technology Advances in Fast Reactors and Accelerator Driven Systems for Actinides and Long-Lived Fission Products Transmutation". Accurate nuclear data are essential for the detailed design, safety assessment and operation of these reactor systems [1,2]. Neutron cross-sections (capture, fission, inelastic) data for minor actinides (MA) are needed with improved accuracy. Decay heat data of MA-dominated fuels as well as delayed neutron data play also a crucial role within the uncertainty assessment as it has been pointed out by NEA [3].

Delayed neutron (DN) data are studied at three different levels, microscopic level or individual precursors, macroscopic level or aggregate precursors and integral measurement level. The objective of the microscopic level is to evaluate fission yields, half-lives and emission probabilities ( $P_n$ ) for each individual precursor as well as their energy spectrum. These data are used to simulate the aggregate behaviour using the summation techniques and to estimate total delayed neutron yield. Comparison with experimental results from the macroscopic level studies allows us to improve existing libraries on DN data.

Developments of new facilities like FAIR facility at GSI will offer the opportunity to use high intensity radioactive beams to investigate exotic nuclear regions, in particular, neutron rich nuclei. The beta decay study of these nuclei is the main subject of the DESPEC experiment at FAIR. Beta delayed neutrons are emitted by excited nuclei formed in beta decay of some fission products, called neutron precursors. Absolute delayed neutron yield, the time dependence on the neutron activity and delayed neutron spectra have to be determined with high accuracy. A neutron spectrometer based on liquid organic scintillation cells has been proposed in order to extract information on neutron emission rate probabilities and neutron energy spectra by means of Time-of-Flight technique (TOF).

The aim of this work is to characterize one of the prototype of the detector cell at known irradiation fields in order to acquire a complete knowledge of the response function and therefore to improve the final design of the spectrometer. Features such as the light output

functions for scattered proton and electrons, the resolution function as well as the neutron detection efficiency have been investigated at different neutron energies. A second objective has been to test the performance of digital electronics in order to develop a digital acquisition system based on fast digitizers for the spectrometer.

The present status of the analysis and the preliminary results will be presented in this work. The experimental conditions, analysis procedure and results obtained are reported in the following sections.

### Experimental details

A set of measurements have been performed at the PIAF facility of PTB [4] institute in Braunschweig (Germany) using two accelerators: the TCC CV-28 cyclotron and the 3.75MV VandeGraaff (VdG). The cyclotron has been used to provide mono-energetic neutron beams above 5MeV through the D(d,n) reaction. The VdG accelerator provided neutron beams with lower energies through the  ${}^7\text{Li}(p,n){}^7\text{Be}$  and T(p,n) ${}^7\text{Be}$  reactions.

Thus, two different experimental set-ups have been arranged in order to irradiate the scintillation detector. In the case of the cyclotron, the cell detector was placed at a distance of 10.5 m from the target position and at the VdG hall the detector was irradiated at different distances, between 1 and 2.5 m depending on the intensity of the neutron fluence.

Several absolute calibrated detectors from the PTB facility were used to monitor the beam and to determine the neutron fluence rate for each measurement. A summary of the neutron energies and physical parameters are reported in table 1.

Neutron energy (MeV)	Reaction	Target ( $\mu\text{g}/\text{cm}^2$ )	Projectile E (MeV)	Distance (cm)	Estimated Fluence rate ( $\text{n cm}^{-2} \text{s}^{-1}$ )
0.144	${}^7\text{Li}(p,n){}^7\text{Be}$	LiF (70)	1.937	100	80
0.250	${}^7\text{Li}(p,n){}^7\text{Be}$	LiF (70)	2.027	150	20
0.565	${}^7\text{Li}(p,n){}^7\text{Be}$	LiF (70)	2.297	150	98
1.2	T(p,n) ${}^3\text{He}$	T/Ti (853)	2.047	200	240
2.5	T(p,n) ${}^3\text{He}$	T/Ti (1910)	3.353	200	810
8.0	D(d,n) ${}^3\text{He}$	D gas	4.858	1050	140
10.0	D(d,n) ${}^3\text{He}$	D gas	6.901	1050	140
12.0	D(d,n) ${}^3\text{He}$	D gas	9.033	1050	140
14.0	D(d,n) ${}^3\text{He}$	D gas	10.927	1050	140

**Table 1.** List of energies and measurements performed at the PTB facilities.

The detector prototype consisted of a commercial cylindrical aluminium cell of the MAB-1F type, filled with BC501A organic scintillation liquid, manufactured by Saint-Gobain. The inner dimensions of the cell were 20 cm of diameter and 5.08 cm of length. The inner walls of the cell were coated with a white diffuse painting, BC622A. One of the large face of the cell was closed with a glass window and coupled to a 5" photomultiplier through a conical light guide of 5 cm made of Plexiglass. The surface of the light guide was partially coated with diffuse painting in order to optimize the light collection. The PMT used was a Photonis model XP4512B of 10 stages, with anode and dynode outputs.

The readout of the detector signals was carried out with a data acquisition system (DAQ) based on digital electronics, a flash-ADC board model DC271 of 8 bit and 1GS/s of sampling rate, manufactured by ACQIRIS. The event trigger of the system was build from a signal from the detector in coincidence with the accelerator signal. This signal was used as external trigger of the digitizer. A scheme of the electronics is shown in figure 1. The anode signal and the signal from accelerator were splitted with a FIFO module and fed into CFD and GDG modules to generate the coincidence that triggered the digitizer. Then, a second branch of each signal was digitized directly in the ACQIRIS board over 1  $\mu\text{s}$  when a trigger occurred. A set of 5000 digitized signals were grouped into iteration and written into files that were transferred to disk as run files. Software routines were developed to determine the parameters needed for the analysis such as the time-of-flight from the time difference between signals, the amplitude of the pulse and the total and delayed charge from the

integration of the pulse area over different time intervals. The parameters were stored in structures and files that conserve the event structure for further analysis.

A digital counter/timer board, model PCI-6602 manufactured by National Instruments was used to count all signals from the different detectors and accelerator in order to estimate the dead-time losses in the ACQIRIS. In general, the acquisition dead-time values were in the range of 4-6% except in the case of 2.5 MeV neutron beam energy where we obtained loss value of 14%.

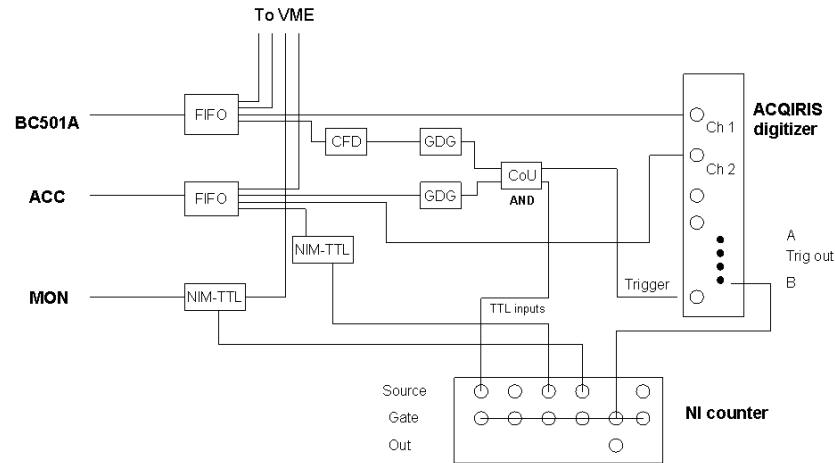


**Figure 1.** Schematic electronics diagram of the digital DAQ system used in this experiment. FIFO stands for Lecroy 928F linear FanOut, CFD stands for Ortec 584 discriminator, GDG stands for Ortec 8020, CoU stands for Ortec 4020.

Time of flight technique has been exploited to select neutrons events from gamma events originated in the reaction due to its larger flying times of the neutrons. Furthermore, the accelerators were run in pulsed mode to optimize the direct neutron events from scattered in surrounding materials and spurious background events.

## Data analysis

The response function is usually express in terms of light units by convention in order to have a common scale. Moreover, the light output function,  $L_p(E)$ , for protons as well as other heavy charged particles, is generally expressed in terms of the electron light output because this quantity has a linear dependence on the electron energy. Then, in order to determine the light output function for protons for the energy range of our measurements, up to 14MeV, a standard analysis procedure has been followed.

### Gamma calibration

The electron light output function,  $L_e(E)$ , has been established to be linear for energies above 50 keV [5], following the expression,  $L_e = E_e - E_0$ , where  $E_e$  is the compton energy of electron and  $E_0$  is an energy offset to compensate the nonlinearity of the light output at low electron energies and has a value of 5 keV. Therefore, a set of standard gamma-ray sources,  $^{22}\text{Na}$ ,  $^{137}\text{Cs}$  and  $^{207}\text{Bi}$ , were used as calibration points using their Compton energy. A  $^{241}\text{Am}$  source was also used, considering the photoelectric peak energy of 60 keV.

Then, the experimental Compton spectrum for each source obtained from the total charge was compared to a MonteCarlo simulation of the Compton convoluted with the appropriate response function for this energy. A MC code [6] based on GEANT4 package has been developed to simulate the detector light response to gamma and neutrons. For a fixed energy the response function is assumed to be Gaussian and can be written as  $G(Q,L) = A \cdot \exp\{ (k \cdot Q - L)^2 / 2\sigma^2 \}$ , where  $k$  is the calibration factor and  $\sigma$  is the detector resolution ( $\Delta L/L$ ). These parameters as well as the position of the experimental Compton edge were determined by fitting the simulated spectra to the experimental one.

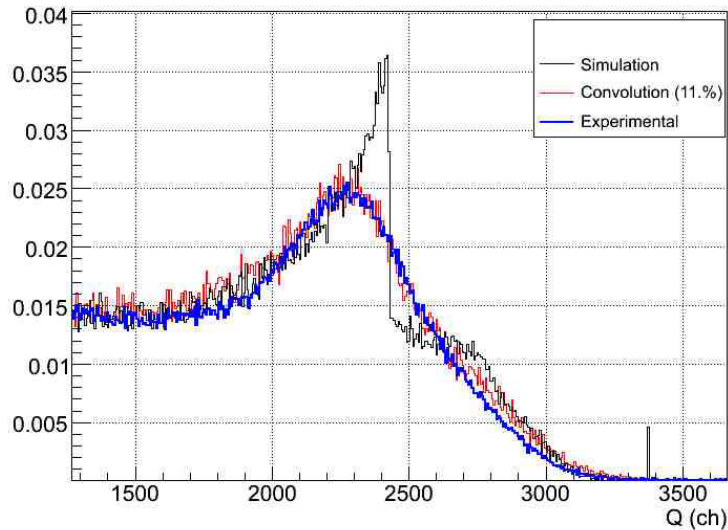


**Figure 2.** Example of the Monte carlo simulation and experimental spectrum for  $^{137}\text{Cs}$  source.

The comparison of both spectra for all gamma sources has allowed us to determine the light output calibration for electrons as a function of the equivalent energy and the resolution function ( $\Delta L/L$ ).

#### Neutron data

Once the total charge was calibrated in terms of energy equivalent, the data were sorted into two-dimensional matrices corresponding to the TOF vs Total charge parameters and Total charge vs delayed-to-total charge ratio parameters. Then, the proton recoil response function for the different neutron energies were obtained according to the following steps:

First, by setting a condition at the peak structure in the TOF spectrum corresponding to the neutron events, the gamma events originated in the reaction were removed. By applying a further condition on the delayed-to-total charge ratio other undesired random events were also discarded. A background subtraction were carried out by setting gates at both sides of the neutron peak of the TOF spectrum.

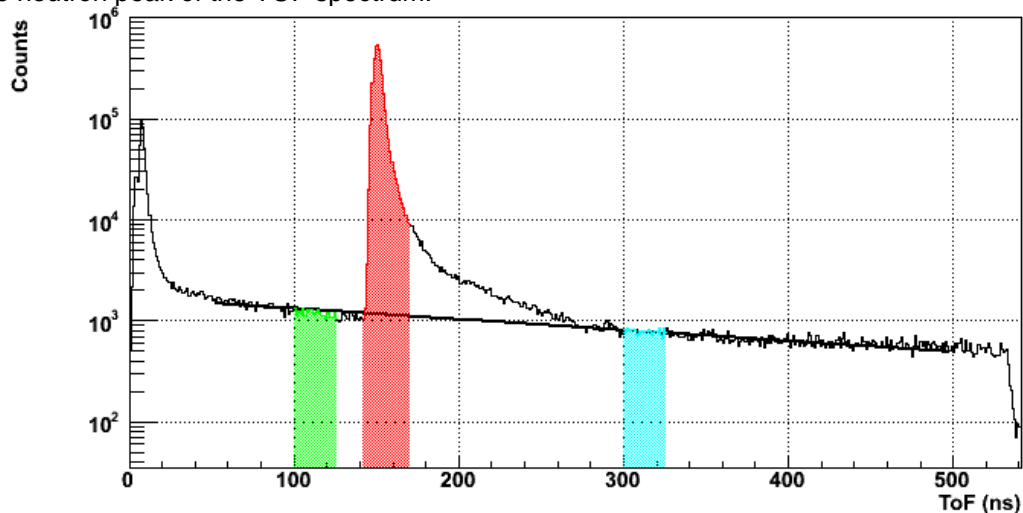


**Figure 3.** Example of measured TOF spectrum. The peak (red area) at around 140 ns corresponds to the neutron of 0.565 MeV. The gamma flash peak is observed at 4.5 ns.

Finally, the experimental spectra were corrected for the acquisition dead-time, determined from the data registered by the NI counter, and normalized to the total neutron fluence in the detector, estimated from the calibrated neutron monitors data. The resulting response distributions, corresponding to the different mono-energetic neutron measurements are shown in Fig.4.

The MC code was used to simulate the neutron response folded with the resolution function deduced for the gamma energies. The experimental proton recoil spectra were compared with the MC simulated responses, in order to check the upper edge of the response functions and thus determine the position  $L_p(E)$  that corresponds to the maximum energy transferred to the recoil. The comparison between experimental and simulated response showed small differences, in particular in the shape of the distribution. The results from these comparisons did not allowed us to obtain a reliable light output function,  $L_p(E)$ , and a further analysis have to be done.

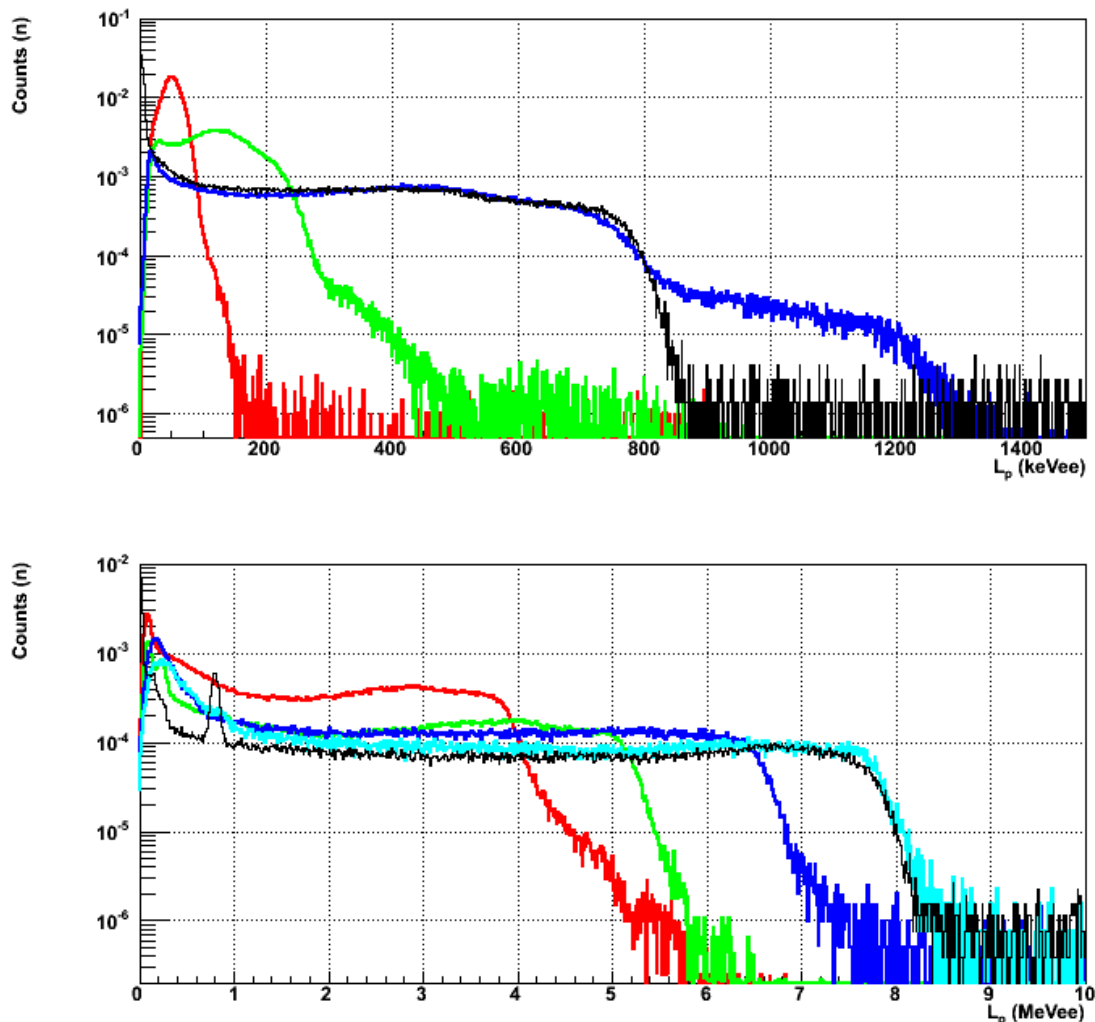


**Figure 4.** Experimental proton recoil response (coloured lines) for mono-energetic neutrons of 0.565, 1.2 and 2.5 MeV from the VdG measurements (upper panel) and for neutrons of 8, 10, 12 and 14 MeV from  $D(d,n)$  reaction (bottom panel). Two MC simulated response for 2.5 MeV and 14 MeV were also shown (black line) for comparison.

### Neutron efficiency

The neutron detection efficiency of the detector cell at a given neutron energy can be deduced by integrating the corresponding response function normalized with the total neutron fluence over the energy range from the threshold energy  $E_{th}$ , up to  $E_{max}=E_n$ . The detection efficiency is strongly affected by the threshold energy for lower neutron energies.

The detection threshold has been deduced from the gamma sources spectra, being 50 keVee in the case of the neutron measurements performed at the VdG accelerator and 100 keVee for the cyclotron measurements. The total fluence values were better estimated for VdG energies than for cyclotron energies because only calibrated factors from the neutron monitors were obtained for the VdG measurements during the run. The experimental

efficiency was then estimated from the integration of the normalized and corrected light output distribution between the detection threshold and the maximum energy.

The efficiency expected with our detector cell has been calculated by means of our Monte Carlo code for different experimental conditions, threshold settings and neutron energy. The calculated efficiency values have been plotted as curves in Fig. 5, together with the experimental data.

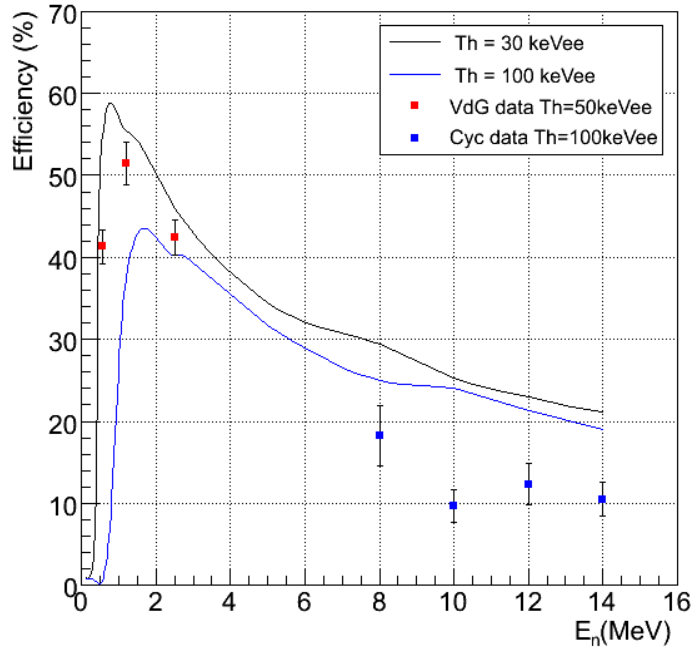


**Figure 5.** Neutron detection efficiency as a function of the neutron energy. The experimental threshold was determined to be 50keVee in the case of VdG measurements and 100keVee for cyclotron measurements.

## Conclusions

The performance of a BC501A liquid organic scintillator cell have been characterized in terms of light output functions for electrons and protons at the PTB accelerator facility. Time of flight technique has been used to reduce the undesired background events.

The experimental light output responses have been calibrated in terms of equivalent energy, and have been compared with simulated spectra. The obtained results were compatible but a further analysis is needed to achieve a reliable results. The data analysis of the PTB neutron monitor will help to improve the ACQIRIS data analysis.

The performance of a digital data acquisition system based on flash-ADC board of 8 bits and 1GS/s of sampling rate has also been tested during the PTB run.

## Acknowledgements

The authors would like to thank the EFNUDAT program for funding support. We would like to thank R. Nolte and collaborators of the Neutron Dosimetry Group for their help during the run and the accelerator staff of PTB. The technical support of Ciemat staff is also acknowledged.

## References

- [1] M. Salvatores. "Future nuclear power systems and nuclear data needs". J. Nucl. Sci. and Tech. Supplement 2, 4-12 (2002).
- [2] Y. Ikeda. "Nuclear data relevant to accelerator driven systems". J. Nucl. Sci. and Tech. Supplement 2, 13-18 (2002).
- [3] A. d'Angelo. "Delayed neutron data". WPEC-6 NEA-OECD. <http://www.nea.fr/>
- [4] Physikalisch-technische Bundesanstalt (PTB). <http://www.ptb.de>
- [5] G. Dietze, H. Klein, Nucl. Instr. and Meth. 193 (1982) 549.
- [6] E. Reillo, Diploma thesis, 2008.

## Cross-section Measurements of (n,xn) Threshold Reactions

*O. Svoboda<sup>1,2)</sup>, A. Krása<sup>1)</sup>, M. Majerle<sup>1)</sup>, J. Vrzalová<sup>1,2)</sup>, V. Wagner<sup>1,2)</sup>*

- 1) Nuclear Physics Institute of the ASCR PRI, 250 68 Řež near Prague, Czech Republic  
 2) Faculty of Nuclear Sciences and Physical Engineering, Czech Technical University in Prague, Břehová 7, 115 19, Prague, Czech Republic  
[svoboda@ujf.cas.cz](mailto:svoboda@ujf.cas.cz)

**Abstract:** There are significant voids in the cross-section libraries of (n,xn) reactions in many materials. This was realized during the "Energy plus Transmutation" project, at which Au, Al, Bi, In and Ta activation detectors were used to measure high-energy neutrons produced in spallation reactions. Threshold (n, $\alpha$ ), (n,p) and (n,xn) reactions were observed with the x up to 9 (threshold  $\sim$ 90 MeV), but almost no experimental cross-section data are available for neutron energies above 20 MeV. Seven successful irradiations were performed last year on quasi-monoenergetic neutron sources based on the  ${}^7\text{Li}(p,n){}^7\text{Be}$  reaction. The (n, $\alpha$ ), (n,p) and (n,xn) cross-sections on Al, Au, Bi, In, I, and Ta were measured in the experiment at TSL in Uppsala at neutron energies 22, 47, and 95 MeV. Further four irradiations were done at NPI in Řež with the neutron beams of 17, 22, 30 and 35 MeV.

### Introduction

We participate in the "Energy plus Transmutation" project (E+T) [1], [2] (concerning Accelerator Driven Systems) being performed at JINR Dubna, Russia. Neutron fluxes produced in the spallation reactions of relativistic light ions on thick, heavy targets are being investigated. For neutron spatial and energetic distributions measurements, threshold reactions on mostly mono-isotopic activation foils are used. But the knowledge of most cross-sections is still insufficient.

Last year three cross-section measurements were performed at The Svedberg Laboratory (TSL) in Uppsala, Sweden, supported by the EFNUDAT project [3]. Neutron beams of 22, 47, and 95 MeV were used to measure cross-sections of (n,xn), (n, $\alpha$ ) and (n,p) threshold reactions on Al, Au, Bi, In, I, and Ta materials. Basic information about the course of cross-section energy dependence at high energies was gained and many of the data are unique and absolutely new. Measurements at Uppsala were during the years 2008-2009 supplemented with four (n,xn) cross-section measurements on the cyclotron in Řež, the Czech Republic, which covered the energy region 17 – 35 MeV and connected newly measured data from Uppsala with already known cross-sections in the libraries.

### State-of-the-art of Neutron Cross-section Libraries

The present status of knowledge of cross-sections for (n,xn) reactions is poor, same as for (n, $\alpha$ ) and (n,p). In EXFOR [4] there are only a few experimentally measured cross-section values for neutron energies above 20 MeV and no cross-section values above 30 – 40 MeV for Au, Al, In, and Ta. The (n,2n) reaction is mostly well known under 20 MeV, (n,3n) and (n,4n) reactions with higher thresholds are known only for few energies. Cross-sections of higher (n,xn) reactions have not been measured up to now. The only one exception is bismuth, on which reactions from (n,4n) to (n,12n) were measured in just one experiment up to 150 MeV [5] and there are no evaluated data available. So, also these cross-sections should be measured again and verified. Concerning the evaluated nuclear data libraries, the situation is similar to EXFOR. At higher energies only a few experimental data exist (e.g. figure 2), the codes have a few points to follow and the predictions are not good or do not exist. In E+T experiments computer code TALYS 1.0 [6] is used together with MCNPX **Hiba! A hivatkozási forrás nem található.**] to calculate cross-sections for the (n,xn) threshold reactions in our neutron activation detectors. Examples of comparison between experimental data from EXFOR, evaluated data from ENDF/B-VII.0 and values calculated by the TALYS 1.0 code are shown in the figures 1 and 2.

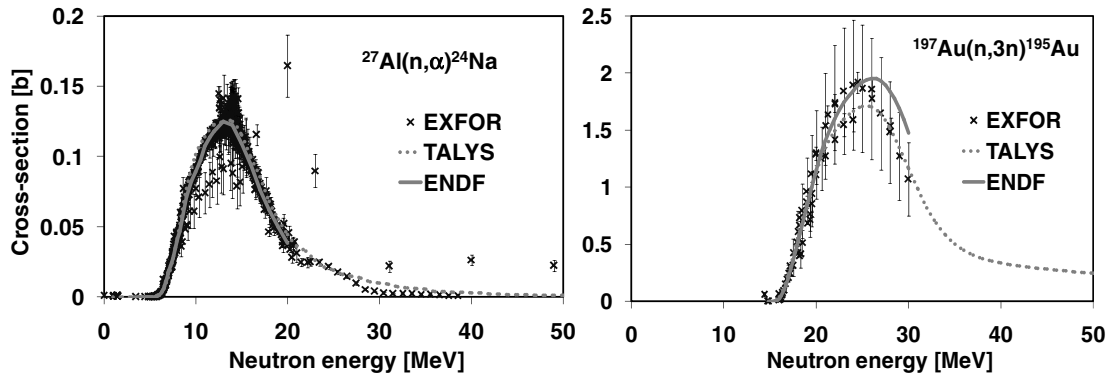


**Figure 1.** Cross-section of  $(n,\alpha)$  reaction in  $^{27}\text{Al}$  (left) and  $(n,3n)$  reaction in  $^{197}\text{Au}$  (right). The measured data (the black crosses) are from the EXFOR *Hiba! A hivatkozási forrás nem található.* database, the solid grey line is from deterministic code TALYS 1.0 [6], and the dashed line is from ENDF/B-VII.0 [8].

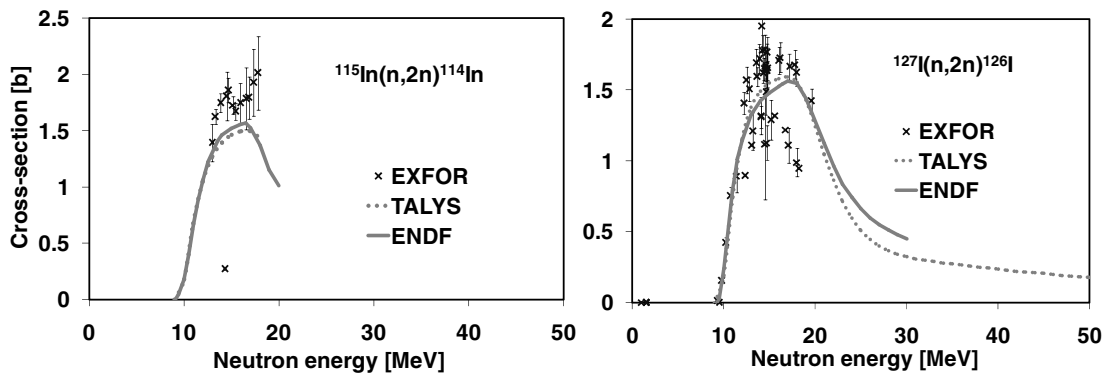


**Figure 2.** Cross-section of  $(n,2n)$  reaction in  $^{115}\text{In}$  (left) and  $^{127}\text{I}$  (right). The measured data (the black crosses) are from the EXFOR [4] database, the dashed line is from deterministic code TALYS 1.0 [6], and the solid grey line is from ENDF/B-VII.0 [8].

### Threshold Energies of $(n,xn)$ , $(n,\alpha)$ and $(n,p)$ Reactions

Threshold energies of  $(n,xn)$ ,  $(n,\alpha)$  and  $(n,p)$  reactions are important in the moment of choosing proper neutron beam energy. They can be found e.g. on the web page Q-TOOL up to  $(n,6n)$  [9]. For higher  $(n,xn)$  reactions the threshold energies can be calculated from the difference in ground state masses of parent and daughter products [10].

**Table 1.** Threshold  $(n,xn)$  reactions in  $^{197}\text{Au}$  and  $^{209}\text{Bi}$  with the half-life of reaction product. The observed isotopes are printed in bold.

Data source	Reaction	Threshold energy [MeV]	Half-life	Reaction	Threshold energy [MeV]	Half-life
Q - TOOL	$^{197}\text{Au}(n,2n)^{196}\text{Au}$	<b>8.1</b>	<b>6.183 d</b>	$^{209}\text{Bi}(n,2n)^{208}\text{Bi}$	7.3	$3.7 \cdot 10^5$ y
	$^{197}\text{Au}(n,3n)^{195}\text{Au}$	<b>14.8</b>	<b>186.1 d</b>	$^{209}\text{Bi}(n,3n)^{207}\text{Bi}$	<b>13.9</b>	<b>31.55 y</b>
	$^{197}\text{Au}(n,4n)^{194}\text{Au}$	<b>23.2</b>	<b>38.02 h</b>	$^{209}\text{Bi}(n,4n)^{206}\text{Bi}$	<b>22.6</b>	<b>6.243 d</b>
	$^{197}\text{Au}(n,5n)^{193}\text{Au}$	<b>30.2</b>	<b>17.65 h</b>	$^{209}\text{Bi}(n,5n)^{205}\text{Bi}$	<b>29.6</b>	<b>15.31 d</b>
	$^{197}\text{Au}(n,6n)^{192}\text{Au}$	<b>38.9</b>	<b>4.94 h</b>	$^{209}\text{Bi}(n,6n)^{204}\text{Bi}$	<b>38.1</b>	<b>11.22 h</b>
Ground-state Masses	$^{197}\text{Au}(n,7n)^{191}\text{Au}$	<b>45.7</b>	<b>3.18 h</b>	$^{209}\text{Bi}(n,7n)^{203}\text{Bi}$	<b>45.2</b>	<b>11.76 h</b>
	$^{197}\text{Au}(n,8n)^{190}\text{Au}$	<b>54.5</b>	<b>42.8 min</b>	$^{209}\text{Bi}(n,8n)^{202}\text{Bi}$	<b>54</b>	<b>1.72 h</b>
	$^{197}\text{Au}(n,9n)^{189}\text{Au}$	61.8	28.7 min	$^{209}\text{Bi}(n,9n)^{201}\text{Bi}$	<b>61.4</b>	<b>1.8 h</b>
	$^{197}\text{Au}(n,10n)^{188}\text{Au}$	<b>70.9</b>	<b>8.84 min</b>	$^{209}\text{Bi}(n,10n)^{200}\text{Bi}$	<b>70.8</b>	<b>36.4 min</b>
	$^{197}\text{Au}(n,11n)^{187}\text{Au}$	77.0	8.4 min	$^{209}\text{Bi}(n,11n)^{199}\text{Bi}$	78.4	27 min
	$^{197}\text{Au}(n,12n)^{186}\text{Au}$	84.7	10.7 min	$^{209}\text{Bi}(n,11n)^{198}\text{Bi}$	86	10.3 min

It is necessary to stress that  $\sigma(E)$  reaches its maximum at the energy of about 10 MeV bigger than the threshold energy, see e.g. the Figure 1.

## Irradiation Facilities

### Cyclotron at TSL Uppsala

In the frame of the EFNUDAT program three irradiations/cross-section measurements at The Svedberg Laboratory (TSL) in Uppsala have been performed. The quasi-monoenergetic 22, 47, and 94 MeV neutron source based on the  ${}^7\text{Li}(p,n){}^7\text{Be}$  reaction [11] was used. High energy protons from the cyclotron at TSL were directed to a thin, lithium target. The produced neutron flux density was up to  $5 \cdot 10^5 \text{ cm}^{-2}\text{s}^{-1}$ . The half of intensity was in the peak with  $\text{FWHM} = 1 \text{ MeV}$  (corresponds to the ground state and first excited state at 0.43 MeV in  ${}^7\text{Be}$ ) and half of intensity was in continuum in lower energies (corresponds to higher excited states, multiple-particle emission etc.), see Figure 3. Proton energy loss amounted 2 - 6 MeV in the target depending on the incident beam energy and target thickness. Downstream the target, the proton beam was deflected by a magnet and guided onto a graphite beam dump. The neutron beam was formed by an iron collimator (50 cm in diameter and 100 cm long) with a circle hole of 122 mm in diameter.

### Cyclotron at Nuclear Physics Institute, Řež

The second quasi-monoenergetic neutron source that was used for  $(n,xn)$  cross-section measurements is in the Nuclear Physics Institute at the Academy of Sciences of the Czech Republic in Řež. Protons from the cyclotron can be directed to the lithium target and quasi-monoenergetic neutrons in the range 10 – 37 MeV can be produced [12]. Rest of the beam is dumped in a graphite stopper placed directly behind the lithium target, no collimators are used.

Neutron source in Řež has a big advantage in a hundred times higher neutron intensity than the neutron source at Uppsala. On the other hand, the produced neutron spectra were not measured, but overtaken from similar target device published in [13]. Moreover, neutron source is close to the cyclotron and both are not shielded, so there is quite strong low energy neutron background. This background does not affect our threshold reactions, but produce  $(n,\gamma)$  reactions in unwanted isotopes.

The  $(n,xn)$  cross-section measurements in Řež were originally started as a test for the cross-section measurements at Uppsala. After the Uppsala measurements they continued as a supplement and they produce data that connect known data from EXFOR and new values from Uppsala. During the measurements various aspects and possible sources of systematic uncertainties are also tested (correction factors on non-point like emitters, coincidences, spectra processing etc.). Up to now four irradiations were performed with proton energies 20, 25, 32.5, and 37 MeV.

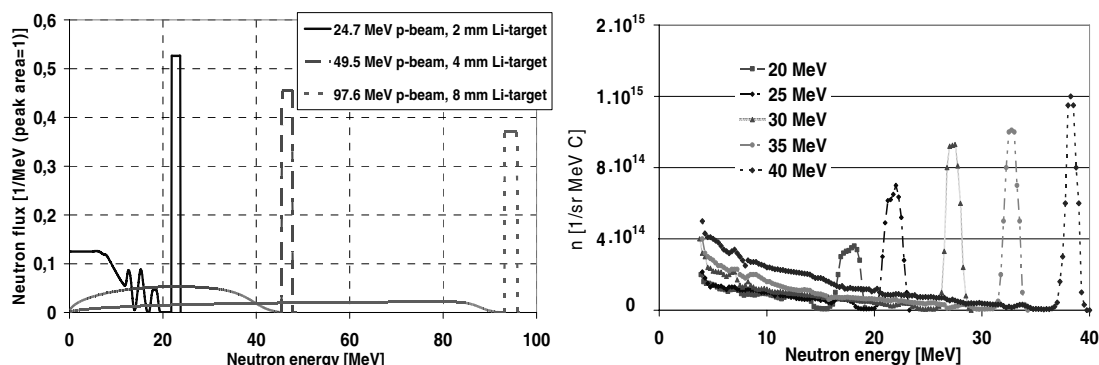


**Figure 3.** Quasi-monoenergetic neutron spectrum from  ${}^7\text{Li}(p,n){}^7\text{Be}$  at the TSL (left) and cyclotron Řež (right) – data overtaken from the facility staff (TSL – A. Prokofiev, Řež – M. Honusek).

## Measurement and Evaluation of Irradiated Samples

Au, Al, Bi, I, In and Ta samples were used in all experiments. Fe, Mg, Ni, and Zn were also used in some experiments in Řež. Materials had (except the iodine) a form of foils with dimensions of 20x20 mm<sup>2</sup> and thickness ranging from 0.05 up to 1 mm. Weights of the foils were from 0.2 up to 7 grams depending on the foil type and cross-section value at respective beam energy. The foils were wrapped in paper to avoid isotope transport between the foils and detector contamination. Iodine samples were in form of solid KIO<sub>4</sub> tablet packed hermetically in plastic.

Typical irradiation time was 8 hours in Uppsala, respectively 12 hours in Řež. Transport from the irradiation hall to the spectrometer took approximately 2 – 10 minutes. After irradiations, activated foils were measured on HPGe detectors. Gained gamma-spectra were evaluated in the DEIMOS-32 code [14]. Yields of observed isotopes were calculated according to the equation (1) with respect to necessary spectroscopic corrections and scaled to 1 gram of target material.

### Spectroscopic Corrections

Various spectroscopic corrections were applied to catch up all possible systematic errors. To the routinely used corrections belonged the correction on decay during irradiation, decay during cooling and measurement, dead-time correction, correction on detector efficiency and gamma-line intensity and real coincidence correction. The self absorption correction was determined to be in extreme case up to the factor of 2 because of big thickness of some foils and low energy of some  $\gamma$ -lines (at most cases typically up to 1.05). Square-emitter correction was determined with the help of MCNPX to be up to the factor of 0.96 because of the close detector geometry. Correction on self-shielding was negligible for the (n,xn) threshold reactions, as it was experimentally proven on the neutron beams in Řež.

All corrections are already used in the Energy plus Transmutation experiments and were many times experimentally tested, so they represent no restriction for the cross-section measurements.

$$N_{yield} = \frac{S_p \cdot C_{abs}(E)}{I_\gamma \cdot \epsilon_p(E) \cdot Coi \cdot C_{area}} \frac{t_{real}}{t_{live}} \frac{1}{m_{foil}} \frac{e^{(\lambda \cdot t_0)}}{1 - e^{(-\lambda \cdot t_{real})}} \frac{\lambda \cdot t_{irr}}{1 - e^{(-\lambda \cdot t_{irr})}} \quad (1)$$

$S_p$  – peak area

$C_{abs}$  – correction for self-absorption

$t_{real}$  – real time of measurement

$\lambda$  – decay constant

$t_0$  – time between irradiation and measurement

$t_{irr}$  – time of irradiation

$I_\gamma$  – intensity of gamma-line

$\epsilon_p$  – peak efficiency of the detector

$Coi$  – correction on coincidences

$C_{area}$  – correction on square-emitter

$t_{live}$  – live time of the measurement

$m_{foil}$  – mass of the foil

### Cross-section determination

Estimated peak of the cross-section and peak of the neutron spectrum were at the same position at some energies and reactions. In these cases the production of the isotope in background could be neglected (was practically equal to zero) and the cross-section can be calculated according to:

$$\sigma = \frac{N_{yield} \cdot S \cdot A}{N_n \cdot N_A} \quad (2)$$

where is:

$\sigma$  – cross-section of the reaction

$N_{yield}$  – yield of selected isotope

$S$  – foil area

$A$  – molar weight

$N_n$  – number of neutrons in the peak

$N_A$  – Avogadro number

In the remaining cases the production in background had to be subtracted. Computed cross-sections from TALYS were folded with the appropriate neutron spectrum and production in peak and in neutron background was assessed. Ratio peak/total production was computed (ratio cancels out possible error in absolute value of the cross-section, but still remains uncertainty in the cross-section shape). The lower is the threshold of the reaction and higher beam energy, the bigger is the uncertainty of this procedure.

## Preliminary Cross-section Results from Uppsala and Řež

Well known (n,2n) reactions are used to check new cross-section data. It is supposed that when these comparisons will be right also the cross-section values at 47 and 94 MeV will be correct with high probability. This is confirmed also in the comparisons with bismuth.

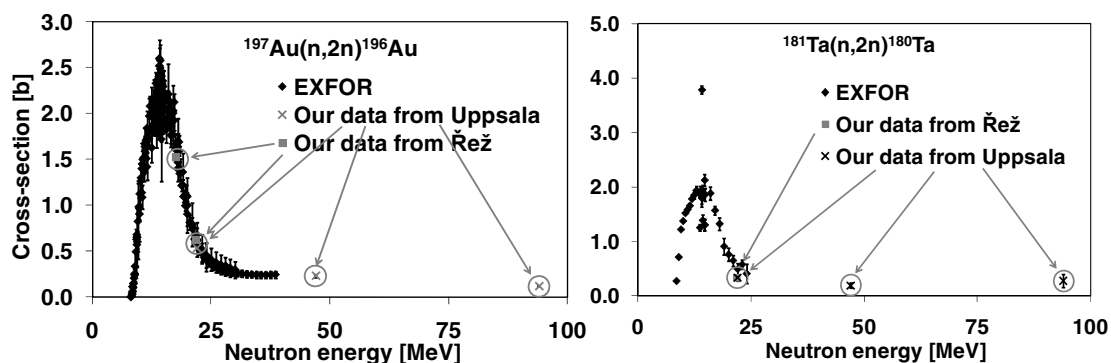


**Figure 4:** Comparison between the EXFOR data and our cross-section results from Uppsala and Řež for the reactions  $^{197}\text{Au}(n,2n)^{196}\text{Au}$  and  $^{181}\text{Ta}(n,2n)^{180}\text{Ta}$ .

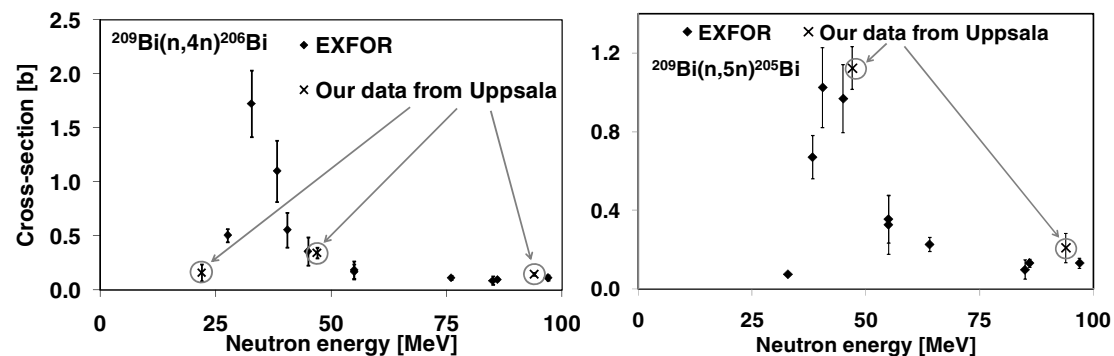


**Figure 5:** Comparison between the EXFOR data and our cross-section results from Uppsala for the reactions (n,4n) and (n,5n) on  $^{209}\text{Bi}$ .

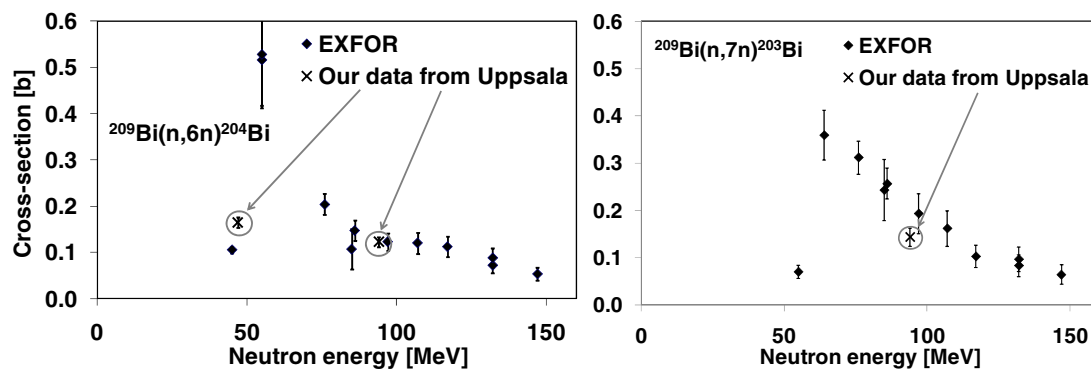


**Figure 6:** Comparison between the EXFOR data and our cross-section results from Uppsala for the reactions (n,6n) and (n,7n) on  $^{209}\text{Bi}$ .

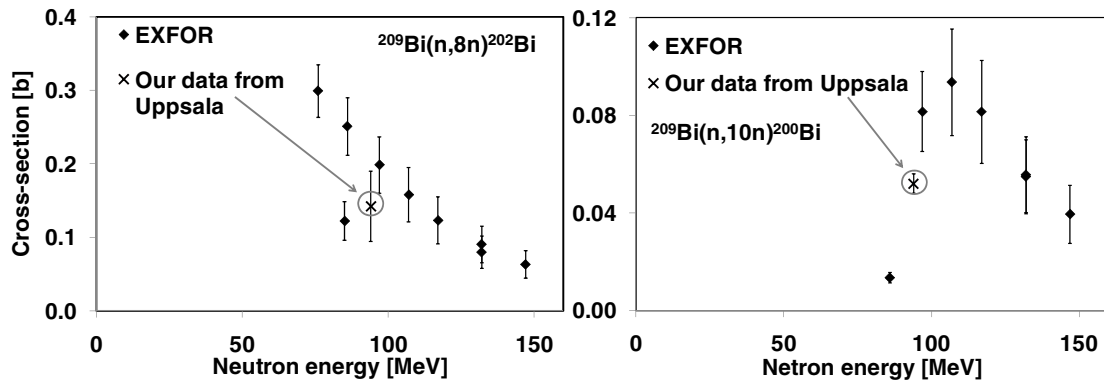


**Figure 7:** Comparison between the EXFOR data and our cross-section results from Uppsala for the reactions  $(n,8n)$  and  $(n,10n)$  on  $^{209}\text{Bi}$ .

Some of the results from the cross-section measurements from Uppsala and Řež from last year are shown in the figures 4 – 7. These results are still preliminary as written in the heading, because the measurements and evaluation of the data from Řež are still under way. During this process we improve our corrections that were also applied for the Uppsala data, so we hope we will be able to lower the uncertainties of Uppsala measurement. Figures 4 - 7 were generated from the EXFOR data with addition of our data from Uppsala and Řež.

## Conclusion

We have performed seven cross-sections measurements of neutron threshold reactions on Al, Au, Bi, I, In, and Ta. We used two quasi-monoenergetic neutron sources in NPI Řež and in TSL Uppsala. The  $(n,xn)$  reactions were measured in the energy range 17 – 94 MeV. Comparisons of newly measured cross-section data with EXFOR have proven that the measurement method and systematic of evaluation are reliable and can offer valuable cross-section data. New irradiations are planned for near future both in NPI Řež and in TSL Uppsala.

## Acknowledgements

Parts of the data presented in the work were supported from the EFNUDAT program. The authors are grateful to P. Bém, M. Honusek and E. Šimečková, who have supported the irradiation of the investigated foils at NPI neutron source and have given the parameters of irradiation.

## References

- [1] Majerle M. et al.: MCNPX simulations of the experiments with relativistic protons directed to thick, lead targets, Nuclear Instruments and Methods in Physics Research A 580 (2007) 110-113
- [2] M. I. Krivopustov et al.: First results studying the transmutation of  $^{129}\text{I}$ ,  $^{237}\text{Np}$ ,  $^{238}\text{Pu}$ , and  $^{239}\text{Pu}$  in the irradiation of an extended natU/Pb-assembly with 2.52 GeV deuterons, Journal of Radioanalytical and Nuclear Chemistry 279 (2009) 567-584
- [3] European Facilities for Nuclear Data Measurements, www.efnudat.eu, 7.9.2009
- [4] Experimental Nuclear Reaction Data (EXFOR/CSISRS) [<http://www.nndc.bnl.gov/exfor/>], 7.9.2009
- [5] Kim E. et al. Measurements of Neutron Spallation Cross-Sections of  $^{12}\text{C}$  and  $^{209}\text{Bi}$  in the 20 To 150 MeV Energy Range, Nuclear Science and Engineering 129 (1998) 209
- [6] Koning A. J. et al.: TALYS-1.0., Proceedings of the International Conference on Nuclear Data for Science and Technology - ND2007, April 22-27, 2007 Nice France, 211-214, ISBN: 978-2-7598-0900-2
- [7] Hendricks J. S. et al.: MCNPX, VERSION 2.6.C, LANL report LAUR-06-7991 (2006)
- [8] Evaluated Nuclear Data File (ENDF/B-VII.0), <http://www.nndc.bnl.gov/exfor/endl00.jsp>, 19.9.2009
- [9] Qtool: Calculation of Reaction Q-values and Thresholds, <http://t2.lanl.gov/data/qtool.html>, 7.9.2009
- [10] Audi G. et al.: The NUBASE Evaluation of Nuclear and Decay Properties, Nuclear Physics A 729 (2003) 3-128
- [11] Prokofiev A. V. et al., The TSL Neutron Beam Facility, Radiation Protection Dosimetry, 126 (2007) 18-22

- [12] Bém P. et al.: The NPI cyclotron-based Fast Neutron Facility, Proceedings of the International Conference on Nuclear Data for Science and Technology- ND2007, April 22-27, 2007 Nice France, 555-558, ISBN: 978-2-7598-0900-2
- [13] Uwamino Y. et al.: High energy p/Li neutron field for activation experiment, Nuclear Instruments and Methods in Physics Research A 389 (1997) P. 463-473
- [14] Frána J., Program DEIMOS32 for Gamma-Ray Spectra Evaluation, Journal of Radio-analytical and Nuclear Chemistry, V.257, (2003), No. 3 P. 583-587



## Author Index

- Agramunt, J. — 149  
 Algora, A. — 149  
 Andriamonje, S. — 33, 39  
 Andrzejewski, J. — 33, 39  
 Aprahamian, A. — 149  
 Aregbe, Y. — 101  
 Audouin, L. — 33, 39  
  
 Bécares, V. — 33, 39  
 Bečvář, F. — 33, 39  
 Belgya, T. — iii, 115, 121  
 Belloni, F. — 33, 39  
 Berthier, B. — 33, 39  
 Berthoumieux, E. — 33, 39  
 Billnert, R. — 127  
 Birgersson, E. — 139  
 Borcea, R. — 133  
 Borella, A. — 27  
 Brugger, M. — 33, 39  
  
 Caballero-Folch, R. — 145  
 Calviani, M. — 33, 39  
 Calviño, F. — 33, 39, 145  
 Cano-Ott, D. — 33, 39, 145, 149  
 Carrapiço, C. — 33, 39  
 Cennini, P. — 33, 39  
 Cerutti, F. — 33, 39  
 Chiaveri, E. — 33, 39  
 Chin, M. — 33, 39  
 Chin, M. P. W. — 45  
 Colonna, N. — 33, 39  
 Cortés, G. — 33, 39, 145  
 Cortés-Giraldo, M. — 33, 39  
  
 Dillmann, I. — 33, 39  
 Domingo-Pardo, C. — 33, 39  
 Dupont, E. — 81  
 Duran, I. — 33, 39  
  
 Eykens, R. — 101  
  
 Fernández-Ordóñez, M. — 33, 39  
 Ferrari, A. — 33, 39  
 Fraile, L. M. — 149  
  
 Gamboni, Th. — 133  
 Ganesan, S. — 33, 39  
 Garcia, A. R. — 149  
 Geerts, W. — 133  
 Giomataris, I. — 39  
 Giubrone, G. — 33, 39  
 Gómez-Hornillos, M. B. — 33, 39, 145  
  
 Gonçalves, I. F. — 33, 39  
 González-Romero, E. — 33, 39  
 Gorini, G. — 51  
 Gorlychev, V. — 145  
 Gottardo, A. — 149  
 Gramegna, F. — 33, 39  
 Grosse, E. — 93  
 Guber, K. H. — 1  
 Guerrero, C. — 33, 39, 149  
 Gundacker, St. — 109  
 Gunsing, F. — 33, 39, 121  
  
 Hambsch, F.-J. — 127, 133, 139  
 Harrisopulos, S. — 33, 39  
 Hawkes, N. P. — 75  
 Heil, M. — 33, 39  
  
 Igashira, M. — 9  
 Ioannides, K. — 33, 39  
  
 Jaime Tornin, R. — 133  
 Jericha, E. — 33, 39  
 Jordan, M. D. — 149  
 Junghans, A. R. — 93  
  
 Kadi, Y. — 33, 39  
 Käppeler, F. — 33, 39  
 Karadimos, D. — 33, 39  
 Karlsson, J. — 127  
 Kharoua, C. — 45  
 Kim, G. N. — 21  
 Kis, Z. — 121  
 Kiyonagi, Y. — 9  
 Kolkowski, P. — 75  
 Kopecky, S. — 15, 27  
 Köster, U. — 65  
 Krása, A. — 155  
 Krtička, M. — 33, 39  
  
 Lebbos, E. — 33, 39  
 Lederer, C. — 33, 39  
 Ledoux, X. — 127  
 Leeb, H. — 33, 39, 109  
 Letourneau, A. — 81  
 Lindroos, M. — 45  
 Losito, R. — 33, 39  
 Lozano, M. — 33, 39  
 Luyckx, K. — 101  
  
 Mach, H. — 149  
 Majerle, M. — 155  
 Marganec, J. — 33, 39

- Marmouget, J.-G. — 127  
Marrone, S. — 33, 39  
Martinez, T. — 33, 39, 145, 149  
Massimi, C. — 27, 33, 39  
Mastinu, P. F. — 33, 39  
Meaze, M. — 33, 39  
Meaze, A. K. M. M. H. — 21  
Mendoza, E. — 33, 39, 149  
Mengoni, A. — 33, 39  
Milazzo, P. M. — 33, 39  
Moens, A. — 101  
Mosconi, M. — 33, 39, 149  
Moxon, M. C. — 27, 51  
Mutti, P. — 81
- Nakamura, S. — 87  
Noah, E. — 45  
Nolte, R. — 33, 39, 149
- Oberstedt, A. — 127, 133, 139  
Oberstedt, S. — 127, 133, 139  
Oh, Y. D. — 21  
Oshima, M. — 9  
Ovejero, M. C. — 33, 39, 149
- Panebianco, S. — 81  
Papaevangelou, T. — 39  
Paradela, C. — 33, 39  
Pavlik, A. — 33, 39  
Peeters, M. — 101  
Perelli Cippo, E. — 51  
Perkowski, J. — 33, 39  
Plag, R. — 33, 39  
Plewinski, F. — 45  
Poch, A. — 145  
Postma, H. — 59  
Praena, J. — 33, 39  
Pretel, C. — 145
- Quesada, J. M. — 33, 39
- Rahman, M. S. — 21  
Rauscher, T. — 33  
Reifarth, R. — 33, 39  
Reillo, E. — 149  
Rubbia, C. — 33, 39
- Sapundjiev, D. — 101  
Sarmiento, R. — 33, 39  
Schillebeeckx, P. — 15, 27, 51, 59  
Sibbens, G. — 101  
Siegler, P. — 15  
Svoboda, O. — 155  
Szentmiklósi, L. — 121
- Tagliente, G. — 33, 39  
Tain, J. L. — 33, 39, 145, 149  
Tarrío, D. — 33, 39  
Tassan-Got, L. — 33, 39  
Thomas, D. J. — 75
- Valiente, J. J. — 149  
Vannini, G. — 33, 39  
Variale, V. — 33, 39  
Vaz, P. — 33, 39  
Ventura, A. — 33, 39  
Vidali, M. — 133  
Villamarin, D. — 149  
Vlachoudis, V. — 33, 39  
Vlastou, R. — 33, 39  
Vrzalová, J. — 155  
Vykydal, Z. — 33, 39
- Wagner, V. — 155  
Wallner, A. — 33, 39  
Weiß, C. — 33, 39



